Structural and electronic investigations of complex intermetallic compounds

by

Hyunjin Ko

A dissertation submitted to the graduate faculty

in partial fulfillment of the requirements for the degree of

DOCTOR OF PHILOSOPHY

Major: Inorganic Chemistry

Program of Study Committee:
Gordon J. Miller, Major Professor
John D. Corbett
Mark Gordon
L. Keith Woo
Vitalij Pecharsky

Iowa State University

Ames, Iowa

2008

… to my mother,

엄마 고맙습니다.

Table of Contents

CHAPTER 1:	**General Introduction**	**1**
	Introduction	1
	Dissertation Organization	12
	References	14
CHAPTER 2:	**Synthesis and Methods**	**17**
	Synthesis	17
	Characterization Techniques and Analysis	20
	Physical Property Measurements	23
	Theory and Electronic Structure Calculations	24
	References	27
CHAPTER 3:	**Rhombohedrally Distorted γ–Brasses $Cr_xFe_{1-x}Ga$: Crystallographic, Magnetic and Electronic Structure Relationships**	**29**
	Abstract	29
	Introduction	30
	Experimental Section	31
	Results and Discussion	35
	Conclusions	59
	References	64
	Supplement Tables and Figures	68

CHAPTER 4: Between Hume-Rothery and Polar Intermetallics: $Ti_{0.86(2)}Ni_{1.95(2)}Ga_{1.2}$: A New *G*-Phase **77**

Abstract 77

Introduction 77

Experimental 79

Results and Discussion 83

Conclusions 94

References 95

CHAPTER 5: Single Crystal X-Ray Diffraction Studies on Ternary $RENiGe_3$ Series (RE = Ce-Nd, Sm, Gd-Lu; Y) **97**

Abstract 97

Introduction 98

Experimental 99

Results and Discussion 104

Conclusions 117

References 119

Supplement Tables 122

CHAPTER 6: Magnetic Structures of MM'As Series (M, M' = Cr, Mn, Fe): a Theoretical Investigation **131**

Abstract 131

Introduction 131

Methods 141

Results and Discussion 143

Conclusions 152

References 154

Supplement Figures 156

CHAPTER 7: General Conclusions 157

Appendix 3.1: Single Crystal Structure of Cr_3Ga 159

Appendix 4.1: Crystal Structures of $V_{0.6}(Co_{1-x}Ga_x)_{2.67}$ series and $Nb_{2.3(1)}RhGa_{1.4(1)}$ 162

Appendix 4.2: Crystal Structure of $Ti_{0.48(1)}NiGa_2$ 169

Appendix 4.3: Single Crystal Structure of $NbGa_3$ 172

Appendix 5.1: Anisotropic Physical Properties of RNi_xGe_3 Series (R = Y, Ce-Nd, Sm, Gd-Lu) 175

Appendix 5.2: Single Crystal Structure of $ErNi_{1.53(1)}Ge_2$ 177

Appendix 6.1: Single Crystal Structure of CeA_2Ge_2 (A = Au, Ag) 180

Appendix 6.2: Single Crystal Structure of $RhZr_2$ 183

Appendix 6.3: Single Crystal X-Ray Diffraction Studies on Ternary $REFe_2Zn_{20}$ Compounds (RE = Gd, Tb) 186

Acknowledgements 206

CHAPTER 1

General Introduction

In solid state chemistry, numerous investigations have been attempted to address the relationships between chemical structure and physical properties. Such questions include: (1) How can we understand the driving forces of the atomic arrangements in complex solids that exhibit interesting chemical and physical properties? (2) How do different elements distribute themselves in a solid-state structure? (3) Can we develop a chemical understanding to predict the effects of valence electron concentration on the structures and magnetic ordering of systems by both experimental and theoretical means? Although these issues are relevant to various compound classes, intermetallic compounds are especially interesting and well suited for a joint experimental and theoretical effort. For intermetallic compounds, the questions listed above are difficult to answer since many of the constituent atoms simply do not crystallize in the same manner as in their separate, elemental structures. Also, theoretical studies suggest that the energy differences between various structural alternatives are small. For example, Al and Ga both belong in the same group on the Periodic Table of Elements and share many similar chemical properties. Al crystallizes in the fcc lattice with 4 atoms per unit cell[39] and Ga crystallizes in an orthorhombic unit cell lattice with 8 atoms per unit cell,[24] which are both fairly simple structures (Figure 1). However, when combined with Mn, which itself has a very complex cubic crystal structure with 58 atoms per unit cell,[26] the resulting intermetallic compounds crystallize in a completely different fashion.

At the 1:1 stoichiometry, MnAl forms a very simple tetragonal lattice with two atoms per primitive unit cell,[40] while MnGa crystallizes in a complicated rhombohedral unit cell with 26 atoms within the primitive unit cell.[26(b)]

Figure 1. Unit cell structures of a) fcc Al, b) tetragonal MnAl, c) cubic α-Mn, d) rhombohedral MnGa, e) orthorhombic Ga.[24] Open circles, black filled circles, and gray filled circles represent Al, Mn and Ga respectively.

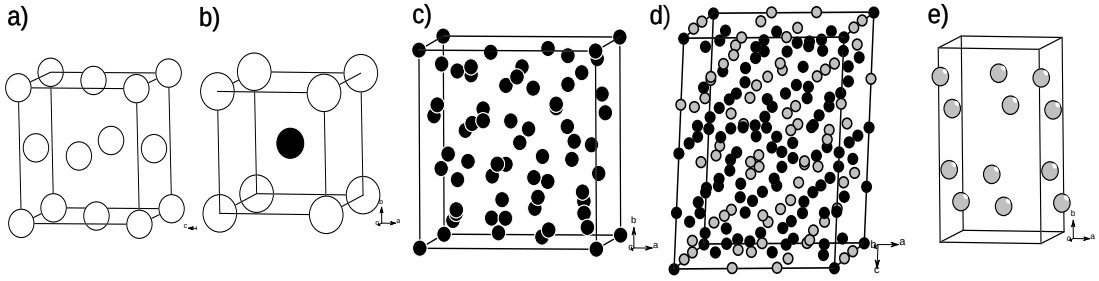

The mechanisms influencing the arrangements of atoms in numerous crystal structures have been studied theoretically by calculating electronic structures of these and related materials. Such calculations allow us to examine various interactions at the atomic scale, interactions which include orbital overlap, two-electron interactions, and Madelung terms. Moreover, these electronic studies also provide links between the angstrom-scale atomic interactions and the macro-scale physical properties, such as magnetism.

Over the past few decades, there have been many significant developments toward understanding structure-bonding-property relationships in extended solids in terms of variables including atomic size, valence electron concentration, and electronegativity. However, many simple approaches based on electron counting, e.g., the octet rule, the 18-electron rule, or Wade's rules[43-46] for boranes, cannot be

applied adequately or universally to many of the more complex intermetallic compounds.

Table 1. Summary of Hume-Rothery electron phase types with $1.0 < vec < 2.0$.[2]

Phase Type	Structure	Pearson symbol	c/a range	*vec* range
α	f.c.c.	cF4		1.00 – 1.42
β	b.c.c	cI2		1.36 – 1.59
μ	Cubic	cI52		1.40 – 1.54
γ	b.c.c.	cI52		1.54 – 1.70
δ	Cubic	cI52		1.55 – 2.00
ξ	h.c.p.	hP2	1.633	1.32 – 1.83
ε	h.c.p.	hP2	1.55 – 1.58	1.65 – 1.89
η	h.c.p.	hP2	1.77 – 1.88	1.93 – 2.0

For intermetallic phases that include late transition metals and post transition main group elements as their constituents, one classification scheme has been developed and effectively applied by using their valence electron count per atom (*vec*). These compounds are known as Hume-Rothery electron phases,[1] and they have a variety of structure types with $vec < 2.0$ as shown in Table 1.

Hume-Rothery Phases

Empirical studies of many alloy systems have shown that one of the most important factors determining the stability of intermediate phases is the valence electron concentration (*vec*). An empirical rule describing the electron concentration

scaled phase stabilization in metals is well known as the Hume-Rothery rule, and the alloys stabilized at specific electron concentrations have been referred to as Hume-Rothery phases.[32-34] Many theoretical studies suggest that the formation of a "pseudogap" at the Fermi level (E_F) in the electronic density of states (DOS) curves must be responsible for this electron concentration scaled, phase stabilization mechanism, because the total kinetic energy of valence electrons would be reduced when E_F falls in a pseudogap. A "pseudogap" is a deep, nonzero relative minimum in the DOS curve between two regions of higher DOS value. For example, in Figure 2, the Fermi level is located at a pseudogap in the DOS shown in contrast to a gap in the lower energy region.

Figure 2. An example of a pseudogap in a DOS curve.

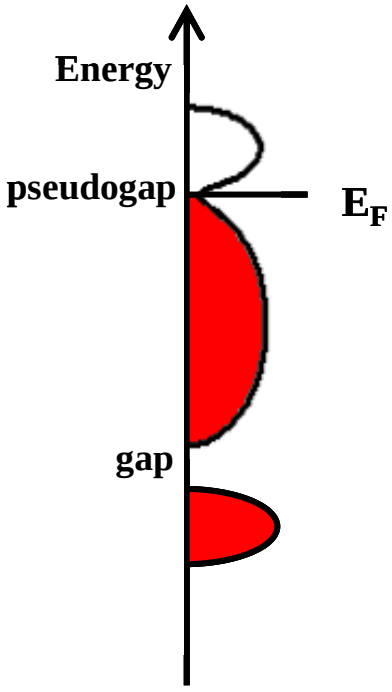

In other words, therefore, the Hume-Rothery phases are electronically stabilized structures by having the Fermi level located in a pseudogap of the density

of states curve and, thereby, lowering the kinetic energy of the valence electrons. Therefore, the factors leading to formation of a pseudogap at E_F should be investigated in order to fully understand the Hume-Rothery stabilization mechanism. A pseudogap is believed to form at E_F when the Fermi sphere with a diameter $2k_F$ makes simultaneous contacts with a number of equivalent Brillouin zone planes associated with the reciprocal lattice vector $\boldsymbol{K}_{hkl}$. Hence, the $2k_F = \boldsymbol{K}_{hkl}$ condition must be directly related to the formation of the pseudogap at E_F. The formation range for phases obtained by alloying noble metals with polyvalent post transition elements is known to be universally scaled by the valence electron per atom ratio e/a. This e/a scaled phase stability of the noble metal based, Hume-Rothery alloys has been discussed in terms of the Fermi surface-Brillouin zone (FS-BZ) interaction.[3, 4]

Hume-Rothery Phases to Quasicrystal Phases

Quasicrystals, discovered by Shechtman et al.[5] in 1984, are a class of intermetallic compounds gaining importance for their electronic, magnetic and mechanical properties. They have now been recognized as a new class of Hume-Rothery alloys, since Tsai et al.[6] and Yokoyama et al.[7] discovered a series of thermally stable Al-Cu-TM (TM = Fe, Ru, Os) and Al-Pd-TM (TM = Mn, Re) quasicrystals at a specific e/a of about 1.75. Quasicrystals are a novel class of intermetallic solids that have rotational symmetries in their diffraction patterns that are incommensurate with translational periodicity, such as 8-fold, 10-fold, or 12-fold rotations. Many quasicrystalline phases are known to have thermodynamically stable, long-range ordered building blocks such as icosahedra and dodecahedra.

Since the structures and atomic distribution in quasicrystals are difficult to solve, periodic approximants are studied, like the icosahedral phase. Such phases

are translationally normal crystalline compounds of a quasicrystal phase.[35] Quasicrystal approximants have unit cells that are believed to be identical to a fragment of the associated quasicrystalline phase, and their compositions lie very closely to the quasicrystalline phase. Crystalline approximants are of significant interest because they allow us to gain a clearer understanding of the structural properties of quasicrystals through precise determination of their atomic structures. They are generally recognized as electron phases that may be described by Hume-Rothery stabilization rules, with restricted ranges of *vec* and with pseudogaps at or near their E_F. The stability of approximants and quasicrystals are explained in terms of their local atomic structures and the resulting electronic densities of states.[36]

Fujiwara made the first *ab initio* band calculations for an approximant to the Al-Mn quasicrystal and revealed the presence of a pseudogap at E_F. He suggested that the location of E_F in the pseudogap most likely stabilizes such complex compounds.[8] The presence of a pseudogap at E_F has been observed in band calculations for other approximants, and, therefore, identified as one determining factor of quasicrystals and their approximants. However, this discussion has not been extended to whether the Brillouin zone planes involved in the $2k_F = \boldsymbol{K}_{hkl}$ condition, are indeed, responsible for producing the pseudogap at E_F.[37]

Due to the icosahedral or dodecagonal symmetry mentioned above for quasicrystals, many approximants are based on concentric shells of icosahedral and dodecagonal cages of atoms.[3] The geometrical features of these polyhedra often lead to crystalline approximants with body-centered cubic unit cells. Icosahedral quasicrystals and their approximants are classified into two families depending on the cluster unit building up its structure: one is described by the rhombic triacontahedron containing 44 atoms; and the other by the Mackay icosahedron containing 54 atoms.

γ - Brass Phases

One important crystalline structure that occurs for elements that also form quasicrystals is the cubic γ-brass structure, which crystallizes in the Laue class $\bar{4}3m$ (point symmetry = T_d) with 52 atoms in the cubic unit cell.[9] One description of the structure involves four fused atom-centered icosahedra,[10,11] which is emphasized in Figure 3. From an historical perspective, γ-brasses are considered to be Hume-Rothery electron phases because their structures are controlled to a large extent by the concentration of valence electrons.[1] Seminal examples include Cu_5Zn_8, Cu_9Al_4 and Pd_2Zn_{11}, which demonstrate the range of compositions as well as the narrowness of *vec* values (all three examples have *vec* values in the range 1.6-1.7 valence *s* and *p* electrons per atom).[12] Recent investigations into changing chemical compositions in the Pd-Zn and Pt-Zn systems show fascinating superstructures along [110] directions involving chains of fused icosahedra,[13] as well as the constancy of a $[Cu_4Zn_4]$ kernel in Cu-Zn phases.[38]

Figure 3. Cubic γ-brass unit cell structure. The black filled circles, large open circles, and small gray filled circles represent Cr, Cr/Al, and Al, respectively.[10]

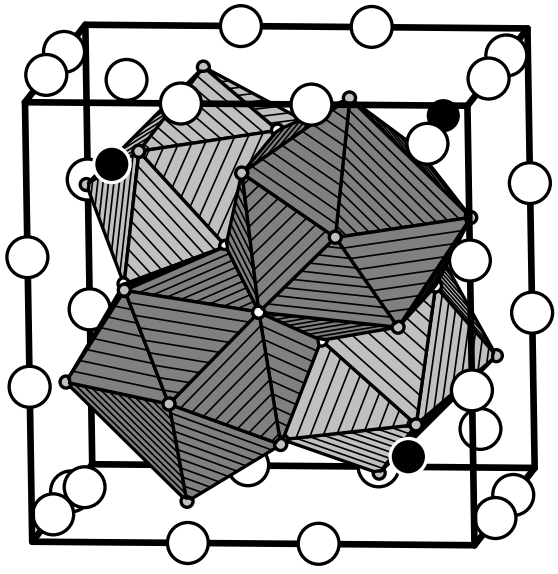

Other examples of cubic γ-brass structures that represent challenges to electron counting include Cr_5Al_8 and $Mn_{1+x}Ga_{1-x,}$ due to their partially filled 3*d* bands.

The relationship of crystal structure according to its *vec* in the γ-brass phases emphasizes the role of electronic structure in influencing atomic arrangements. In fact, the same is true of most quasicrystals. Ever since Fujiwara's first band structure calculations on the approximants of Al-Mn quasicrystals revealed the existence of a pseudogap at the Fermi level (E_F),[9] numerous empirical and *ab initio* studies have shown that the stability of various quasicrystalline phases and their approximants arise from a similar outcome. Thus, many quasicrystals and their approximants are "electron phases," because the total energy of valence electrons is reduced when E_F falls in a pseudogap, which is known as the Hume-Rothery stabilization rule.

Heusler Phases (Colorings of BCC)

Heusler alloys belong to a class of ternary intermetallics with the stoichiometric composition X_2YZ (X, Y = transition metal; Z = main group element), of which the most important contain copper, manganese, and aluminum. These alloys crystallize in the cubic Cu_2MnAl-type structure (space group $Fm\bar{3}m$). Of these, many are ferromagnetic or half-metallic, and have attracted particular interest due to their unique transport, electronic, thermoelastic and magnetic properties, which markedly depend on the X component.[14]

The face-centered cubic (fcc) Heusler phases can be viewed as four interpenetrating fcc lattices, each of which originate, respectively, at (000), (1/4,1/4,1/4), (1/2,1/2,1/2) and (3/4,3/4,3/4) of the cubic unit cell. Of these, two are equally occupied by the X element (1/4,1/4,1/4) and (3/4,3/4,3/4) and the resulting

structure is a different coloring of the body-centered cubic (bcc) lattice that either the CsCl-type or the NaTl-type structure, which is the Zintl phase, based solely on the atomic distribution in the unit cell.[15]

One of the most thoroughly studied prototypes of the Heusler alloys is the ferromagnetic and thermoelastic Ni_2MnGa (Figure 4), which is best known as the shape-memory alloy used in magnetic actuators.[17] Ni_2MnGa undergoes a martensitic transition from a high-temperature, cubic Heusler-type structure to a corresponding tetragonal structure with a 6.6% *c*-axis contraction at 200 K. The magnetic field-induced strain observed in Ni_2MnGa differs from common magnetostriction involving distortion of the crystal lattice.[18-19]

Figure 4. The fcc Heusler structure of Ni_2MnGa. The small circles, large open circles, and large filled circles represent Ni, Mn, and Ga, respectively.[16]

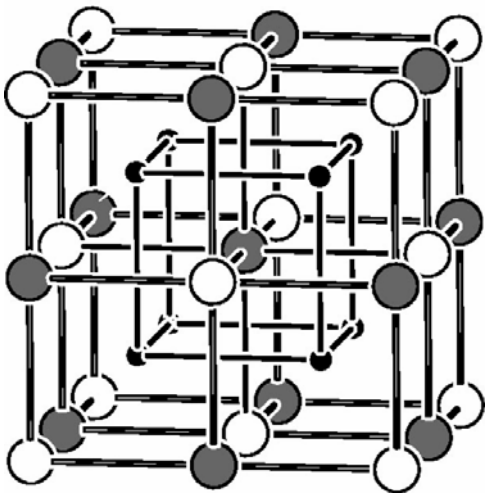

During investigations of structure-property relationships in these Heusler alloys, scientists have realized that the magnetic properties and, particularly, the magnetic transition temperature of Ni-Mn-Ga[41] alloys (and substitution for Ga with other elements) are very sensitive to fluctuations in composition. For example, by

changing the composition slightly from the 2-1-1 stoichiometry, differences in magnetic entropy of up to 15 J/kgK at the corresponding transition temperatures can be achieved.[18, 20-21,42] The idea of *vec* could also be applied to understand the nature of the lattice transformation in Ni_2MnGa, which is caused by a Jahn-Teller effect.[22] Thus, the electronic structure plays an important role in determining the magnetic properties of Heusler compounds. Two typical features in the DOS for the large group of Heusler alloys include (1) an energy gap between valence *s* states and mixed *p-d* states; and (2) their electrical behaviors structure that range from metallic to semimetallic to semiconducting behavior.

Research Motivations

In terms of molecular orbital theory, Nature often finds interatomic interactions to be optimized at particular distances by completely filling bonding states and leaving antibonding states empty.[31] In complex solid-state structures with numerous interatomic contacts, many competing interactions make it difficult to optimize all bonds. If this optimization cannot be established for a given structure and chemical composition, the structural instabilities (i.e., those showing antibonding interactions at the Fermi level) could be removed by a variety of chemical, structural, and electronic modifications, all of which affect the orbital interactions and the associated electronic density of states. These modifications include structural distortions, creation of vacancies or mixed site occupancies, and spin polarization, among others. Moreover, the complexity of crystal orbitals and their dependence on *k*-points adds further challenges in interpreting the electronic structure from an atomistic perspective. Crystal orbital Hamilton Population (COHP) analysis is a powerful yet simple tool that is widely used among theoretical solid-state chemists.

For a particular interatomic interaction, the DOS is weighted by the corresponding Hamiltonian matrix element to generate a COHP curve within the theoretical framework of density functional theory. The sum of Kohn-Sham eigenvalues (ε_i), the band energy, can be partitioned into interatomic ($j = k$) and interatomic ($j \neq k$) contributors according to

$$\sum_i \varepsilon_i = \sum_j \sum_k \int_{-\infty}^{\varepsilon_F} dECOHP_{jk}(E)$$

There have been many studies devoted to gain insights about structure-composition-property relationships in complex solids. While experimental results have demonstrated that the properties of materials can be tuned and enhanced based on their structural modifications and chemical composition changes, a clear mechanistic understanding of the relationship between the three has not yet emerged. Perhaps the greatest challenge to the development of this link is lack of intermediate phases, which can combine simple and complex structures with different properties.

Figure 5. A classification triangle for intermetallics.

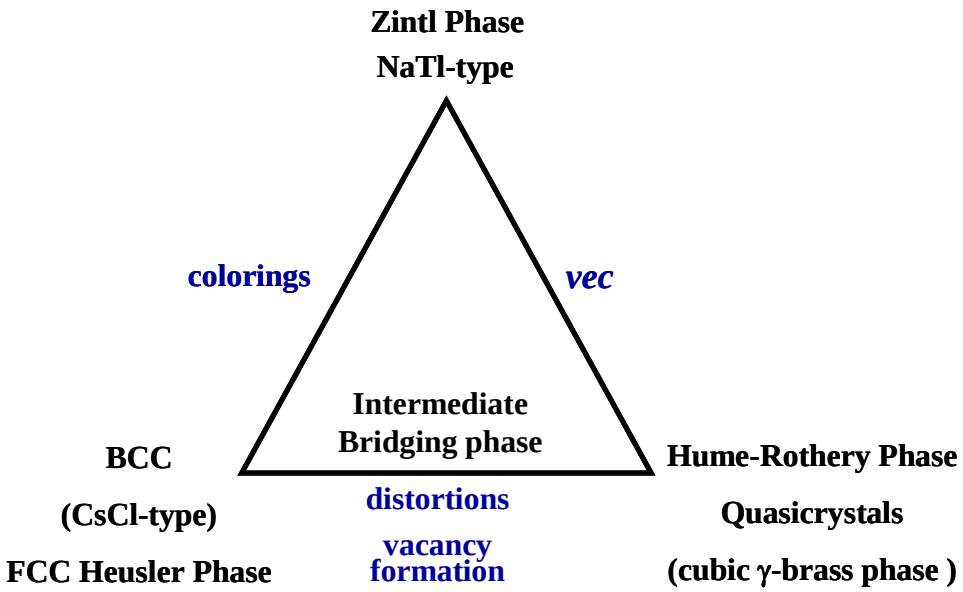

In Figure 5, previously discussed intermetallic phases are located on each vertex of the phase triangle. The sides of this triangle represent characteristics that link different types of phases. For instance, the fcc Heusler phase can be viewed as a different coloring of the bcc NaTl-type Zintl phase. If all atoms in these two unit cells would be colored with the same atom, they would look identical. However, if this Heusler phase goes through a structural change by either a lattice distortion or by creating vacancies, then the cubic γ-brass (Hume-Rothery) phase can be constructed via formation of some intermediate bridging phase.

One theme that establishes the connecting link in the triangle in Figure 4 can be seen by a COHP analysis. When the Fermi level for a given chemical structure is located among antibonding states, Nature often adopts a new electronic structure to move the Fermi level away from these states by: (1) shifting the majority spin states to lower energy and minority spin states to higher energy to create itinerant magnetic order; (2) distorting the lattice structure to specifically eliminate the antibonding interactions; or (3) changing chemical composition by allowing shared site occupancies and/or by creating vacancies which modify the valence electron count or eliminate antibonding interaction. In this dissertation, we attempt to explore these electronic responses for various examples representing different parts of the triangle.

Chapter 2 describes general experimental and theoretical methods used throughout the dissertation.

Chapter 3 discusses syntheses and structural characterization of the $Cr_xFe_{1-x}Ga$ series. These 3*d* transition metal gallide phases adopt rhombohedrally distorted γ-brass structures, and the local spin states of the magnetically active 3*d* elements, Cr

and Fe, are oriented in complex one-dimensional icosahedra chain with intrinsic magnetically frustrated environments.

Chapter 4 provides an introduction to the intermetallic phase that bridges the Heusler phase and the γ-brass structure; an observation that for the first time, begin to establish relationships between these diverse compound classes. $Ti_{0.80(2)}Ni_{1.83(2)}Ga_{1.12}$ adopts a structure with a different coloring of the defect-bcc network related to the fcc "$TiNi_2Ga$" Heusler phase, but with ordered vacancies. This structure is directly related to the γ-brass structure sharing its 26-atom cluster building block, and the existence of a pseudogap at the Fermi level by optimizing short interatomic contacts (COHP analysis) also provides a similar electronic picture as the γ-brass phases.

Chapter 5 focuses on the interplays between electronic structure, crystallographic structure, and chemical composition as part of a study of new rare-earth intermetallics. Large single crystals of the $RENi_{1-x}Ge_3$ family (RE = Ce-Nd, Sm, Gd-Er, Y) were grown in a Ge flux for physical property measurements. Here, the competition to obtain energetic stability occurs between the compound's lattice energy and Ni concentration, which affects the total valence electron count. Studies of crystal structures and COHP analyses indicate that a decreasing Ni content is needed to maintain electronic stability. $YbNiGe_3$ and $LuNiGe_3$ crystallize in new structure types.

Chapter 6 summarizes theoretical investigations on Cu_2Sb-type MM′As (M, M′ = Cr, Mn, Fe). This study focuses on the spin orientations of 3*d* metals in tetrahedral and square pyramidal environments for various valence electron counts. From the computational results, two spin sublattices are distorted especially in the vicinity of

the Fermi level, and the tetrahedral site has the larger effect in structure stabilization with a majority of the states located around the Fermi energy.

References

[1] Hume-Rothery, W. *J. Inst. Met*. **1926**, 35, 295.

[2] Barrett, C.; Massalski, T. B.; *Structure of Metals*, Pergamon Press, 3rd ed. **1980**, 248.

[3] Mizutani, U.; Takeuchi, T.; Fourne´e, V.; Sato, H.; Banno, E.; Onogi, T. *Scripta mater*. 44, **2001**, 1181.

[4] Tsuei, C. C.; Newkirk, L. R. *Phys. Rev*., 183, 3, **1969**, 623.

[5] Schechtman, D.; Blech, I.; Gratias, D.; Cahn, J. W. *Phys. Rev. Lett*. 53, **1984**, 1951.

[6] Tsai, A. P.; Guo, J. Q.; Abe, E.; Takakura, H.; Sato, T. J. **Nature**, 408, **2000**, 537.

[7] Tsai, A. P.; Yokoyama, Y.; Inoue, A.; Masumoto, T. *Jpn. J. Appl. Phys*., 20, **1990**, L1161.

[8] Fujiwara, J. *Phys. Rev*. B40, **1989**, 942.

[9] Bradley, A. J.; Gregory, C. H. *Philosophical Magazine*, 12, **1931**, 143

[10] Brandon, J. K.; Pearson, W. B.; Riley, P. W.; Chieh, C.; Stokhuyzen, R. *Acta. Crystal. B* 33, **1977**, 1088.

[11] Ellner, M.; Braun, B.; Predel, Z. *Metalkde.* 80, **1989**, 374.

[12] Hoistad, L. M.; Lee, S. *J. Am. Chem. Soc*. **1991**, 113, 8216.

[13] Tamura, R.; Nishimoto, K.; Takeuchi, S. *Phys. Rev. B.* 71, **2005**, 092203.

[14] Bradley, A. J.; Rogers, J. W. *Proc. Royal. Soc. London. A*. 144, 852, **1934**, 340.

[15] Parlyuk, V. V.; Dmytriv, G. S.; Chumak, I. V.; Ehrenberg, H. *J. Solid State Chem*. 178, **2005**, 3303.

[16] Bungaro, C.; Rabe, K. M.; Corso, A. D. *Phys. Rev. B*. 68, **2003**, 134104

[17] *Proc.* SMART-2000 (*Sendai, Japan*)

[18] Webster, P. J.; Ziebeck, K. R. A.; Town, S. L.; Peak, M. S. *Phil. Mag. B.* 49, **1984**, 295

[19] Ma, Y; Awaji, S.; Watanabe, M.; Matsumoto, M; Kobayashi, N. *Solid State Commun*, 113, **2000**, 671

[20] Ullakko, K.; Huang, J. K.; Kantner, C.; O'handley, R. C.; Kokorin, V. V. *J. Appl. Phys. Lett.*, 69, **1996**, 1966.

[21] Matsui, M.; Asano, H.; Ohmori, K.; Murakami, D.; Nakakura, T. *Dig. IEEE Int. Magnetics Conf. INTERMAG Asia*, **2005**, 1939.

[22] Jiang, C.; Wang, J.; Xu, H. *Dig. IEEE Int. Magnetics Conf. INTERMAG Asia,* **2005**, 1941.

[23] Villars, P. *Pearson's Handbook*, ASM International, **1997.**

[24] Goldman, A. I.; Kelton, R. F. *Rev. Mod. Phys*. **1993**, 65, 213.

[25] Zijlstra, E. S.; Bose, S. K. *Phys. Rev. B* 184205, **2004**, 70.

[26] (a) Gourdon, O.; Miller, G. J. *J. Solid State Chem*. 173, **2003**, 137.

(b) Gourdon, O.; Bud'ko, S.; Williams, D.; Miller, G. J. *Inorg. Chem.* **2004**, 43, 3210

[27] Tremolet de Lacheisserie, E. du. *Magnetostriction: Theory and Applications of Magnetoelasticity.* Boca Raton, FL: CRC Press, **1993**.

[28] Hoffmann R. *Solids and Surfaces: A chemist's View of Bonding in Extended Structures*, VCH, 3 **1988**.

[29] Hoffmann, R. *J. Chem. Phys*. **1963**, 39, 1397.

[30] Burdett, J. K. Chemical Bonding in Solids, Oxford University Press, New York, **1995**.

[31] Weiss, P. *J Phys*. **1907**, 6, 661.

[32] Mott, N. F.; Jones, H. *The Theory of the Properties of Metals and Alloys*, Dover, **1958**.

[33] Barrett, C.; Massalski, T. B. *Structure of Metals*, McGraw Hill, **1966**.

[34] Massalski, T. B.; Mizutani, U. *Progr. Mater. Sci*. **1978**, 22, 151.

[35] Shechtman, D. ; Blech, I.; Gratias, D.; Cahn, J. W. *Phys. Rev. Lett*. **1984**, 53, 1951.

[36] Trambly de Laissardière, G.; Fujiwara, T. *Materials Science Forum*. **1994**, 150-151, 417.

[37] Mizutani, U.; Asahi, R.; Sato, H.; Takeuchi, T. *Philosophical Magazine*. **2006**, 86, 645.

[38] Gourdon, O.; Gout, G.; Williams, D. J.; Proffen, T.; Hobbs, S.; Miller, G. J. *Inorg. Chem.* **2007**, 46(1), 251.

[39] Otte, H. M.; Montague, W. G.; Welch, D. O. *J. Appl. Phys*. **1963**, 34, 3149.

[40] Koester, W.; Wachtel, E. *Zeits. fuer Metal*. **1960**, 51, 271.

[41] Buschow, K. H. J.; van Engen, P. G.; Jongebreur, R. *J. Magn. Mag. Mater*. **1983**, 38, 1.

[42] Albertini, F.; Canepa, F.; Cirafici, S.; Franceschi, E. A.; Napoletano, M.; Paoluzi, A.; Pareti, L.; Solzi, M. *J. Magn. Mag. Mater*. **2004**, 272-276(Pt. 3), 2111.

[43] Wade, K.; *Chem. Commun*. **1971**, 792.

[44] Wade, K.; *Adv. Inorg. Chem. Radiochem*. **1976**, 18, 1.

[45] Mingos, D. *Nat. Phys. Sci*. **1972**, 236, 99.

[46] Mingos, D. *Acc. Chem. Res*. **1984**, 17, 311.

CHAPTER 2

Experimental Methods

Synthesis

The search for new materials with desired physical properties begins with synthetic challenges that emphasize the significance of selecting the optimum preparation method which must be based on knowledge of material handling, pretreatment, and homogenizing methods with benefits and limitations of each technique and its subsequent influences on the research objectives.

Starting Materials

High purity elements are used as starting materials designed to prepare 0.5 g of a hypothetical target phase in all the reactions performed. A list of these elements is given in Table 1.

Most of the elements are used as received from the manufacturer, but an extra preparatory step is applied to a few cases when necessary. For highly sensitive reactants, surface impurities such as metal oxides are either etched using appropriate acidic solution[1] or mechanically filed after the oxide impurities are diffused to the surface by arc-melting, then rinsed with water, dried, and given a final rinse again with acetone.

Table 1. Reactant Elements Used for Material Preparations.

Element	Source	Purity	Form
RE	Ames Lab.	> 99.99 %	Chunks, ~ 2 g
Co	Ames Lab.	99.995%	Pieces, < 0.5 g
Cr	*Alfa Aesar*	99.99%	Pieces, 3-8 mm
Fe	*Alfa Aesar*	99.97+%	Pieces, 12 mm
Ga	*Alfa Aesar*	99.9999%	Ingots, ~ 2.5 g
Mn	*Alfa Aesar*	99.99%	Pieces, < 0.5 g
Nb	Ames Lab.	99.8%	Rod, ~ 10 g
Ni	Ames Lab.	99.98%	Wire, 1.0 mm
Pt	Ames Lab.	99.99%	Pieces, < 0.3 g
Rh	Ames Lab.	99.95%	Pieces, < 0.1 g
Sn	Ames Lab.	99.999%	Pieces, < 0.5 g
Ti	Ames Lab.	99.95%	Foil, < 0.75 mm
V	Ames Lab.	99.7%	Foil, < 0.5 mm
Zn	Ames Lab.	99.996%	Chunks, ~ 2 g

Reaction Containers

One of the important aspects of solid-state synthesis is selection of a proper material for a reaction container. For most cases, a silica tube is used as the reaction vessel if the elements don't attack the container. Whenever required, other reaction vessels are considered, e.g. alumina crucibles where Ga metal is used as a flux material. The silica tube is first rinsed with distilled water, then the residual water is dried off with acetone followed by oven-baking at 393 K for ca. 2-3 hrs. After the initial cleaning, the tubes are treated with a gas/oxygen torch flame under dynamic

vacuum ($p < 5 \times 10^{-6}$ torr) to eliminate residual hydroxides from the inner wall of the tube, and, finally, are sealed off.

Arc Melting

For high reaction temperatures, initial melting of stoichiometric quantities of high purity reactant elements is accomplished in an arc-melting furnace[1]. Typically, the weighed elements are placed on a water-cooled copper hearth under an argon atmosphere at a slightly greater pressure than the atmospheric pressure. A sharp, thoriated tungsten electrode is used to create an arc between the electrode and the copper hearth to achieve temperatures ca. 3273 K.

This technique provides an advantage by overcoming kinetic barriers in solid state reactions, and also shortens the reaction time relative to the ones done in a tube furnace. On the other hand, the continuously water-cooled copper hearth brings a disadvantage of creating temperature gradients between the top and bottom of the sample resulting in compositional variations throughout the sample. By turning over the sample and repeating the arc-melting process several times, a homogeneous sample can be achieved. Another problem occurs when using elements with high vapor pressures or with very different densities. To overcome the inevitable mass loss of these reactants, a slight excess (usually 0.5 - 1.0 wt. %) of the particular element is loaded.

Furnaces

Most reactions are carried out in a tube furnace which can achieve temperatures up to 1473 K. The reaction temperature profile is controlled by a programmable temperature controller equipped with a J-type thermocouple. The

reactants are melted and typically allowed to homogenize at 1273-1323 K for 24-48 hours. Then, the crystals are encouraged to nucleate and grow by slow cooling to the target annealing temperature at a rate of 1 K/min. This procedure usually yields single crystals suitable for subsequent X-ray diffraction experiments.

Visual Inspection

Initial product characterization is performed by visual inspection of the samples. From the colors and possible morphologies of the products, qualitative analysis of product yield is estimated as well as the possibility of side-reaction products with impurities, e.g., reactions with the reaction container. Also, the brittleness, crystal shapes, and crystallinity are examined.

Characterization

Powder X-ray Diffraction Analysis

The primary method of product characterization is Guinier X-ray powder diffraction using a *Huber* 670 image plate camera. The samples are ground and evenly dispersed on a *Mylar* film aided by using petroleum jelly in hexane. The incident X-ray radiation is Cu $K_{\alpha 1}$ (λ = 1.540598Å) and the 2θ values range from 4 to 100° at 0.005° increments. A typical data collection is obtained by scanning the image plate 10 times after an exposure time of 1 hour at room temperature.

The lattice parameters of the sample are indexed by a least squares fit of the 2θ values for the diffraction intensities, and the phase purity is also estimated for crystalline phases present in the sample.[9-10] From these indexed intensities, the structure type is compared with the simulated patterns from known crystal structures generated by the program *PowderCell*[2]. If an unknown structure is recognized, the

reflections are manually indexed and compared against the results from single crystal X-ray diffraction experiments. For accurate lattice constants as well as the crystal symmetry, it is critical to obtain high quality powder patterns.

Single Crystal X-Ray Diffraction Analysis

Additional information about the crystal structure is obtained by single crystal X-ray diffraction. Suitable crystals, usually with well-defined facets and reflective surfaces, are selected and mounted on silica fibers, then transferred to one of two single crystal X-ray diffractometers, either the *Bruker SMART APEX CCD* or the *STOE-IPDS*. Each diffractometer uses monochromated Mo K_α radiation (λ = 0.71073 Å). The initial determination of the lattice type and parameters is completed using a random search subroutine by collecting twenty-five reflections. From the information on possible lattice types obtained by indexing and refining reflections and determining the orientation matrix, measurement parameters such as data collection ranges and exposure times are optimized using software packages accompanying the diffractometer controller.

A typical data collection on the *Bruker CCD* is completed in a hemisphere or full-sphere of reciprocal space with 0.3° scans in ω for 10 sec/frame. Data processing includes Lorentz polarization correction and an empirical absorption correction using the *SAINT*[3] and *SADABS*[4] program suites and including correction factors for a cylindrical, plate-like, or spherical crystal shape as necessary[5]. Then, the absorption corrected data are averaged in the corresponding space group to generate a reduced data set for use in subsequent structure refinements.

Data collected on the *STOE* image plate is processed by a numerical absorption correction using the *X-shape and X-red* software packages[6]. Then, the

averaged and merged data sets are used in structure determinations and refinements.

The structure refinements are carried out with the *SHELXTL*[7] program suite by full-matrix, least-squares refinements on F^2 using reflections with $I > 2\sigma(I)$. Atomic positional parameters, site occupancies, isotropic (U_{eq}) and anisotropic (U_{ij}) thermal displacement parameters, and the extinction coefficients (g) are refined for a complete structure solution. For an isotropic model, the atomic displacement parameters (B or U_{eq}) are related by the scattering factor for a stationary atom $f(\theta)$ and for the vibrating atom $f'(\theta)$.

$$f'(\theta) = f(\theta)\exp(-B\sin^2\theta/\lambda^2) = f(\theta)\exp(-8\pi^2 U\sin^2\theta/\lambda^2)$$

The equivalent isotropic temperature factor[8] corresponds to a sphere with a volume that is equal to the ellipsoid represented as:

$$U_{eq} = \frac{1}{3}\sum_i\sum_j U_{ij}a_i^* a_j^* \vec{a}_i\vec{a}_j$$

The anisotropic temperature factor is described by a combination of three tensors: the overall translation represented by the six independent components of a symmetric tensor T, the rotary oscillation also represented by a symmetric tensor L, and screw motion represented by an unsymmetrical tensor S. For an anisotropic model, six components are used in the exponent of the scattering factor equation:

$$-B\sin^2\theta/\lambda^2$$
$$= -2\pi^2(U_{11}h^2a^{*2} + U_{22}k^2b^{*2} + U_{33}l^2c^{*2} + 2U_{23}klb^*c^* + 2U_{13}hla^*c^* + 2U_{12}hka^*b^*)$$

The extinction coefficient, g, is a parameter centered in the relation

$$F_{c(corr)} = \frac{F_c}{1 + gF_c^2 \cdot L_p}$$

where L_p is the Lorentz - polarization factor.

The solution of the crystal structure refinement is evaluated and reported with the corresponding statistical terms, which include the final residual electron densities

and *R*-values:

$$R = \frac{\sum |F_0| - |F_c|}{\sum |F_0|}$$

$$R_w = \left[\frac{\sum w\left(|F_0| - |F_c|\right)^2}{\sum w F_0^{\,2}} \right]^{1/2}$$

for refinement on F where $w = \frac{1}{\sigma_F^{\,2}}$.

Chemical Analysis

Elemental analyses by energy dispersive X-ray spectroscopy are performed on a *JEOL 840A* scanning electron microscope in collaboration with Dr. Warren Straszheim in the Materials Science and Engineering Department. The instrument is equipped with an *IXRF Systems* Iridium X-ray analyzer with *Kevex Quantum* thin-window Si(Li) detector. Typical data collections utilize a 20 kV accelerating voltage and a 30 mA beam current. For accurate path length calculations of the back-scattered electrons, the samples are prepared by polishing the surfaces to flatness within a microscale. The standardless method is used with elemental references as internal standards.

Magnetic Susceptibility Measurements

Magnetic susceptibility measurements are obtained using a *Quantum Design MPMS-5 SQUID* magnetometer in collaboration with Dr. Sergey L. Bud'ko and Prof. Paul Canfield in the Department of Physics and Astronomy. A typical set of magnetic susceptibility (χ) data are measured from 1.7 to 300 K on ca. 20 mg of polycrystalline samples in applied magnetic fields of 1 kOe and 10 kOe with a 7 T superconducting magnet. The collected data are assessed with the magnetic property

measurement system (*MPMS-5*[11]) software unless otherwise indicated.

Effective magnetic moments (μ_{eff}) and Weiss temperatures (Θ_{w}) are calculated for samples in temperature ranges where paramagnetic Curie-Weiss behavior is observed, which is common for temperatures exceeding 100 K. The susceptibility obtained from linear regression of $1/\chi$ versus T plots is given by:

$$\chi = \frac{\left(\frac{N\mu_{eff}^2}{3k_B}\right)}{(T - \Theta_w)},$$

where N is the number of magnetic atoms, and k_{B} is the Boltzman constant.

Electronic Structure Calculations

Tight-Binding Approximation

The tight-binding[12] method of modeling the electronic structure of materials is one of the most widely used computational techniques. This approach works by replacing the many-body Hamiltonian operator with a parameterized Hamiltonian matrix and by solving the Schrödinger equation using an atomic-like basis set. The atomic-like set has the same symmetry properties as the atomic orbitals. The tight-binding approach has been demonstrated to work very well for covalently bonded systems such as C, Si, Ga, Ge, In, etc and *d*-band transition metals.

Extended Hückel Method

Electronic structure calculations with the Extended Hückel approach are performed using the tight-binding approximation, and the energy density of states (DOS) and crystal orbital overlap population curves (COOP) are calculated using special sets of *k* points[13]. The calculations include overlaps out to two neighboring

unit cells along every translation vector. A Mulliken population analysis is particularly useful to give insights on the site preferences in the crystal structures.

The total DOS of a system is defined as:

$$g(E) = \sum_n \delta(E - E_n)$$

where the sum runs over all energy states E_n of the system. The DOS is just the number of energy levels between E and $E+dE$ divided by the infinitesimal energy interval dE. For crystals with perfectly periodic atomic arrangements:

$$g(E) = \sum_k \delta(E - E(k)) .$$

The sum runs over all possible values of the wave vector k, but in actual calculations we restrict k to the first Brillouin zone[14]. The DOS concept is extremely useful in electronic structure calculations, especially given that the DOS is an experimentally measurable quantity by a variety of techniques such as scanning tunneling microscopy. From the calculated DOS, the Fermi energy is obtained by filling up the lowest energy states each with two electrons until the total number of electrons is achieved.

Linear Muffin-Tin Orbital (LMTO) Method

More extensive theoretical studies of electronic structure are carried out by self-consistent calculations within density functional theory by using the tight-binding, linear muffin-tin-orbital (TB-LMTO) method[15-18] within the atomic sphere approximation (ASA) using the Stuttgart code[19]. Exchange and correlation are treated in a local spin density approximation (LSDA).[20] All relativistic effects except spin-orbit coupling are taken into account using a scalar relativistic approximation.[21] Within the ASA, space is filled with overlapping Wigner-Seitz (WS) atomic spheres. The radii of the WS spheres are obtained by requiring the

overlapping potential to be the best possible approximation to the full potential according to an automatic procedure.[22] Interstitial voids are filled by generating zero potential WS spheres without significantly increasing the overlapping sphere volume to fill 100% of the unit cell volume with WS spheres. The reciprocal space integrations to determine the self-consistent total energies and charge densities with the convergence criterion of 0.136 meV, densities of states (DOS) and crystal orbital Hamilton populations (COHP) [13] are performed by the tetrahedron method[14] in the irreducible wedges of the corresponding Brillouin zones.

Methods based on the density functional theory (DFT) are the most widely used first principles methods in computational materials science and solid-state chemistry and physics. This is due to their high computational efficiency and very good accuracy for ground state electronic properties. DFT starts with a consideration of the entire many-body electron system. Within DFT, all aspects of the electronic structure of the system of interacting electrons in the potential generated by atomic cores are determined completely by the electronic charge density $\rho(r)$[23]. This allows the wavefunctions to be scaled down from 3*N* variables to 3 variables, where *N* represents the total number of electrons in the system. In DFT, the total energy has three contributions: (1) a kinetic energy term; (2) a Coulomb energy term from the classical electrostatic interactions among all charged particles; and (3) the exchange-correlation energy term capturing all many-body electron-electron interactions:

$$E[\rho] = \sum_{m}^{occup} \varepsilon_m - \frac{1}{2}\iint \frac{\rho(r_1)\rho(r_2)}{|r_1 - r_2|} dr_1 dr_2 - \int V_{xc}(r)\rho(r)dr + E_{xc}[\rho(r)].$$

The unknown correlation interactions can be estimated by using the local density approximation (LDA)[24], which turns out to be surprisingly reliable for many

systems including metals and transition metal compounds. In this approximation, the exchange-correlation energy is taken from the known results in a homogeneous electron gas of constant density.

For systems containing unpaired electrons, the spin-polarized density functional theory[25] has been developed. In this theory, both the electron density and the spin density are fundamental quantities with the net spin density being the difference between the up-spin and the down-spin electrons:

$$\sigma(\mathrm{r}) = \rho\uparrow(\mathrm{r}) - \rho\downarrow(\mathrm{r})$$

where the total electron density (ρ) is the sum of these two densities and spin polarization (ζ) is:

$$\rho(\mathrm{r}) = \rho\uparrow(\mathrm{r}) - \rho\downarrow(\mathrm{r})$$

$$\zeta(r) = \frac{\rho\uparrow(r) - \rho\downarrow(r)}{\rho(r)}.$$

References

[1] Wendelstorf, J.: *Proc. 2nd Int. SteelSim.* **2007**, Austria, 433.

[2] Kraus, W.; Nolze, G.; *PowderCell 1.8*, **1996**.

[3] SMART; Bruker AXS, Inc.; Madison, WI, **1996.**

[4] Blessing, R. H.: An empirical correction for absorption anisotropy. *Acta. Cryst.*. **1995**, A 51, 33.

[5] Busing, W.R.; Levy, H.A. *Acta Cryst*., **1957**, 10, 180-182.

[6] Stoe & Cie; *X-SHAPE* (Version 1.03) and *IPDS Program Package* (Version 2.89). Stoe & Cie, Darmstadt, Germany, **1998**.

[7] *SHELXTL*; Brucker AXS, Inc.; Madison, WI, **1996**.

[8] Kartha, G.; Ahmed, F. R.; *Acta Crystallographica*, **1960**, 13 (7), 532–534.

[9] Larson, A. C.; Von Dreele, R. B. *GSAS: General Structure Analysis System*. **1985.**

[10] Rietveld, H. M. *J. Appl. Crystallogr*. **1969**, 2, 65.

[11] Quantum Design; Quantum Design, Inc.; San Diego, CA, **2000**.

[12] Goringe, C. M.; Bowler, D. R.; Hernández, E.; Rep. Prog. Phys. **1997**, 60, 1447.

[13] Dronskowski, R.; Blöchl, P. *J. Phys. Chem*. **1993**, 97, 8617.

[14] Blöchl, P. E.; Jepsen, O.; Andersen, O.K. *Phys Rev.* **1994**, B49, 16223.

[15] Andersen, O. K. *Phys. Rev.* **1975**, B12, 3060.

[16] Andersen, O. K.; Jepsen, O. *Phys. Rev. Lett.* **1984**, 53, 2571.

[17] Andersen, O. K.; Jepsen, O.; Glötzel, D. In *Highlights of Condensed-Matter Theory*; Bassani, F.; Fumi, F.; Tosi, M. P.; Lambrecht, W. R. L.; Eds.; North-Holland: New York, **1985**.

[18] Andersen, O. K. *Phys. Rev.* **1986**, B34, 2439.

[19] The Stuttgart Tight-Binding LMTO-ASA program Version 4.7; Max-Planck-Institut für Festkörperforschung, Stuttgart, Germany **1998**.

[20] Von Barth, U.; Hedin, L. *J. Phys. C* **1972**, 5, 1629.

[21] Koelling, D. D.; Harmon, B.N. *J. Phys. C* **1977**, 10, 3107.

[22] Jepsen, O.; Anderson, O. K. *Z. Phys. B* **1995**, 97, 35.

[23] Burdett, J. K. Chemical Bonding in Solids, Oxford University Press, New York, **1995**.

[24] Ammeter, J. H.; Bürgi, H. B; Thibeault, J. C.; Hoffmann, R. *J. Am. Chem. Soc.* **1978**, 100, 3686.

[25] Pauling, L.; Kamb, B. *Proc. Natl. Acad. Sci. USA*, **1986**, 83, 3569.

CHAPTER 3

Rhombohedrally Distorted γ–Brasses $Cr_xFe_{1-x}Ga$: Crystallographic, Magnetic and Electronic Structure Relationships

(manuscript in preparation for submission to *Inorganic Chemistry*)

*Hyunjin Ko,[#] Olivier Gourdon,[%] Delphine Gout,[%] Eun-Deok Mun,[&] and Gordon J. Miller[#]**

[#] Department of Chemistry, Iowa State University and Ames Laboratory, Ames, Iowa 50011-3111,

[%] Los Alamos National Laboratory, Los Alamos, New Mexico 87545,

[&] Department of Physics and Astronomy, Iowa State University, Ames, Iowa 50011-3111

ABSTRACT

A series of rhombohedrally distorted γ-brass structures involving a mixture of magnetically active 3*d* elements Cr and Fe, $Cr_xFe_{1-x}Ga$, are investigated by crystallographic, magnetic, and theoretical approaches. Powder X-ray diffraction experiments on $Cr_xFe_{1-x}Ga$ result in unit cell volume decrease as Fe content increases. Neutron powder diffraction and X-ray single crystal diffraction experiments reveal M2 site prefers to have Cr atoms while M3 site prefers to have Fe atoms. Antiferromagnetically ordered metals resulting in overall ferromagnetically ordered unit cell are observed by a susceptibility measurement. A first principles calculation indicated an existence of the Fermi level in a pseudogap.

Introduction

The relationship between crystal structure and valence electron concentration (*vec* = # valence electrons / # atoms in the chemical formula) in γ-brass phases emphasizes how electronic structure can influence chemical compositions and atomic arrangements in complex intermetallic compounds. The γ-brass structure belongs to a class of "Hume-Rothery" phases, which involve late and post-transition metals, whose structures are controlled by their *vec* values.[37-39] Specifically, γ-brasses exist for *vec* values in the range 1.6 – 1.7, as found for Cu_5Zn_8, Cu_9Al_4, and Pd_2Zn_{11}.[40] To determine the *vec* in these phases, only valence *s* and *p* electrons are utilized. Extensive first principles calculations on various γ-brass structures identify the existence of a pseudogap in the density of states (DOS) curve at the corresponding Fermi levels. Although the structure itself leads to local minima in the electronic DOS curves at the Fermi level, the atomic distribution enhances the pseudogap, as in the Cu-Zn system, for example.[36] In the Zn-Pd and Cd-Pd systems, slight variations in chemical composition lead to superstructure behavior of the γ-brass phases.[41] The presence of a pseudogap in the DOS led to a cluster-counting rule that correctly accounts for the periodicity along a single dimension.

In addition to these crystalline intermetallics, many quasicrystals are also called "Hume-Rothery electron phases." Ever since Fujiwara's first band structure calculations on the approximants to Al-Mn quasicrystals revealed the existence of a pseudogap at the Fermi level,[9] numerous empirical and *ab initio* studies have shown that the stability of various quasicrystalline phases and their approximants also give a similar outcome. This so-called "Hume-Rothery stabilization rule" is important for the stability of many quasicrystals and their approximants.

As part of an effort to study the properties and electronic structures of

quasicrystal approximants, we reported on the magnetic and structural characteristics of the series, MGa (M = Cr, Mn, Fe), which adopt the rhombohedral Cr_5Al_8 structure type.[10(b)] In fact, this structure is a rhombohedral distortion of the cubic γ-brass structure, and this distortion has been attributed to electronic ("band structure") factors.[4] The isostructural series, CrGa-MnGa-FeGa, also shows a variation from antiferromagnetic to ferromagnetic behavior, which is important for gaining insights into the relationship between itinerant magnetism and energy band filling.[10] In the present chapter, we report on the crystal structures of the ternary series $Cr_xFe_{1-x}Ga$, as well as their magnetic properties and theoretical electronic structures to examine the relationships among structure, composition and properties of quasicrystal approximants.

Experimental Section

Synthesis. Eleven compositions in the series of $Cr_xFe_{1-x}Ga$ ($0 \leq x \leq 1$) samples were prepared by heating the pure elements under controlled environments. Prior to these reactions, Cr metal pieces (irregular, 99.99%, Alfa-Aesar) were cleaned in an acidic solution (1:3 ratio by volume of concentrated nitric and hydrochloric acids) for approximately 30 seconds, and rinsed with methanol; Fe metal pieces (irregular, 99.97+%, Alfa-Aesar) were cleaned in an acidic ethanol solution (10:1 ratio by volume of ethanol and concentrated nitric acid) for 2 minutes, and rinsed with methanol; while Ga metal ingots (99.99%, Alfa-Aesar) were used without any pretreatment. To prevent the formation of any oxide phases and to minimize the formation of other impurities, the elements were then individually melted in an arc furnace on a copper hearth under an argon atmosphere. The subsequent surface oxide layer of the ingots was removed by filing. The stoichiometric mixtures of

$Cr_xFe_{1-x}Ga$ ($0 \leq x \leq 1$; increments of 0.1; loading errors were less than 0.01% by weight for 3g samples) were heated in sealed, evacuated silica tubes at 1323 K for 80 hours to promote the optimum diffusion of Cr and Fe metals into liquid Ga. After cooling at the rate of 1 K/min. to 1123 K, the homogenized sample was annealed at 1123 K for 1 week. Termination of the solid state reaction occurred by turning off the furnace and the product was allowed to be naturally cooled down to room temperature. Visual inspections and powder X-ray diffraction experiments are taken after > 4 months of product formation. The product appears to be stable against decomposition in both air and moisture over a period of several months at room temperature.

Chemical Analysis. The phase purity of the products was analyzed by Energy Dispersive Spectroscopy (EDS) (quantitative analysis) using a *JEOL* 840A scanning electron microscope, equipped with an *IXRF* Systems Iridium X-ray analyzer with *Kevex* Quantum thin-window Si(Li) detector for quantitative chemical analysis by standardless method. Typical data collections utilized a 20 kV accelerating voltage and a 30 mA beam current. No significant oxygen or silicon contamination was observed for all products.

Diffraction Experiments. Phase analysis was performed by powder X-ray diffraction (PXRD) at room temperature and crystal structures were confirmed and further refined by single-crystal X-ray diffraction (SXRD). Temperature-dependent neutron powder diffraction was carried out specifically on "$Cr_{0.5}Fe_{0.5}Ga$" to obtain atomic distributions and possible magnetic structures.

Powder X-ray Diffraction: Phase characterizations were performed on several separately prepared samples from each of the products by room-temperature powder

X-ray diffraction using an *Enraf Nonius Guinier* camera with Cu K_α radiation (λ = 1.540598 Å) and Si as an internal standard. Patterns were collected for 2θ values ranging from 10º to 95º at increments of 0.02º. Lattice parameters were determined by the Rietveld[15] profile fitting method using program *Rietica* for all samples; atomic parameters were refined using the General Structure Analysis System (*GSAS*) program package[11] for the single phase sample of "$Cr_{0.5}Fe_{0.5}Ga$." Furthermore, to compare with subsequent neutron powder diffraction experiments, temperature-dependent powder X-ray diffraction measurements were carried out on "$Cr_{0.5}Fe_{0.5}Ga$" for eight different temperatures between ca. 15 K and 300 K. All the powder experiments required an exposure time of 120 min or more to obtain peak intensities high enough to be refined because all patterns showed very high background intensities.

Single Crystal X-Ray Diffraction. Several irregularly shaped small crystals with the average approximate dimensions of (120 μm^3) were selected from crushed samples of various $Cr_xFe_{1-x}Ga$ products and mounted on glass fibers. Each data set was collected on a *Bruker Apex* diffractometer at 295(2) K using monochromated MoK_α radiation (λ = 0.71073 Å) and a detector-to-crystal distance of 5.990 cm. Diffraction data were collected in a hemisphere or full sphere of reciprocal space with 0.3^o scans in ω for an exposure time of 10 sec per frame up to a maximum 2θ value of 56.55^o. Intensities were extracted and then corrected for Lorentz and polarization effects using the *SAINT* program.[12] The program *SADABS* was used for empirical absorption corrections.[13] To complete the analysis, full-matrix least-squares refinements on F^2 were performed by using the *SHELXTL-PLUS* programs.[14]

Neutron Powder Diffraction on $Cr_{0.5}Fe_{0.5}Ga$. Due to the nearly indistinguishable X-ray scattering factors between Cr and Fe, neutron powder diffraction experiments

were performed on a ca. 5 g powder sample of "$Cr_{0.5}Fe_{0.5}Ga$" to achieve better resolution of the transition metal site occupancies. Indeed, the elastic neutron cross sections for Cr (1.66×10^{-24} cm^2) and Fe (11.22×10^{-24} cm^2) are significantly different to allow us to refine site distributions accurately. Time-of-flight (TOF) neutron diffraction data were collected at 11 K, 30 K, and 295 K on the Neutron Powder Diffractometer (NPDF) at the Manuel Lujan Neutron Scattering Center of Los Alamos National Laboratory. This instrument is a high-resolution powder diffractometer located at flight path 1, 32 m from the spallation neutron target. The data were collected using the 148°, 119°, 90° and 46° banks, which cover a *d*-spacing range from 0.12 to 7.2 Å.

The structures at 11 K, 30 K and 295 K were refined using the *GSAS* package with a Rietveld profile analysis program[15] by using the MnGa structure as the starting structural model. The refinements were performed using the four banks (148°, 119°, 90° and 46°) simultaneously to obtain unit cell parameters, atomic positions, and equivalent isotropic displacement parameters. Background coefficients, scale factors, isotropic strain terms in the profile function, and sample absorption were also refined for a total of 63 parameters using the centrosymmetric space group $R\bar{3}m$. Alternative refinements were carried out in the space groups $R3m$ and $R\bar{3}$. To elucidate the arrangement and concentration of Cr and Fe in "$Cr_{0.5}Fe_{0.5}Ga$", the occupancies were also refined, which added three parameters.

Magnetic Susceptibility Measurements. A polycrystalline sample of "$Cr_{0.5}Fe_{0.5}Ga$" was used for magnetic susceptibility measurements over the temperature range from 1.7-300 K in applied magnetic fields of 1 and 10 kOe by employing a Quantum Design superconducting quantum interference device (SQUID) magnetometer with a 7-T superconducting magnet. Temperature-dependent

magnetization data were collected after the powder sample was placed in a gel-capsule fixed in a straw by first measuring zero-field cooled (ZFC) magnetization, and then the field-cooled (FC) data. All collected data were assessed with the magnetic property measurement system (MPMS-5) software supplied by Quantum Design.[16]

Electronic Structure Calculations. Theoretical electronic structures on various models of $Cr_xFe_{1-x}Ga$ were calculated self-consistently by using the tight-binding, linear muffin-tin-orbital (TB-LMTO) method[17-20] within the atomic sphere approximation (ASA) using the Stuttgart code.[21] Exchange and correlation were treated in a local spin density approximation (LSDA).[22] All relativistic effects except spin-orbit coupling were taken into account using a scalar relativistic approximation.[23] Within the ASA, space is filled by overlapping Wigner-Seitz (WS) atomic spheres. The radii of these WS spheres were obtained by requiring the overlapping potential to be the best possible approximation to the full potential according to an automatic procedure.[24] The WS radii for the atomic sites determined by this procedure are in the ranges 1.465-1.535 Å for Ga sites, 1.461-1.475 Å for Cr, and 1.455-1.481 Å for Fe. The basis set included 4*s* and 4*p* orbitals for Ga; 4*s*, 4*p* and 3*d* orbitals for Cr and Fe. The reciprocal space integrations to determine the self-consistent total energies and charge densities, densities of states (DOS) curves and crystal orbital Hamilton population (COHP)[25] curves were performed by the tetrahedron method[26] using 417 *k*-points for $Cr_7Fe_6Ga_{13}$ and 189 *k*-points for the rest of the model structures in the irreducible wedges of the corresponding Brillouin zones.

Results and Discussion

Phase Identification. Results obtained from energy dispersive spectroscopy, as well

Table 1. Phase analysis for ternary $Cr_xFe_{1-x}Ga$ specimens by EDS, PXRD, and SXRD. In PXRD, secondary phases are listed for each sample. For XRD, refined lattice constants and essential statistics are included. Compositions are represented using Ga as a reference, in accord with our formulation for $Cr_xFe_{1-x}Ga$.

Loaded Composition	$Cr_{0.1}Fe_{0.9}Ga$	$Cr_{0.2}Fe_{0.8}Ga$	$Cr_{0.3}Fe_{0.7}Ga$	$Cr_{0.4}Fe_{0.6}Ga$	$Cr_{0.5}Fe_{0.5}Ga$	$Cr_{0.6}Fe_{0.4}Ga$	$Cr_{0.71}Fe_{0.3}Ga$	$Cr_{0.8}Fe_{0.2}Ga$	$Cr_{0.9}Fe_{0.1}Ga$
EDS									
Majority	$Cr_{0.1}Fe_{0.9}Ga$	$Cr_{0.25}Fe_{0.75}Ga$	$Cr_{0.35}Fe_{0.65}Ga$	$Cr_{0.4}Fe_{0.6}Ga$	$Cr_{0.5}Fe_{0.5}Ga$	$Cr_{0.56}Fe_{0.43}Ga$	$Cr_{0.54}Fe_{0.45}Ga$	$Cr_{0.7}Fe_{0.23}Ga$	$Cr_{0.8}Fe_{0.14}Ga$
Minority	$Cr_{0.04}Fe_{0.73}Ga$	$Cr_{0.1}Fe_{0.65}Ga$		$Cr_{0.25}Fe_{0.5}Ga$		$Cr_{0.4}Fe_{0.3}Ga$, $Cr_{0.33}Fe_{0.33}Ga$	$Cr_{0.33}Fe_{0.33}Ga$, $Cr_{0.25}Ga$	$Cr_{0.5}Fe_{0.17}Ga$	$Cr_{0.6}Fe_{0.1}Ga$, $Cr_{0.25}Ga$
Trace		$Cr_{0.4}Fe_{1.8}Ga$	$Cr_{0.83}Fe_{1.5}Ga$						
PXRD									
Primary	$R\bar{3}m$								
Secondary	Fe_3Ga_4 ($C2/m$)	Fe_3Ga_4 ($C2/m$)					Cr_3Ga ($Pm\bar{3}n$) $FeGa_3$ ($P4_2/mnm$)	Cr_3Ga ($Pm\bar{3}n$) $FeGa_3$ ($P4_2/mnm$)	Cr_3Ga ($Pm\bar{3}n$)
a, b Å	12.4776(1)	12.4838(2)	12.5810(5)	12.5255(7)	12.5505(1)	12.5627(4)	12.6120(5)	12.6376(6)	
c, Å	7.7829(1)	8.0131(4)	7.9103(3)	7.8509(2)	7.8563(2)	7.8538(3)	7.8960(5)	8.441(1)	
Volume, Å^3	1049.38(2)	1081.48(5)	1084.30(7)	1066.70(2)	1071.69(2)	1073.44(6)	1087.70(7)	1167.5(2)	
R	R_p=1.47	R_p=2.25	R_p=2.08	R_p=1.68	R_p=1.66	R_p=1.99	R_p=3.27	R_p=3.87	
	R_{wp}=2.34	R_{wp}=5.22	R_{wp}=3.74	R_{wp}=2.73	R_{wp}=2.50	R_{wp}=4.03	R_{wp}=6.71	R_{wp}=8.14	
Single crystal XRD									
Refined composition	$Cr_{0.06(0)}Fe_{0.94(0)}Ga$	$Cr_{0.24(23)}Fe_{0.76(23)}Ga$	$Cr_{0.25(16)}Fe_{0.75(16)}Ga$	$Cr_{0.50(12)}Fe_{0.50(12)}Ga$	$Cr_{0.58(11)}Fe_{0.42(11)}Ga$	$Cr_{0.67(11)}Fe_{0.33(11)}Ga$	$Cr_{0.47(11)}Fe_{0.53(11)}Ga$	$Cr_{0.33(14)}Fe_{0.67(14)}Ga$	$Cr_{0.81(11)}Fe_{0.19(11)}Ga$
A, b Å	12.4695(18)	12.4927(18)	12.5161(18)	12.5398(18)	12.5527(9)	12.5595(18)	12.5743(18)	12.6153(18)	12.6431(18)
C, Å	7.7807(16)	7.8070(16)	7.8263(16)	7.8481(16)	7.8581(13)	7.8550(16)	7.8717(16)	7.8833(16)	7.8985(16)
Volume, Å^3	1047.7(3)	1055.2(3)	1061.8(3)	1068.8(3)	1072.3(2)	1073.1(3)	1077.9(3)	1086.5(3)	1093.4(3)
Data/parameters	307/30	328/32	330/32	332/32	314/32	330/32	334/31	331/30	336/30
R [$I>2\sigma(I)$]	R_1=0.0404	R_1=0.0506	R_1=0.0590	R_1=0.0427	R_1=0.0281	R_1=0.0502	R_1=0.0378	R_1=0.0711	R_1=0.0400
	R_w=0.0825	R_w=0.1109	R_w=0.1105	R_w=0.0853	R_w=0.0664	R_w=0.1168	R_w=0.0788	R_w=0.1305	R_w=0.0860
Peak/hole, e/Å^3	1.380/-1.721	1.770/-2.471	1.425/-2.125	1.479/-1.496	2.267/-1.792	2.074/-1.524	1.253/-1.395	2.531/-2.525	1.265/-1.934

as powder and single crystal X-ray diffraction, are summarized in Table 1. Most specimens showed multiple phases by EDS. Throughout the composition range in $Cr_xFe_{1-x}Ga$ from x = 0.1 to x = 0.9, the major phase was identified as the rhombohedral Cr_5Al_8-type structure, and the subsequent refinements proceeded well using the centrosymmetric space group $R\bar{3}m$. The equimolar mixture, $Cr_{0.5}Fe_{0.5}Ga$, produced an essentially single-phase product according to both EDS and PXRD measurements. Fe-rich samples ($x < 0.5$) yielded majority products near the targeted compositions. For loaded compositions with $x \leq 0.2$, a monoclinic Fe_3Ga_4-type phase could be indexed by PXRD as a secondary phase. On the other hand, Cr-rich samples ($x > 0.5$) typically resulted in the targeted structure with lower Cr content as well as other ternary phases. For the range $0.7 \leq x \leq 0.9$, a cubic Cr_3Ga-type structure was indexed, and for the samples with x = 0.7 and 0.8, an additional tetragonal $FeGa_3$-type phase was also identified by PXRD. Throughout the entire composition range, no other impurity peaks were observed by PXRD. For the binary specimens, the Fe-Ga preparation yielded a mixture of Fe_3Ga_4, Fe_2Ga and FeGa; the Cr-Ga preparation produced CrGa, Cr_3Ga, Cr_2Ga, and $CrGa_4$.

Structure Determinations. The structures of $Cr_xFe_{1-x}Ga$ were solved by both powder and single crystal X-ray diffraction; the refinement results are summarized in Tables 1 and 2. The variations in lattice parameters with composition are in good agreement between powder and single crystal diffraction results. Furthermore, the refined compositions from single crystal X-ray diffraction analyses are consistent with those from EDS: Cr-rich specimens showed refined compositions with a reduced Cr:Fe ratio than the loaded composition. Figure 1 illustrates the variation in volume per $Cr_xFe_{1-x}Ga$ formula unit based on refined chemical compositions and corresponding diffraction data: only the single crystal X-ray diffraction refinements

Table 2. Atomic parameters and isotropic temperature factors (Å^2) for the $Cr_xFe_{1-x}Ga$ phases.

Atom		SOF(Cr/Fe)	*x*	*y*	*z*	U_{eq}
Loaded:	$Cr_{0.1}Fe_{0.9}Ga$			Refined:	$Cr_{0.06(0)}Fe_{0.94(0)}Ga$	
Ga1	3*a*		0	0	0	0.007(1)
Ga2	18*h*		0.2321(1)	0.1161(1)	0.5758(2)	0.009(1)
Ga3	18*g*		0.3854(1)	3854(1)	1/2	0.007(1)
M1	3*b*	0/1	0	0	1/2	0.005(1)
M2	18*h*	0.14/0.86(10)	0.4322(2)	0.2161(1)	0.4111(2)	0.005(1)
M3	18*h*	0/1	-0.0723(1)	0.0723(1)	0.2498(2)	0.006(1)
Loaded:	$Cr_{0.2}Fe_{0.8}Ga$			Refined:	$Cr_{0.24(23)}Fe_{0.76(23)}Ga$	
Ga1	3*a*		0	0	0	0.008(1)
Ga2	18*h*		0.2325(2)	0.1163(1)	0.5750(2)	0.007(1)
Ga3	18*g*		0.3857(2)	3857(2)	1/2	0.005(1)
M1	3*b*	0.3/0.7(3)	0	0	1/2	0.005(1)
M2	18*h*	0.34/0.66(15)	0.4333(2)	0.2167(1)	0.4103(3)	0.003(1)
M3	18*h*	0.12/0.88(15)	-0.0719(1)	0.0719(1)	0.2492(3)	0.004(1)
Loaded:	$Cr_{0.3}Fe_{0.7}Ga$			Refined:	$Cr_{0.25(16)}Fe_{0.75(16)}Ga$	
Ga1	3*a*		0	0	0	0.007(1)
Ga2	18*h*		0.2329(2)	0.1164(1)	0.5746(3)	0.009(1)
Ga3	18*g*		0.3859(2)	3859(2)	1/2	0.007(1)
M1	3*b*	0.5/0.5(3)	0	0	1/2	0.003(2)
M2	18*h*	0.36/0.64(15)	0.4335(2)	0.2168(1)	0.4109(3)	0.007(1)
M3	18*h*	0.09/0.91(15)	-0.0720(1)	0.0720(1)	0.2502(3)	0.007(1)
Loaded:	$Cr_{0.4}Fe_{0.6}Ga$			Refined:	$Cr_{0.50(12)}Fe_{0.50(12)}Ga$	
Ga1	3*a*		0	0	0	0.009(1)
Ga2	18*h*		0.2330(1)	0.1165(1)	0.5745(2)	0.010(1)
Ga3	18*g*		0.3858(1)	3858(1)	1/2	0.008(1)
M1	3*b*	0.6/0.4(2)	0	0	1/2	0.003(2)
M2	18*h*	0.70/0.30(11)	0.4341(2)	0.2170(1)	0.4114(3)	0.006(1)
M3	18*h*	0.28/0.72(11)	-0.0718(1)	0.0718(1)	0.2498(2)	0.007(1)

Loaded:	$Cr_{0.6}Fe_{0.4}Ga$			Refined:	$Cr_{0.65(14)}Fe_{0.35(14)}Ga$	
Ga1	3*a*		0	0	0	0.009(1)
Ga2	18*h*		0.2339(2)	0.1169(1)	0.5736(2)	0.008(1)
Ga3	18*g*		0.3855(1)	0.3851(1)	1/2	0.007(1)
M1	3*b*	0.80/0.20(16)	0	0	1/2	0.003(2)
M2	18*h*	0.67/0.33(7)	0.4359(2)	0.2179(1)	0.4108(3)	0.006(1)
M3	18*h*	0.34/0.66(7)	-0.0712(1)	0.0712(1)	0.2498(2)	0.005(1)
Loaded:	$Cr_{0.7}Fe_{0.3}Ga$			Refined:	$Cr_{0.47(11)}Fe_{0.53(11)}Ga$	
Ga1	3*a*		0	0	0	0.006(1)
Ga2	18*h*		0.2336(1)	0.1168(1)	0.5741(2)	0.008(1)
Ga3	18*g*		0.3854(1)	3854(1)	1/2	0.006(1)
M1	3*b*	0/1	0	0	1/2	0.006(1)
M2	18*h*	0.70/0.30(10)	0.4351(2)	0.2176(1)	0.4111(2)	0.004(1)
M3	18*h*	0.31/0.69(10)	-0.0717(1)	0.0717(1)	0.2498(2)	0.005(1)
Loaded:	$Cr_{0.8}Fe_{0.2}Ga$			Refined:	$Cr_{0.33(14)}Fe_{0.67(14)}Ga$	
Ga1	3*a*		0	0	0	0.006(1)
Ga2	18*h*		0.2346(2)	0.1173(1)	0.5727(3)	0.010(1)
Ga3	18*g*		0.3852(2)	3852(2)	1/2	0.008(1)
M1	3*b*	1/0	0	0	1/2	0.003(2)
M2	18*h*	0/1	0.4373(3)	0.2187(2)	0.4111(4)	0.006(1)
M3	18*h*	0.55/0.45(18)	-0.0715(2)	0.0715(2)	0.2505(4)	0.006(1)
Loaded:	$Cr_{0.9}Fe_{0.1}Ga$			Refined:	$Cr_{0.81(11)}Fe_{0.19(11)}Ga$	
Ga1	3*a*		0	0	0	0.005(1)
Ga2	18*h*		0.2349(1)	0.1175(1)	0.5730(2)	0.009(1)
Ga3	18*g*		0.3846(1)	3846(2)	1/2	0.007(1)
M1	3*b*	1/0	0	0	1/2	0.003(1)
M2	18*h*	1/0	0.4371(2)	0.2185(1)	0.4118(3)	0.005(1)
M3	18*h*	0.59/0.41(10)	-0.0717(1)	0.0717(1)	0.2503(2)	0.005(1)

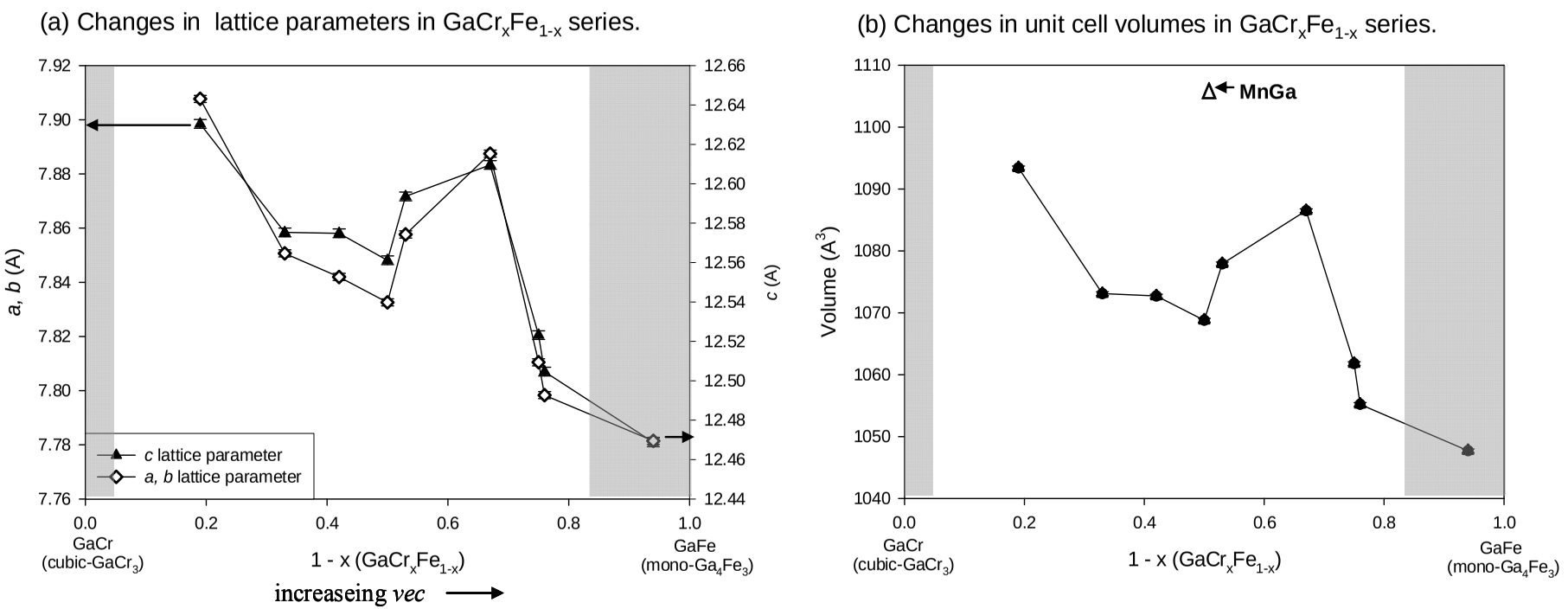

Figure 1. Lattice parameters and unit cell volume changes from Single crystal refinement results on $Cr_xFe_{1-x}Ga$ series as a function of loading composition.

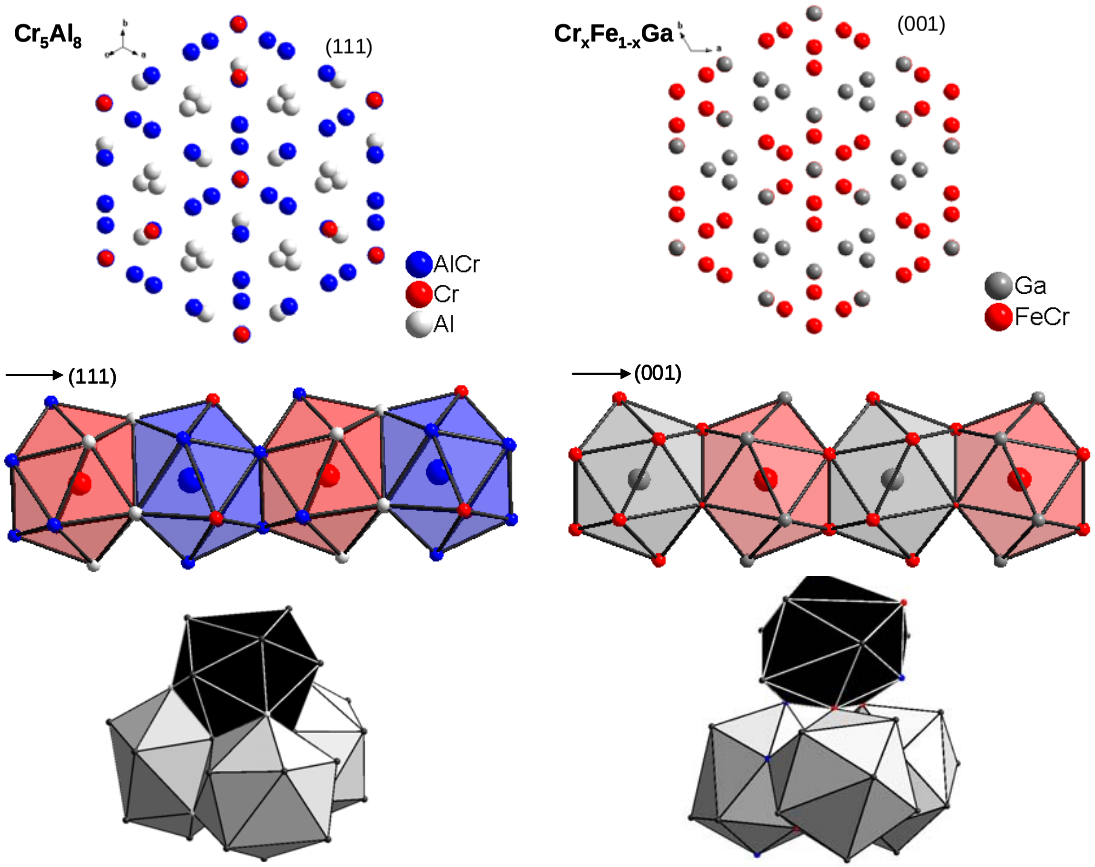

Figure 2. Structural comparison between cubic γ-brass Cr_5Al_8 and rhombohedrally distorted $Cr_xFe_{1-x}Ga$ system. Projection view of the 1-D icosahedra chains shown in cubic Cr_5Al_8 γ-brass structure in (111) direction (left, top) and trigonal $Cr_xFe_{1-x}Ga$ in *c*-direction (right, top). One dimensional icosahedra chain in Cr_5Al_8 (left, middle) and in $Cr_xFe_{1-x}Ga$ (right, middle). Tetrahedron icosahedra basic building block in two systems (bottom). Al & Ga are in white where the transition metals are in black and grey in the last picture.

were used for this plot due to the high backgrounds on the powder X-ray diffraction patterns. According to Figure 1, as the Fe content increases, there is a monotonic decrease in the volume, which is consistent with the size relationship between Cr and Fe atoms based on 12-coordinate metallic radii (r_{Cr} = 1.26 Å and r_{Fe} = 1.25 Å).[42] Furthermore, we have no conclusive evidence for the existence of a rhombohedral phase for Cr-rich samples, at least for x > 0.33. On Figure 1, we include the volume for MnGa, which is considerably larger than the isoelectronic and equiatomic $Cr_{0.5}Fe_{0.5}Ga$.

Single crystal X-ray diffraction experiments on selected crystals from each of the products yielded atomic positions and an estimation of the site occupancies for Cr and Fe atoms. Table 2 lists the atomic coordinates, site occupancies, and equivalent displacement parameters for the single crystal samples listed in Table 1. Figure 2 illustrates views of a representative $Cr_xFe_{1-x}Ga$ structure both parallel and perpendicular to the *c*-axis. These views are compared with related views of the cubic γ-brass structure, views that are parallel and perpendicular to the [111] direction of the cubic cell. Based on the centrosymmetric space group $R\bar{3}m$, the Cr_5Al_8 structure type contains six atoms in the asymmetric unit: three sites are occupied by Ga; three sites are occupied by non-statistical mixtures of Cr and Fe atoms. The rhombohedral structures of $Cr_xFe_{1-x}Ga$ are built of chains of face-sharing, atom-centered icosahedra along the *c*-axis. There are two types of icosahedra: (i) Ga-centered, $(Cr, Fe)_{12}$ icosahedra; and (ii) (Cr, Fe)-centered, $[(Cr, Fe)_6Ga_6]$ icosahedra, which alternate along the *c*-axis. Each of these icosahedra is surrounded by a pentagonal dodecahedron: around (i) is found a $[(Cr, Fe)_2Ga_{18}]$ polyhedron; around (ii) occurs a $[(Cr, Fe)_6Ga_{14}]$ dodecahedron. With these pseudo-pentagonal polyhedra forming important building blocks, these structures are interesting for their

relationships with icosahedral quasicrystals and their crystalline approximants.

To gain a better understanding of the distribution of Cr and Fe atoms in these phases, as well as to explore possible magnetic structures, temperature-dependent neutron diffraction measurements on a polycrystalline sample of "$Cr_{0.5}Fe_{0.5}Ga$" were conducted. Figure 3 illustrates the observed and calculated neutron diffraction patterns at 295 K as an example. Figure 4 illustrates the temperature-dependent lattice constants as measured by both neutron and X-ray powder diffraction; the trends are identical, while the lattice parameters determined from the neutron data are systematically lower than those obtained from X-ray diffraction. Refinements of the neutron data, which included background coefficients, scale factors, profile functions and absorption coefficients, as well as relaxing the site occupancies for Cr and Fe, smoothly converged to give solutions with χ_2 values, respectively, of 4.504, 4.781, and 3.694 at 11 K, 30 K, and 295 K. Additional refinements were evaluated for space groups $R3m$ and $R\bar{3}$, neither of which resulted in significant improvements to the results. Table 3 summarizes the atomic parameters, site occupation factors, and equivalent isotropic displacement parameters for the asymmetric unit (again based upon the space group $R\bar{3}m$).

Based on the neutron refinements, the refined average composition of the powder sample "$Cr_{0.5}Fe_{0.5}Ga$" in the unit cell is $Cr_{19.7(4)}Fe_{19.3(4)}Ga_{39}$, or $Cr_{0.505(1)}Fe_{0.495(1)}Ga$. The special position, Wyckoff site 3*b* is slightly richer in Cr than Fe. Among the two distinct sites building up the $(Cr, Fe)_{12}$ icosahedra centered by Ga atoms, the trigonal faces linked to the 3*b* site are richer in Fe atoms; the "waist" of the icosahedron is richer in Cr atoms. According to these refinements, these site occupancies are approximately 2/3 occupancy by Cr atoms at the M1 site, and the other site (M2) connecting the adjacent icosahedra shows approximately 2/3

Table 3. Fractional atomic coordinates, site occupation factors and equivalent isotropic displacement parameters for $Cr_{0.5}Fe_{0.5}Ga$ at 11 K, 30 K and 295 K as refined by neutron powder diffraction (Rietveld method-space group *R-3m*).

Sites	SOF (Cr/Fe)	x	y	z	U_{eq}
11 K					
Cell parameters		*a*=*b*=12.5172(2) Å, *c*=7.83255(15) Å			
Ga1 (3*a*)		0	0	0	0.00506(13)
Ga2 (18*h*)		0.23328(4)	0.11664(2)	0.57472(5)	0.00448(7)
Ga3 (18*g*)		0.38580(3)	0.38580(3)	0.5	0.00412(7)
M3 (3*b*)	0.577(5)/0.423(5)	0	0	0.5	0.00247(6)
M1 (18*h*)	0.625(2)/0.375(2)	0.43369(4)	0.21684(2)	0.41218(6)	0.00363(6)
M2 (18*h*)	0.366(3)/0.634(3)	-0.07156(2)	0.07156(2)	0.24985(6)	0.00407(6)
30 K					
Cell parameters		*a*=*b*=12.5170(2) Å, *c*=7.83261(15) Å			
Ga1 (3*a*)		0	0	0	0.00507(13)
Ga2 (18*h*)		0.23327(4)	0.11664(2)	0.57471(5)	0.00459(7)
Ga3 (18*g*)		0.38576(3)	0.38576(3)	0.5	0.00414(7)
M3 (3b)	0.568(5)/0.432(5)	0	0	0.5	0.00288(8)
M1 (18*h*)	0.627(2)/0.373(2)	0.43370(4)	0.21685(2)	0.41221(6)	0.00365(8)
M2 (18*h*)	0.366(3)/0.634(3)	-0.07156(2)	0.07156(2)	0.24989(6)	0.00402(8)
295 K					
Cell parameters		*a*=*b*=12.5448(4) Å, *c*=7.8557(2) Å			
		(Powder X-ray diffraction: *a*=*b*=12.54653(32) Å, *c*=7.85602(21) Å)			
Ga1 (3*a*)		0	0	0	0.0096(2)
Ga2 (18*h*)		0.23302(5)	0.11651(3)	0.57462(8)	0.01167(15)
Ga3 (18*g*)		0.385303	0.385303	0.5	0.01008(14)
M3 (3*b*)	0.587(9)/0.413(9)	0	0	0.5	0.0054(3)
M1 (18*h*)	0.636(1)/0.364(1)	0.433807	0.216902	0.411183	0.00720(15)
M2 (18*h*)	0.383(5)/0.617(5)	-0.071547	0.071547	0.249712	0.00744(12)

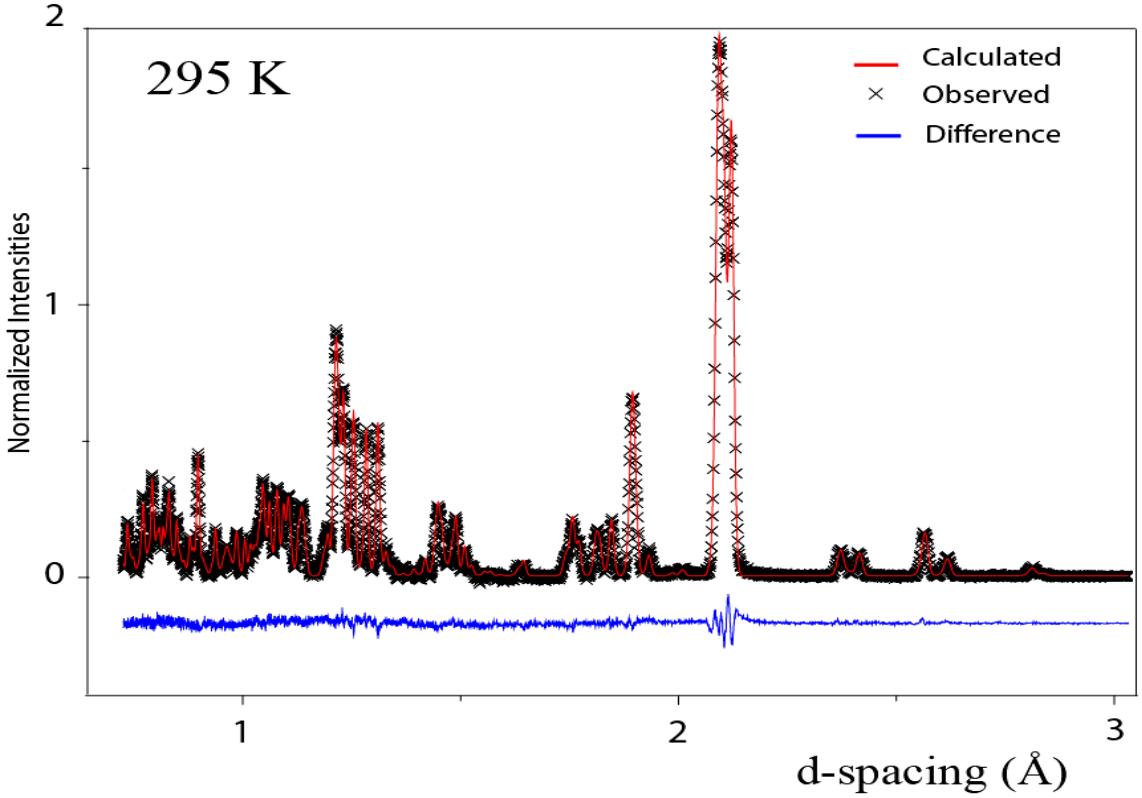

Figure 3. $Cr_{0.5}Fe_{0.5}Ga$ neutron powder pattern obtained on NPDF at 295 K. Tick marks indicate positions of the Bragg reflections. The difference between the observed and the calculated pattern is shown below the tick marks .

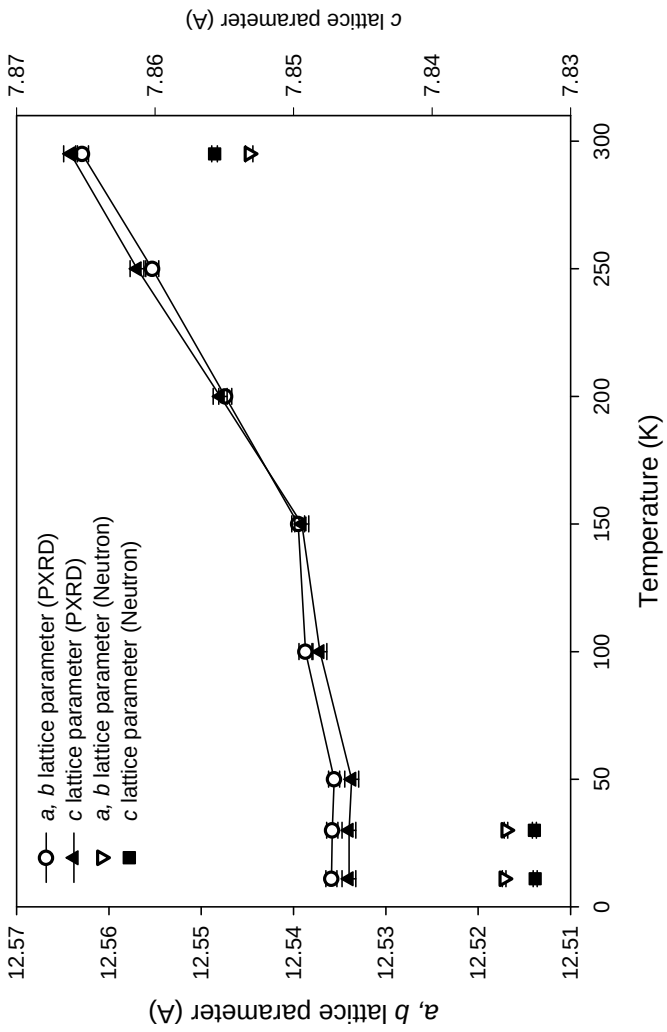

Figure 4. Non-linear temperature dependences of the lattice parameters from the powder X-ray diffraction (PXRD) and neutron diffraction refinement results.

occupancy by Fe atoms.

A neutron pair-distribution-function (PDF) analysis was also performed to investigate local structure. A combined study of Rietveld and neutron PDF analysis is generally helpful to provide information about the long-, medium- and short-range ordering in a structure. Indeed, Rietveld analysis determines only the average long-range structure because it only takes into account the intensity and the position of the Bragg peaks, whereas PDF analysis also includes information contained in the diffuse scattering. This additional information is very helpful to identify the existence of any possible short-range order. Moreover, PDF analysis allows the structure to be refined at various ranges in distance *r*. In the case of "$Cr_{0.5}Fe_{0.5}Ga$," we are particularly interested to know if any special local ordering is observable between Cr and Fe atoms for any length scale, as well as to distinguish between centrosymmetric or noncentrosymmetric space groups.

Neutron PDFs were corrected for background, the incident neutron spectrum, absorption and multiple scattering, and normalized using the vanadium spectrum to obtain the total scattering structure factor, $S(Q)$, using the program *PDFgetN*.[27] The PDF $G(r)$ was obtained from $S(Q)$ via the Fourier transform

$$G(r) = 4\pi r\left[\rho(r) - \rho_0\right] = \frac{2}{\pi}\int_0^{Q_{\max}} Q\left[S(Q) - 1\right]\sin Qr\, dQ\,,$$

where $\rho(r)$ and ρ_0, respectively, are the atomic pair number density and average number density. The data were terminated at $Q_{\max} = 40$ Å^{-1}. PDF modeling was carried out using the program *PDFGUI*[28] by using the results obtained from the Rietveld refinement as the starting structural model. At first, we relaxed numerous symmetry constraints but no significant improvements were observed, which indicates that the centrosymmetric space group $R\bar{3}m$ is the best choice to describe the average structure. Secondly, a total relaxation has been investigated to model

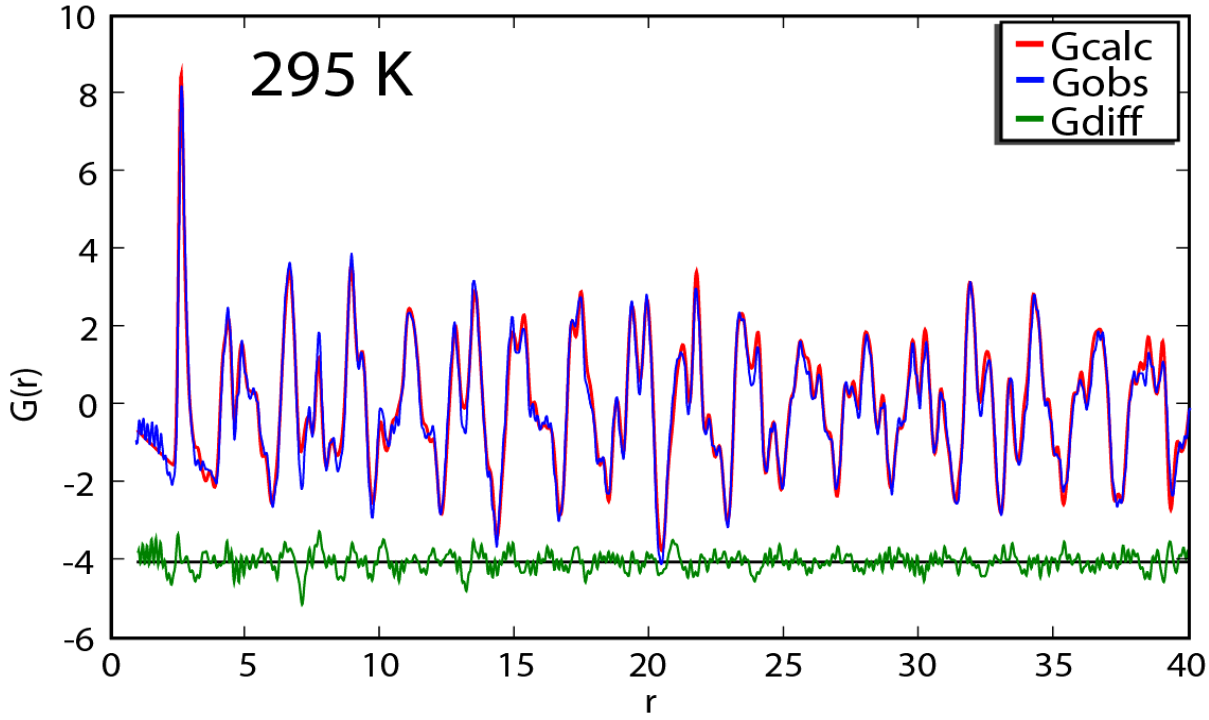

Figure 5. PDF refinement over the rmin 1.0 – rmax 40 Å range for $Cr_{0.5}Fe_{0.5}Ga$. The red, blue and green curves correspond to the G(r) calculated, observed and the difference, respectively.

possible short range ordering on the network of Cr and Fe sites, e.g., local domains of Cr or Fe atoms as "islands" or "strips." As presented in Figure 5, the fit is impressively good up to r = 40 Å, which implies that no disorder is observable at least up to that length scale. Therefore, neutron PDF analysis indicates that the local structure and the average structure obtained from Rietveld refinement are quite similar.

Magnetization Studies. According to our phase analysis by EDS and PXRD, only the loaded sample $Cr_{0.5}Fe_{0.5}Ga$ produced single-phase product. Thus, temperature-dependent magnetic susceptibility measurements were limited to this sample. Figure 6 illustrates the temperature-dependent inverse susceptibility curve measured in a 1 kOe external field. A low-field transition from paramagnetic to ferrimagnetic ordering was observed near 25 K as an upturn in the inverse susceptibility curve. Above 25 K, the linear behavior suggests Curie-Weiss behavior with an effective magnetic moment of 0.27 μ_B. Extrapolating the linear curve yields a Weiss constant of ca. –15.3 K. The upper inset in Figure 6 shows the low-temperature field-cooled and zero field-cooled susceptibilities, from which a Néel temperature (T_N) is estimated to be 20.0(5) K. Also seen in the $\sigma(H)$ curves from the lower inset to Figure 6 is a small hysterisis with metamagnetic-like behavior, which is indicated by changes in $(\partial^2 H/\partial\sigma^2)$ going from low field to high field in the lower field region. It is apparent from the upper inset to Figure 6 describing the behavior of $\chi(T)$ at low temperatures, $GaCr_{0.5}Fe_{0.5}$ orders antiferromagnetically below 20.0(5) K with spin fluctuations.

The variation of the lattice parameters with temperature, as observed by both neutron and X-ray powder diffraction, shows nonlinear behavior at lower temperatures. The high-temperature, paramagnetic phase exhibits a larger volume, than the extrapolation of the low-temperature lattice constants to higher temperatures. Thus, we see the existence of magnetostriction.[28] This is further confirmed by

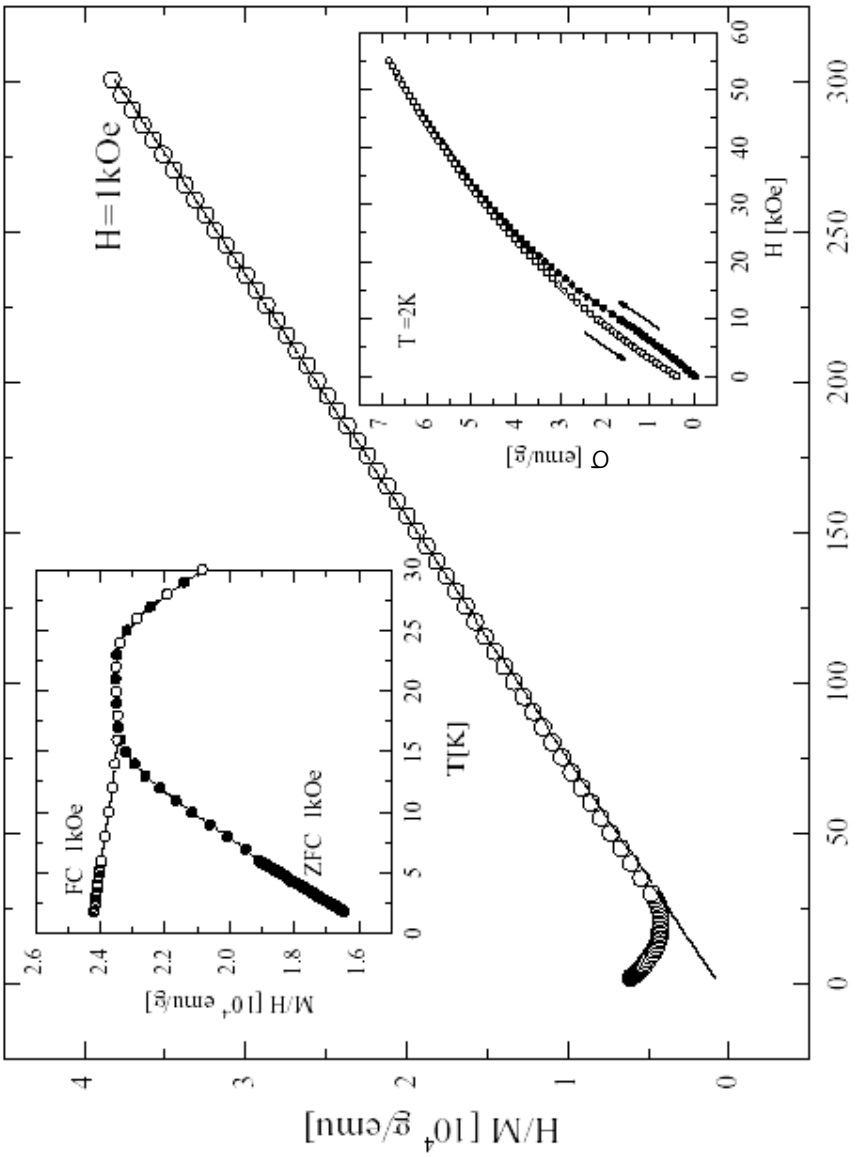

Figure 6. Magnetic susceptibility measured on powder samples of $Cr_{0.5}Fe_{0.5}Ga$.

looking at the reflections in real space rather than in reciprocal space obtained by Fourier transformation of the raw neutron powder diffraction data to generate the pair distribution function (PDF, $Q(r)$).[28] As shown in Figure 5, reflections are split more at 30 K than at 11 K while going through the magnetic phase transition around 20 K. This is unusual since PDF curves show peak smoothing effects upon temperature increase suggesting possible atomic reorientations of the metals during the magnetic phase transition without any lattice transformation.[42]

Relationship to γ-Brasses. The rhombohedral structures of $Cr_xFe_{1-x}Ga$ are closely related to the cubic γ-brass structure by showing similar one-dimensional chains of icosahedra, and are isostructural with many rhombohedrally distorted Cr_5Al_8-type structures with $\alpha < 90°$ found in the Al-Cr, Al-Cu, Ga-Cr, Ga-Mn, and Ga-Fe systems.[4] All structures share the fundamental building block of four tetrahedrally fused icosahedra, which are illustrated in Figure 1. In the cubic γ-brass structure, four icosahedra construct a perfect tetrahedron by sharing faces, but in the rhombohedrally distorted structure, three icosahedra share faces with one sitting on top of the other three sharing only edges.

Another description of cubic γ-brass structures utilizes a body-centered cubic packing of 26-atom clusters formed by the following "shells" of atoms: (i) an inner tetrahedron; (ii) an outer tetrahedron of sites capping each face of the inner tetrahedron; (iii) an octahedron sitting over each edge of the outer tetrahedron; and (iv) a distorted cuboctahedron. A recent investigation of $Cu_{5\pm x}Zn_{8\mp x}$, which combined neutron powder diffraction with electronic structure theory, demonstrated that the inner tetrahedron is always fully occupied by Zn atoms, the outer tetrahedron is always fully occupied by Cu atoms, and that the range in composition occurs by subsequent statistical occupation by Cu and Zn atoms in the octahedron and

cuboctahedron.[36] The structures of $Cr_xFe_{1-x}Ga$ resemble this pattern: (i) the inner tetrahedron is formed by the transition metals Cr and Fe (M1 + 3 M3 sites); (ii) the outer tetrahedron is exclusively formed by Ga atoms (Ga1 + 3 Ga2 sites); (iii) the octahedron involves three transition metals and three Ga atoms (3 Ga2 + 3 M2 sites); and (iv) the cuboctahedron contains six transition metals and six Ga atoms (6 Ga3 + 3 M2 + 3 M3 sites). Thus, the two inner tetrahedra form a kernel, $[M_4Ga_4]$, while the outer octahedron and cuboctahedron provide a 3D template in which these clusters are encapsulated. This template shows mixed site occupancies in either an ordered (as in $Cr_xFe_{1-x}Ga$) or disordered (as in $Cu_{5\pm x}Zn_{8\mp x}$) manner.

Pearson et al. have suggested that the rhombohedral distortion of the cubic γ-brass structure occurs as a result of band structure energy stabilization when the number of conduction electrons per 52-atom unit cell increases from the range ca. 84-90 electrons (*vec* = 1.615 – 1.730) to values ca. 95-100 electrons (*vec* = 1.827 – 1.923).[4] In this formalism, only valence *s* and *p* electrons are counted; valence *d* electrons do not contribute. The contribution of the transition metals to the number of conduction electrons is confusing in this context: in some counting schemes, Cr and Fe would contribute no conduction electrons; in others, they would be counted as one electron.[4] Nevertheless, the total valence electron counts for the cubic and rhombohedral cases differ significantly: if we include all valence *d* electrons, including the 3*d* core like electrons for the post-transition element Ga, then the valence electron count for the $Cr_xFe_{1-x}Ga$ series would range from 9.5-10.5 *spd* electrons per atom, while the cubic γ-brasses would require ca. 11.6 *spd* electrons per atom. Nevertheless, based upon the phases showing rhombohedral distortions, the Fermi level will fall among valence *d* orbitals of the transition metal, whereas the γ-brasses show the valence *d* bands to be somewhat below the Fermi level.

Electronic Structure. The calculated electronic structures of various models from the $Cr_xFe_{1-x}Ga$ series were determined and analyzed to assess the trends in observed compositions, the distribution of Cr and Fe atoms in the structure, and to understand the magnetic character of $Cr_{0.5}Fe_{0.5}Ga$.

Phase analysis: Through a combination of EDS and diffraction experiments, the $Cr_xFe_{1-x}Ga$ series does not form a homologous series between CrGa and FeGa. Cr-rich samples tend toward multiple phases with the rhombohedral phase showing a Fe content higher than the loaded composition. On the other hand, Fe-rich samples produce rhombohedral phases with compositions in line with the loaded ones. To gain some insights into this trend, the total energies of various models of the mixed-metal systems $Cr_{13-n}Fe_nGa_{13}$, $0 \le n \le 13$ are compared against the appropriate mixture of $Cr_{13}Ga_{13}$ and $Fe_{13}Ga_{13}$. Figure 7 illustrates the trend in these relative energies, which can be expressed as

$$\Delta E(n,i) = E^{(i)}(n) - \frac{n}{13}E^{(1)}(13) - \frac{13-n}{13}E^{(1)}(0),$$

where $E^{(i)}(n)$ is the total energy of Model *i* of $Cr_nFe_{13-n}Ga_{13}$. Therefore, $E^{(1)}(0)$ and $E^{(1)}(13)$ are the total energies, respectively, of $Cr_{13}Ga_{13}$ and $Fe_{13}Ga_{13}$. Figure 7 displays the results as a band of accessible energy differences because there are three different sites available for Cr and Fe atoms in the rhombohedral structure. The trend in this energy difference curve resembles the effect of different third moments of the electronic densities of states on the relative total energies.[40] According to this moments argument, the weighted average of the third moments of the densities of states of $Cr_{13}Ga_{13}$ and $Fe_{13}Ga_{13}$ will be higher than the third moments of $Cr_nFe_{13-n}Ga_{13}$. The third moment is a measure of the skewness of the density of states function, and indicates the differences in three-membered rings in the different

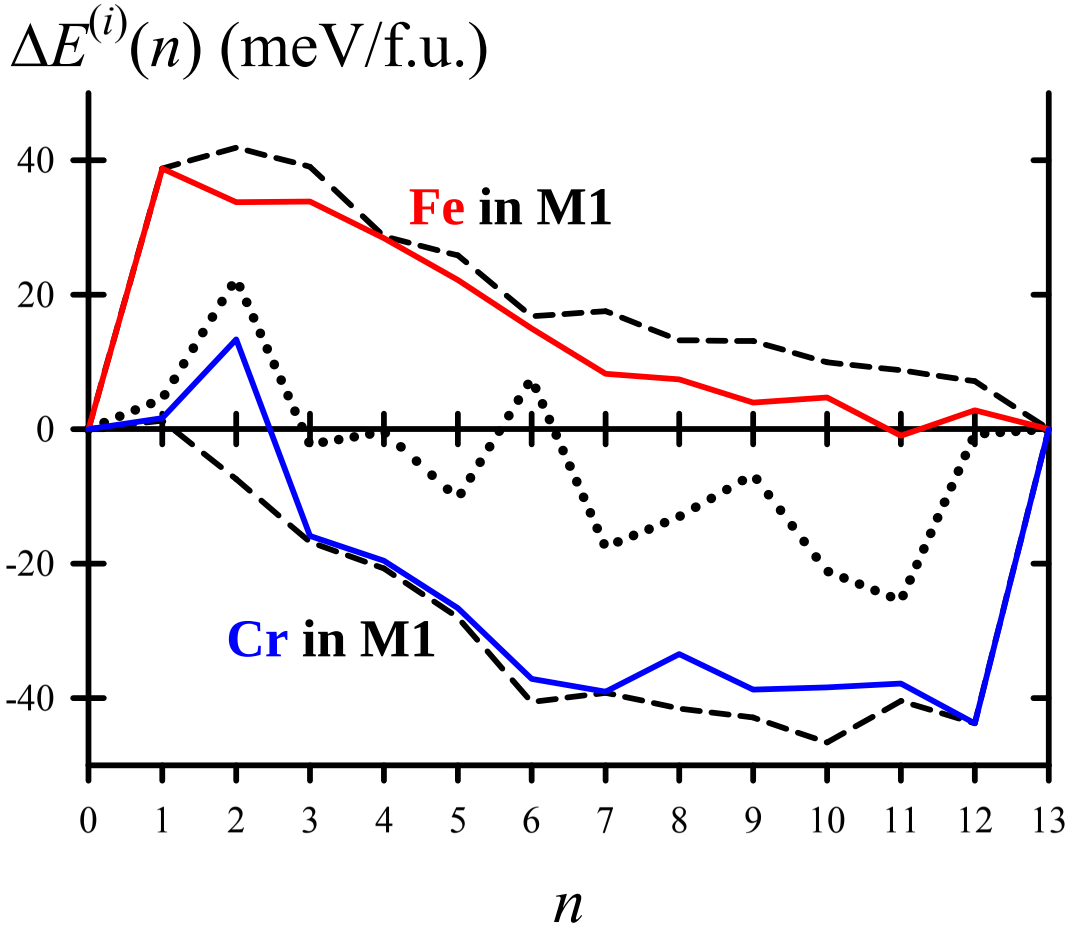

Figure 7. Relative energy trend in (Cr,Fe)Ga phases. When the energy is negative, $Cr_{13-n}Fe_nGa_{13}$ is preferred. When the energy is positive, a mixture of $Cr_{13}Ga_{13}$ and $Fe_{13}Ga_{13}$ is preferred. The two dashed lines represent the upper and lower limits from the calculations; the blue line gives energies when Cr occupies the M1 (3*b*) site; the red line gives energies when Fe occupies the M1 (3*b*) site; the dotted line is the "average" value, but it has not been calculated exhaustively.

structures. In this case, a ring corresponds to a sequence of atoms connected to each other by valence orbital overlap.

In Figure 7, the energetic trends are highlighted for Cr and Fe atoms, respectively, occupying the 3*b* special position in the rhombohedral structure, which is the transition metal site at the center of $[M_6Ga_6]$ icosahedra and which also link two adjacent Ga-centered M_{12} icosahedra along the *c*-axis. There is a clear preference for Cr in this special position over Fe atoms. The next preference for Cr is the M1 site, although the corresponding energy differences become less distinguishing. According to the refinement of site occupancies in $Cr_{0.5}Fe_{0.5}Ga$ by neutron diffraction, this theoretical conclusion is in line with experiment.

Spin polarized TB-LMTO-ASA band calculations were performed for several hypothetical model structures to see the effects of different "coloring" schemes on the electronic structures of the models: (1) $Cr_7Fe_6Ga_{13}$ (2) $Cr_6Fe_7Ga_{13}$ (3) $Cr_6Fe_6MnGa_{13}$ (4) $Mn_{13}Ga_{13}$ using the atomic structure data obtained by the single crystal X-ray diffraction structure refinement results on $Cr_{0.5}Fe_{0.5}Ga$. The first model (1) represents the structure which is closest to the refined atomic structure from the neutron analysis with simplified metal site occupancies; for example, M1 site is slightly more occupied by Cr than Fe therefore Cr was used for this site for the calculation. However, electronically this would not be the closest structure to resemble the refined composition. So Models (3) & (4) were constructed to represent structures with numbers of valence electrons closer to the refined composition. For Model (3), only the M1 site at the center of the icosahedra is occupied by Mn to reach the total valence electron count of 130 e-, whereas all metal sites are occupied by Mn in Model (4) to achieve the same number of valence electrons; the valence electron for the refined composition $Cr_{19.68}Fe_{19.32}Ga_{39}$ is 129.88

e-. Model (4) also gives an idea about the "coloring" effect by having a homoatomic transition metal gallide rather than heteroatomic transition metal gallide. In addition, to examine the effect of Fe in the icosahedra site (3*b*), a calculation on Model (2) was also carried out.

The resulting DOS curves are shown in Figure 8 and 9 for calculations on model structures (1)-(4). It can be clearly seen that the states from all three metal sites are widely spread over the energy range from above the Fermi energy down to lower than −5 eV and the Fermi levels lie in the pseudogap, which suggests that the structure is influenced by favorable metal-metal orbital mixing. In Figure 8, the Fermi levels for CrGa ad FeGa also indicated to give an idea of qualitative limits of structural flexibility. Furthermore, the pseudogap is created by the Fe-3*d* and Cr-3*d* orbital mixing when forming the icosahedra as shown in the figure (1a); the Cr in the center of the (3*b*) site does not contribute significantly to the formation of the pseudogap at the Fermi level. The Fermi level for 130 e- is found on a sharp declining slope of the DOS, which achieved electronic stabilization via spin polarization. Increasing the electron count will lead to further splitting of the majority and minority spin bands; decreasing the electron count will lead to disproportionation into CrGa and a Fe-richer $Cr_xFe_{1-x}Ga$ phases. By placing Mn in the (3*b*) site, the structure now is considerably altered with high magnetic moments on two different metal sites (Table 4). In DOS Figure (3) & (4), the downspin states are splitted shifting the Fermi level not at the pseudogap. However, about 2.5 eV above the Fermi level, a pseudogap could be found which suggests the structure might be possible to aim for this optimization point by having higher *vec* with Fe-richer composition.

The splitting of the DOS profile is noticeable in the vicinity of the Fermi level

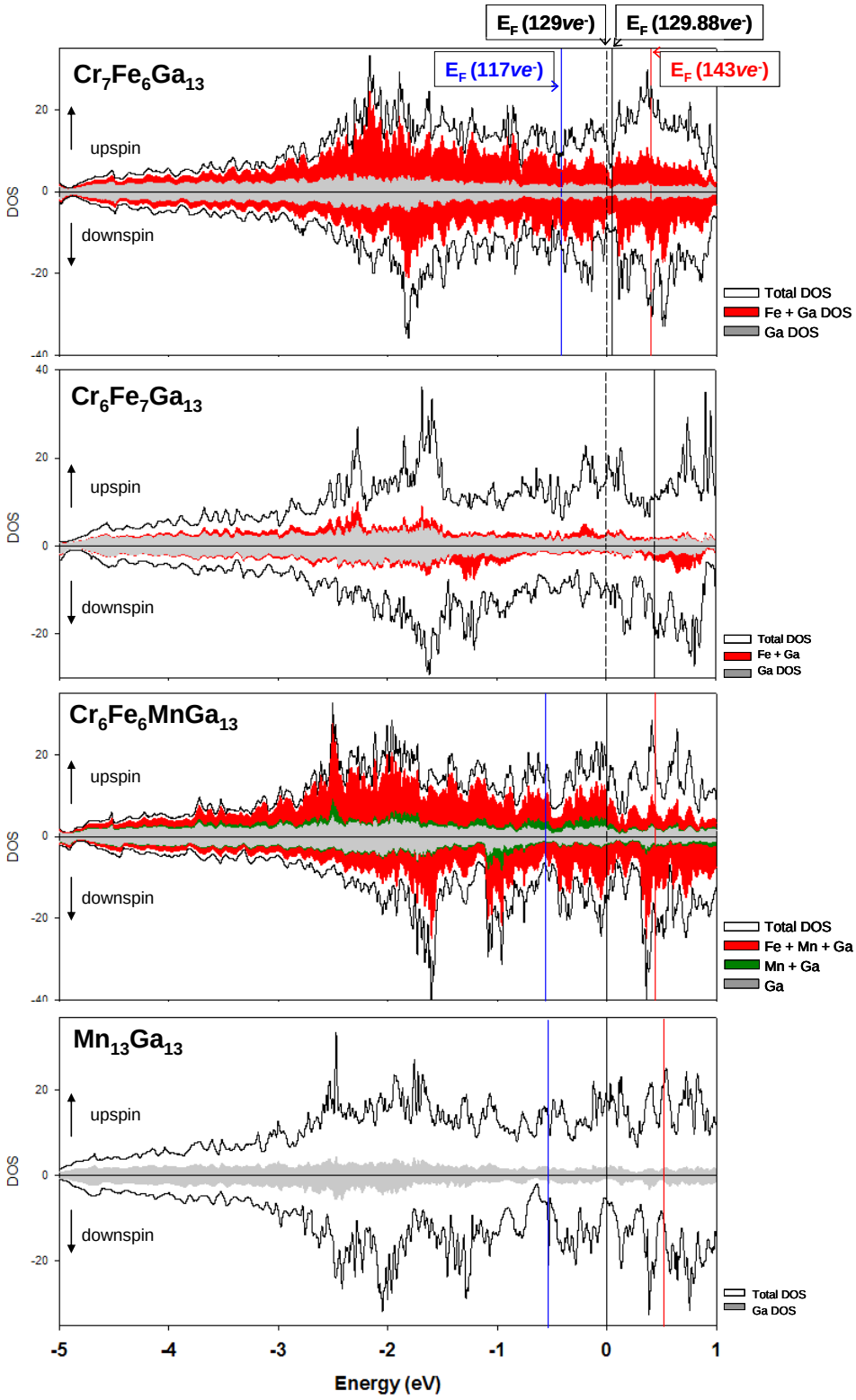

Figure 8. Density of States curves for: (1) $Cr_7Fe_6Ga_{13}$ (2) $Cr_6Fe_7Ga_{13}$ (3) $Cr_6Fe_6MnGa_{13}$ (4) $Mn_{13}Ga_{13}$ (top to bottom). The dotted lines represent the E_F obtained from calculations while the solid lines represent the E_F for experimentally obtained electron counts.

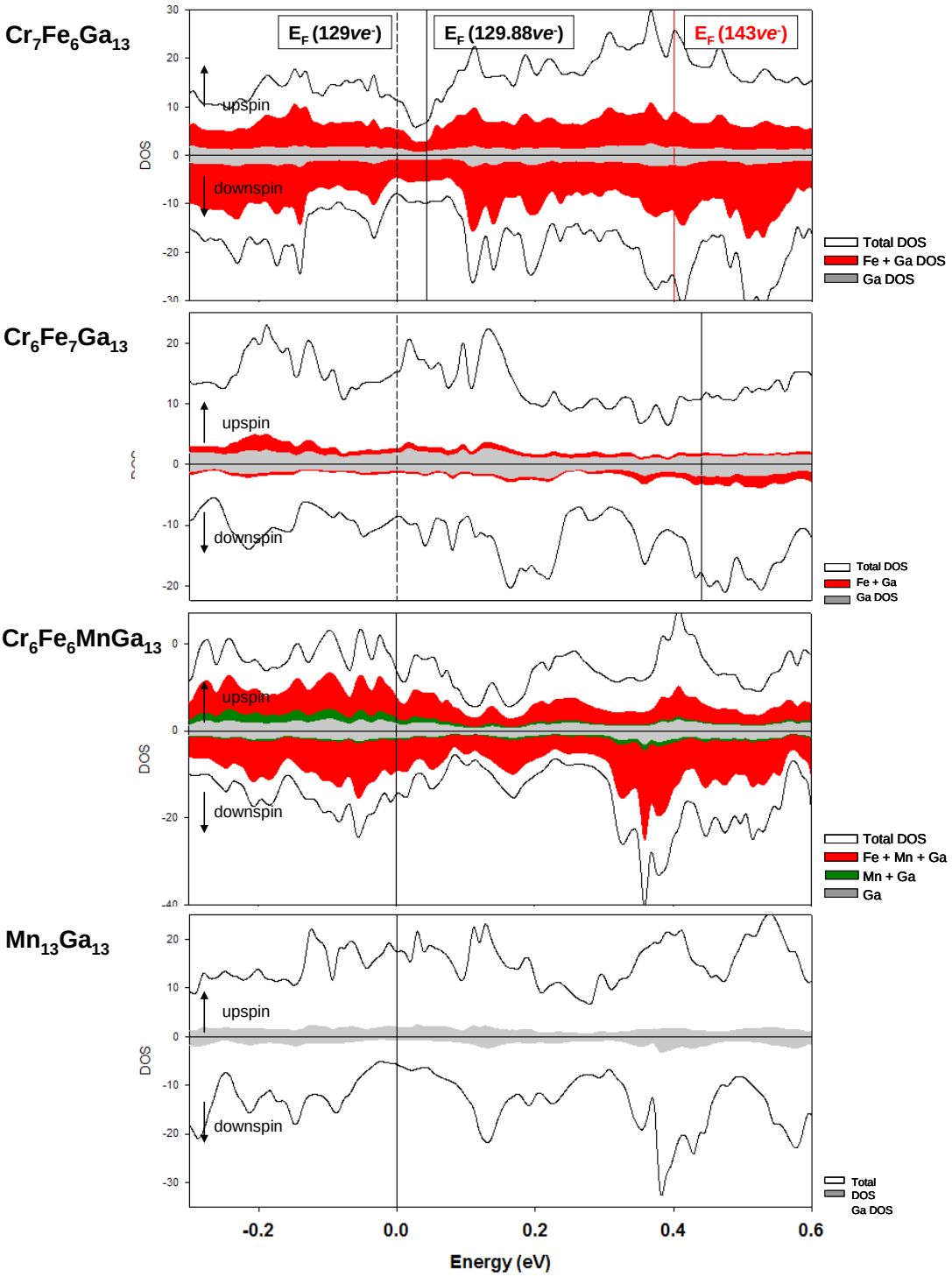

Figure 9. Density of states curves for: (1) $Cr_7Fe_6Ga_{13}$ (2) $Cr_6Fe_7Ga_{13}$ (3) $Cr_6Fe_6MnGa_{13}$ (4) $Mn_{13}Ga_{13}$ (top to bottom) in the vicinity of the Fermi level.

especially for the majority states. This is possibly a consequence of the metal-metal interaction in the icosahedra network induced by the itinerant magnetism of the individual transition metals. When Fe centers the icosahedra network, as shown in DOS Figure (2), the Fermi level is not near the pseudogap, which indirectly suggests these structures favors Cr-rich icosahedra centers, in agreement with the experimental results.

Table 4 summarizes the calculated magnetic moments in model structures (1) – (4). Although isostructural with previously studied binaries CrGa,[10(b)] MnGa,[10(a)] and FeGa[10(b)] with significant atomic magnetic moments (M_{Cr} = ~ 0.8 μB, M_{Mn} = ~2.0 μB, and M_{Fe} = ~ 2.1 μB), the ternary compound was calculated to give the ferrimagnetic structure with close to quenched local magnetic moments for all atoms including the transition metals. The two (18*h*) sites are antiferromagnetically oriented with higher local moments in M3 site in Model (1) and (2), whereas M3 site's local moment is significantly lower than the moment in M2 site in Model (3). In Model (4), all three metal sites have similar local moments.

In Figure 10, Crystal Orbital Hamilton Population (COHP) curves are shown for the three predominant interactions constructing the icosahedra in Models (1) - (4): M-M interactions at 2.514 Å; M-M interactions at 2.590 Å; and Ga-M interactions at 2.708 Å. In the Mn system (right), many of the antibonding states are filled, especially for the minority spin states. In the Cr-Fe case, heteroatomic interactions induce a significant decrease in splitting between the two spin states resulting in shift of the Fermi level toward the cross-over point. In both cases, the possible bonding optimizations can occur on all three contacts by removing valence electrons.

Conclusions

Figure 10. Crystal Orbital Hamilton Population curves for (1) $Cr_7Fe_6Ga_{13}$ (2) $Cr_6Fe_7Ga_{13}$ (3) $Cr_6Fe_6MnGa_{13}$ (4) $Mn_{13}Ga_{13}$ model structures (left to right). Three different bonding interactions composing icosahedron are shown with individual spin states.

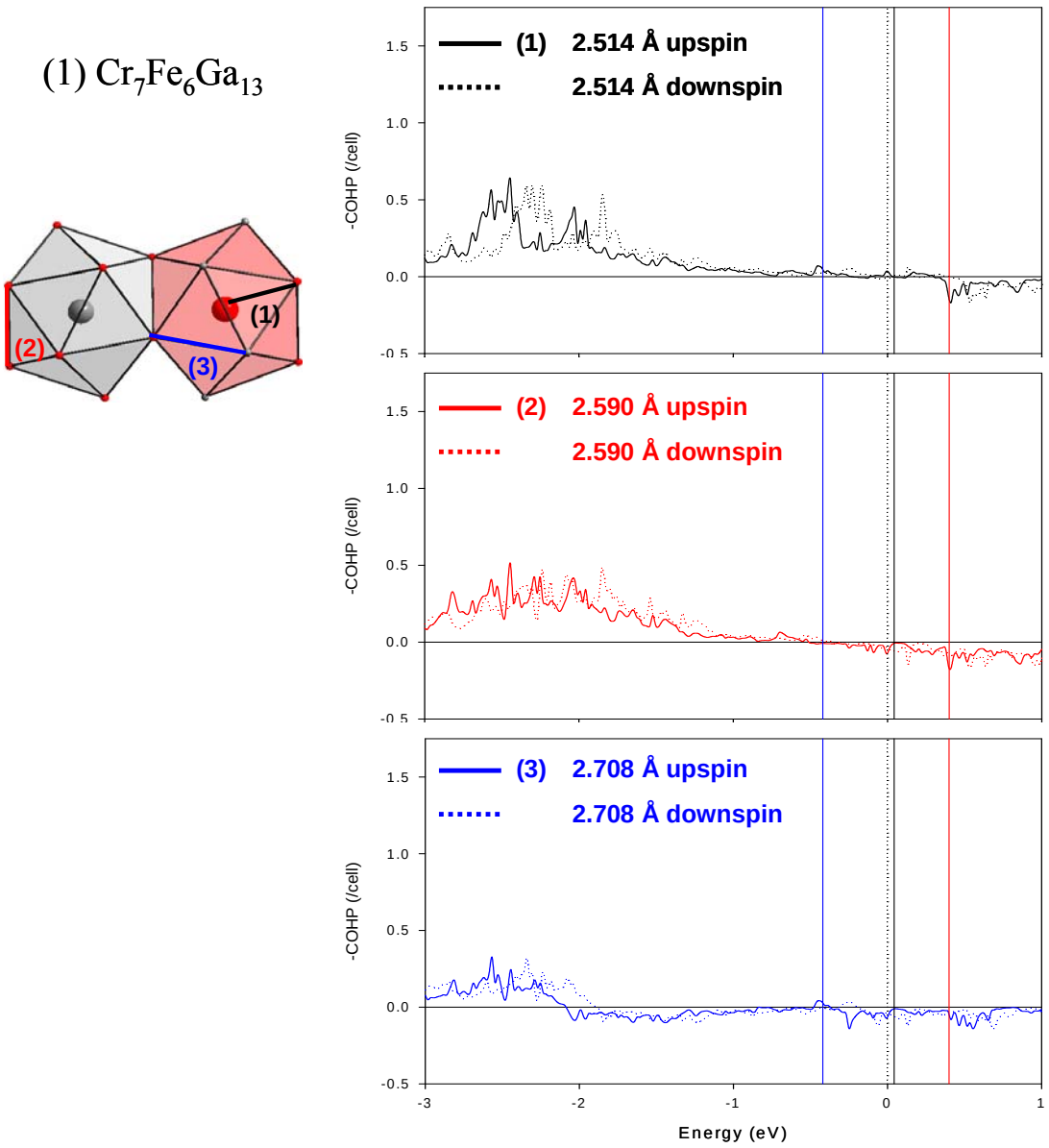

(2) $Cr_6Fe_7Ga_{13}$

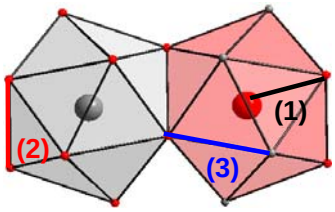

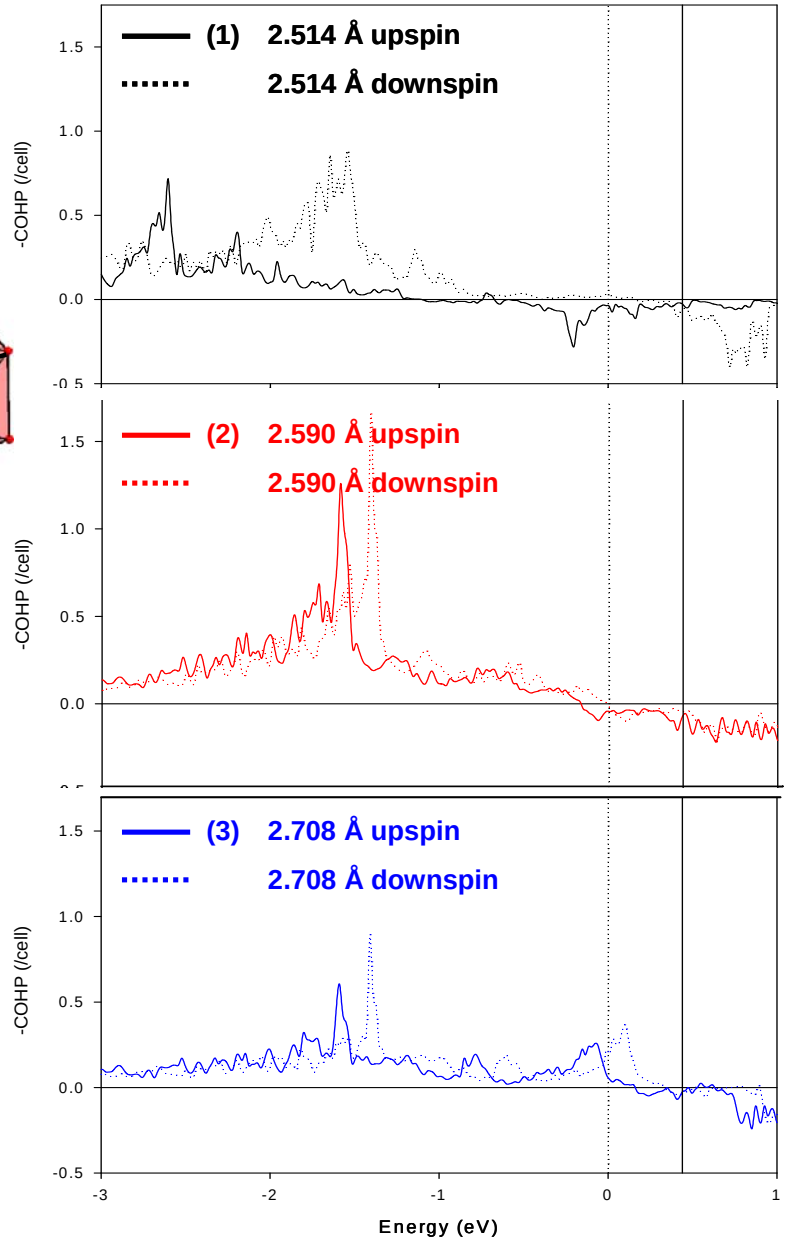

(3) $Cr_6Fe_6MnGa_{13}$

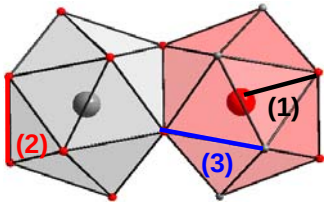

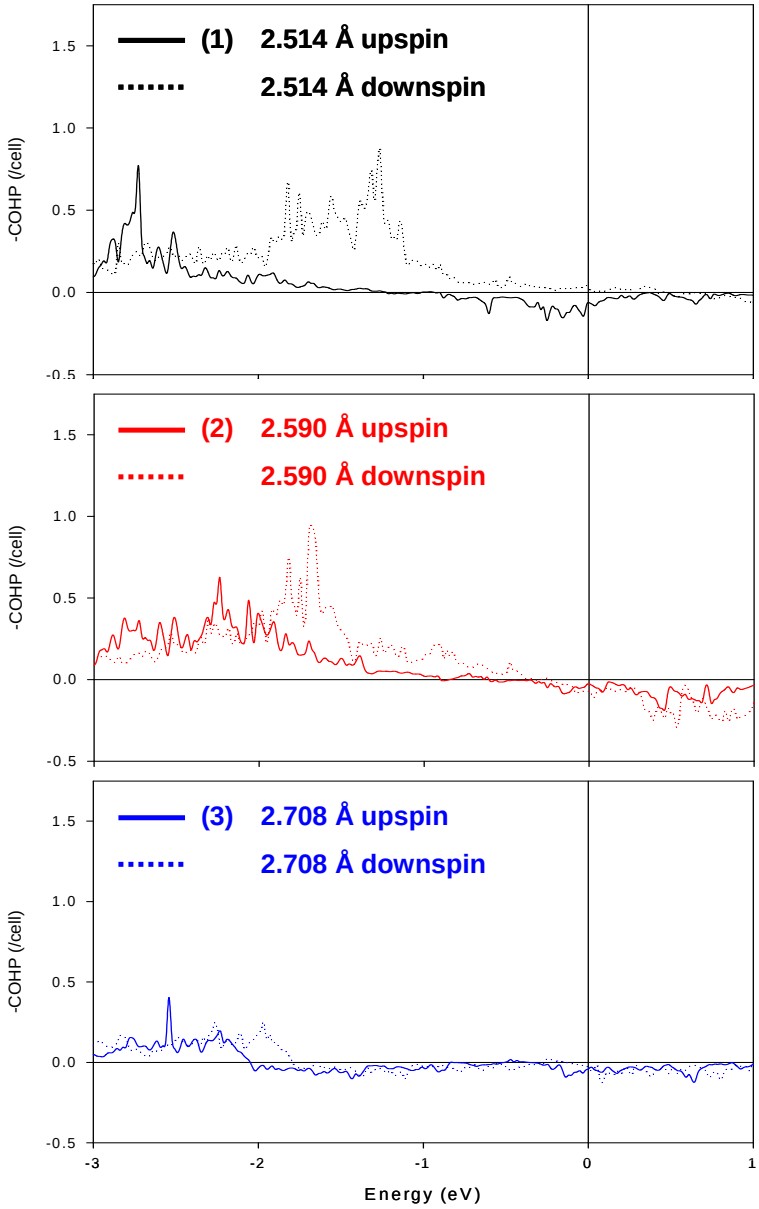

(4) $Mn_{13}Ga_{13}$

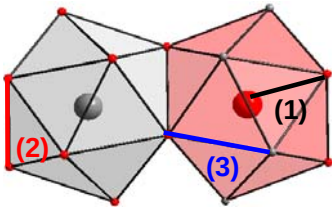
(1)
(2)
(3)

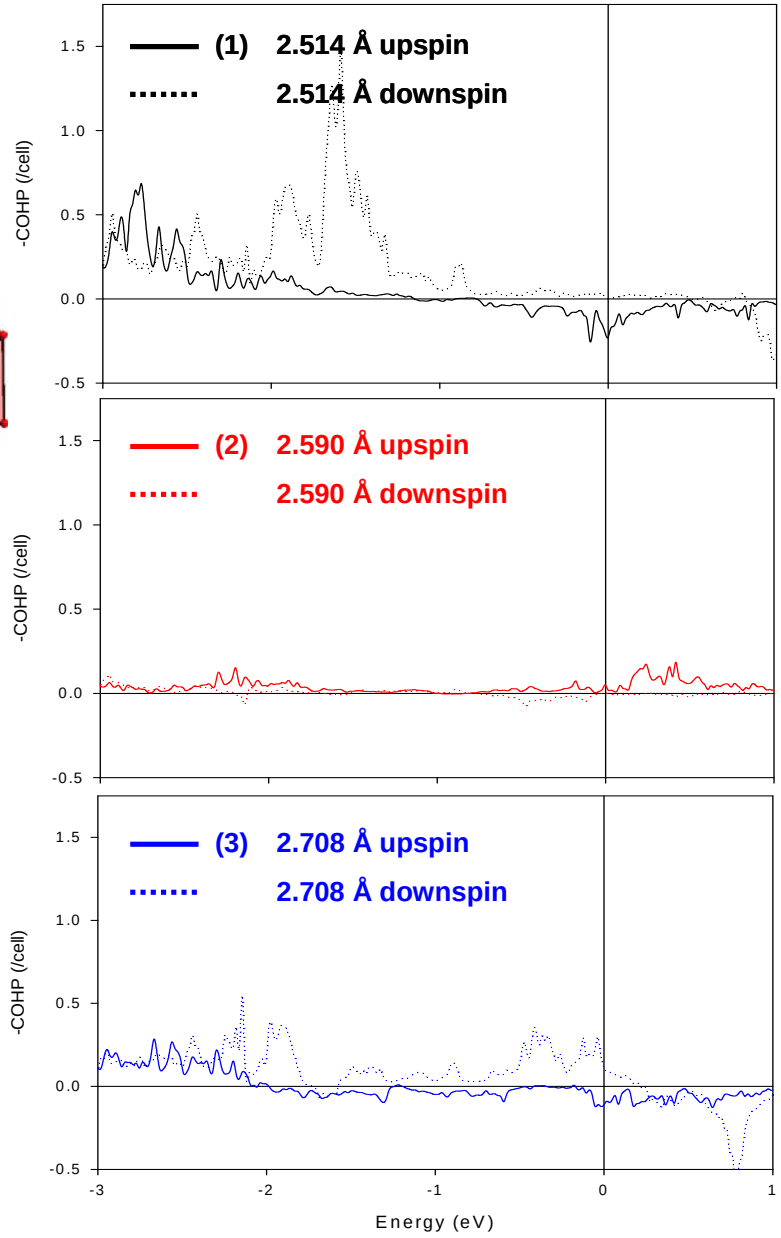
(1) 2.514 Å upspin
2.514 Å downspin
(2) 2.590 Å upspin
2.590 Å downspin
(3) 2.708 Å upspin
2.708 Å downspin
-COHP (/cell)
Energy (eV)

The cubic γ-brass structure of Cr_5Al_8 and rhombohedral $Cr_xFe_{1-x}Ga$ have similar crystal structural schematics with a one-dimensional icosahedra network isolated by the surrounding IIIB elements. However, as shown in Figure 1, trigonal distortion occurs from the cubic γ-brass structure in the $Cr_xFe_{1-x}Ga$ series via shift of one icosahedron unit from the tetrahedrally stacked icosahedra cluster. Also, the band structure calculations indicated the existence of the pseudogap near the Fermi energy that favored the structural distortion to accommodate the changes in electron counts. Also the analysis on PDF refinements from neutron diffraction experiments showed how the local structural coloring of individual transition metals occur in those systems which could not be seen by Rietveld analysis.

Acknowledgements

This manuscript has been authored at Iowa State University of Science and Technology under Contract No. W-7405-ENG-82 with the U.S. Department of Energy. The United States Government retains and the publisher, by accepting the article for publication, acknowledges that the United States Government retains a non-exclusive, paid-up, irrevocable, world-wide license to publish or reproduce the published form of this manuscript, or allow others to do so, for United States Government purposes.

References

[1] Schechtman, D.; Blech, I.; Gratias, D.; Cahn, J. W. *Phys. Rev. Lett*. **1984**, 53, 1951.

[2] Goldman, A. I.; Kelton, R. F. *Rev. Mod. Phys*. **1993**, 65, 213.

[3] Zijlstra, E. S.; Bose, S. K. *Phys. Rev. B* 184205, **2004**, 70.

[4] Brandon, J. K.; Pearson, W. B.; Riley, P. W.; Chieh, C.; Stokhuyzen, R. *Acta. Crystal. B* 33, **1977**, 1088.

[5] Ellner, M.; Braun, B.; Predel, Z. *Metalkde.* 80, **1989**, 374.

[6] Hume-Rothery, W. *J. Inst. Met*. **1926**, 35, 295.

[7] Hoistad, L. M.; Lee, S. *J. Am. Chem. Soc*. **1991**, 113, 8216.

[8] Tamura, R.; Nishimoto, K.; Takeuchi, S. *Phys. Rev. B* 71, **2005**, 092203.

[9] Fujiwara, J. *Phys. Rev*. B40, **1989**, 942.

[10] (a) Gourdon, O.; Miller, G. J. *J. Solid State Chem*. 173, **2003**, 137.

(b) Gourdon, O.; Bud'ko, S.; Williams, D.; Miller, G. J. *Inorg. Chem.* **2004**, 43, 3210

[11] Larson, A. C.; Von Dreele, R. B. *GSAS: General Structure Analysis System*. **1985**

[12] SMART; Bruker AXS, Inc.; Madison, WI, **1996.**

[13] Andersen, O. K.; Jepsen, O. *Phys. Rev. Lett.* **1984**, 53, 2571.

[14] Blessing, R. H.: An empirical correction for absorption anisotropy. *Acta. Cryst.*. **1995**, A 51, 33.

[15] Rietveld, H. M. *J. Appl. Crystallogr*. **1969**, 2, 65.; Hunter, B. A.; Howard, C. J. Rietica; Australian Nuclear Science and Technology Organization: Menai, Australia (2000).

[16] Quantum Design; Quantum Design, Inc.; San Diego, CA, **2000**.

[17] Andersen, O. K. *Phys. Rev.* **1975**, B12, 3060.

[18] Andersen, O. K.; Jepsen, O. *Phys. Rev. Lett.* **1984**, 53, 2571.

[19] Andersen, O. K.; Jepsen, O.; Glötzel, D. In *Highlights of Condensed-Matter Theory*; Bassani, F.; Fumi, F.; Tosi, M. P.; Lambrecht, W. R. L.; Eds.; North-Holland: New York, **1985**.

[20] Andersen, O. K. *Phys. Rev.* **1986**, B34, 2439.

[21] The Stuttgart Tight-Binding LMTO-ASA program Version 4.7; Max-Planck-Institut für Festkörperforschung, Stuttgart, Germany **1998**.

[22] Von Barth, U.; Hedin, L. *J. Phys. C* **1972**, 5, 1629.

[23] Koelling, D. D.; Harmon, B.N. *J. Phys. C* **1977**, 10, 3107.

[24] Jepsen, O.; Anderson, O. K. *Z. Phys. B* **1995**, 97, 35.

[25] Dronskowski, R.; Blöchl, P. *J. Phys. Chem*. **1993**, 97, 8617.

[26] Blöchl, P. E.; Jepsen, O.; Andersen, O.K. *Phys Rev.* **1994**, B49, 16223.

[27] Peterson, P. F.; Gutmann, M.; Proffen, Th.; Billinge, S. J. L., PDFgetN: A user-friendly program to extract the total scattering structure function and the pair distribution function from neutron powder diffraction data, *J. Appl. Crystallogr.* **2000**, 33, 1192.

[28] Proffen, Th.; Billinge, S. J. L.; PDFFIT, *J. Appl. Crystallogr.* **1999**, 32, 572-575.

[29] Tremolet de Lacheisserie, E. du. *Magnetostriction: Theory and Applications of Magnetoelasticity.* Boca Raton, FL: CRC Press, **1993**.

[30] Hoffmann R. *Solids and Surfaces: A chemist's View of Bonding in Extended Structures*, VCH, 3 **1988**.

[31] Hoffmann, R. *J. Chem. Phys*. **1963**, 39, 1397.

[32] Burdett, J. K. Chemical Bonding in Solids, Oxford University Press, New York, **1995**.

[33] Ammeter, J. H.; Bürgi, H. B; Thibeault, J. C.; Hoffmann, R. *J. Am. Chem. Soc.* **1978**, 100, 3686.

[34] Pauling, L.; Kamb, B. *Proc. Natl. Acad. Sci. USA*, **1986**, 83, 3569.

[35] Farrow, C. L.; Juhas, P.; Liu, J. W.; Bryndin, D.; Bozin, E. S.; Bloch, J.; Proffen, Th.; Billinge, S. J. L. PDFfit2 and PDFgui: computer programs for studying nanostructure in crystals. *J. Phys.: Condens. Matter* **2007**, 19, 335219.

[36] Gourdon, O.; Gout, D.; Williams, D. J.; Proffen, T.; Hobbs, S.; Miller, G. J. *Inorg. Chem*. **2007**, 46, 251.

[37] Mott, N. F.; Jones, H. *The Theory of the Properties of Metals and Alloys*, Dover, **1958**.

[38] Barrett, C.; Massalski, T. B. *Structure of Metals*, McGraw Hill, **1966**.

[39] Massalski, T. B.; Mizutani, U. *Progr. Mater. Sci*. **1978**, 22, 151.

[40] Mizutani, U.; Asahi, R.; Sato, H.; Takeuchi, T. *Philosophical Magazine*. **2006**, 86, 645.

[41] Gourdon, O.; Izaola, Z.; Elcoro, L.; Petricek, V.; Miller, G. J. *Philosophical Magazine,* **2006**, 86, 3-5, 419.

[42] Billinge, S. J. L.; Proffen, Th.; Petkov, V.; Sarrao, J. L.; Kycia, S. *Physical Review B*. **2000**, 62(2), 1203.

Supplement table 1. Single Crystal X-ray diffraction data and structure refinement results for $Cr_xFe_{1-x}Ga$.

Empirical formula	$Cr_{0.06(0)}Fe_{0.94(0)}Ga$	$Cr_{0.24(23)}Fe_{0.76(23)}Ga$
Temperature	293(2) K	293(2) K
Wavelength	0.71073 Å	0.71073 Å
Crystal system	rhombohedral	rhombohedral
Space group	$R\bar{3}m$	$R\bar{3}m$
Unit cell dimensions	a = 12.4695(18) Å c = 7.7807(16) Å γ = 120°	a = 12.4927(18) Å c = 7.8070(16) Å γ = 120°
Volume	1047.7(3) $Å^3$	1055.2(3) $Å^3$
Z	12	12
Absorption coefficient	14.511 mm^{-1}	14.409 mm^{-1}
F(000)	972	972
Theta range for data collection	3.23 to 28.17°.	3.22 to 28.15°.
Index ranges	$-16 \le h \le 10$, $-12 \le k \le 15$, $-8 \le l \le 9$	$-16 \le h \le 13$, $-13 \le k \le 15$, $-6 \le l \le 10$
Reflections collected	1192	2262
Independent reflections	307 [R(int) = 0.0736]	328 [R(int) = 0.0671]
Completeness to theta = 28.25	92.7 %	98.2 %
Refinement method	Full-matrix least-squares on F^2	Full-matrix least-squares on F^2
Data / restraints / parameters	307 / 0 / 30	328 / 0 / 32
Goodness-of-fit on F^2	1.343	1.455
Final R indices [I>2sigma(I)]	R_1 = 0.0404, wR_2 = 0.0825	R_1 = 0.0506, wR_2 = 0.1109
R indices (all data)	R_1 = 0.0422, wR_2 = 0.0836	R_1 = 0.0509, wR_2 = 0.1110
Extinction coefficient	0.00131(10)	0.00164(17)
Largest diff. peak and hole	1.381 and -1.720 e. $Å^{-3}$	1.770 and -2.471 e.$Å^{-3}$

Empirical formula	$Cr_{0.25(16)}Fe_{0.75(16)}Ga$	$Cr_{0.50(12)}Fe_{0.50(12)}Ga$
Temperature	293(2) K	293(2) K
Wavelength	0.71073 Å	0.71073 Å
Crystal system	rhombohedral	rhombohedral
Space group	$R\bar{3}m$	$R\bar{3}m$
Unit cell dimensions	a = 12.5161(18) Å c = 7.8263(16) Å γ = 120°	a = 12.5398(18) Å c = 7.8481(16) Å γ = 120°
Volume	1061.8(3) $Å^3$	1068.8(3) $Å^3$
Z	12	12
Absorption coefficient	14.320 mm^{-1}	14.226 mm^{-1}
F(000)	972	972
Theta range for data collection	3.21 to 28.12°.	3.20 to 28.06°.
Index ranges	$-16 \le h \le 15$, $-16 \le k \le 12$, $-10 \le l \le 9$	$-16 \le h \le 9$, $-15 \le k \le 16$, $-10 \le l \le 9$
Reflections collected	2281	2279
Independent reflections	330 [R(int) = 0.0801]	332 [R(int) = 0.0507]
Completeness to theta = 28.25	98.5 %	99.1 %
Refinement method	Full-matrix least-squares on F^2	Full-matrix least-squares on F^2
Data / restraints / parameters	330 / 0 / 32	332 / 0 / 32
Goodness-of-fit on F^2	1.379	1.354
Final R indices [I>2sigma(I)]	R_1 = 0.0590, wR_2 = 0.1105	R_1 = 0.0427, wR_2 = 0.0853
R indices (all data)	R_1 = 0.0597, wR_2 = 0.1107	R_1 = 0.0433, wR_2 = 0.0855
Extinction coefficient	0.00072(10)	0.00074(8)
Largest diff. peak and hole	1.425 and -2.125 e $Å^{-3}$	1.479 and -1.496 e $Å^{-3}$

Empirical formula	$Cr_{0.58(11)}Fe_{0.42(11)}Ga$	$Cr_{0.67(11)}Fe_{0.33(11)}Ga$
Temperature	293(2) K	293(2) K
Wavelength	0.71073 Å	0.71073 Å
Crystal system	rhombohedral	rhombohedral
Space group	$R\bar{3}m$	$R\bar{3}m$
Unit cell dimensions	a = 12.5527(9) Å c = 7.8581(13) Å γ = 120°	a = 12.5595(18) Å c = 7.8550(16) Å γ = 120°
Volume	1072.3(2) $Å^3$	1073.1(3) $Å^3$
Z	12	12
Absorption coefficient	14.179 mm^{-1}	14.169 mm^{-1}
F(000)	972	972
Theta range for data collection	3.20 to 28.08°.	3.20 to 28.20°.
Index ranges	$-15 \le h \le 15$, $-15 \le k \le 15$, $-10 \le l \le 10$	$-10 \le h \le 16$, $-16 \le k \le 10$, $-10 \le l \le 10$
Reflections collected	2960	2242
Independent reflections	314 [R(int) = 0.0666]	330 [R(int) = 0.1119]
Completeness to theta = 28.25	93.5 %	97.9 %
Refinement method	Full-matrix least-squares on F^2	Full-matrix least-squares on F^2
Data / restraints / parameters	314 / 0 / 31	330 / 0 / 32
Goodness-of-fit on F^2	0.713	1.284
Final R indices [I>2sigma(I)]	R_1 = 0.0305, wR_2 = 0.0917	R_1 = 0.0502, wR_2 = 0.1168
R indices (all data)	R_1 = 0.0305, wR_2 = 0.0917	R_1 = 0.0502, wR_2 = 0.1168
Extinction coefficient	0.00154(16)	0.0032(3)
Largest diff. peak and hole	1.017 and -1.537 e.$Å^{-3}$	2.074 and -1.524 e $Å^{-3}$

Empirical formula	$Cr_{0.47(11)}Fe_{0.53(11)}Ga$	$Cr_{0.33(14)}Fe_{0.67(14)}Ga$
Temperature	293(2) K	293(2) K
Wavelength	0.71073 Å	0.71073 Å
Crystal system	rhombohedral	rhombohedral
Space group	$R\bar{3}m$	$R\bar{3}m$
Unit cell dimensions	a = 12.5743(18) Å c = 7.8717(16) Å γ = 120°	a = 12.6153(18) Å c = 7.8833(16) Å γ = 120°
Volume	1077.9(3) $Å^3$	1086.5(3) $Å^3$
Z	12	12
Absorption coefficient	14.106 mm^{-1}	13.993 mm^{-1}
F(000)	972	972
Theta range for data collection	3.19 to 28.25°.	3.19 to 28.25°.
Index ranges	$-15 \le h \le 15$, $-16 \le k \le 14$, $-10 \le l \le 10$	$-16 \le h \le 16$, $-16 \le k \le 16$, $-4 \le l \le 10$
Reflections collected	2294	2288
Independent reflections	334 [R(int) = 0.0577]	331 [R(int) = 0.0401]
Completeness to theta = 28.25	98.5 %	97.1 %
Refinement method	Full-matrix least-squares on F^2	Full-matrix least-squares on F^2
Data / restraints / parameters	334 / 0 / 31	331 / 0 / 30
Goodness-of-fit on F^2	1.378	1.457
Final R indices [I>2sigma(I)]	R_1 = 0.0378, wR_2 = 0.0788	R_1 = 0.0711, wR_2 = 0.1305
R indices (all data)	R_1 = 0.0378, wR_2 = 0.0788	R_1 = 0.0712, wR_2 = 0.1305
Extinction coefficient	0.00139(11)	0.00066(11)
Largest diff. peak and hole	1.253 and -1.395 e. $Å^{-3}$	2.531 and -2.525 e $Å^{-3}$

Empirical formula	$Cr_{0.81(11)}Fe_{0.19(11)}Ga$
Temperature	293(2) K
Wavelength	0.71073 Å
Crystal system	rhombohedral
Space group	$R\bar{3}m$
Unit cell dimensions	a = 12.6431(18) Å c = 7.8985(16) Å γ = 120°
Volume	1093.4(3) $Å^3$
Z	12
Absorption coefficient	13.905 mm^{-1}
F(000)	972
Theta range for data collection	3.18 to 28.25°.
Index ranges	$-16 \leq h \leq 15$, $-16 \leq k \leq 16$, $-10 \leq l \leq 6$
Reflections collected	2298
Independent reflections	336 [R(int) = 0.0667]
Completeness to theta = 28.25	98.0 %
Refinement method	Full-matrix least-squares on F^2
Data / restraints / parameters	336 / 0 / 30
Goodness-of-fit on F^2	1.438
Final R indices [I>2sigma(I)]	R_1 = 0.0400, wR_2 = 0.0860
R indices (all data)	R_1 = 0.0400, wR_2 = 0.0860
Extinction coefficient	0.00233(16)
Largest diff. peak and hole	1.265 and -1.934 e.$Å^{-3}$

Supplement table 2. Anisotropic displacement parameters ($Å^2 \times 10^3$) for $Cr_xFe_{1-x}Ga$. The anisotropic displacement factor exponent takes the form: $-2\pi^2[h^2 a^{*2} U_{11} + ... + 2 h k a^* b^* U_{12}]$

	U_{11}	U_{22}	U_{33}	U_{23}	U_{13}	U_{12}
Loaded:	$Cr_{0.1}Fe_{0.9}Ga$			Refined:	$Cr_{0.06(0)}Fe_{0.94(0)}Ga$	
Ga1	7(1)	7(1)	5(2)	0	0	4(1)
Ga2	6(1)	12(1)	7(1)	0(1)	0(1)	3(1)
Ga3	8(1)	8(1)	7(1)	-1(1)	1(1)	5(1)
M1	4(1)	4(1)	4(2)	0	0	2(1)
M2	7(1)	6(1)	3(1)	0(1)	0(1)	3(1)
M3	7(1)	7(1)	3(1)	0(1)	0(1)	2(1)
Loaded:	$Cr_{0.2}Fe_{0.8}Ga$			Refined:	$Cr_{0.24(23)}Fe_{0.76(23)}Ga$	
Ga1	9(2)	9(2)	4(2)	0	0	5(1)
Ga2	4(1)	10(1)	5(1)	0(1)	0(1)	2(1)
Ga3	6(1)	6(1)	6(1)	-1(1)	1(1)	4(1)
M1	2(2)	2(2)	0(3)	0	0	1(1)
M2	4(2)	4(1)	2(1)	0(1)	0(1)	2(1)
M3	4(1)	4(1)	1(1)	0(1)	0(1)	0(1)
Loaded:	$Cr_{0.3}Fe_{0.7}Ga$			Refined:	$Cr_{0.25(16)}Fe_{0.75(16)}Ga$	
Ga1	7(1)	7(1)	6(2)	0	0	3(1)
Ga2	5(1)	11(1)	8(1)	0(1)	0(1)	2(1)
Ga3	7(1)	7(1)	10(1)	-1(1)	1(1)	4(1)
M1	1(3)	1(3)	7(4)	0	0	1(1)
M2	7(2)	6(1)	7(2)	0(1)	0(1)	3(1)
M3	6(1)	6(1)	9(2)	0(1)	0(1)	2(1)
Loaded:	$Cr_{0.4}Fe_{0.6}Ga$			Refined:	$Cr_{0.50(12)}Fe_{0.50(12)}Ga$	
Ga1	8(1)	8(1)	10(2)	0	0	4(1)
Ga2	5(1)	13(1)	8(1)	0(1)	0(1)	3(1)
Ga3	8(1)	8(1)	10(1)	-1(1)	1(1)	5(1)
M1	3(2)	3(2)	4(3)	0	0	2(1)
M2	6(1)	6(1)	6(1)	0(1)	0(1)	3(1)

M3	6(1)	6(1)	5(1)	0(1)	0(1)	2(1)
Loaded:	$Cr_{0.6}Fe_{0.4}Ga$		Refined:	$Cr_{0.65(14)}Fe_{0.35(14)}Ga$		
Ga1	10(1)	10(1)	7(2)	0	0	5(1)
Ga2	4(1)	11(1)	7(1)	0(1)	0(1)	2(1)
Ga3	7(1)	7(1)	8(1)	-1(1)	1(1)	4(1)
M1	2(2)	2(2)	5(3)	0	0	1(1)
M2	6(1)	5(1)	6(1)	0(1)	1(1)	3(1)
M3	5(1)	5(1)	6(1)	0(1)	0(1)	2(1)
Loaded:	$Cr_{0.7}Fe_{0.3}Ga$		Refined:	$Cr_{0.47(11)}Fe_{0.53(11)}Ga$		
Ga1	5(1)	5(1)	8(1)	0	0	3(1)
Ga2	3(1)	11(1)	8(1)	0(1)	0(1)	1(1)
Ga3	5(1)	5(1)	10(1)	-1(1)	1(1)	3(1)
M1	5(1)	5(1)	8(2)	0	0	3(1)
M2	4(1)	3(1)	6(1)	0(1)	0(1)	2(1)
M3	4(1)	4(1)	5(1)	0(1)	0(1)	1(1)
Loaded:	$Cr_{0.8}Fe_{0.2}Ga$		Refined:	$Cr_{0.33(14)}Fe_{0.67(14)}Ga$		
Ga1	8(2)	8(2)	4(3)	0	0	4(1)
Ga2	4(1)	15(1)	8(1)	0(1)	1(1)	2(1)
Ga3	8(1)	8(1)	11(1)	-1(1)	1(1)	5(1)
M1	3(2)	3(2)	5(4)	0	0	1(1)
M2	5(2)	5(1)	6(2)	0(1)	0(1)	3(1)
M3	5(2)	5(2)	6(2)	-1(1)	1(1)	2(1)
Loaded:	$Cr_{0.9}Fe_{0.1}Ga$		Refined:	$Cr_{0.81(11)}Fe_{0.19(11)}Ga$		
Ga1	8(1)	8(1)	0(1)	0	0	4(1)
Ga2	6(1)	15(1)	3(1)	0(1)	0(1)	3(1)
Ga3	9(1)	9(1)	6(1)	-1(1)	1(1)	6(1)
M1	4(1)	4(1)	0(2)	0	0	2(1)
M2	6(1)	6(1)	2(1)	1(1)	2(1)	3(1)
M3	6(1)	6(1)	1(1)	-1(1)	1(1)	2(1)

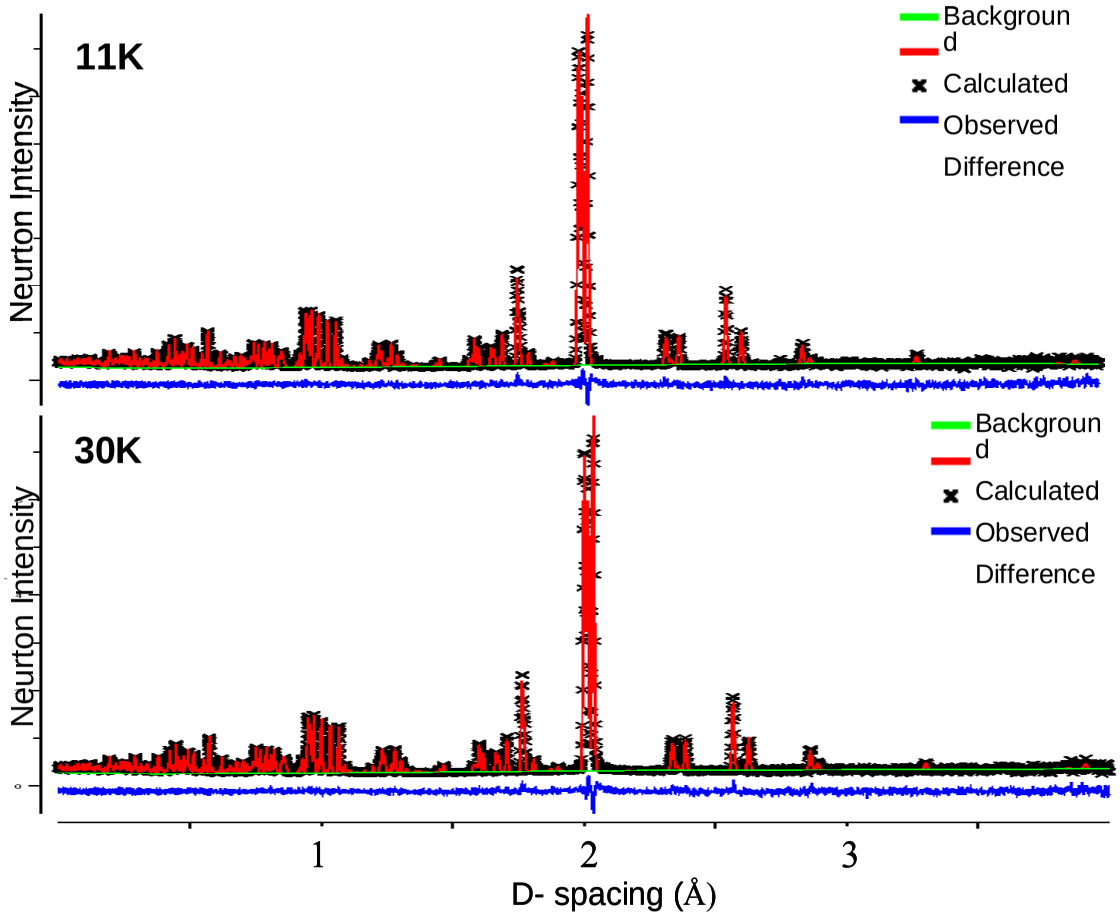

Supplement Figure 1. $Cr_{0.5}Fe_{0.5}Ga$ neutron powder pattern obtained on NPDF at 11 and 30 K. Tick marks indicate positions of the Bragg reflections. The difference between the observed and the calculated pattern is shown below the tick marks .

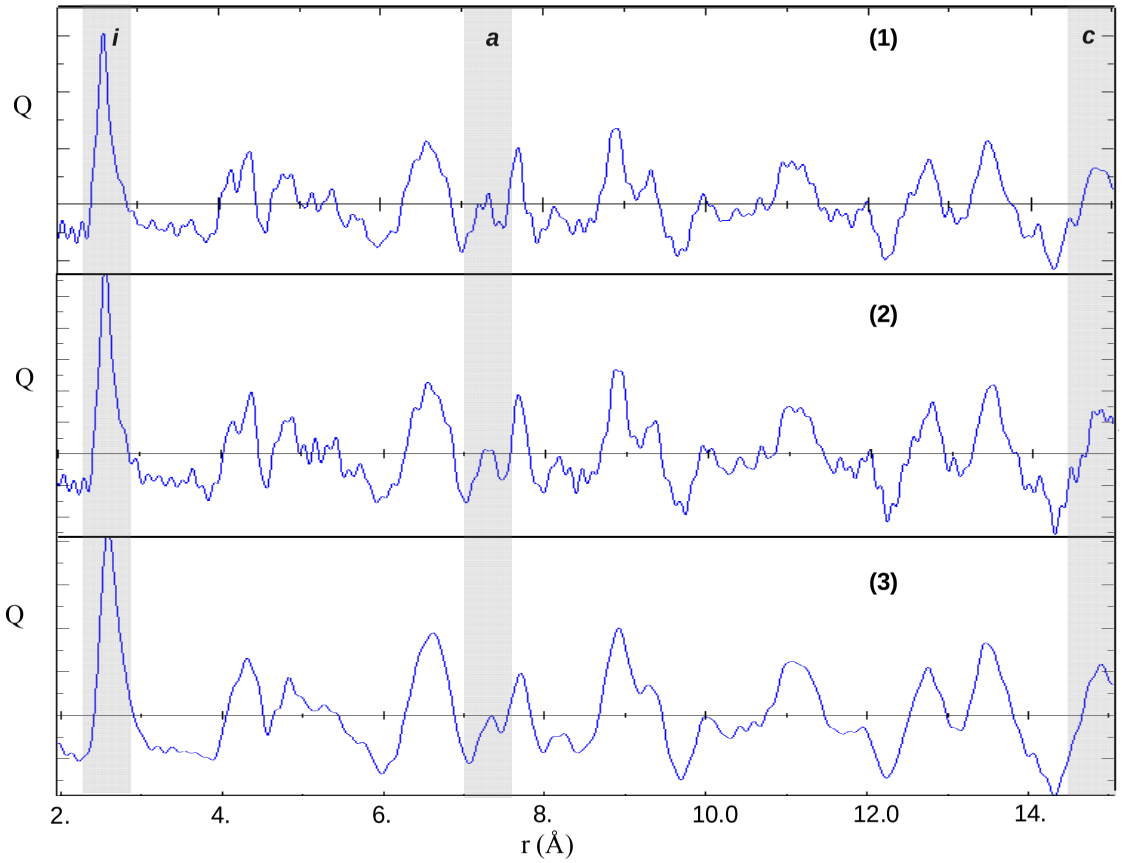

Supplement Figure 2. Pair Distribution Function as a function of scattering distances (bond distances) transformed from the neutron powder diffraction data of experiments at temperatures (1) 11K, (2) 30K, and (3) 295K. Three regions are highlighted to represent *i*: bond distances constructing the icosahedra chain, *a*: *a* and *b* lattice parameters, and *c*: *c* lattice parameter.

CHAPTER 4

Between Hume-Rothery and Polar Intermetallics: $Ti_{3.2(1)}Ni_{7.3(1)}Ga_{4.5}$: A New *G*-Phase

(manuscript in preparation for submission to Inorganic Chemistry)

*Hyunjin Ko, and Gordon J. Miller**

*Department of Chemistry, Iowa State University and Ames Laboratory, Ames, Iowa 50011-3111, USA

ABSTRACT

A new Ti-Ni-Ga compound, $Ti_{3.2(1)}Ni_{7.3(1)}Ga_{4.5}$, has been prepared in a Ga flux and structurally and electronically characterized. The new compound adopts a coloring of the cubic $Sc_{11}Ir_4$-type (G-phase) structure, Pearson symbol *cF*120; a = 11.7075(14) Å, space group $Fm\bar{3}m$(No. 225), Z = 4. The new compound deviates from the face-centered cubic "$TiNi_2Ga$" Heusler-type compound by introducing ordered vacancies at some Ti positions and a different coloring of Ni and Ga atoms on the bcc network. The atomic positions also show relationships to cubic γ-brass structures, but is based upon a 2×2×2 super-cell of the bcc unit cell, and develop a three-dimensional network of vertex-sharing icosahedra. Electronic structure calculations indicate that the chemical composition, atomic distribution, as well as structure are strongly influenced by a pseudogap in the electronic density of states curve. This pseudogap separates bonding Ti–(Ni, Ga) states from antibonding Ti–(Ni, Ga) states. In effect, such compounds represent a link between Hume-Rothery electron phases and polar intermetallics, both of which are controlled by the occupation of electronic states.

Introduction

Structure-composition-property relationships in intermetallic compounds are governed largely by their electronic structures, but chemically derived rules to help target intermetallics with specific chemical or physical features remain elusive. Many structures based on close packed arrangements of atoms rely on modifications of the free-electron model to explain their electronic structures; one set of examples is the Hume-Rothery electron compounds. These densely packed intermetallics involve late transition metals and post-transition metals and adopt fcc, bcc, γ-brass, and hcp structures that follow their valence s and p electron concentrations. On the other hand, polar intermetallics, e.g., $BaAl_4$, involve combinations of active, electropositive metals (Ba) with electronegative metals (Al), which form complex two- or three-dimensional networks that indicate some degree of covalent bonding. The active metals donate some or all of their valence electrons to satisfy chemical bonding requirements in the electronegative metal network. In both types of intermetallics, the electronic density of states (DOS) curves typically show a pseudogap at the Fermi level. In the cubic γ-brass phases, the origin of the pseudogap is the ordering of vacancies in a 3×3×3 super-cell of bcc atomic packing that is further enhanced by both slight atomic displacements around each vacancy as well as atomic distributions in these binary alloys. On the other hand, in polar intermetallics, the pseudogap arises from a tendency to optimize bonding interactions within the electronegative metal network, which is dictated by orbital overlap and can also be modified by the atomic distributions.

In this work, we report a cubic, icosahedral network in the new ternary compound $Ti_{0.80(2)}Ni_{1.83(2)}Ga_{1.12}$, which shows relationships to both Hume-Rothery type γ-brasses as well as polar intermetallics. This compound was prepared as part of an effort to explore the stability range and possible magnetic structures of mixed-

metal gallides, $(T_xT'_{1-x})Ga$, which are based on the isostructural series CrGa-MnGa-FeGa. Pseudobinary compounds $(Cr_xFe_{1-x})Ga$ exist that are isostructural, and this new compound was discovered through attempts to prepare $(Ti_xNi_{1-x})Ga$. Upon successful preparation and characterization of this complex intermetallic, we further characterized this compound and the system by theoretical calculations.

Experimental

Synthesis. The title compound was originally extracted and identified from a preparation of "$TiNiGa_2$" and was subsequently obtained in high yield, as based on X-ray powder diffraction, by loading "$TiNi_2Ga_2$" using elemental Ga (99.9999 %, ingots, Alfa Aesar), Ti (99.95 %, foil, Ames Laboratory), and Ni (99.99 %, wire, Ames Laboratory) in an evacuated ($< 10^{-4}$ torr) sealed silica tube. The mixture was heated to 1373 K, and then slowly cooled to 1123 K at a rate of 1 K/min. Following 48 hours of annealing at 1123 K, the furnace was turned off and the final product was cooled down to room temperature.

Chemical Analysis. Chemical composition of the title compound was analyzed by Energy Dispersive Spectroscopy (EDS) using a *JEOL* 8400A scanning electron microscope, equipped with an *IXRF* Systems Iridium X-ray analyzer with *Kevex Quantum* thin-window Si(Li) detector for quantitative chemical analysis; the resulting compositions complemented the results from refinements of single crystal X-ray analysis. To acquire flat, microscopically smooth surfaces each sample was polished by sandpaper and fine leather, and subsequently inspected by back scattering and topological modes to determine the sites for elemental analysis. Typical data collections utilized a 20 kV accelerating voltage and a 30 mA beam current. To

carry out both quantitative and qualitative analyses, Ti, Ni, and Ga internal standards were used with the standardless method.

X-ray Diffraction. XRD patterns of powdered samples were obtained with a Huber image plate using an Enraf Nonius Guinier camera and monochromatic Cu $K\alpha_1$ radiation (λ = 1.540598 Å) at ambient temperature (ca. 295 ± 2 K) and Si as an internal standard. Powdered samples were homogeneously dispersed on a Mylar film with the aid of a little petroleum jelly. The step size was set at 0.02º and the exposure time was 1 hr. for 2θ values ranging from 10º to 95º. Data acquisition was controlled via the in-situ program. A major phase was identified to adopt a cubic lattice, space group $Fm\bar{3}m$, with the occurrence of additional peaks assigned to elemental Ga. The lattice parameter, a = 11.7071(14) Å, was obtained from least squares refinement with the aid of a Rietveld refinement program.[7]

Block-like crystals (typical crystal dimensions: 50 × 50 × 50 μm^3) suitable for structure determination were selected from the products and mounted on glass fibers. Data were collected using a *STOE IPDS2* (image plate diffraction system) diffractometer at 295 ± 2 K with monochromated Mo $K\alpha_1$ radiation (λ = 0.71073 Å; 50 kV and 40 mA) and a detector-to-crystal distance of 100 mm. Diffraction data were collected in the full sphere of reciprocal space for an exposure time of 3 min per frame up to 2θ = 58.12º. Intensities were extracted and then corrected for Lorentz and polarization effects using the SAINT program.[8] The program SADABS was used for empirical absorption correction.[10] Structure refinements (full-matrix least-squares on F^2) were performed by using the SHELXTL-PLUS programs.[22] The refinement results are summarized in Tables 1 and 2.

Magnetic Studies. Temperature-dependent magnetic susceptibility measurements

Table 1. Crystal data and structure refinements of the single crystal.

composition	$Ti_{0.86(2)}Ni_{1.95(2)}Ga_{1.2}$
space group (Pearson symbol)	$Fm\bar{3}m$
lattice parameters, Å	a = 11.7075(14)
volume, Å^3	1604.7(3)
Z	4
Diffractometer; wavelength, Å	*STOE-IPDS;* 0.71073 (Mo Kα radiation)
2θ range	6.02 to 58.12°.
index ranges	$0 \le h \le 10$, $0 \le k \le 11$, $1 \le l \le 6$
independent reflections	144 [$R_{(int)}$ = 0.0225]
completeness to $2\theta_{max}$	100.0 %
data/parameters	144 / 17
goodness-of-fit on F^2	1.127
final R indices [$I/\sigma(I) > 2$]	R_1 = 0.0445, wR_2 = 0.1035
R indices (all data)	R_1 = 0.0607, wR_2 = 0.1077
extinction coefficient	0.00069(13)
largest diff. peak/hole, e/Å^3	1.259 / -1.566

Table 2. Atomic parameters and isotropic temperature factors (Å^2) for the $Ti_{0.80(2)}Ni_{1.83(2)}Ga_{1.12}$ phase.

atom	*Wyck.*		occup.	*x*	*y*	*z*	$U_{eq.}$
Ga1	4*a*		1	0	0	0	0.0024(1)
Ga2	32*f*		1	0.1504(1)	0.1504(1)	0.1504(1)	0.0025(1)
Ni1	24*d*		1	0	1/4	1/4	0.0022(1)
Ni2	32*f*		1	0.1212(1)	0.1212(1)	0.3789(1)	0.0017(1)
Ti1	24*e*		1	0	0	0.2215(4)	0.0022(1)
M3	4*b*	Ni3	0.6(1)	1/2	1/2	1/2	0.0018(2)
	4*b*	Ti3	0.4(1)	1/2	1/2	1/2	0.0018(2)

were conducted using a *Quantum Design, MPMS-5 SQUID* magnetometer. The measured temperature range was 1.8 K-300 K with a magnetic field range of 0.1-5.5 T. Magnetic measurements were carried out on bulk samples (approximately 300 mg) from the same preparations as the one used for powder diffraction experiments. The measurement yielded Pauli-paramagnetic behavior.

Electronic Structure Calculations. The theoretical electronic structures of model and actual $Ti_{0.80(2)}Ni_{1.83(2)}Ga_{1.12}$ and related structures were calculated self-consistently by the tight-binding linear muffin-tin-orbital (TB-LMTO) method[9,11-12] within the atomic sphere approximation (ASA) using the *STUTTGART* program.[23] Exchange and correlation were treated in a local spin density approximation (LSDA).[13] All relativistic effects except spin-orbit coupling were taken into account using a scalar relativistic approximation.[14] Within the ASA, space is filled with overlapping Wigner-Seitz (WS) atomic spheres. The radii of the WS spheres were obtained by requiring the overlapping potential to be the best possible approximation to the full potential according to an automatic procedure.[15] The WS radii for the atomic sites determined by this procedure are 1.5058 Å for Ti, 1.3832 Å for Ni, and 1.5058 Å for Ga for all calculations. The basis set included 4s, 4p, and 3d orbitals for Ti and Ni; 4s and 4p orbitals for Ga. The reciprocal space integrations to determine the self-consistent charge densities, densities of states (DOS) and crystal orbital Hamilton populations (COHP)[16] were performed by the tetrahedron method[17] using 897 k-points for $TiNi_2Ga$ and 145 *k*-points for a model structure ($TiNi_{2.5}Ga_{1.5}$) in the irreducible wedges of the corresponding Brillouin zones for the models.

To study the site preference of metal atoms in $Ti_{0.80(2)}Ni_{1.83(2)}Ga_{1.12}$-type structures, semi-empirical, Extended Hückel[18,20-21] (EHT) calculations were performed. In EHT, the atomic orbitals are expressed as Slater-type orbitals: single-

zeta functions for Ga; and double-zeta functions for Ti and Ni. All atomic orbital overlaps are calculated within two nearest neighbor cells in each independent crystallographic direction. Diagonal Hamiltonian matrix elements are given by valence state orbital energies derived from atomic spectra; off-diagonal Hamiltonian matrix elements are approximated by the weighted Wolfsberg-Helmholz approximation.[19] Integrated quantities, e.g., band energies and Mulliken populations at each site were obtained using a special point set of 483 *k*-points in the irreducible wedge of the first Brillouin zone.

Results and Discussion

$Ti_{0.80(2)}Ni_{1.83(2)}Ga_{1.12}$ crystallizes in the cubic $Sc_{11}Ir_4$-structure type, Pearson symbol *cP*120, which has 8 formula units per unit cell, so we can also formulate the compound as $Ti_{3.2(1)}Ni_{7.3(1)}Ga_{4.5}$. This structure is face-centered cubic, space group $Fm\bar{3}m$ (No. 225), with six atomic positions in the asymmetric unit. The optimal refinement yields segregation of Ti, Ni, and Ga atoms on all but one site in the asymmetric unit. A summary of crystallographic data, atomic positions, site occupancy factors and temperature displacements factors, as well as significant interatomic distances are listed in Tables 1-4. According to this refinement, and keeps in mind the $Sc_{11}Ir_4$-type description, gives a re-formulation as $(Ti_3Ni_4Ga_4)[Ti_{0.2}Ni_{3.3}Ga_{0.5}]$.

The structure of $Ti_{3.2(1)}Ni_{7.3(1)}Ga_{4.5}$, illustrated in Figure 1, is isopointal to that of $Sc_{11}Ir_4$, but the structural framework is distinct because Ni atoms preferentially occupy the Ir site, while the Sc site are nearly uniformly distributed by Ti, Ni, and Ga. Two alternative structural prototypes include the Th_6Mn_{23}- or $MgCu_{16}Si_7$-types: the Ti

Table 3. Selected interatomic distances.

atoms	distance, Å	atoms	distance, Å
Ga1 – Ga2	3.049(1)	Ni1 – Ni2	2.562(1)
Ti1	2.594(5)	Ti1	2.946(1)
Ga2 – Ni1	2.413(1)	Ni2 – Ni2	2.837(3)
Ni2	2.719(2)	Ti1	2.723(3)
Ti1	2.625(2)	M3	2.457(2)

Table 4. Anisotropic displacement parameters ($Å^2$) for $Ti_{0.80(2)}Ni_{1.83(2)}Ga_{1.12}$. The anisotropic displacement factor exponent takes the form: $-2\pi^2[h^2 a^{*2} U^{11} + ... + 2 h k a^* b^* U^{12}]$

	U_{11}	U_{22}	U_{33}	U_{23}	U_{13}	U_{12}
Ga1	0.0024(1)	0.0024(1)	0.0024(1)	0	0	0
Ga2	0.0025(1)	0.0025(1)	0.0025(1)	0.004(1)	0.004(1)	0.004(1)
Ni1	0.0019(1)	0.0023(1)	0.0023(1)	-0.001(1)	0	0
Ni2	0.0017(1)	0.0017(1)	0.0017(1)	0.000(1)	0.000(1)	0.000(1)
Ti1	0.0022(1)	0.0022(1)	0.0024(2)	0	0	0
M3	0.0018(2)	0.0018(2)	0.0018(2)	0	0	0

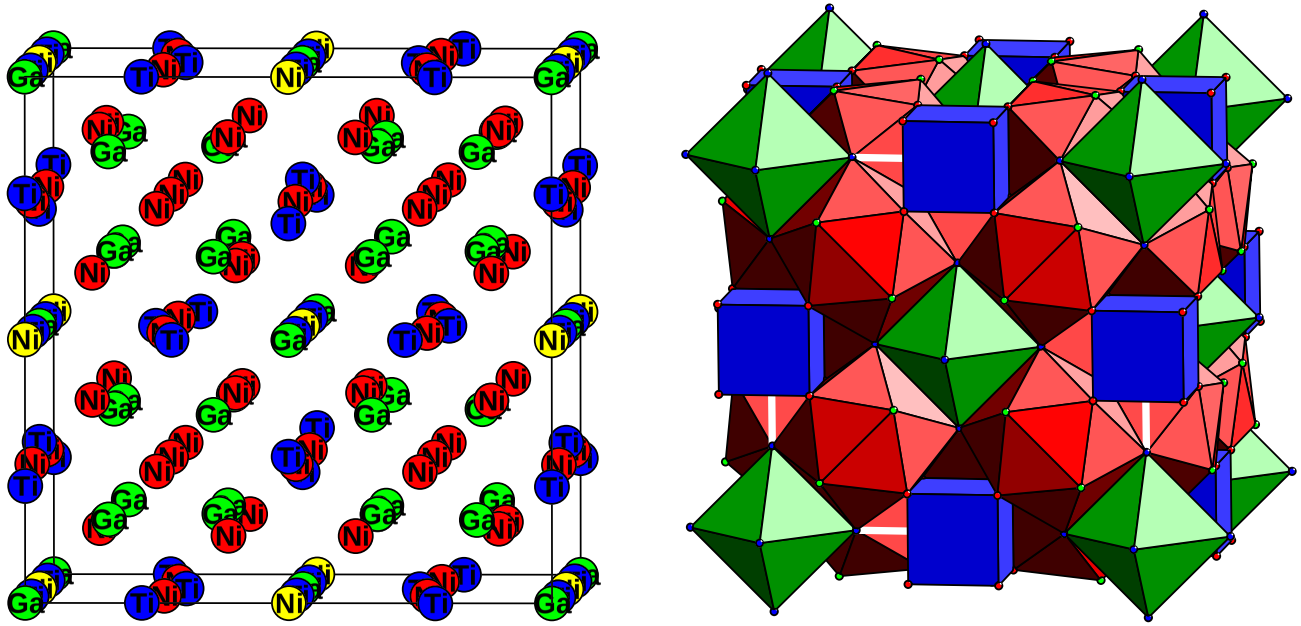

Figure 1. Unit cell structure and polyhedra structure of cubic $Ti_{0.80}Ni_{1.83}Ga_{1.12}$ (a = 11.7075 Å, space group $Fm\bar{3}m$). Blue represent Ti, red represents Ni atoms and green represents Ga atoms.

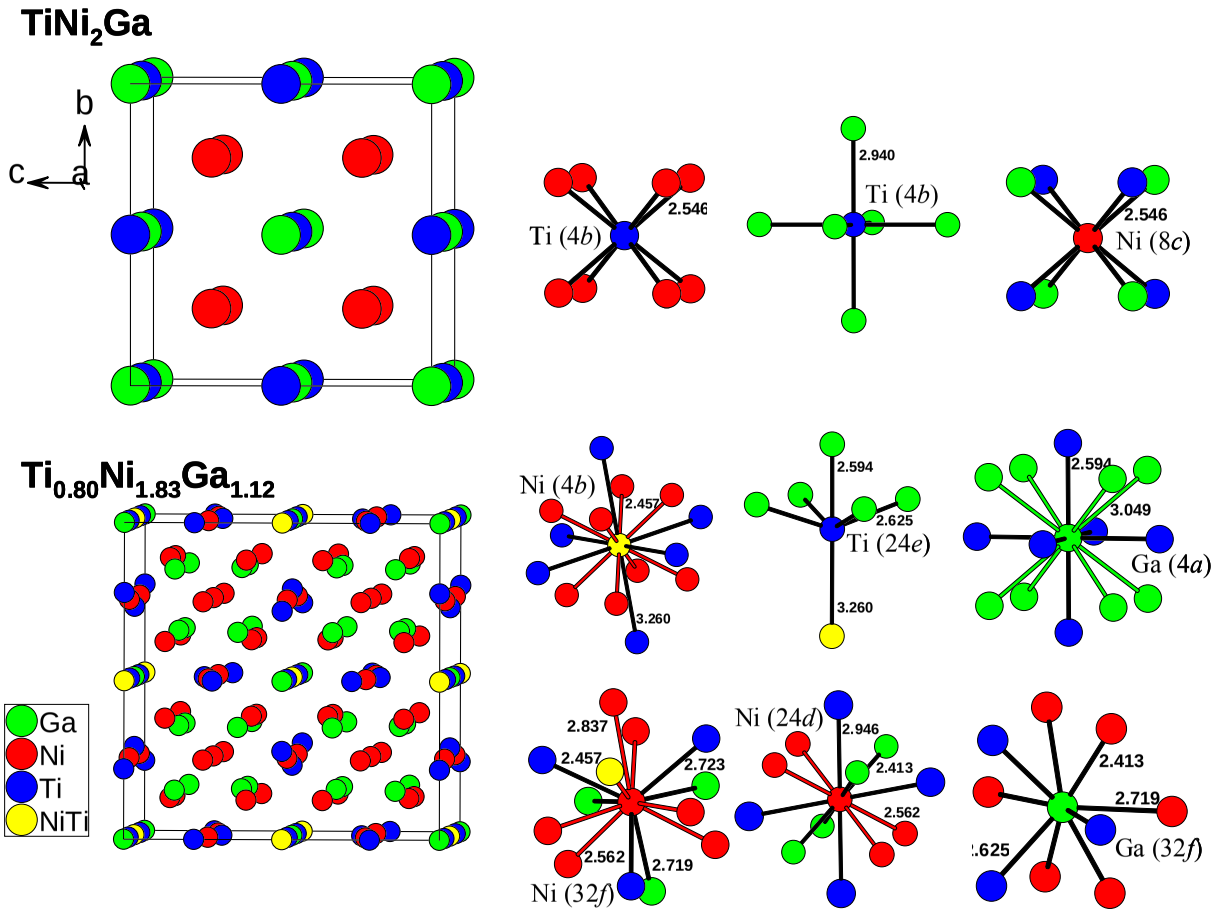

Figure 2. Unit cell structures of (1) $TiNi_2Ga$ Heusler phase (a = 5.88Å, space group $Fm\bar{3}m$) and (2) $Ti_{0.80}Ni_{1.83}Ga_{1.12}$ distorted defect phase. Local coordinations around each site with various bond distances are shown.

atoms occupy solely the Th or Mg positions while the Ni and Ga atoms are distributed among the Mn or Cu/Si sites. In these types, however, one special position (0,0,0) is vacant, but filled with Ga in $Ti_{3.2(1)}Ni_{7.3(1)}Ga_{4.5.}$

From a different perspective, this structure involves a network consisting of three basic building blocks: octahedra, cubes, and icosahedra. To achieve this, we start with the bcc-based Heusler phase structure for $TiNi_2Ga$,[6] as highlighted in Figure 2, which illustrates the local coordination around each atom for these two arrangements. Cubic and octahedral environments are found in both $TiNi_2Ga$ as well as in $Ti_{0.80(2)}Ni_{1.83(2)}Ga_{1.12}$. Based on the Heusler phase aristotype $TiNi_2Ga$, the observed phase can be formulated as $(Ti_{0.75}\square_{0.25})(NiGa)(Ti_{0.05}Ni_{0.825}Ga_{0.125})$. From this there are three significant modifications: (1) there are vacancies at 25% of the Ti sites in an ordered fashion. In the observed unit cell, these vacancies are located at the 8*c* sites (1/4,1/4,1/4). These Ti sites and vacancies sit at the center of a Ni cube. (2) these vacancies trigger the substitution of electron-rich Ga atoms to replace one-half of the Ni atoms in the cubic arrangement resulting in two distinct tetrahedra, one by Ga and the other by Ni atoms. (3) The Ga site is almost replaced by Ni atoms, with some occupation by Ti atoms, as well. The vacancy and subsequent reassembly of polyhedra leads to nearly icosahedral local symmetry at the Ni1 sites. Each of these icosahedra is connected throughout the lattice by 4 Ga1 centered octahedra and 4 M1 centered cubes sharing edges with the distorted icosahedra making a cube (see Figure 1). The Ga1 position is coordinated by 6 Ti atoms at 2.595 Å in an octahedron and 8 Ni3 atoms in a cube at 2.467 Å. With one exception, the one between M3(Ni/Ti) and 8 Ni2 sites in cubic coordination, most of the interactions comprising the distorted icosahedron account for the shortest distances within the crystal structure, some of which include Ga1-Ti2 at 2.595(5) Å, Ga2-Ti2 at 2.625(2)

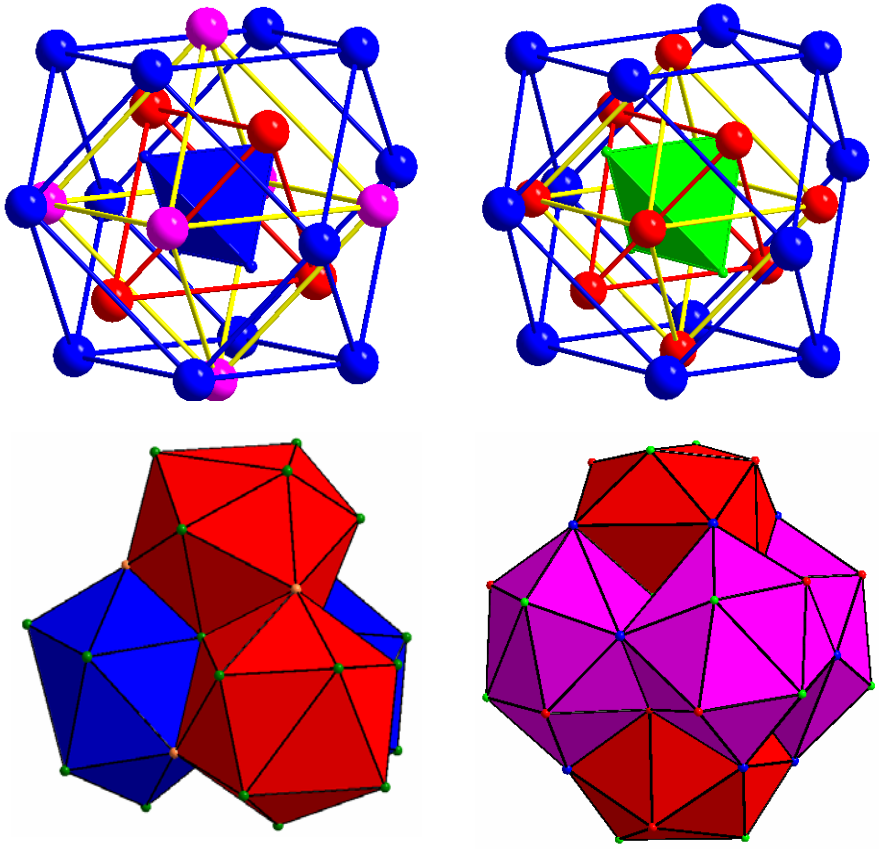

Figure 3. γ-brass cluster views in cubic γ-brass Cu_5Zn_8 and distorted cluster views in cubic $Ti_{0.80}Ni_{1.83}Ga_{1.12}$.

Å, Ga2-Ni2 at 2.413(1) Å and Ni2-Ni3 at 2.5619(9) Å.

The distorted defect structure also resembles that of the cubic γ-brass structure. As shown in Figure 3, the 26-atom, 'γ-brass cluster' can also be extracted from $Ti_{0.80(2)}Ni_{1.83(2)}Ga_{1.12}$. These clusters consist of an inner tetrahedron of Ga atoms, an outer tetrahedron of Ni atoms, an octahedron by Ni atoms surrounding these tetrahedra, and, finally, a cuboctahedron of Ti atoms encapsulating all polyhedra. The difference between the cubic γ-brass structures, e.g. Cu_5Zn_8, and the cubic $Ti_{0.80(2)}Ni_{1.83(2)}Ga_{1.12}$ comes from the assembly of these building blocks. In γ-brass, these 26-atoms clusters are packed in a body-centered array, and face each other via the eight triangular faces of the cuboctahedron. As a result, four face-sharing icosahedra, centered by atoms at the outer tetrahedron, come together to form the tetrahedral poly-cluster along {111} directions, as illustrated in Figure 3. On the other hand, in $Ti_{0.80(2)}Ni_{1.83(2)}Ga_{1.12}$, the same cluster units are assembled by sharing the six rectangular faces with each other along {100} directions to build a face-sharing octahedron of icosahedra, also shown in Figure 3.

Another relationship to the cubic γ-brass structure is evident in the ordered arrangement of vacancies at the Ti sites. γ-brass is a distortion of a 3×3×3 supercell of bcc packing that has vacancies located at the corners and center of the unit cell (2 vacancies for 54 positions). From perspective of the Heusler alloy, $Ti_{0.80(2)}Ni_{1.83(2)}Ga_{1.12}$ is a 2×2×2 supercell of this aristotype, or a 4×4×4 supercell of bcc packing. As shown in Figure 4, if simple bcc or the CsCl-type structure is denoted as the $1\times1\times1$ structure, then the $TiNi_2Ga$ Heusler phase could be viewed as a 2×2×2 superstructure with one additional coloring resulting in two types of interpenetrating cubic cells (TiGa) and (NiNi). Similarly, the unit cell of the G-phase $Ti_{0.80(2)}Ni_{1.83(2)}Ga_{1.12}$ contains eight 2×2×2 supercells built of two types of

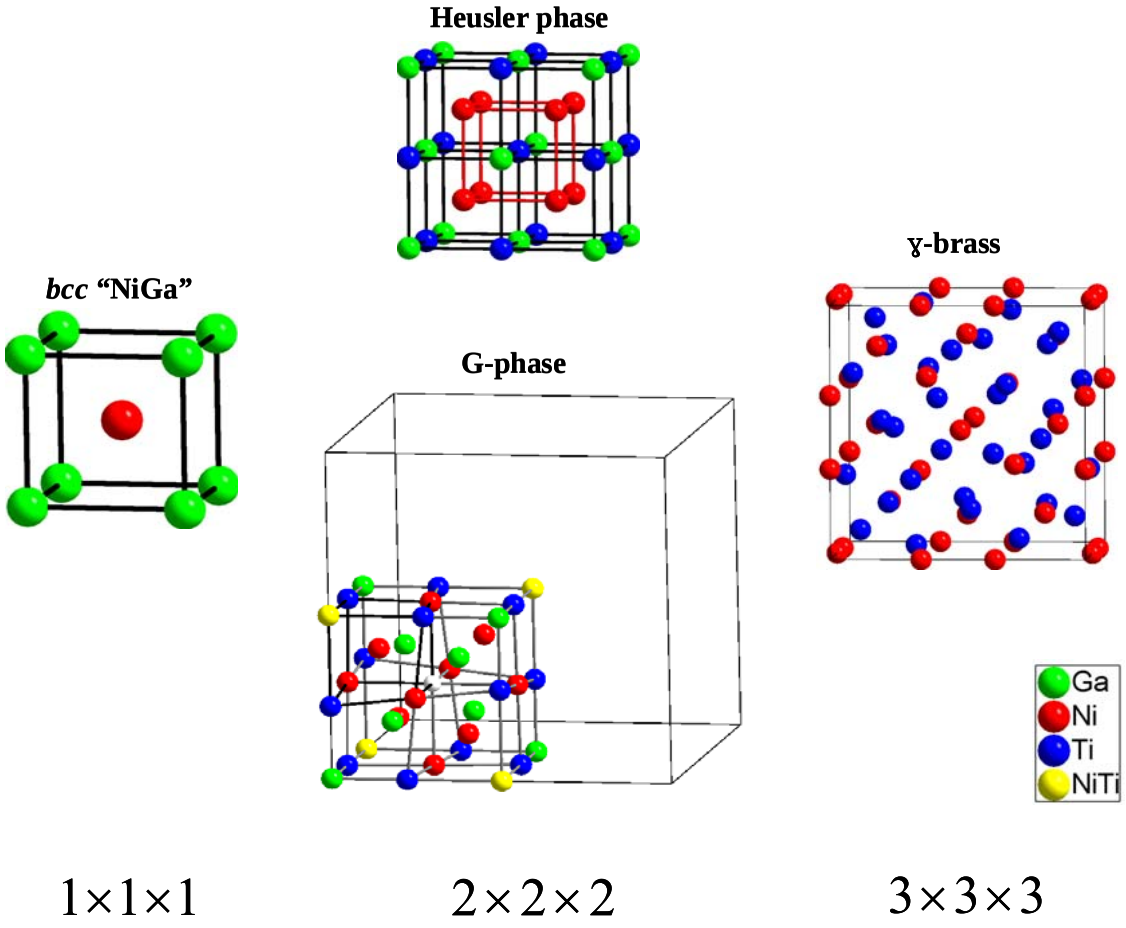

Figure 4. Structural relationships between the Heusler phase, *G*-phase ($Ti_{0.80}Ni_{1.83}Ga_{1.12}$), and γ-brass phase.

distorted bcc subcells in an alternating manner: (i) $Ni[Ti_{3.4}\square Ni_{3.6}]_{1/8}$ and (ii) $Ga[Ti_3\square Ni_3Ga]_{1/8}$. To complete the unit cell, 4 sets of each of these 2×2×2 supercells are assembled together in an alternating pattern resulting in a face centered cubic lattice with a 4×4×4 supercell of bcc packing. The vacancies, therefore, actually distribute to give a 2×2×2 supercell of bcc packing before atomic displacements and distributions create the network of icosahedra, cubes, and octahedra and the ultimate 4×4×4 supercell. $TmRuGa_3$ is a recent example of a structure that follows this 2×2×2 supercell created by vacancies in bcc packing.[24]

The nature of the distortion and atomic distributions were examined by first principles and semi-empirical calculations on a variety of model undistorted and distorted structures. For the experimentally refined $Ti_{0.80(2)}Ni_{1.83(2)}Ga_{1.12}$ compound, the model structure $Ti_{0.75}Ni_{1.875}Ga_{1.125}$ with fully occupied Ni in the 4b site was used. Total DOS and COHP curves for various interatomic interactions obtained from TB-LMTO-ASA calculations are illustrated in Figure 5. Calculations based on the LSDA were also explored, but converged to the same solution as obtained by LDA, so we continued with just LDA. This conclusion, nevertheless, agrees with Pauli paramagnetism obtained from magnetic susceptibility measurements.

As expected from the structural similarities in the defect structure with the γ-brass structure, $Ti_{0.75}Ni_{1.875}Ga_{1.125}$ can also be viewed as an electronically stabilized Hume-Rothery phase. The DOS in Figure 5 shows that the Fermi energy falls in a sharp yet narrow pseudogap, which is the evident feature in icosahedral Hume-Rothery phases.

The corresponding COHP analysis reveals a complex interplay of metal-metal interactions at the Fermi level that certificate to this observation. Before describing these points, we focus on the electronic structure of the Heusler alloy

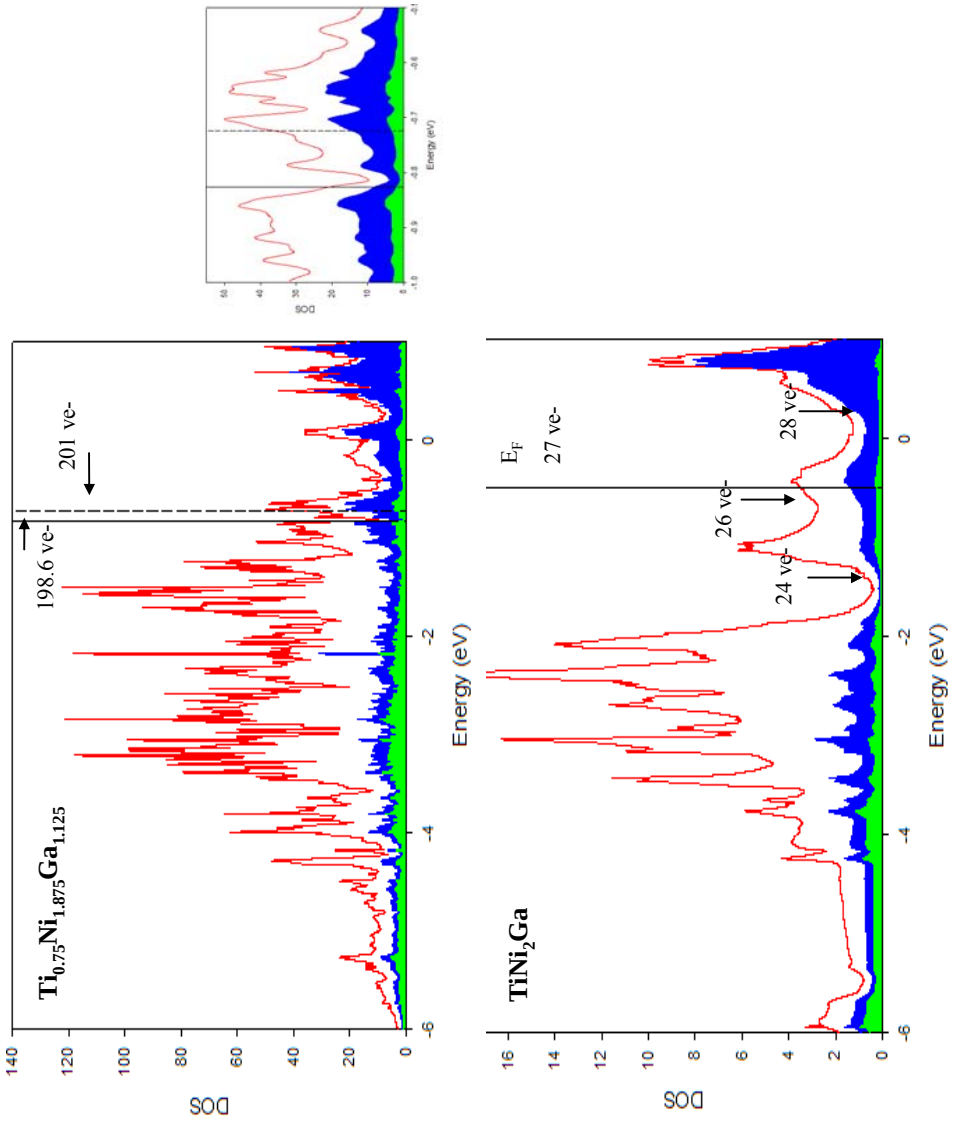

Figure 5. DOS of $TiNi_2Ga$ and $Ti_{0.75}Ni_{1.875}Ga_{1.125}$. In DOS curves, total DOS are represented by red lines and blue and green for Ti + Ga and Ga, respectively. And the calculated Fermi energy is plotted as the dotted line, where the refined valence electron count is plotted as a solid line.

Figure 6. COHP curves for (1) $Ti_{0.75}Ni_{1.875}Ga_{1.125}$ and (2) $TiNi_2Ga$. The calculated Fermi energy is plotted as the dotted line, where the refined valence electron count is plotted as a solid line. Weighed total COHP curves are shown for both structures (left). For $TiNi_2Ga$, the interactions between Ni–Ti (blue) and M–Ga (M = Ni; yellow, Ti; green) exhibit bonding characteristics, and Ni–Ni interactions at 2.940Å (red) shows antibonding characteristic at the Fermi energy. For $Ti_{0.75}Ni_{1.875}Ga_{1.125,}$ the Ni–Ni interaction at 2.456 Å lies in a pseudogap at the Fermi level. The Ga–Ti interactions making octahedron at 2.595Å (green) and 2.627Å (blue) both have bonding characteristic at the Fermi level, and Ti–Ni interaction at 3.259Å (pink) shows nonbonding characteristic. Both Ga–Ni at 2.412Å (green) and Ni–Ti at 2.946Å (blue) show bonding characteristic at the Fermi level. The Ni – Ni at 2.562Å (red) crosses over from antibonding to nonbonding at the Fermi level.

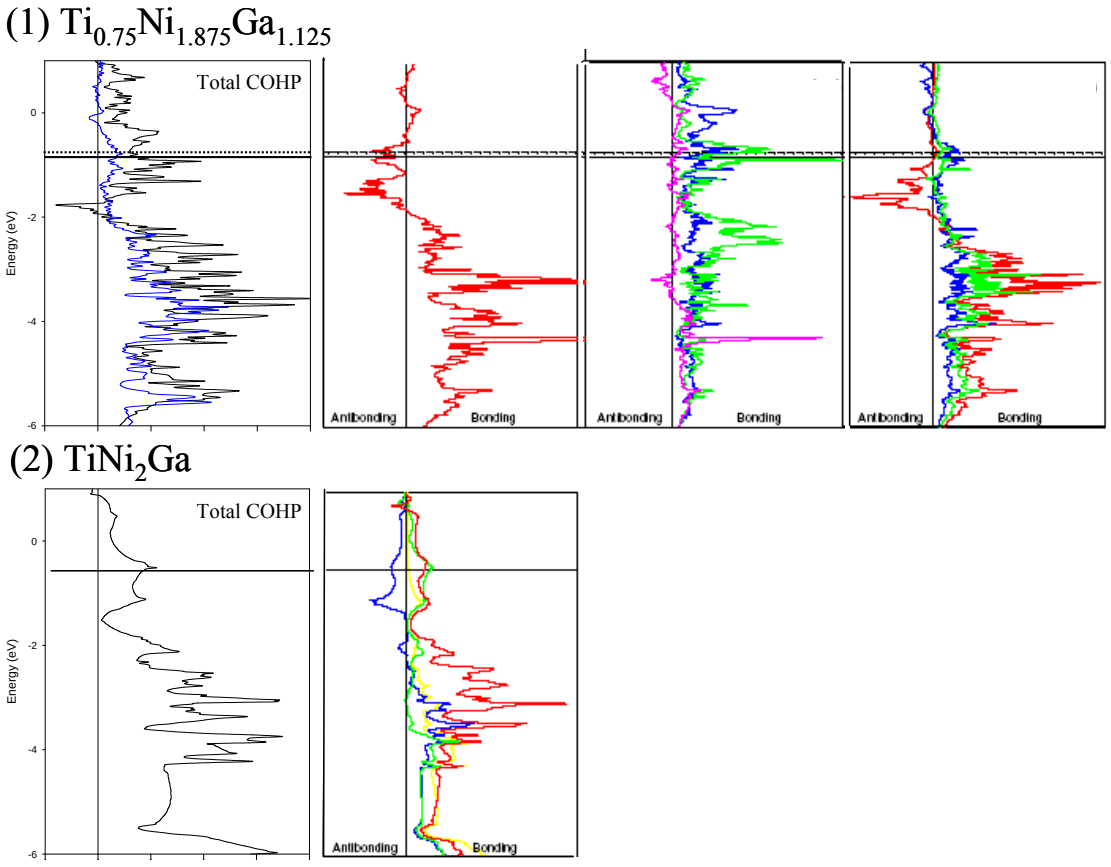

$TiNi_2Ga$, also shown in Figure 5. The Fermi level (27 electrons) lies in a ca. 1.8 eV band containing 2 crystal orbitals. The COHP analysis indicates the Fermi level falls among Ni-Ni antibonding interactions, but Ti-Ni and Ni-Ga weak bonding interactions. The DOS at the Fermi level is a peak; by lowering the valence electron count, this level can move to a minimum, i.e., a pseudogap. There is a clear pseudogap at 24 valence electrons, but this drop is electron count would deplete a significant number of metal-metal bonding state.

For $Ti_{0.75}Ni_{1.875}Ga_{1.125,}$ the district pseudogap for 168 electrons, which is the "equivalent" of 24 electrons in $TiNi_2Ga$ is missing. Nevertheless, there is a sharp pseudogap at the Fermi level for electron count close to 200 valence electrons. The model $Ti_{0.75}Ni_{1.875}Ga_{1.125}$ contains 201 electrons; the observed composition $Ti_{0.75}Ni_{1.875}Ga_{1.125}$ has 198.6 electrons. The COHP analysis, though showing no clear crossover from bonding to antibonding states at the pseudogap, does involve a combination of antibonding Ni-Ni and weak bonding Ti-Ni and Ti-Ga interactions.

Conclusion

A new intermediate compound bridging the Heusler phase with the γ-brass phase is prepared in a Ga flux and its crystal structure was characterized. From the COHP analysis, structural flexibilities towards more electron deficient composition suggested the possibility of larger distortion and/or mixing. This final distorted structure mimics the same building block in the γ-brass structure, and both structures' electronic studies showed the formation of the pseudogap at the Fermi level.

Acknowledgements

References

[1] Bradley, A. J.; Rodgers, J. W., *Proc. Royal Soc. London. A.* (144) 852, **1934**(3), 340

[2] Pavlyuk, V. V.; Dmytriv, G. S.; Chumak, I. V.; Ehrenberg, H.; Pauly, H., *J. Solid State Chem*. 178, **2005**, 3303

[3] Fujiwara, *J. Phys. Rev*. B40, **1989**, 942

[4] Fujii, S.; Ishida, S.; Asano, S.; *J. Phy. Soc. Japan*, **1989**, 58(10), 3657

[5] Chabot B., Cenzual K., Parthe E., *Acta Crystallogr*. **1980**, 36B, 7

[6] Markiv, V. Ya.; Gladyshevskii, E. I. (Hladyshevskii, E. I.); Kuz'ma, Yu. B., *Dopovidi Akademii Nauk Ukrains'koi RSR*. **1962**(10), 1329-1331

[7] Rietveld, H. M. *J. Appl. Crystallogr*. **1969**, 2, 65

[8] SMART; Bruker AXS, Inc.; Madison, WI, **1996**.

[9] Andersen, O. K.; Jepsen, O. *Phys. Rev. Lett*. **1984**, 53, 2571.

[10] Blessing, R. H.: An empirical correction for absorption anisotropy. *Acta. Cryst*.. **1995**, A 51, 33.

[11] Andersen, O. K. *Phys. Rev*. **1975**, B12, 3060.

[12] Andersen, O. K.; Jepsen, O.; Glötzel, D. In Highlights of Condensed-Matter Theory; Bassani, F.; Fumi, F.; Tosi, M. P.; Lambrecht, W. R. L.; Eds.; North-Holland: New York, **1985**.

[13] Von Barth, U.; Hedin, L. *J. Phys. C* **1972**, 5, 1629.

[14] Koelling, D. D.; Harmon, B.N. *J. Phys. C* **1977**, 10, 3107.

[15] Jepsen, O.; Anderson, O. K. *Z. Phys. B* **1995**, 97, 35.

[16] Dronskowski, R.; Blöchl, P. *J. Phys. Chem*. **1993**, 97, 8617.

[17] Blöchl, P. E.; Jepsen, O.; Andersen, O.K. *Phys Rev*. **1994**, B49, 16223.

[18] Hoffmann, R. *J. Chem. Phys*. **1963**, 39, 1397-1412.

[19] Wolfsberg, M.; Helmholz, L. J. *J. Chem. Phys*. **1952**, 20, 837.

[20] Dronskowski, R.; Blöchl, P. *J. Phys. Chem*. **1993**, 97, 8617.

[21] Blöchl, P. E.; Jepsen, O.; Andersen, O.K. *Phys Rev*. **1994**, B49, 16223.

[22] SHELXTL; Brucker AXS, Inc.; Madison, WI, **1996**.

[23] The Stuttgart Tight-Binding LMTO-ASA program Version 4.7; Max-Planck-Institut für Festkörperforschung, Stuttgart, Germany **1998**.

[24] Sichevich, O. M.; Bruskov, V. A.; Grin, Y. *Kristallografiya.* **1989**, 34(6), 1571.

CHAPTER 5

Structural and Compositional Studies of the Flux-Grown $RENi_{1-x}Ge_3$ Series (RE = Ce-Nd, Sm, Gd-Lu; Y)

(manuscript in preparation for submission to Inorganic Chemistry)

*Hyunjin Ko,# E. D. Mun,% Sergey L. Bud'ko,& P. C. Canfield,& and Gordon J. Miller#**

Department of Chemistry, Iowa State University and Ames Laboratory, Ames, Iowa 50011-3111,
% Department of Physics and Astronomy, Iowa State University, Ames, Iowa 50011-3111
& Department of Physics and Astronomy, Iowa State University and Ames Laboratory,
Ames, Iowa 50011-3111

ABSTRACT

Flux-grown single crystals of the $RENi_{1-x}Ge_3$ family (RE = Ce-Nd, Sm, Gd-Er, Yb-Lu; Y) have been characterized by powder and single crystal X-Ray diffraction methods to determine trends in crystal structures and refined chemical compositions as part of a complete study of their magneto-structural relationships. Most $RENi_{1-x}Ge_3$ examples (RE = Ce-Nd, Sm, Gd-Er; Y) adopt the orthorhombic $SmNiGe_3$-type structure, space group *Cmmm,* with lattice parameters decreasing essentially linearly along the sequence of rare-earth elements from $CeNiGe_3$ to $ErNi_{0.61}Ge_3$. $YbNiGe_3$ crystallizes in a new structure, which forms a tetragonal lattice, space group $I4_1/amd$ with lattice parameters a = 4.0347(6) Å, c = 43.211(9) Å. $LuNiGe_3$ also adopts a new structure type, which is distorted from the orthorhombic crystal class of the $SmNi_{1-x}Ge_3$-type structures. This new structure type is

monoclinic, space group *C2/m* with lattice parameters a = 7.8521(16) Å, b = 7.9384(16) Å, c = 10.700(2) Å, and β = 100.530(3)°. On proceeding left to right along the Lanthanide series, deficiencies at the Ni site of $RENiGe_3$ increase up to the Er compound followed by lattice distortions. Possible electronic driving forces for these vacancies were investigated by first principles, tight-binding calculations of the electronic structures.

Introduction

Ternary intermetallic materials that specifically contain a combination of a rare-earth element, a 3*d* transition metal, and a tetrelide element, *i.e*., Si, Ge, or Sn, are attracting attention of condensed matter physicists and solid-state chemists because this compound class exhibits various technologically advantageous physical properties such as heavy fermion behavior and superconductivity, as well as numerous magnetic ordering patterns[1-3] that provide opportunities to better understand interatomic exchange interactions such as Kondo[4] and RKKY interactions[5]. A crucial part of this research activity is the development of flux-growth strategies to prepare single crystals suitable for both property measurements and structural characterizations. Such samples allow thorough determination of structure-composition-property relationships in these phases. Another issue is to design structures in which the rare-earth metal occupies an uniaxial environment so that magnetic anisotropy can be easily investigated by oriented single crystals. With these concepts in mind, we have carried out a systematic study of the $RETGe_3$ class of phases (RE = rare-earth metal; T = group VIIIA transition metal).

$RETGe_3$ intermetallic compounds are reported to crystallize exclusively in one of three structural families: (1) the cubic $Yb_3Rh_4Sn_{13}$-type[6] (space group $Pm\bar{3}n$); (2)

tetragonal $BaNiSn_3$-type[7] (space group *I4mm)*; or (3) orthorhombic $SmNiGe_3$-type[8] (space group *Cmmm*). Specific examples in the cubic class include the $LaTGe_3$ series (T = Co, Rh, Ir;[9] Ru, Os), and tetragonal examples include $NdCoGe_3$[10], $CeTGe_3$ (T = Fe, Co),[11] and $EuCoGe_3$.[12] To our knowledge, however, systematic structural investigations of single crystalline samples of orthorhombic, $SmNiGe_3$-type $RENiGe_3$ compounds have not been reported. The $RENiGe_3$ series was initially grown in a germanium flux to explore the magnetic properties of rare-earth elements in locally orthorhombic environments.[13] Herein, we report the detailed crystal structures of flux-grown single crystals of $RENiGe_3$ (RE = Y, Ce-Nd, Sm, Gd-Er), and the theoretical electronic structure studies of $CeNiGe_3$ and $ErNiGe_3$ to understand the refined Ni contents, which tend to decrease along the series, i.e., the series should be formulated as $RENi_{1-x}Ge_3$. During the course of our investigations, we have identified two new structures in the Yb and Lu cases: a tetragonal $YbNi_{1.04(6)}Ge_{2.89(5)}$ and a monoclinic $LuNi_{0.41(4)}Ge_{3.07(4)}$.

Experimental

Synthesis. The series of $RENi_{1-x}Ge_3$ compounds (RE = Y, Ce-Nd, Sm, Gd-Lu) was prepared via a flux-growth method using excess Ge as the flux by mixing the pure elements, RE, Ni, and Ge in a 1:1.6:9 molar ratio, respectively, and heating to 1323 K in an alumina crucible. Crystalline specimens are centrifuged from the flux at elevated temperatures, and subsequently treated with nitric acid and rinsed in an ultrasonic bath to remove excess flux. The resulting samples are not reactive when exposed to air or moisture. These procedures successfully yielded crystalline samples for further physical and structural characterization. "$EuNiGe_3$" was targeted using the same synthetic procedure without yielding suitable products for further

characterization. Detailed synthetic procedures for the entire series are reported in a separate paper.[13]

Structural Analysis

Powder X-Ray Diffraction. Phase characterizations were performed on flux-grown samples by room-temperature, X-ray powder diffraction using a *Rigaku MiniFlex* diffractometer at room temperature with CuK_α radiation (λ = 1.540598 Å) with a Si standard. The diffraction patterns were collected for 2θ values ranging from 10º to 100º at increments of 0.02º. The lattice parameters were determined by the Rietveld profile fitting method[14] using the *Rietica* refinement program.[15]

Single Crystal X-Ray Diffraction. From flux-grown, plate-like crystalline pieces, those with lustrous surfaces were isolated and several irregularly shaped crystals with average approximate dimensions of (100 μm)^3 were selected from crushed samples and mounted on glass fibers. Room temperature X-ray diffraction intensities were recorded on a *STOE-IPDS*(II) *(Image Plate Diffraction System)* single crystal diffractometer with monochromated Mo *K*α radiation (λ = 0.71073 Å, 50 kV and 40 mA) and detector to crystal distance of 100 mm.

A numerical absorption correction was applied to the data using program *X-shape* (*STOE*), which corrects symmetry equivalent reflections while optimizing a convex polyhedron for the crystal shape. Due to the large linear absorption of the rare-earth elements, consideration of the differences in the path lengths of the symmetry equivalent reflections resulted in significant improvements of R_{int} for all crystalline specimens. The structures were solved by direct methods and refined by full-matrix least squares against F^2 for all reflections using the *SHELXTL* program suite[16]. All refined parameters including anisotropic displacement parameters and site occupancies were simultaneously refined for all atoms, while the occupancy

parameter of the rare-earth atom was held constant.

Chemical Analysis. The chemical composition of $RENi_{1-x}Ge_3$ samples were analyzed by Energy Dispersive Spectroscopy (EDS) using a *JEOL 840A* scanning electron microscope, equipped with an *IXRF Systems Iridium X-ray analyzer* with *a Kevex* Quantum thin-window Si(Li) detector for quantitative chemical analysis with the standardless method and a 20 kV accelerating voltage and a 30 mA beam current. The results showed no significant oxygen content.

Electronic Structure Calculations. To investigate issues of chemical bonding and possible electronic factors influencing vacancies of the Ni sites in the $RENi_{1-x}Ge_3$ series, electronic structures for $CeNiGe_3$ and $ErNiGe_3$ were calculated self-consistently by the tight-binding linear muffin-tin-orbital (TB-LMTO) method[17-20] within the atomic sphere approximation (ASA) using the Stuttgart code*: LMTO Version 47*. The local spin density approximation (LSDA)[21] was used to treat exchange and correlation. All relativistic effects except spin-orbit coupling were taken into account using a scalar relativistic approximation.[22] The radii of the overlapping, space filling Wigner-Seitz (WS) atomic spheres were obtained by requiring the overlapping potential to be the best possible approximation to the full potential according to an automatic procedure.[23] The WS radii for the atomic sites determined by this procedure are 2.501 Å for Ce, 2.411 Å for Er, 1.47-1.60 Å for Ge, and 1.38-1.49 Å for Ni. The basis set included 4*s* and 4*p* orbitals for Ge; 4*s*, 4*p* and 3*d* orbitals for Ni, and 6*s, 6p* and 5*d* orbitals for Ce and Er; the 6*p* orbitals were downfolded[40] and the 4*f* electrons were treated as core electrons. Reciprocal space integrations to determine the self-consistent charge densities, densities of states (DOS) and crystal orbital Hamilton populations (COHP)[24] curves were performed on both structures by the tetrahedron method[25] using 301 irreducible ***k***-points within the

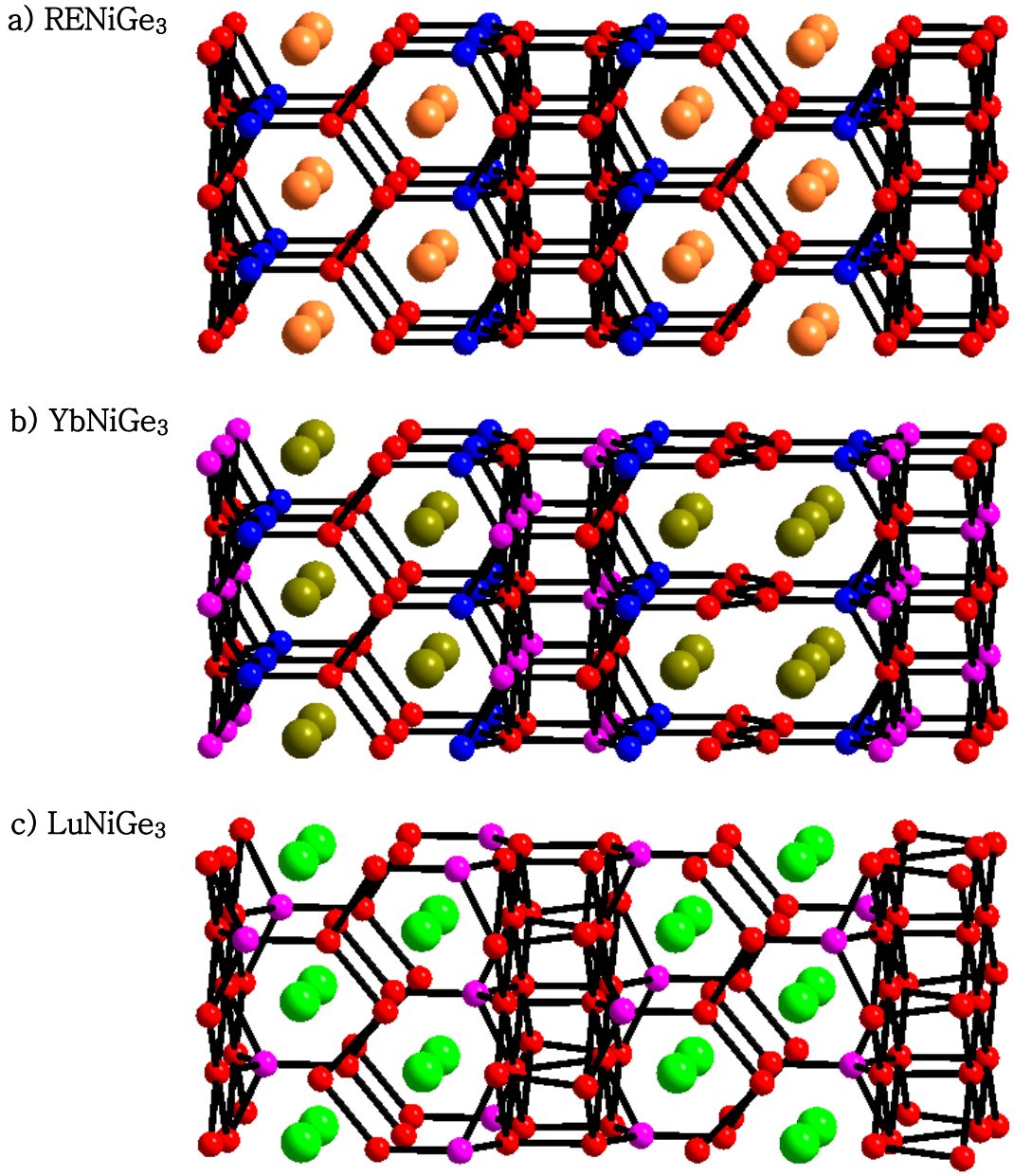

Figure 1. Views of the crystal structures of a) orthorhombic *Cmmm* $RENiGe_3$ (RE = Y, Ce-Nd, Sm, Gd-Er) down the *c*-axis, b) tetragonal *I4₁/amd* $YbNiGe_3$ down the *a*-axis, and c) monoclinic *C2/m* $LuNiGe_3$ down the *b*-axis. Ge atoms are in red, Ni atoms are in blue, where the sites with mixed Ge/Ni occupancies are shown in purple, and the rare earth atoms are drawn in larger spheres.

Table 1. Selected crystallographic data for $RENiGe_3$ series.

	$YNiGe_3$	$CeNiGe_3$	$PrNiGe_3$	$NdNiGe_3$	$SmNiGe_3$	$GdNiGe_3$	$TbNiGe_3$	$DyNiGe_3$	$HoNiGe_3$	$ErNiGe_3$	$YbNiGe_3$	$LuNiGe_3$
space group	*Cmmm*	*Cmmm*	*Cmmm*	*Cmmm*	*Cmmm*	*Cmmm*	*Cmmm*	*Cmmm*	*Cmmm*	*Cmmm*	*$I4_1/amd$*	*C2/m*
PXRD												
***a*, Å**	4.0543(1)	4.1384(2)	4.1249(1)	4.1087(1)	4.0824(5)	4.0551(2)	4.0380(0)	4.0231(1)	4.0061(3)	3.9704(0)	4.0503(0)	7.8622(0)
***b*, Å**	21.520(6)	21.838(4)	21.794(8)	21.740(9)	21.645(9)	21.560(2)	21.497(9)	21.444(4)	21.383(8)	21.197(0)		7.9457(0)
***c*, Å**	4.0617(3)	4.1695(1)	4.1557(2)	4.1372(3)	4.1055(1)	4.0786(7)	4.0585(4)	4.0438(2)	4.0305(2)	4.0126(0)	43.274(2)	10.711(9)
β, °												100.53(3)
Volume, $Å^3$	354.38(0)	376.82(0)	373.60(0)	369.56(0)	362.79(0)	356.58(0)	352.31(0)	348.87(0)	345.27(0)	337.71(0)	709.9(1)	669.1(7)
Single crystal XRD												
refined comp.	$YNi_{0.92(1)}Ge_3$	$CeNi_{0.98(1)}Ge_3$	$PrNi_{0.98(1)}Ge_3$	$NdNi_{0.97(1)}Ge_3$	$SmNi_{0.93(1)}Ge_3$	$GdNi_{0.87(1)}Ge_3$	$TbNi_{0.86(2)}Ge_3$	$DyNi_{0.82(2)}Ge_3$	$HoNi_{0.77(2)}Ge_3$	$ErNi_{0.61(3)}Ge_3$	$YbNi_{1.04(6)}Ge_{2.89(5)}$	$LuNi_{0.41(4)}Ge_{3.07(4)}$
Z	4	4	4	4	4	4	4	4	4	4	8	8
volume, $Å^3$	352.52(12)	376.69(13)	372.74(13)	368.47(12)	362.36(12)	355.21(12)	352.12(12)	348.33(12)	344.51(12)	336.20(12)	703.4(2)	655.7(2)
abs. Coeff, mm^{-1}	23.267	20.075	20.717	21.391	22.69	24.217	25.054	25.901	26.827	28.203	28.324	31.177
data/parameters	482/23	506/23	507/23	506/23	495/23	485/23	490/23	482/23	480/23	302/23	473/24	1489/52
goodness-of-fit	1.102	0.879	0.943	1.079	1.042	1.096	0.943	0.934	1.161	0.98	0.945	1.006
final R [*I>2σ(I)*]	R_1=0.0404	R_1=0.0386	R_1=0.0330	R_1=0.0432	R_1=0.0491	R_1=0.0421	R_1=0.0422	R_1=0.0417	R_1=0.0515	R_1=0.0601	R_1=0.0248	R_1=0.0434
	R_w=0.0825	R_w=0.0837	R_w=0.0.0698	R_w=0.1263	R_w=0.1308	R_w=0.01012	R_w=0.0861	R_w=0.0938	R_w=0.1330	R_w=0.1386	R_w=0.0508	R_w=0.1034
peak/	1.380/	4.371/	4.213/	3.549/	4.993/	5.020/	4.086/	3.685/	4.743/	5.816/	2.014/	6.718/
hole, e/$Å^3$	-1.721	-3.238	-4.612	-2.043	-3.874	-2.552	-5.221	-6.367	-4.039	-3.454	-2.484	-3.476

orthorhombic Brillouin zones.

Results and Discussion

Systematic diffraction studies of the $RENi_{1-x}Ge_3$ series resulted in three related structures as shown in Figure 1. Moreover, Table 1 summarizes selected crystallographic and analytical data for these structures. For most of the rare-earth metals, viz., RE = Ce-Nd, Sm, Gd-Er and Y, $RENi_{1-x}Ge_3$ adopts an orthorhombic lattice, whereas $YbNiGe_3$ adopts a tetragonal lattice, and $LuNi_{1-x}Ge_3$ adopts a monoclinic lattice. All structures have in common a three-dimensional network of Ni and Ge atoms consisting of zig-zag chains of Ge atoms and two-dimensional slabs of (distorted) square nets of Ni and Ge atoms. The RE atoms surround the zig-zag chains and sit in the large cavities of the networks. Furthermore, compounds formed with the later rare-earth metals typically yield sub-stoichiometric content of Ni atoms, except in the Yb case. In this regard, both chemical analysis from EDS measurements and refinements from single crystal XRD investigations agree; Table 1 includes both results for comparison. According to EDS studies, a "Ni_3Ge_4" phase frequently occurs as a by-product, in addition to Ge.

Both PXRD and single crystal XRD studies led us to believe that the orthorhombic structure was adopted by $TmNiGe_3$ compound; however, due to the poor crystallinity of the $TmNiGe_3$ samples, no conclusive refinement of the single crystal structure was successively obtained. During our investigation, we identified $ErNiGe_3$ crystals adopting a monoclinic lattice resulting in an anomalous composition from single crystal X-Ray diffraction refinement process. Consequently, for $ErNiGe_3$ samples two separate batches were prepared to resolve the ambiguities in the possible lattice distortions. Both orthorhombic as well as monoclinic solutions were

found resulting in two completely different refinement compositions. This could not be clearly distinguished solely by powder X-Ray diffraction experiments due to the high noise level of the diffraction profiles. The orthorhombic lattice parameters were refined as a = 3.9594(8) Å, b = 21.273(4) Å, and c = 4.0063(8) Å with $ErNi_{0.61(3)}Ge_3$, and the monoclinic lattice refinement gave rise to the unit cell with a = 8.0044(16) Å, b = 7.9260(16) Å, c = 21.562(4) Å, and β = 100.67(3)°, space group C2/m, and a refined composition of $ErNi_{1.53(1)}Ge_2$. The EDS analysis clearly indicates that this also belongs to the $SmNiGe_3$ and crystallizes in the orthorhombic lattice since the composition of the system was confirmed to be $ErNi_{0.60(2)}Ge_{2.86(1)}$. For detailed refinement parameters of the monoclinic phase, see Appendix 5.2.

In addition, the anisotropic crystal topologies and the much longer b-axis unit cell parameters affected the anisotropic thermal displacement parameters throughout the series resulting in slightly elongated thermal ellipsoids. After taking numerical absorption corrections, the degrees of elongation were decreased significantly. As for the latter $RENi_{1-x}Ge_3$ (RE = Ho, Dy, Er; Lu) with larger partial occupancies at the Ni sites, we observed possible superstructure formations resulting in satellite diffraction peaks positioned half-way between major reflections along (010) and (001) directions.

1) $RENiGe_3$ (RE = Ce-Nd, Sm, Gd-Er; Y)

Diffraction symmetry and systematic absences confirm the *Cmmm* space group for the series of orthorhombic structures. The refined lattice parameters and significant crystallographic data are listed in Table 1; atomic coordinates, site occupancies, and isotropic displacement parameters are summarized in Table 2. All of these $RENiGe_3$ phases adopt the orthorhombic $SmNiGe_3$-type structure. The

Table 2. Atomic coordinates and isotropic displacement parameters for $RENiGe_3$ series.

atom	site	occup.	*x*	*y*	*z*	U_{eq}.
Y	4*j*	1	0	0.3314(1)	1/2	0.013(1)
Ge1	4*j*	1	0	0.2162(1)	0	0.015(1)
Ge2	4*i*	1	0	0.4429(1)	0	0.016(1)
Ge3	4*i*	1	1/2	0.4430(1)	1/2	0.015(1)
Ni	4*i*	0.922(12)	1/2	0.3897(1)	0	0.014(1)
Ce	4*j*	1	0	0.3322(1)	1/2	0.009(1)
Ge1	4*j*	1	0	0.0562(1)	1/2	0.013(1)
Ge2	4*i*	1	0	0.2163(1)	0	0.011(1)
Ge3	4*i*	1	0	0.4437(1)	0	0.013(1)
Ni	4*i*	0.981(12)	0	0.1086(1)	0	0.011(1)
Pr	4*j*	1	0	0.3320(1)	1/2	0.013(1)
Ge1	4*j*	1	0	0.2162(1)	0	0.016(1)
Ge2	4*i*	1	0	0.4436(1)	0	0.018(1)
Ge3	4*i*	1	1/2	0.4437(1)	1/2	0.017(1)
Ni	4*i*	0.979(11)	1/2	0.3912(1)	0	0.016(1)
Nd	4*j*	1	0	0.3320(1)	1/2	0.017(1)
Ge1	4*j*	1	0	0.2162(1)	0	0.019(1)
Ge2	4*i*	1	0	0.4436(1)	0	0.021(1)
Ge3	4*i*	1	1/2	0.4435(1)	1/2	0.020(1)
Ni	4*i*	0.973(14)	1/2	0.3910(1)	0	0.019(1)
Sm	4*j*	1	0	0.3317(1)	1/2	0.016(1)
Ge1	4*j*	1	0	0.2163(1)	0	0.018(1)
Ge2	4*i*	1	0	0.4432(1)	0	0.020(1)
Ge3	4*i*	1	1/2	0.4432(1)	1/2	0.020(1)
Ni	4*i*	0.926(12)	1/2	0.3905(1)	0	0.017(1)
Gd	4*j*	1	0	0.1685(1)	1/2	0.011(1)
Ge1	4*j*	1	0	0.2840(1)	0	0.014(1)
Ge2	4*i*	1	0	0.0570(1)	0	0.017(1)
Ge3	4*i*	1	1/2	0.0569(1)	1/2	0.016(1)
Ni	4*i*	0.870 (10)	1/2	0.1097(1)	0	0.013(1)
Tb	4*j*	1	0	0.3315(1)	1/2	0.016(1)
Ge1	4*j*	1	0	0.0572(1)	1/2	0.022(1)
Ge2	4*i*	1	0	0.2158(1)	0	0.021(1)

Ge3	4*i*	1	0	0.4427(1)	0	0.024(1)
Ni	4*i*	0.860(16)	0	0.1101(1)	0	0.021(1)
Dy	4*j*	1	0	0.3314(1)	1/2	0.014(1)
Ge1	4*j*	1	0	0.2157(1)	0	0.019(1)
Ge2	4*i*	1	0	0.4425(1)	0	0.022(1)
Ge3	4*i*	1	1/2	0.4427(1)	1/2	0.020(1)
Ni	4*i*	0.820(15)	1/2	0.3899(1)	0	0.018(1)
Ho	4*j*	1	0	0.3314(1)	1/2	0.015(1)
Ge1	4*j*	1	0	0.2154(1)	0	0.021(1)
Ge2	4*i*	1	0	0.4423(1)	0	0.023(1)
Ge3	4*i*	1	1/2	0.4426(1)	1/2	0.023(1)
Ni	4*i*	0.772(15)	1/2	0.3898(1)	0	0.018(1)
Er	4*j*	1	0	0.3314(1)	1/2	0.020(1)
Ge1	4*j*	1	0	0.0581(2)	1/2	0.030(1)
Ge2	4*i*	1	0	0.2137(2)	0	0.027(1)
Ge3	4*i*	1	0	0.4416(2)	0	0.031(1)
Ni	4*i*	0.61	0	0.1094(3)	0	0.021(2)
Yb	8*e*	1	1/2	1/4	0.0409(1)	0.012(1)
Ge1	8*e*	1	0	3/4	0.0169(1)	0.014(1)
Ge2	8*e*	1	1/2	3/4	0.0967(1)	0.016(1)
Ni1	8*e*	0.926(10)	0	3/4	0.0697(1)	0.014(1)
M (Ni/Ge)	8*e*	0.11/0.89(5)	0	1/4	0.0965(1)	0.016(1)
Lu	8*j*	1	0.0840(1)	0.2514(1)	0.3376(1)	0.009(1)
Ge1	4*i*	1	0.0086(2)	0	0.1176(1)	0.011(1)
Ge2	4*i*	0.959(11)	0.8578(2)	0	0.4129(2)	0.011(1)
Ge3	4*i*	1	0.3544(2)	0	0.4368(1)	0.010(1)
Ge4	4*i*	1	0.0505(2)	1/2	0.1188(1)	0.010(1)
Ge5	8*j*	1	0.7795(1)	0.2308(1)	0.1173(1)	0.010(1)
M (Ni/Ge)	4*i*	0.81/0.19(7)	0.3039(2)	0	0.2182(2)	0.010(1)

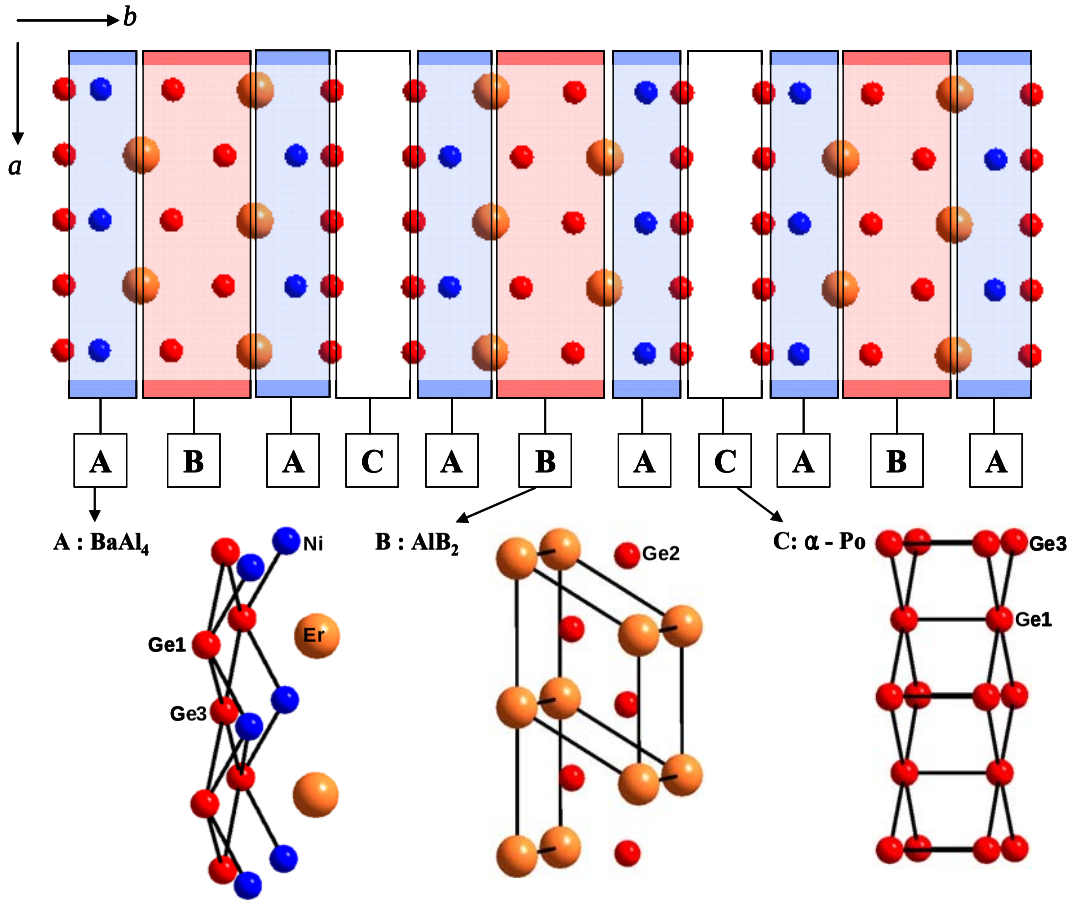

Figure 2. Structure frangments in $RENiGe_3$ (RE = Y; Ce – Er). On the bottom left, the blue shaded fragment of $BaAl_4$-type structure is shown, then the sections shaded in red represents the AlB_2-type fragments, and the simple α-Po type fragments completes the whole construction of the structural motif.

refined lattice parameters obtained by both powder and single crystal X-Ray diffraction experiments showed excellent agreement within the standard deviations. Proceeding from the larger to the smaller rare-earth systems, all lattice parameters nearly linearly decreased: ca. 4.3% for *a*-; ca. 4.0% for *c*-; and ca. 2.9% for the *b*-axis. Furthermore, the overall volume decreased by ca. 11%. These results are consistent with the lanthanide contraction that occurs when adding electrons to the 4*f* orbitals, which ineffectively shield the nucleus and leads to a corresponding increase in the effective nuclear charge across the lanthanide series of elements.[26]

Figure 2 shows the three two-dimensional structural building blocks and the construction sequence of these units along the *b*-axis that have been used to describe this type of structure[38]: (**A**) resembles the two-dimensional network on one side of the rare earth metals (Ba site) found in the tetragonal $BaAl_4$-type[27] structure; (**B**) follows the atomic arrangement found in the hexagonal AlB_2-type[28] structure; and (**C**) adopts the atomic arrangement of the α-Po-type[29] lattice. In $RENiGe_3$ phases, slab (A) is composed of Ge and Ni atoms in a puckered square network with RE-Ni distances of 3.1–3.2 Å and Ni-Ge distances of 2.25-2.3 Å. Slab (**B**) contains rare-earth atoms with Ge filling the trigonal prismatic holes with the following distances RE-RE ca. 4.0 Å, RE-Ge ca. 3.0 Å, and Ge-Ge ca. 2.6 Å. Slab (**C**) is composed only of Ge atoms making a two-dimensional network with $d_{Ge\text{-}Ge}$ ca. 2.5 Å and ca. 2.8 Å. The three slabs are assembled via condensation in a sequence …**ABAC**… along the *b*-axis. As shown in the Figure 3, the rare earth – rare earth, rare earth – germanium, and germanium – germanium interatomic distances of are compatible with the average distances found in other intermetallic systems, whereas the interatomic distances with nickel atoms are slightly shorter than the distances found in other structures containing Ni and Ge atoms (e.g. $d_{Ni\text{-}Ge}$ = 2.477Å in $U_3Ni_6Ge_2$)[30],

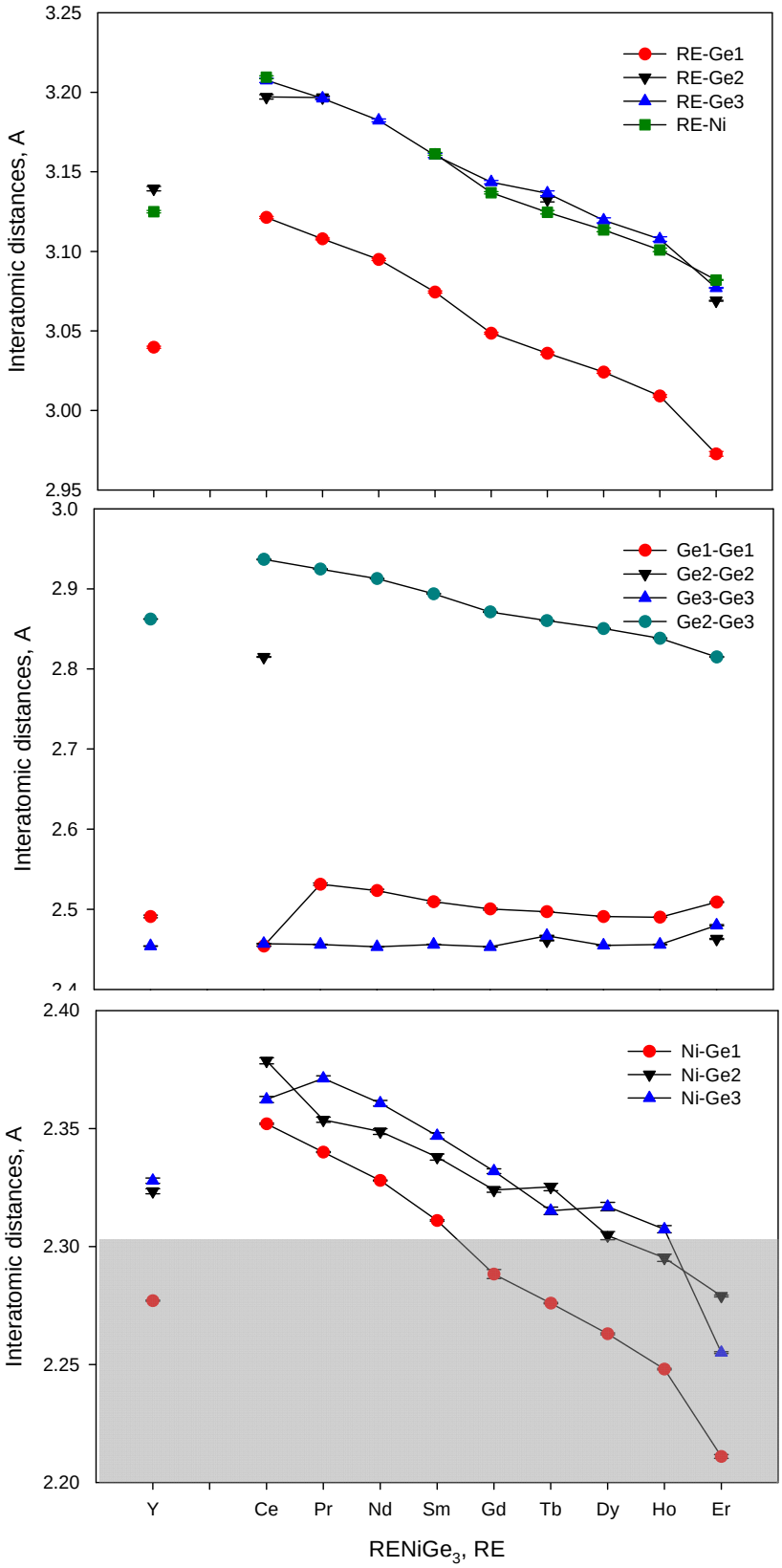

Figure 3. Selected interatomic distances of orthorhombic $RENiGe_3$ series (RE = Y, Ce-Nd, Sm, Gd-Er).

short distances in average covalent radii scale are highlighted in the gray area.

The RE atoms are coordinated by 10 Ge atoms and 4 Ni atoms (CN = 14), as shown in Figure 4, in a distorted, intermetallic, based-capped hexagonal prism, which is frequently observed in rare-earth intermetallics, as in hexagonal $GdPt_2Sn$[39]. These polyhedra share square faces along the *a*- and *b*- directions and hexagonal faces along the *c*- direction. These hexagonal prisms are formed by 8 Ge atoms and 4 Ni atoms with 4 additional Ge atoms capping the prismic squares of the polyhedra (Figure 3(b)).

The close interatomic distances between germanium and nickel atoms could be explained by the occurrence of partial occupancies at the Ni site since the diffracted electron density represents the average value over many unit cells, and also the consequent enlargement of the thermal displacement parameters at the Ni site simultaneously contributed to give the shortened distances. The changes in Ni site occupancies are summarized in Figure 5. Increasing the Ni site vacancies on proceeding from left to right along the 4*f* series correlates with the chemical pressure provided by the lanthanide contraction. In the $RENi_{1-x}Ge_3$, the RE elements provide 3 valence electrons, but the Ni atoms formally contribute 0 valence *s* and *p* electrons, if the 3*d* band is filled. However, as the rare-earth elements varies, there are anticipated changes in RE-Ni and possible Ni-Ge interactions involving empty 5*d* bands at the rare-earth metal and nearly filled 3*d* bands at Ni.

In the calculated DOS curve for $CeNiGe_3$ shown in Figure 6(a), Ni 3*d* states dominate from –2.5 eV up to the Fermi level, whereas between –5 eV and –2.5 eV, Ni and Ge valence orbitals contribute evenly. Below –5 eV states are almost exclusively from Ge 4*p* bands contributions. The Ge 4*s* states are observed to make only a small contribution in the energy window shown although Ge-*s* states are often

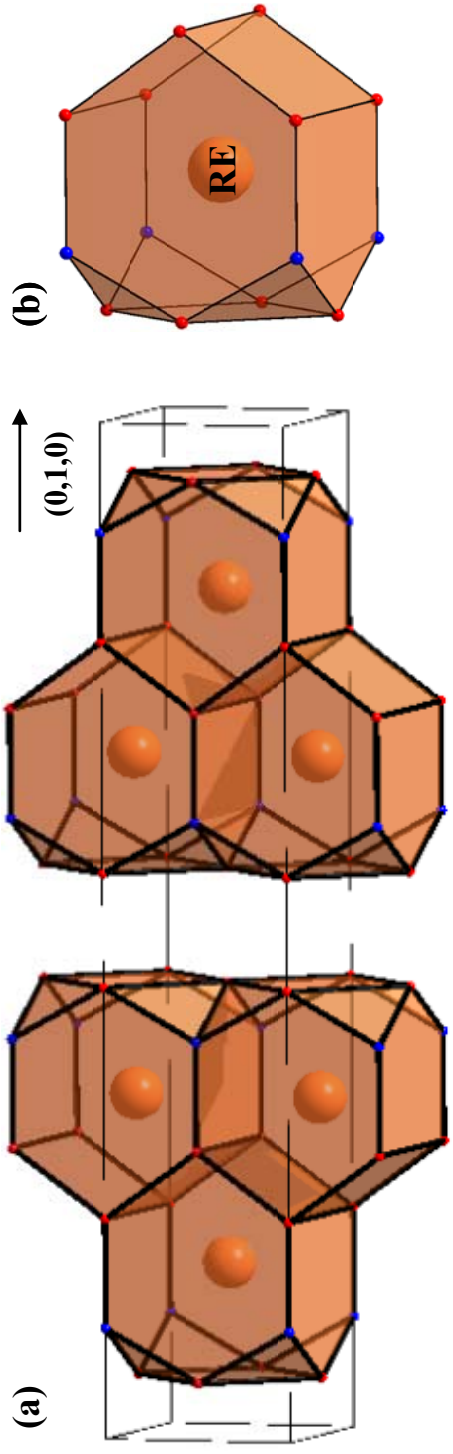

Figure 4. RE local coordination. (a) Unit cell is shown with slightly rotated *c* projection view. Ge atoms are in red and Ni in blue. (b) Local coordination around the RE metal.

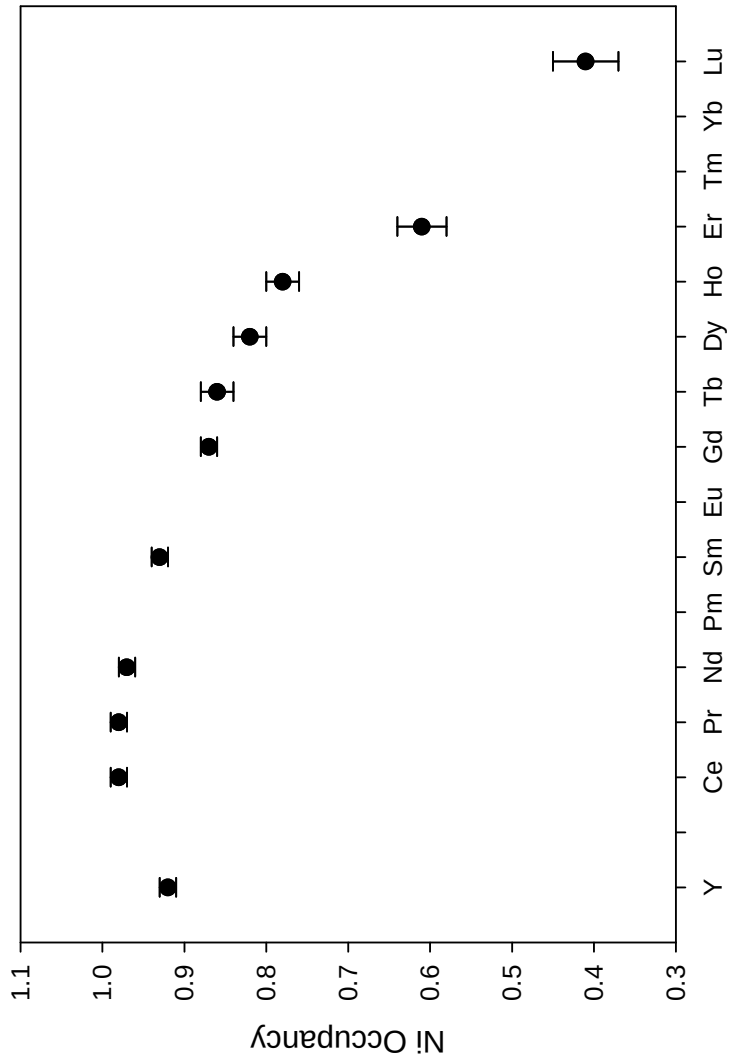

Figure 5. Trends in Ni site occupancies in YNi_xGe_3 and $RENi_xGe_3$ series.

observed to provide a broad occupied s band in many intermetallic systems. The small contribution of the Ge 4*s* states is interpreted to be a result of the interaction between Ge 4*s* and Ni 4*s* states resulting in a shift of Ge 4*s* states to a lower energy region.[41] The valence band within ca. 6 eV of the Fermi level is divided into two regions: (1) from –4.5 to –2.5 eV, there is strong mixing between Ni 3*d* and Ge 4*p* states; and (2) above -2.5 eV, there is predominantly Ni 3*d* bands. In the $ErNiGe_3$ DOS curve, similar contributions are observed from Ni 3*d* and Ge 4*p* states. However, the major difference was found below the energy window of –6 eV. In the Ce system, Ge 4*p* bands are divided into two contributions with one set located below –6.5 eV creating a gap in DOS curve. The Er system was found to have all Ge 4*p* states delocalized below –12 eV to the Fermi level without creating any gap in DOS curve.

In Figure 7, COHP curves of three Ni-Ge interactions in both $CeNiGe_3$ (left) and $ErNiGe_3$ (right) compounds are plotted. In both cases, the Fermi level lies around the energy where the bonding-to-antibonding crossover occurs. In the Ce system, the most noticeable crossover occurs for the Ge-Ge interaction at 2.455 Å within a 0.2 eV energy window at the Fermi level, but in the Er system, the Fermi level lies in the middle of a broad crossover energy window of almost 2 eV found in two Ge-Ge interactions at 2.465 and 2.503 Å. This COHP crossover suggests that the structure of the compounds is trying to optimize these particular interactions by minimizing the occupation of antibonding states.

2) $RENiGe_3$ (RE = Yb, Lu)

$YbNiGe_3$ crystallizes in a new type of crystal structure, adopting a tetragonal crystal class, space group $I4_1/amd$, with lattice parameters a = 4.0347(6) Å, c =

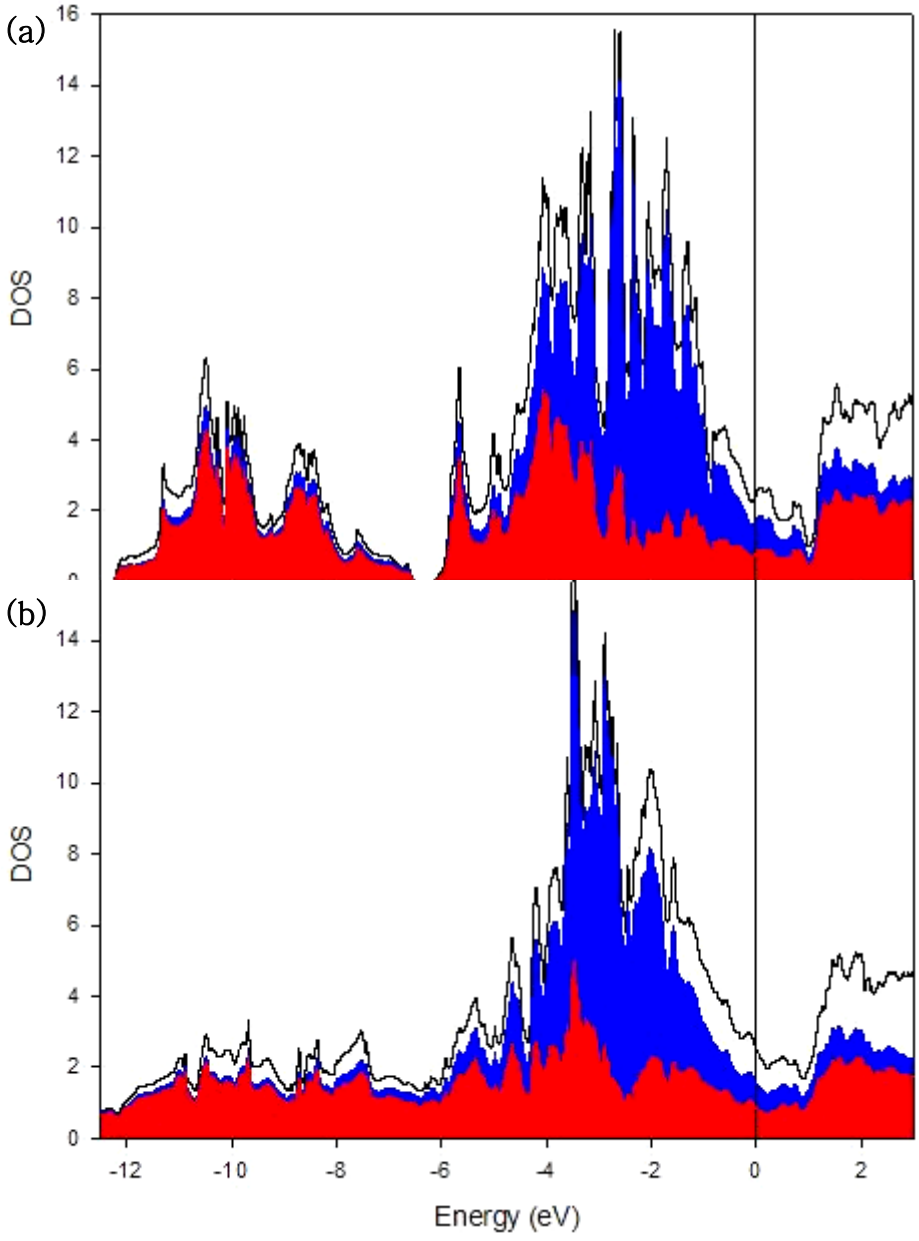

Figure 6. Density of States (DOS) of (a) $CeNiGe_3$ and (b) $ErNiGe_3$. Black solid line represents the total DOS, Ge states in red, and Ni state in blue. The Fermi level is set to zero.

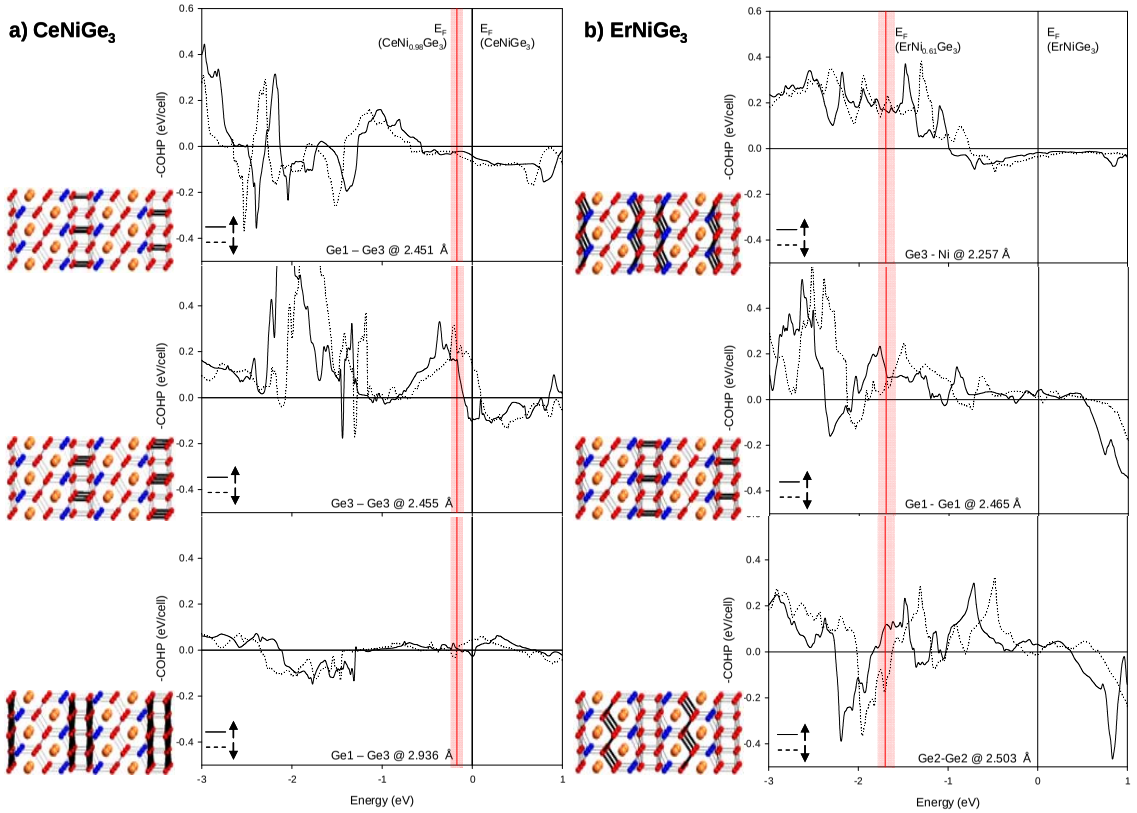

Figure 7. Crystal Orbital Hamilton Polulation (COHP) curves of selected bonds of (a) $CeNiGe_3$ and (b) $ErNiGe_3$. Solid lines represent the spin-up states and the dotted lines show the interactions of the spin-down states. Calculated Fermi energies of the stoichiometric $RENiGe_3$ are indicated by the black line and the estimated Fermi based on the refined compositions $CeNi_{0.98}Ge_3$ and $ErNi_{0.61}Ge_3$ are drawn in red line with the error ranges. When the –COHP > 0, the states are populating the bonding orbitals, and –COHP < 0 means the states are populating the antibonding orbitals, and –COHP = 0 corresponds to the nonbonding states.

43.211(9) Å, and yielded the refined composition of $YbNi_{1.04(6)}Ge_{2.89(5)}$. This structure is a different stacking scheme from the orthorhombic $SmNiGe_3$-type resulting in a doubled *b*-axis as shown in Figure 8. $YbNiGe_3$ adopts the same fundamental building blocks found in the $SmNiGe_3$-type structure. Starting from this structure, half of the unit cell is rotated by 90° along the *b*-axis before completing the whole unit cell construction as shown in Figure 8. Consequently, the resulting structure has …**ADACABAC**… sequence instead of the …**ABACABAC**… sequence. The new building block, slab (**D**), replaces 50% of the (**B**) slab, and is similar to slab (**B**) with one-half of it layer shifted to create additional mirror planes within the structure. During refinement of $YbNiGe_3$, a significant improvement in the refinement factor was obtained by allowing one of the Ge sites to be mixed partially occupied by Ni atoms. This change in $YbNiGe_3$ occurs within the (**C**) building block. Instead of forming an α-Po-type fragment with Ge atoms occupying the vertices, Ni atoms share occupancies at alternating positions in this building block (Figure 1). This causes a symmetry breaking by eliminating mirror planes, and leads to a doubling of the *b*-direction.

$LuNiGe_3$ also crystallizes in a distortion of the orthorhombic $SmNiGe_3$-type structure, adopting a monoclinic structure, space group *C2/m* with lattice parameters *a* = 7.8521(16) Å, *b* = 7.9384(16) Å, *c* = 10.700(2) Å, and β = 100.53(03)°, which is another new structure type (Figure 1). As in $YbNiGe_3$, Ni/Ge mixed occupancy is also observed. As shown in Figure 1, all systems share similar building blocks, but the differences in crystal lattice is induced from distortions in the Ni-Ge framework. This new phase has positions with similar local environments as in $SmNiGe_3$-type structures but with changes in bond distances.

Conclusions

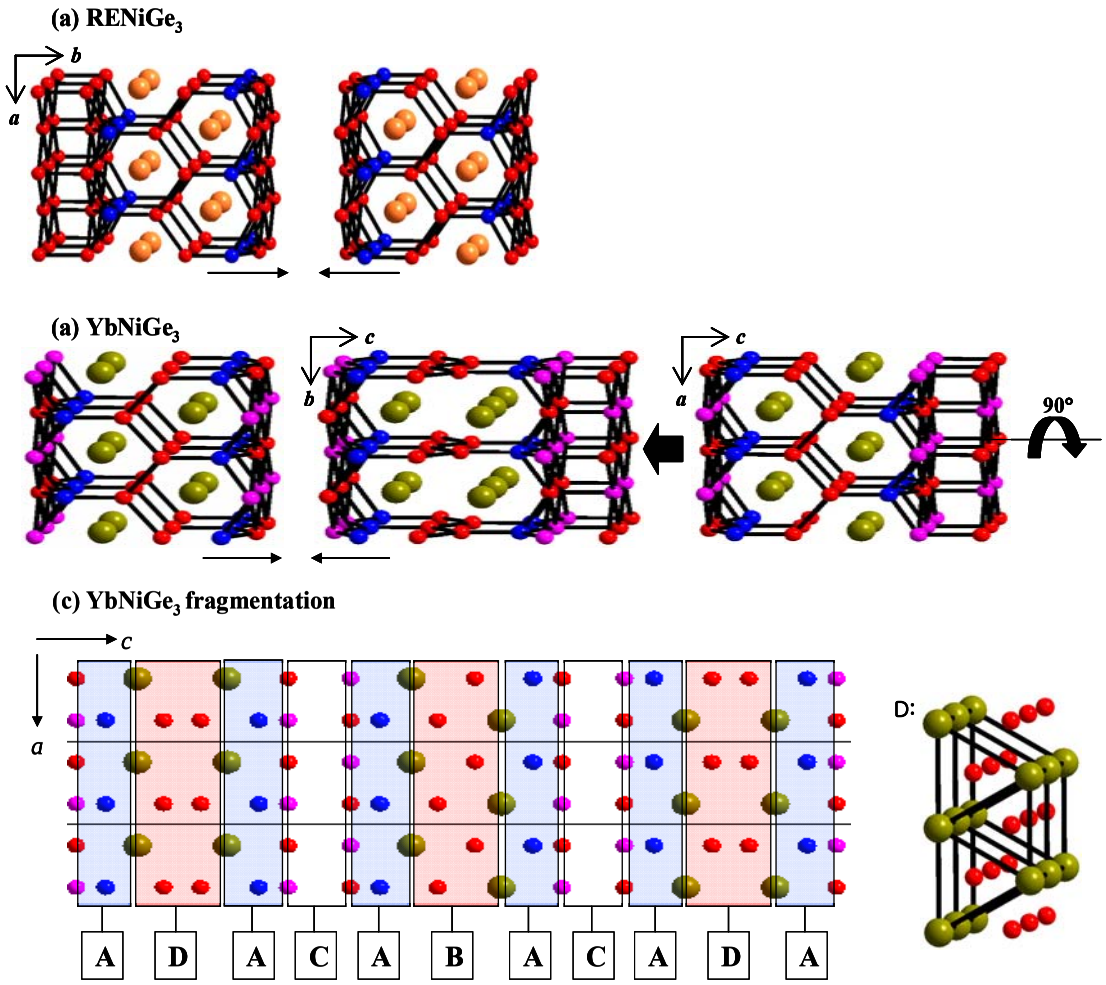

Figure 8. Structure fragmentations in $YbNiGe_3$. Yb are shown in green, Ge are in red, and Ni are in blue and the atoms in the mixed site of Ge/Ni are colored in purple. Structure assembly of (a) $RENiGe_3$, (b) $YbNiGe_3$, and resulting fragmentations in $YbNiGe_3$.

Investigations on flux-grown single crystals of the $RENiGe_3$ series have been conducted for their crystal structures, compositions, and as well as theoretical studies on the electronic structures. COHP analysis has suggested electronically driven structural stability arises to avoid occupying antibonding Ge-Ge and Ge-Ni states. Prior to a structural distortion, Ni deficiencies occur to minimize this antibonding population by increasing the chemical pressure with the lanthanide contraction.

Acknowledgements

This manuscript has been authored at Iowa State University of Science and Technology under Contract No. W-7405-ENG-82 with the U.S. Department of Energy. The United States Government retains and the publisher, by accepting the article for publication, acknowledges that the United States Government retains a non-exclusive, paid-up, irrevocable, world-wide license to publish or reproduce the published form of this manuscript, or allow others to do so, for United States Government purposes.

References

[1] Ramakrishnan, S.; Mydosh, J. *J. Magn. Magn. Mater*. **2007**, 310, 207.

[2] Kawasaki, Y.; Ishida, K.; Obinata, K.; Tabuchi, K.; Kashima, K.; Kitaoka, Y.; Trovarelli, O.; Geibel, C.; Steglich, F. *Hyperfine Interactions*, **2001**, 133, 163.

[3] Marasinghe, G.; Han, J.; James, W.; Yelon, W.; Ali, N. *J. Appl. Phys*. **2002**, 91(10), 7863.

[4] Jones, C.; Gordon, R.; Cho, B.; DiSalvo, F.; Kim, J.; Stewart, G. *Physica B*, **1999**, 262, 284.

[5] Chevalier, B.; Pasturel, M.; Bobet, J.-L.; Decourt, R.; Etourneau, J.; Isnard, O.; Sanchez Marcos, J.; Rodriguez Fernandez, J. *J. Alloys Compd*, **2004**, 383, 4.

[6] Westerveld, J. P. A.; Lo Cascio, D. M. R.; Bakker, H. *J. Phys. F: Met. Phys.* **1987**, 17, 1963.

[7] Doerrscheidt, W.; Schaefer, H. *J. Less-Common Metals*, **1978**, 58, 209.

[8] Salamakha, P.; Konyk, M.; Sologub, O.; Bodak, O. *J. Alloys Compd*. **1996**, 236, 206.

[9] Venturini, G.; Meot-Meyer, M.; Malaman, B.; Roques, B. *J. Less Common Met*. **1885**, 113, 197.

[10] Yan, J.; Qin, W.; Ou, X.; Zeng, L.; Hao, J. *Rare Metals*, **1998**, 17(2), 109.

[11] Yan, J.; Wu, S.; Ou, X.; Zeng, L.; Hao, J. *Powder Diffraction*, **1998**, 13(4), 241.

[12] Pecharsky, V.; Hyun, O.; Gschneider, K. *Phys. Rev. B.* **1993**, 47(18), 11839.

[13] Mun, E.; Bud'ko, S.; Canfield, P.; Ko, H.; Miller, G. to be submitted.

[14] Rietveld, H. *Journal of Applied Crystallography* , **1969**, 2, 65.

[15] Hunter, B.; Howard, C. *Rietica*, Australian Nuclear Science and Technology Organization : Menai, Australia, **2000**.

[16] SHELXTL; Brucker AXS, Inc.; Madison, WI, **1996**.

[17] Andersen, O. K. *Phys. Rev.* **1975**, B12, 3060.

[18] Andersen, O. K.; Jepsen, O. *Phys. Rev. Lett.* **1984**, 53, 2571.

[19] Andersen, O. K.; Jepsen, O.; Glötzel, D. In *Highlights of Condensed-Matter Theory*; Bassani, F.; Fumi, F.; Tosi, M. P.; Lambrecht, W. R. L.; Eds.; North-Holland: New York, **1985**.

[20] Andersen, O. K. *Phys. Rev.* **1986**, B34, 2439.

[21] Von Barth, U.; Hedin, L. *J. Phys. C* **1972**, 5, 1629.

[22] Koelling, D. D.; Harmon, B.N. *J. Phys. C* **1977**, 10, 3107.

[23] Jepsen, O.; Anderson, O. K. *Z. Phys. B* **1995**, 97, 35.

[24] Dronskowski, R.; Blöchl, P. *J. Phys. Chem*. **1993**, 97, 8617.

[25] Blöchl, P. E.; Jepsen, O.; Andersen, O.K. *Phys Rev.* **1994**, B49, 16223.

[26] Medarde M. *J. Phys.: Condens. Matter*. **1997**, 9, 1679.

[27] Andress, K.; Alberti, E. *Zeit. Fuer Metal*. **1935**, 27(6), 126.

[28] Hofmann, W.; Jaeniche, W. *Naturwissenschaften* **1935**, 23, 851.

[29] Desando, R.; Lange, R. *J. Chem. Phys*. **1949**, 17, 1293.

[30] Perricone, A.; Noël, H. *J. Alloys Compd.* **2004***,* 383, 251.

[31] Tremolet de Lacheisserie, E. du. *Magnetostriction: Theory and Applications of Magnetoelasticity.* Boca Raton, FL: CRC Press, **1993**.

[32] Hoffmann R. *Solids and Surfaces: A chemist's View of Bonding in Extended Structures*, VCH, 3 **1988**.

[33] Hoffmann, R. *J. Chem. Phys*. **1963**, 39, 1397.

[34] Burdett, J. K. Chemical Bonding in Solids, Oxford University Press, New York, **1995**.

[35] Ammeter, J. H.; Bürgi, H. B; Thibeault, J. C.; Hoffmann, R. *J. Am. Chem. Soc.* **1978**, 100, 3686.

[36] Pauling, L.; Kamb, B. *Proc. Natl. Acad. Sci. USA*, **1986**, 83, 3569.

[37] The Stuttgart Tight-Binding LMTO-ASA program Version 4.7; Max-Planck-Institut für Festkörperforschung, Stuttgart, Germany **1998**.

[38] Pani, M.; Manfrinetti, P.; Fornasini, M. *Acta Cryst.* **1995***,* C51, 1725.

[39] Xue, B.; Hulliger, F.; Baerlocher, C.; Estermann, M. *J. Alloys Compd*. **1993**, 191(2), L9.

[40] Lambrecht, W. R. L.; Andersen, O. K. *Physical Review B*. **1986**, 34(4), 439.

[41] Shim, I.; Kingcade, J. E., Jr.; Gingerich, K. A. *J. Chem. Phys*. **1988**, 89(5), 3104.

Supplement Table 1. Detailed crystallographic data for $RENiGe_3$ series.

	$YNiGe_3$	**$CeNiGe_3$**	**$PrNiGe_3$**
Single crystal XRD			
Refined composition	$YNi_{0.92(1)}Ge_3$	$CeNi_{0.98(1)}Ge_3$	$PrNi_{0.98(1)}Ge_3$
crystal system	orthorhombic	orthorhombic	orthorhombic
space group	*Cmmm*	*Cmmm*	*Cmmm*
***a*, Å**	4.044(8)	4.1353(8)	4.1174(8)
***b*, Å**	21.515(4)	21.838(4)	21.789(4)
***c*, Å**	4.0517(8)	4.1712(8)	4.1548(8)
Z	4	4	4
Volume, Å^3	352.52(12)	376.69(13)	372.74(13)
density (calculated), mg/m^3	3.442	3.673	3.719
F(000)	326	364	366
Absorption Coefficient, mm^{-1}	23.267	20.075	20.717
method/program	empirical / SADABS	empirical / SADABS	empirical / SADABS
Theta range	3.79 to 34.65°.	3.73 to 34.61°	3.74 to 35.15°.
***hkl* ranges**	$-6 \le h \le 6$	$-6 \le h \le 6$	$0 \le h \le 6$
	$-34 \le k \le 34$	$-34 \le k \le 34$	$0 \le k \le 34$
	$0 \le l \le 6$	$-6 \le l \le 5$	$0 \le l \le 6$
R_{int}	0.1085	0.1099	0
Refinement method	Full-matrix least-squares on F^2	Full-matrix least-squares on F^2	Full-matrix least-squares on F^2
Data/parameters	482/23	506/23	507/23
Completeness to max 2θ	99.20 %	99.50 %	96.60 %
Restraints	0	0	0
Goodness-of-Fit	1.102	0.879	0.943
final R [*I>2σ(I)*]	$R_1 = 0.0404$	$R_1 = 0.0386$	$R_1 = 0.0330$
	$R_w = 0.0825$	$R_w = 0.0837$	$R_w = 0.0698$
R indices (all data)	$R_1 = 0.0736$	$R_1 = 0.0617$	$R_1 = 0.0538$
	$R_w = 0.1043$	$R_w = 0.1133$	$R_w = 0.0744$
Extinction Coefficient	0.040(2)	0.0139(9)	0.0073(5)
Peak/hole, e/Å^3	1.380/-1.721	4.371/-3.238	4.213/-4.612

	$NdNiGe_3$	$SmNiGe_3$	$GdNiGe_3$
Single crystal XRD			
Refined composition	$NdNi_{0.97(1)}Ge_3$	$SmNi_{0.93(1)}Ge_3$	$GdNi_{0.87(1)}Ge_3$
crystal system	orthorhombic	orthorhombic	orthorhombic
space group	*Cmmm*	*Cmmm*	*Cmmm*
***a*, Å**	4.1051(8)	4.0822(8)	4.0508(8)
***b*, Å**	21.715(4)	21.635(4)	21.551(4)
***c*, Å**	4.1334(8)	4.1028(8)	4.0688(8)
Z	4	4	4
Volume, Å^3	368.47(12)	362.36(12)	355.21(12)
density (calculated), mg/m^3	3.792	3.912	4.055
F(000)	368	372	376
Absorption Coefficient, mm^{-1}	21.391	22.69	24.217
method/program	empirical / SADABS	empirical / SADABS	empirical / SADABS
Theta range	3.75 to 35.04°.	3.77 to 34.82°.	3.78 to 34.59°.
***hkl* ranges**	$-6 \le h \le 6$	$-6 \le h \le 6$	$-6 \le h \le 6$
	$-34 \le k \le 34$	$-29 \le k \le 34$	$-33 \le k \le 34$
	$0 \le l \le 6$	$0 \le l \le 6$	$0 \le l \le 6$
R_{int}	0.1064	0.0733	0.0948
Refinement method	Full-matrix least-squares on F^2	Full-matrix least-squares on F^2	Full-matrix least-squares on F^2
Data/parameters	506/23	495/23	485/23
Completeness to max 2θ	98.40 %	98.80 %	99.10 %
Restraints	0	0	0
Goodness-of-Fit	1.079	1.042	1.096
final R [*I>2σ(I)*]	$R_1 = 0.0432$	$R_1 = 0.0491$	$R_1 = 0.0421$
	$R_w = 0.1263$	$R_w = 0.1308$	$R_w = 0.01012$
R indices (all data)	$R_1 = 0.0513$	$R_1 = 0.0535$	$R_1 = 0.0444$
	$R_w = 0.1328$	$R_w = 0.1340$	$R_w = 0.01033$
Extinction Coefficient	0.044(3)	0.048(4)	0.120(7)
Peak/hole, e/Å^3	3.549/-2.043	4.993/-3.874	5.020/-2.552

	$TbNiGe_3$	$DyNiGe_3$	$HoNiGe_3$
Single crystal XRD			
Refined composition	$TbNi_{0.86(2)}Ge_3$	$DyNi_{0.82(2)}Ge_3$	$HoNi_{0.77(2)}Ge_3$
crystal system	orthorhombic	orthorhombic	orthorhombic
space group	*Cmmm*	*Cmmm*	*Cmmm*
***a*, Å**	4.0352(8)	4.0200(8)	4.0030(8)
***b*, Å**	21.521(4)	21.437(4)	21.382(4)
***c*, Å**	4.0548(8)	4.042(8)	4.0249(8)
Z	4	4	4
Volume, Å^3	352.12(12)	348.33(12)	344.51(12)
density (calculated), mg/m^3	4.107	4.185	4.255
F(000)	378	380	382
Absorption Coefficient, mm^{-1}	25.054	25.901	26.827
method/program	empirical / SADABS	empirical / SADABS	empirical / SADABS
Theta range	3.79 to 34.81°.	3.80 to 34.79°.	3.81 to 34.78°.
***hkl* ranges**	$0 \le h \le 6$	$0 \le h \le 6$	$-6 \le h \le 6$
	$0 \le k \le 34$	$0 \le k \le 33$	$-33 \le k \le 34$
	$0 \le l \le 6$	$0 \le l \le 6$	$0 \le l \le 6$
R_{int}	0	0	0.1114
Refinement method	Full-matrix least-squares on F^2	Full-matrix least-squares on F^2	Full-matrix least-squares on F^2
Data/parameters	490/23	482/23	480/23
Completeness to max 2θ	99.80 %	99.40 %	99.80 %
Restraints	0	0	0
Goodness-of-Fit	0.943	0.934	1.161
final R [*I>2σ(I)*]	$R_1 = 0.0422$	$R_1 = 0.0417$	$R_1 = 0.0515$
	$R_w = 0.0861$	$R_w = 0.0938$	$R_w = 0.1330$
R indices (all data)	$R_1 = 0.0547$	$R_1 = 0.0544$	$R_1 = 0.0564$
	$R_w = 0.0892$	$R_w = 0.0975$	$R_w = 0.1361$
Extinction Coefficient	0.097(6)	0.0110(9)	0.055(4)
Peak/hole, e/Å^3	4.086/-5.221	3.685/-6.367	4.743/-4.039

	$ErNiGe_3$	$YbNiGe_3$	$LuNiGe_3$
Single crystal XRD			
Refined composition	$ErNi_{0.61(3)}Ge_3$	$YbNi_{1.04(6)}Ge_{2.89(5)}$	$LuNi_{0.41(4)}Ge_{3.07(4)}$
crystal system	orthorhombic	tetragonal	monoclinic
space group	*Cmmm*	$I4_1/amd$	*C2/m*
***a*, Å**	3.9583(8)	4.0347(6)	7.8521(16)
***b*, Å**	21.215(4)	4.0347(6)	7.9384(16)
***c*, Å**	4.0036(8)	43.211(9)	10.700(2)
β, °			100.53(03)
Z	4	8	8
Volume, Å^3	336.20(12)	703.4(2)	655.7(2)
density (calculated), mg/m^3	4.383	4.245	4.573
F(000)	384	776	780
Absorption Coefficient, mm^{-1}	28.203	28.324	31.177
method/program	empirical / SADABS	empirical / SADABS	empirical / SADABS
Theta range	1.92 to 29.03°	5.08 to 34.83°.	3.68 to 34.76°.
***hkl* ranges**	$0 \le h \le 5$	$-4 \le h \le 4$	$-12 \le h \le 12$
	$0 \le k \le 28$	$0 \le k \le 6$	$0 \le k \le 12$
	$0 \le l \le 5$	$0 \le l \le 68$	$0 \le l \le 17$
R_{int}	0	0.018	0
Refinement method	Full-matrix least-squares on F^2	Full-matrix least-squares on F^2	Full-matrix least-squares on F^2
Data/parameters	302/23	473/24	1489/52
Completeness to max 2θ	100.00 %	97.90 %	99.30 %
Restraints	0	0	0
Goodness-of-Fit	0.98	0.945	1.006
final R [*I>2σ(I)*]	$R_1 = 0.0601$	$R_1 = 0.0248$	$R_1 = 0.0434$
	$R_w = 0.1386$	$R_w = 0.0508$	$R_w = 0.1034$
R indices (all data)	$R_1 = 0.0735$	$R_1 = 0.0460$	$R_1 = 0.0572$
	$R_w = 0.1432$	$R_w = 0.0537$	$R_w = 0.1074$
Extinction Coefficient	0.016(2)	0.00376(17)	0.0159(7)
Peak/hole, e/Å^3	5.816/-3.454	2.014/-2.484	6.718/-3.476

Supplement Table 2. Anisotropic displacement parameters of $RENiGe_3$.

Atom	U_{11}	U_{22}	U_{33}	U_{23}	U_{13}	U_{12}
Y	0.015(1)	0.012(1)	0.012(1)	0	0	0
Ge1	0.014(1)	0.015(1)	0.015(1)	0	0	0
Ge2	0.018(1)	0.012(1)	0.018(1)	0	0	0
Ge3	0.019(1)	0.012(1)	0.014(1)	0	0	0
Ni	0.017(1)	0.010(1)	0.015(1)	0	0	0
Ce	0.007(1)	0.010(1)	0.015(1)	0	0	0
Ge1	0.016(1)	0.008(1)	0.018(1)	0	0	0
Ge2	0.008(1)	0.010(1)	0.020(1)	0	0	0
Ge3	0.010(1)	0.010(1)	0.024(1)	0	0	0
Ni	0.010(1)	0.011(1)	0.019(1)	0	0	0
Pr	0.012(1)	0.011(1)	0.017(1)	0	0	0
Ge1	0.013(1)	0.012(1)	0.022(1)	0	0	0
Ge2	0.016(1)	0.012(1)	0.026(1)	0	0	0
Ge3	0.020(1)	0.011(1)	0.020(1)	0	0	0
Ni	0.016(1)	0.012(1)	0.020(1)	0	0	0
Nd	0.019(1)	0.012(1)	0.019(1)	0	0	0
Ge1	0.021(1)	0.012(1)	0.023(1)	0	0	0
Ge2	0.023(1)	0.013(1)	0.027(1)	0	0	0
Ge3	0.027(1)	0.011(1)	0.023(1)	0	0	0
Ni	0.023(1)	0.013(1)	0.022(1)	0	0	0
Sm	0.022(1)	0.014(1)	0.012(1)	0	0	0
Ge1	0.022(1)	0.014(1)	0.017(1)	0	0	0
Ge2	0.027(1)	0.015(1)	0.019(1)	0	0	0
Ge3	0.030(1)	0.013(1)	0.017(1)	0	0	0
Ni	0.025(1)	0.013(1)	0.014(1)	0	0	0
Gd	0.012(1)	0.013(1)	0.009(1)	0	0	0
Ge1	0.013(1)	0.015(1)	0.014(1)	0	0	0
Ge2	0.021(1)	0.014(1)	0.016(1)	0	0	0
Ge3	0.019(1)	0.012(1)	0.017(1)	0	0	0
Ni	0.015(1)	0.012(1)	0.012(1)	0	0	0
Tb	0.016(1)	0.017(1)	0.017(1)	0	0	0
Ge1	0.023(1)	0.018(1)	0.026(1)	0	0	0
Ge2	0.018(1)	0.022(1)	0.023(1)	0	0	0
Ge3	0.029(1)	0.020(1)	0.023(1)	0	0	0

Ni	0.022(1)	0.016(1)	0.024(1)	0	0	0
Dy	0.015(1)	0.015(1)	0.012(1)	0	0	0
Ge1	0.017(1)	0.021(1)	0.017(1)	0	0	0
Ge2	0.030(1)	0.016(1)	0.018(1)	0	0	0
Ge3	0.022(1)	0.016(1)	0.024(1)	0	0	0
Ni	0.021(1)	0.014(1)	0.017(1)	0	0	0
Ho	0.012(1)	0.015(1)	0.019(1)	0	0	0
Ge1	0.013(1)	0.024(1)	0.024(1)	0	0	0
Ge2	0.027(1)	0.018(1)	0.026(1)	0	0	0
Ge3	0.018(1)	0.016(1)	0.034(1)	0	0	0
Ni	0.015(1)	0.014(1)	0.023(1)	0	0	0
Er	0.019(1)	0.016(1)	0.025(1)	0	0	0
Ge1	0.022(2)	0.018(2)	0.050(2)	0	0	0
Ge2	0.021(2)	0.031(2)	0.029(2)	0	0	0
Ge3	0.047(2)	0.019(2)	0.028(2)	0	0	0
Ni	0.022(4)	0.014(3)	0.028(4)	0	0	0
Yb	0.012(1)	0.012(1)	0.013(1)	0	0	0
Ge1	0.018(1)	0.011(1)	0.014(1)	0	0	0
Ge2	0.023(1)	0.012(1)	0.013(1)	0	0	0
Ni	0.017(1)	0.015(1)	0.011(1)	0	0	0
M	0.023(1)	0.011(1)	0.013(1)	0	0	0
Lu	0.010(1)	0.010(1)	0.008(1)	0.000(1)	0.000(1)	0.000(1)
Ge1	0.010(1)	0.012(1)	0.009(1)	0	-0.001(1)	0
Ge2	0.010(1)	0.010(1)	0.013(1)	0	0.003(1)	0
Ge3	0.010(1)	0.014(1)	0.006(1)	0	0.000(1)	0
Ge4	0.011(1)	0.011(1)	0.008(1)	0	0.001(1)	0
Ge5	0.011(1)	0.011(1)	0.008(1)	-0.001(1)	0.000(1)	0.000(1)
M	0.012(1)	0.012(1)	0.007(1)	0	-0.001(1)	0

Supplement Table 3. Selected interatomic distances of orthorhombic $RENiGe_3$ series (RE = Y, Ce-Nd, Sm, Gd-Er) tetragonal $YbNiGe_3$, and monoclinic $LuNiGe_3$.

Bond type	distance (Å)	Bond type	distance (Å)
Y – Ge1	3.0397(7)	Ce – Ge1	3.1971(14)
	3.2009(14)	Ce – Ge2	3.1213(7)
Y – Ge2	3.1394(14)		3.2795(14)
Y – Ge3		Ce – Ge3	3.2075(14)
Y - Ni	3.1249(8)	Ce - Ni	3.2095(9)
		Ge1 – Ge1	2.454(3)
Ge1 – Ge1	2.4910(16)	Ge2 – Ge2	2.5390(18)
Ge2 – Ge3	2.8623(4)	Ge3 – Ge3	2.457(3)
Ge3 – Ge3	2.454(3)	Ge1 – Ge3	2.9368(4)
Ge1 – Ni	2.277(2))	Ge1 – Ni	2.3787(13)
Ge2 – Ni	2.3234(11)	Ge2 – Ni	2.352(3)
Ge3 – Ni	2.3279(11)	Ge3 – Ni	2.3623(13)
Pr – Ge1	3.1078(6)	Nd – Ge1	3.0949(7)
	3.2689(12)		3.2541(12)
Pr – Ge2	3.1967(11)	Nd – Ge2	
Pr – Ge3	3.1863(12)	Nd – Ge3	3.1752(12)
Pr – Ni	3.1961(8)	Nd – Ni	3.1823(9)
Ge1 – Ge1	2.5313(15)	Ge1 – Ge1	2.5233(17)
Ge2 – Ge3	2.9247(4)	Ge2 – Ge3	2.9128(4)
Ge3 – Ge3	2.456(3)	Ge3 – Ge3	2.453(3)
Ge1 – Ni	2.340(2)	Ge1 – Ni	2.328(2)
Ge2 – Ni	2.3537(11)	Ge2 – Ni	2.3487(12)
Ge3 – Ni	2.3712(11)	Ge3 – Ni	2.3607(12)
Sm – Ge1	3.0744(7)	Gd – Ge1	3.0485(6)
	3.2323(13)		3.2153(10)
Sm – Ge2	3.1670(13)	Gd – Ge2	3.1474(10)
Sm – Ge3	3.1603(13)	Gd – Ge3	3.1435(10)
Sm – Ni	3.1613(9)	Gd – Ni	3.1368(7)
Ge1 – Ge1	2.5095(18)	Ge1 – Ge1	2.5004(14)
Ge2 – Ge3	2.8938(4)	Ge2 – Ge3	2.8711(4)

Ge3 – Ge3	2.456(3)	Ge3 – Ge3	2.453(2)
Ge1 – Ni	2.311(3)	Ge1 – Ni	2.2883(19)
Ge2 – Ni	2.3379(13)	Ge2 – Ni	2.3240(10)
Ge3 – Ni	2.3469(13)	Ge3 – Ni	2.3319(10)
Tb – Ge1	3.1326(15)	Dy – Ge1	3.0241(8)
Tb – Ge2	3.0359(8)		3.2008(16)
	3.2104(16)	Dy – Ge2	3.1224(16)
Tb – Ge3	3.1365(15)	Dy – Ge3	3.1195(16)
Tb – Ni	3.1246(11)	Dy – Ni	3.1135(12)
Ge1 – Ge1	2.461(4)	Ge1 – Ge1	2.491(2)
Ge2 – Ge2	2.497(2)	Ge2 – Ge3	2.8504(4)
Ge3 – Ge3	2.467(4)	Ge3 – Ge3	2.455(4)
Ge1 – Ge3	2.8603(4)	Ge1 – Ni	2.263(4)
Ge1 – Ni	2.3252(16)	Ge2 – Ni	2.3046(17)
Ge2 – Ni	2.276(3)	Ge3 – Ni	2.3169(18)
Ge3 – Ni	2.3151(16)		
Ho – Ge1	3.0091(8)	Er – Ge1	3.069(3)
	3.1943(16)	Er – Ge2	2.9727(15)
Ho – Ge2	3.1108(14)		3.201(3)
Ho – Ge3	3.1077(14)	Er – Ge3	3.077(3)
Ho – Ni	3.1009(11)	Er – Ni	3.082(3)
Ge1 – Ge1	2.490(2)	Ge1 – Ge1	2.463(7)
Ge2 – Ge3	2.8383(4)	Ge1 – Ge3	2.8150(4)
Ge3 – Ge3	2.456(3)	Ge2 – Ge2	2.509(5)
Ge1 – Ni	2.248(3)	Ge3 – Ge3	2.480(8)
Ge2 – Ni	2.2952(15)	Ge1 – Ni	2.279(4)
Ge3 – Ni	2.3073(15)	Ge2 – Ni	2.211(8)
		Ge3 – Ni	2.255(4)
Yb – Ge1	3.0360(5)	Lu – Ge2	2.9206(13)
	3.2106(10)		3.0366(12)
Yb – Ge3	3.1358(9)	Lu – Ge3	2.9941(12)
Yb – Ni	3.1130(6)		3.0867(12)
Ge1 – Ge1	2.4900(12)	Lu – Ge4	3.0422(13)

Ge2 – Ge3	2.4575(14)	Lu – Ni	3.0552(14)
	2.8530(4)	Ge1 – Ge5	2.5672(15)
Ge1 – Ni	2.2836(16)	Ge2 – Ge2	2.635(3)
Ge2 – Ni	2.3247(8)	Ge2 – Ge3	2.521(3)
	2.8530(4)	Ge3 – Ge3	2.434(3)
		Ge5 – Ge5	2.4876(19)
		Ge5 – Ge6	2.3865(14)
		Ge3 – Ni	2.299(2)
		Ge5 – Ni	2.3865(14)

CHAPTER 6

Magnetic Structures of MM′As Series (M, M′ = Cr, Mn, Fe): a Theoretical Investigation

ABSTRACT

Among the large family of transition metal pnictides, MM′As (M, M′ = Cr, Mn, Fe) are particularly interesting due to their various crystallographic and magnetic structural transitions as a function of metal content. To understand the electronic properties of these systems, we have carried out electronic structure calculations within density functional theory (DFT) using tight-binding linear muffin-tin orbital (TB-LMTO) method with the local spin density approximation (LSDA). MM′As (M, M′ = Cr, Mn, Fe) compounds were studied among tetragonal Cu_2Sb-type.

Introduction

A large class of intermetallic compounds, particularly ones with group 6, 7, and 8 transition metals, adopting the tetragonal Cu_2Sb-type crystal structure (space group P_4/nmm) has attracted much interest due to their rich variety of magnetic orderings. In the Cu_2Sb-type structure, there are two crystallographically inequivalent metal sites: the M(I) sites, Wyckoff position 2*a,* which are tetrahedrally coordinated by the anions (Sb sites); and M(II) sites, Wyckoff position 2*c,* in square pyramidal coordination. The anion site, Wyckoff position 2*c,* is occupied by a nonmetal atom (Figure 1). In particular, the transition metal arsenides exhibit peculiar magnetic properties; among these, some have itinerant character, while others show localized states, both of which result in almost all possible magnetic behaviors:

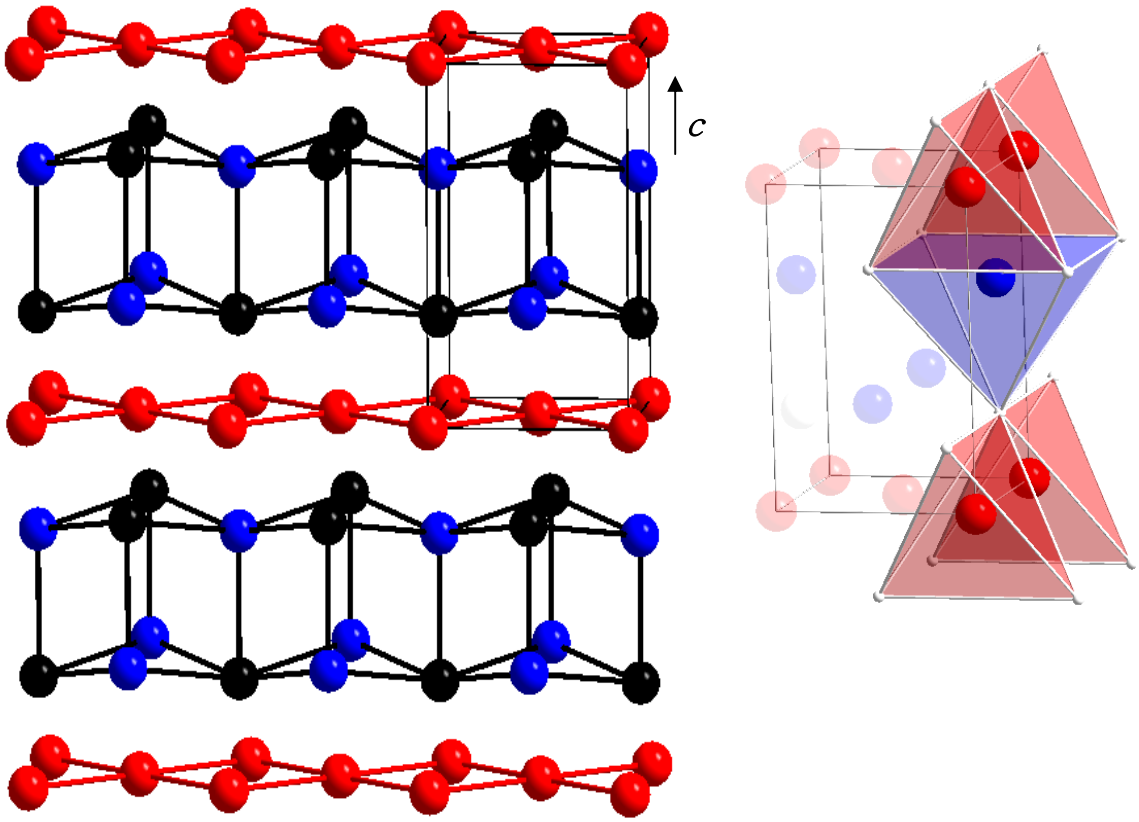

Figure 1. Crystal structures of Cu_2Sb-type MM′As. M(I) sites are shown in red, M(II) in blue, and As are shown in black (in later figures as well).

Table 1. Lattice parameters of MM′As series.

	Cr_2As	**Mn_2As**	**MnFeAs**	**Fe_2As**
a	3.603	3.76	3.7429	3.63
c	6.338	6.265	6.0292	5.98
2*c* site M(II) z_1	0.325	0.265	0.331	0.735
2*c* site As z_2	0.725	0.67	0.735	0.33
#e- of metals	12	14	15	16

Table 2. Summary of Crystal Structure of Cr_2As

Temperature	***a* (Å)**	***c* (Å)**	**Magnetic lines**
90 K	3.60(3)	6.33(8)	observed
293 K	3.60(3)	6.33(8)	Not observed
486 K	3.62(2)	6.37(0)	Not observed

ferromagnetism, antiferromagnetism, ferrimagnetism, and paramagnetism. Numerous empirical and theoretical studies have been pursued to explain the relationship between crystal structure and magnetic properties in these compounds; however, a clear picture has yet to emerge. From a technical point of view, M_2As and MM′As are interesting due to their large magnetic entropy changes over magnetic ordering temperature, which is near room temperature, when undergoing magnetic phase transitions, thus being potential candidates for large magnetocaloric effect materials. In this section, the crystal structures and magnetic properties by both experimental and theoretical investigations of Cr_2As, Mn_2As, MnFeAs, and Fe_2As are summarized.

Cr_2As

The crystal and magnetic structure of Cr_2As was studied by Watanabe *et. al.* [1] with powder neutron diffraction measurements at three different temperatures (90 K, 293 K, and 486 K). An antiferromagnetic to paramagnetic transition was determined at 393 K by magnetic susceptibility and specific heat measurements[2]. Below the Néel temperature, purely magnetic reflections in the neutron diffraction patterns were observed, which were indexed as $\left(00\frac{1}{2}\right)$, $\left(10\frac{1}{2}\right)$, $\left(10\frac{3}{2}\right)$, and a very weak $\left(00\frac{3}{2}\right)$ reflections. These $\left(hk\frac{l}{2}\right)$ reflections indicate that a doubling of the crystallographic unit cell along the *c*-axis is required to describe the magnetic unit cell. The finite (100) reflection intensity disagreed with Yuzuri and Yamada's[3] proposed model of a magnetic structure with ferromagnetically coupled M(I) sites within the (001) planes. Also, according to Watanabe et al., the weak intensity at $\left(00\frac{3}{2}\right)$ and the strong

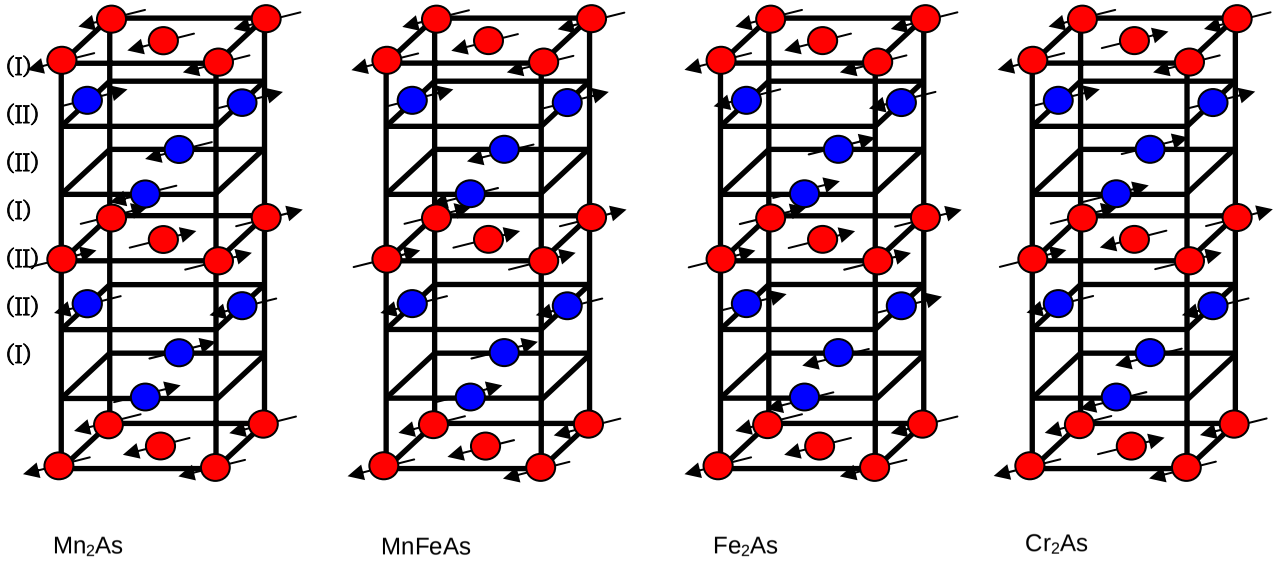

Figure 2. Magnetic structures of MM′As. M(I) sites are shown in red, M(II) in blue, and As are not shown (in later figures as well).

intensity at $\left(10\frac{3}{2}\right)$ agreed with the model that proposed ferromagnetic coupling between Cr atoms in the M(II) sites with each other in the doubled magnetic unit cell as shown in Figure 2.

Based on this proposed magnetic structure and assuming the local magnetic moments lie only in the (001) plane, the local magnetic moments for Cr(I) and Cr(II) were calculated from just the (112) nuclear intensity using the magnetic form factor (Cr and As) after Pauling and Sherman[4]: Cr(I), $\mu_I = 1.1 \pm 0.1\ \mu_B$; and Cr(II), $\mu_{II} = 1.2 \pm 0.1\ \mu_B$.[1,5] A combination of single crystal and powder time-of-flight (TOF) neutron diffraction studies on various compositions and heat-treated specimens confirmed the doubling of the chemical sublattice for the magnetic unit cell. But, in previous work, the existence of the (100) reflection, which should have been absent, was deceiving and originated from the overlapping (110) reflection of Cr_2O_3 contamination. Using low temperature, neutron diffraction results on samples with the exact composition $Cr_{2.0}As$, the intensities were calculated to be in good agreement with the observed intensities of the magnetic model structure and local moments as shown in Model (2) of Figure 2 resulting in local moments: Cr(I), $\mu_I = 0.40 \pm 0.08\ \mu_B$; and Cr(II), $\mu_{II} = 1.34 \pm 0.06\ \mu_B$.

Both Watanabe et al. and Yamaguchi et al. constructed their magnetic structures based on the assumption of exchange coupling antiparellel to the (001) direction and assigning the oxidation states to be Cr^{+}(I), Cr^{++}(II) and As^{3-}, which were predicted by Goodenough[6]. However, neither the neutron studies nor torque measurements gave any conclusive results on the actual direction of the local magnetic moments.

Mn_2As

In the early 1960's, Yuzuri and Yamada[7] also reported the tetragonal Cu_2Sb-type crystal structure and antiferromagnetically coupled magnetic structure of Mn_2As with the Néel temperature of 573 K by X-ray powder diffraction, thermal analysis, magnetic susceptibility, and specific heat measurements. From the thermomagnetic curve under a magnetic field of 8000 Oe, the effective magnetic moment per Mn atom was obtained to be 5.2 μ_B. However, a trace amount of Mn_3As_2 was unavoidable, and gave rise to weak ferromagnetism with a Curie temperature at 273 K. In addition, they proposed a magnetic structure of Mn_2As that resembled the magnetic lattice of Mn_2Sb (see Figure 1) and used molecular field theory[26] to explain the nature of the magnetic properties. The calculated Néel temperature as well as the estimated heat absorption in the antiferromagnetic-to-paramagnetic transition, however, was too different from the experimentally determined values to clearly validate their model.

In 1962, Adelson *et. al.* carried out a neutron diffraction experiment on polycrystalline Mn_2As at room temperature and determined the local magnetic moments for Mn(I) and Mn(II) sites, respectively to be 3.7 μ_B and 3.5 μ_B[8]. A doubling of the *c*-axis to generate the magnetic lattice was clearly resolved by the $\left(00\frac{3}{2}\right)$ and $\left(10\frac{1}{2}\right)$ reflections with better estimation of the effective magnetic moments obtained by minimizing the extinction effects using a thin crystal sample. But, the repeated magnetic cell was simply adopted from the previous work[7] without any further confirmation.

Fe_2As

Fe_2As is among the most investigated for its magnetic properties by many groups with contradictory results for its magnetic behavior. The crystal structure of

Fe_2As was determined by X-ray and neutron diffraction methods on pillar-shaped single crystals at room temperature by Elander et al.[6] and Katsuraki[9], respectively.

The first magnetic model proposed an antiferromagnetic structure with a Néel temperature of ca. 323 K, and a *c*-axis doubled from the chemical unit cell, which was confirmed by the disappearing magnetic reflections, $\left(00\frac{1}{2}\right)$, $\left(00\frac{3}{2}\right)$, $\left(00\frac{5}{2}\right)$, and $\left(00\frac{7}{2}\right)$, from single crystal neutron diffraction experiments[10], that had been postulated by Achiwa based on susceptibility measurements. Katsuraki also stated that from the absence of the odd *h* (*h*00) reflections in the neutron diffraction results, the magnetic moments are evidently aligned perpendicular to the *c*-axis. The Néel temperature of 323 K was confirmed again by Katsuraki by a temperature dependent study of the $\left(00\frac{1}{2}\right)$ neutron reflection intensity on two pieces of pillar-shaped Fe_2As single crystals[11]. This study showed complete disappearance of the $\left(00\frac{1}{2}\right)$ reflection intensity at ca. 323 K while the other nuclear intensities of (h00) and (hh0) showed no changes over the temperature range from 298 K to 333 K.

Shortly after, Achiwa and Takaki reported a different Néel temperature of 353 K based on magnetic anisotropy and field dependence of magnetization measurements on a single crystal disk of Fe_2As at liquid nitrogen temperatures[12]. In 1966, Katsuraki and Achiwa showed their agreement with the Néel temperature of Fe_2As to be 353 ± 1 K based on magnetic susceptibility measurements with a torsion balance, powder and single crystal neutron diffraction experiments, as well as the temperature dependence of the reflection intensity[13]. Furthermore, the effective magnetic moment was estimated to be 4.66 μ_B per Fe atom. They also observed Curie-Weiss behavior of the susceptibility curve above the Néel temperature, which showed deviations above 773 K due to the existence of a magnetite impurity.

MnFeAs

A powder X-ray diffraction study using Fe Kα radiation was performed first in 1966 to determine the lattice parameters of tetragonal, Cu_2Sb-type FeMnAs (a = 3.73(5) Å, c = 6.03(5) Å).[15] These lattice parameters are close to the mean value of the lattice parameters (a = 3.698 Å, c = 6.129(5) Å) of the parent systems Fe_2As[16] (a = 3.627 Å, c = 5.981 Å) and Mn_2As[17] (a = 3.769 Å, c = 6.278 Å), which is determined by neutron powder diffraction experiment.

In the M(I) layer, the atoms form a square net with short M(I)–M(I) distances, and M(II) atoms form a puckered square nets with arsenides building slab based on tetragonal boxes (Figure 1). In MnFeAs, the in-plane Fe(I)–Fe(I) distance is 2.64 Å, whereas the Fe(I)–As distance is 2.45 Å. Moreover, Mn(II)–Mn(II) distance is 3.35 Å, and Mn(II)–As at 2.68 and 2.44 Å. The closest Fe(I)–Mn(II) distance is 2.73 Å. Furthermore, this short interlayer M(I)–M(II) distance exists throughout all MM′As cases. Consequently, given these geometrical relationships, it is difficult to predict the electronic properties and dimensionality of interlayer interactions.

Magnetic susceptibility measurements indicated antiferromagnetism in FeMnAs with a Néel temperature of ca. 463 K, which is also near the mean value (462 K) of the Néel temperatures of the parent binary systems - Fe_2As (351 K) and Mn_2As (573 K). [15]

According to powder neutron diffraction, additional reflections were observed below the Néel temperature at $\left(h, k, \frac{1}{2}l\right)$, which gives rise to doubled magnetic unit cell along the c-axis of the crystallographic unit cell. The local magnetic moments are 0.2 μ_B for Fe(I) and 3.6 μ_B for Mn(II), which were calculated based on comparison with simulated intensities, and the assumption that the magnetic lattice of MnFeAs resembles that of Mn_2As, which was supported by comparing the local moment on Fe

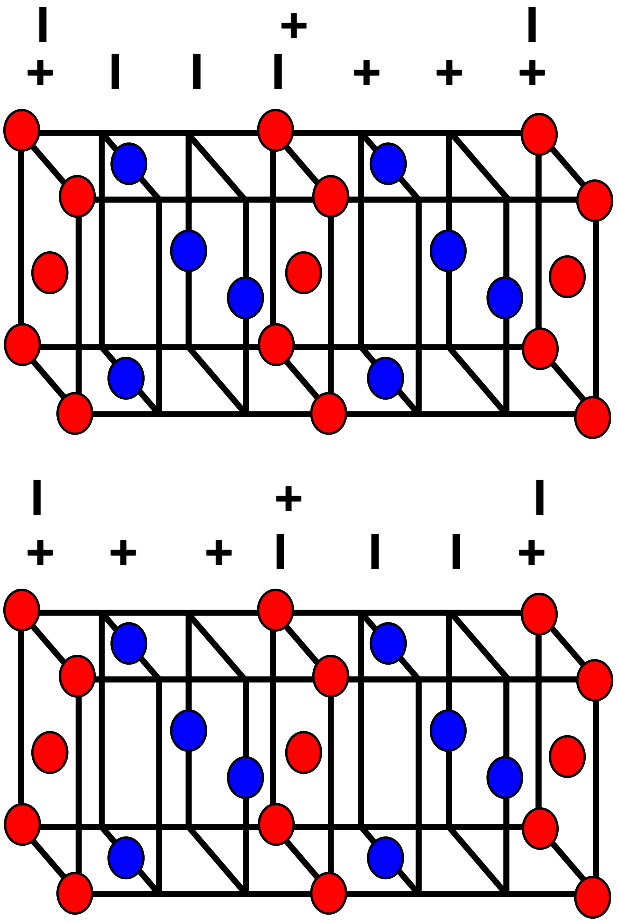

Figure 3. Proposed magnetic structure of Cr_2As. Only metal atoms are shown. Cr (I) in red and Cr (II) in blue.

sites from Mössbauer measurements (μ_{Fe} = 0.2 μ_B) without additional supporting evidence.

In 1988, Sugiyama *et.* al. investigated the magnetic field induced phase transitions for the $Fe_{2-x}Mn_xAs$ series by applying high values of the local moments a magnetization field with changing temperatures on powdered samples of $Fe_{2-x}Mn_xAs$ (x = 1.29, 1.35)[18] that best fit over the range of composition studied were determined to be: Fe(I), μ_I = 1.55 μ_B; and Mn(II), μ_{II} = 1.20 μ_B.

Further studies of the magnetic phase diagram of $Fe_{2-x}Mn_xAs$ have been carried out by Baron *et* al. using Rietveld analysis of neutron powder diffraction results at 10, 295, and 523 K. At 10 K, they observed a similar but not identical ferrimagnetic behavior for $Fe_{0.72}Mn_{1.28}As$ along both the *a*- and *c*- axes using a collinear antiferromagnetic model initially constructed by Yoshii and Katsuraki with noncompensating magnetic moments.[19]

At 295 K, the Mn_2As-type antiferromagnetic unit cell was obtained with local magnetic moments: Fe(I), μ_I = 1.01(2) μ_B; and Mn(II), μ_{II} = 3.17(5) μ_B. At 523 K, paramagnetic behavior was observed.

For all these studies, electronic structure calculations of these compounds can help to eliminate speculations, which were made previously, and to provide the opportunity for a better understanding the many interesting physical properties that arise from the interplay between the valence electrons of the main group element and the conduction electrons of the metal, especially the 3*d* electrons, which contribute to itinerant magnetism.

Methods

Tight Binding, Linear Muffin-Tin Orbital (TB-LMTO) method using density

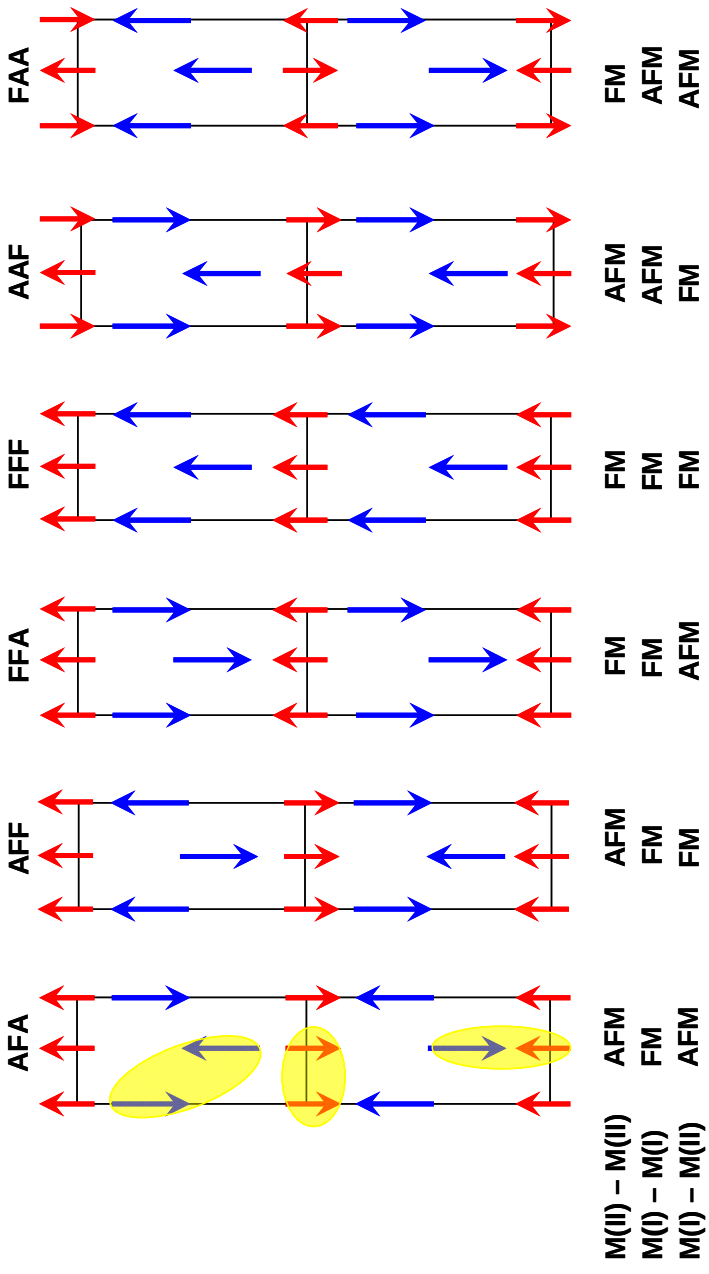

Figure 4. Modes of magnetic structure of MM′As series. Spin states are indicated with arrows. M(I) sites states are shown with red arrows and blue for M(II) states. The names of magnetic modes and local orientations are indicated.

functional theory was used for all electronic structure investigations in the atomic sphere approximation (ASA). Exchange and correlation were treated in a local spin density approximation (LSDA).[16] All relativistic effects except spin-orbit coupling were taken into account using a scalar relativistic approximation.[17] Within ASA, space is filled with overlapping Wigner-Seitz (WS) atomic spheres. The radii of the WS spheres were obtained by requiring the overlapping potential to be the best possible approximation to the full potential according to an automatic procedure.[18] The WS radii for the atomic sites determined by this procedure are 1.623 Å for Cr, 1.683-1.725 Å for Mn, 1.592-1.647 Å for Fe, and 1.659-1.723 Å for As. The basis set included 4*s*, 4*p*, and 3*d* orbitals for Cr, Mn, and Fe; 4*s* and 4*p* orbitals for As. The reciprocal space integrations to determine the self-consistent charge densities, densities of states (DOS) and crystal orbital Hamilton populations (COHP)[19] were performed by the tetrahedron method[20] using 196 *k*-points in the irreducible wedges of the corresponding Brillouin zones.

Results and Discussions

For these compounds, the transition metal ordering, their magnetic ordering as well as their local moments were studied.

For each compound, six different magnetic structures were constructed, some of which involved a doubled *c*-axis with respect to the crystallographic unit cell. For computational purposes, M(I) metals were located at M_I1 (0,0,0), M_I2 (0,0,1/2), M_I3 (1/2,1/2,0), and M_I4 (1/2,1/2,1/2) (eg. Fe1 at (0,0,0) for Fe_2As); M(II) metals were located at $M_{II}5$ (0,1/2,z) , $M_{II}6$ (1/2,0,z) , $M_{II}7$ (0,1/2, $\bar{z}$), and $M_{II}8$ (1/2,0, $\bar{z}$). To label these different magnetic structures, a three letter naming scheme was used that describes the symmetry of the exchange coupling between adjacent planes of atoms

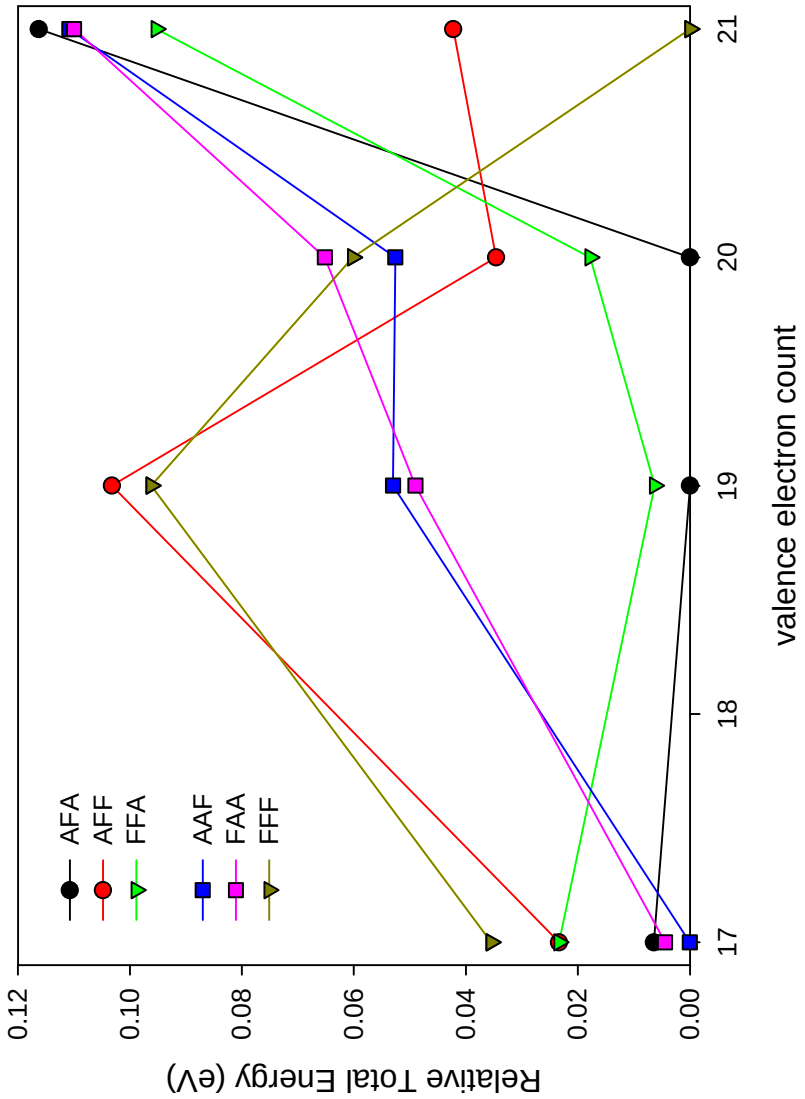

Figure 5. Calculated relative total energies of MM′As series.

along the c-axis: the first letter (A or F) for coupling between M_I site; the second letter (A or F) for coupling between M_{II} sites; and the third letter (A or F) for coupling between M_I and M_{II} sets. These modes are shown in Figure 4. For example, the experimentally obtained magnetic structure of MnFeAs would be designated as AAF. (see Figure 2)

In Figure 5, the relative total energies of all modes of magnetic structures are plotted for MM′As. In Cr_2As, the FAA mode was reported to be the most probable magnetic structure as discussed in the previous section. From carefully converged calculations, the energies of the AAF and FAA remain very close: the AAF mode is slightly more favorable than FAA by 4.4 meV. This mode has ferromagnetically ordered spins between M_I and M_{II} sites and antiferromagnetic ordering between sites with the same site symmetry. The energy difference is too small to make a clear conclusion on the nature of the magnetic order in the two varieties.

The values of the total energies of Mn_2As and MnFeAs indicated that the AFA mode is energetically more favorable than all other modes. These calculation results agree with those reported. However, only 6.3 meV difference in total energy from FFA suggests a possibility to have a magnetic transition to a different spin arrangement at higher temperature.

The results of calculations on Fe_2As are not in agreement with reported results in terms of total energies. From neutron diffraction experiments, as mentioned earlier, AFF was expected to be the most favorable mode. However, our calculation results indicated that FFF had lower total energy than AFF by 42.3 meV.

The calculated total DOS curves of MM'As are shown in Figure 6. At each site, a local coordinate system is set to the corresponding crystallographic coordinate system: *c*-axis is designated as the local *z*-axis, and *a, b*-axis are designated as the

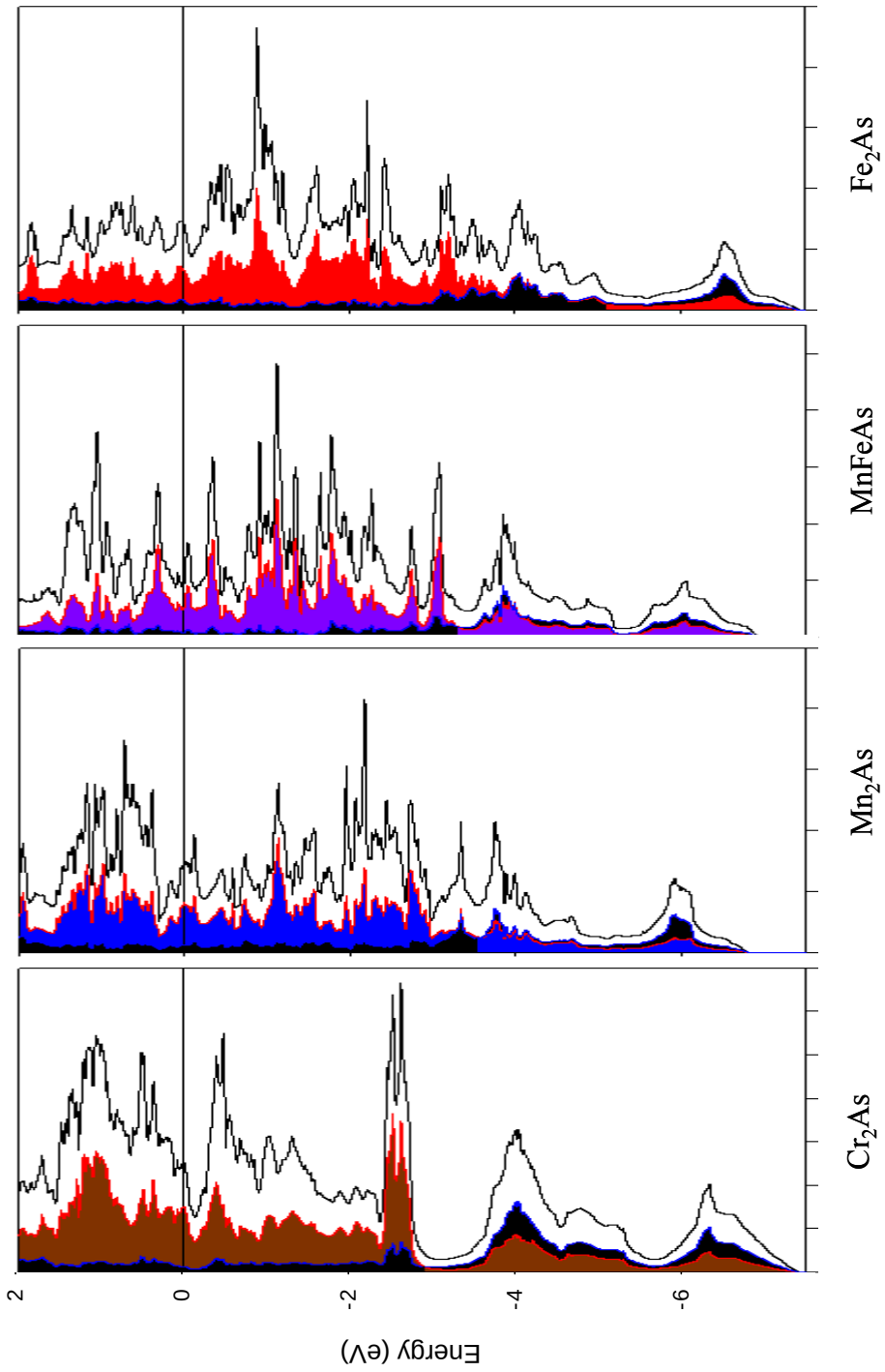

Figure 6. Total DOS plots of MM′As series. From left: Cr_2As, Mn_2As, MnFeAs, and Fe_2As. Arsenide states are shown in black shades and M(I) states are shown in colored shade. Horizontal line indicates the Fermi energy.

Table 3. Calculated average magnetic moments (μ_B) of MM′As.

Mode	AFA	AFF	FFA	FFF	AAF	FAA
Cr_2As						
Total	0	0.0102	3.640	0	0	0
CrI	0.460(0)	0.039(1)	0.471 (17)	1.981(2)	0(0)	0.297(0)
CrII	1.629(10)	1.258(5)	1.418(3)	3.500(1)	0(0)	1.691(0)
Mn_2As						
Total	0	0.0181	3.33	13.4	0	0
MnI	2.028(0)	1.795(0)	1.964(0)	1.691(0)	1.650(0)	1.560(25)
MnII	2.745(4)	2.200(0)	2.796(0)	1.691(0)	2.297(0)	2.396(3)
MnFeAs						
Total	0.034	0.013	7.521	16.990	0.008	0.014
FeI	1.854(3)	1.854(3)	1.981(2)	1.981(2)	1.977(1)	1.840(0)
MnII	3.511(1)	3.510(1)	3.500(1)	3.500(1)	3.307(6)	3.726(0)
Fe_2As						
Total	0.0659	0	2.67	16.4	0.001	0
FeI	0.548(1)	2.213(0)	1.783(0)	2.251(0)	1.630(1)	1.626(0)
FeII	1.633(2)	1.941(2)	1.131(0)	1.937(0)	1.658(0)	1.505(0)

local *x, y*-axis. In a square pyramidal field, degenerate 3*d* atomic orbitals split into (d_{xz}, d_{yz}), d_{z2}, d_{xy}, and d_{x2-y2} manifolds, whereas in the tetrahedral environment of arsenides, the 3*d* levels are split into (d_{xz}, d_{yz}), d_{xy}, d_{z2}, and d_{x2-y2} manifolds. These respective environments result in totally different DOS features within the MM′As structures. The first noticeable feature in these curves is in the Cr_2As DOS profile as compared to the other three systems. Mn_2As, MnFeAs, and Fe_2As show essentially continuous DOS curves, but a discontinuous energy region is observed for the Cr_2As. The lower part of the valence band at –2.7 eV is formed by bonding overlap between Cr d_{xz} and d_{yz} states with As *p* states. It is separated by a pseudogap over the range of –2.7 to –3.5 eV.

In the spin polarized DOS curves in Figure 7, the transition metal states are clearly identified by separate contributions from square pyramidal and tetrahedral environments. From these plots, it is evident that significant mixing occurs between Cr *d* and As *p* states resulting in shifts of the bonding states to create a pseudogap. Within the valence band, two parts can be considered. While the lower energy part, located at –2.5 ~ –2.0 eV, is composed mainly of metal d_{xz} and d_{yz} states, the higher energy part from –2 eV to the Fermi level is dominated by the d_{z2} and d_{xy} states, which are split into majority and minority spin states almost symmetrically and, thus, responsible for the magnetic moment. The levels at and just above the Fermi level are formed mainly by d_{xy}, and d_{x2-y2} states with d_{x2-y2} states giving significant contribution to the upper DOS. The d_{x2-y2} states are shifted to higher energy, well above the Fermi level relative to d_{xy} states, by forming the base of the pyramid.

The calculated local magnetic moments are summarized in Table 3. Larger magnetic moments in Mn_2As, MnFeAs, and Fe_2As lead to greater separations between majority and minority spin states, resulting in observable differences of the

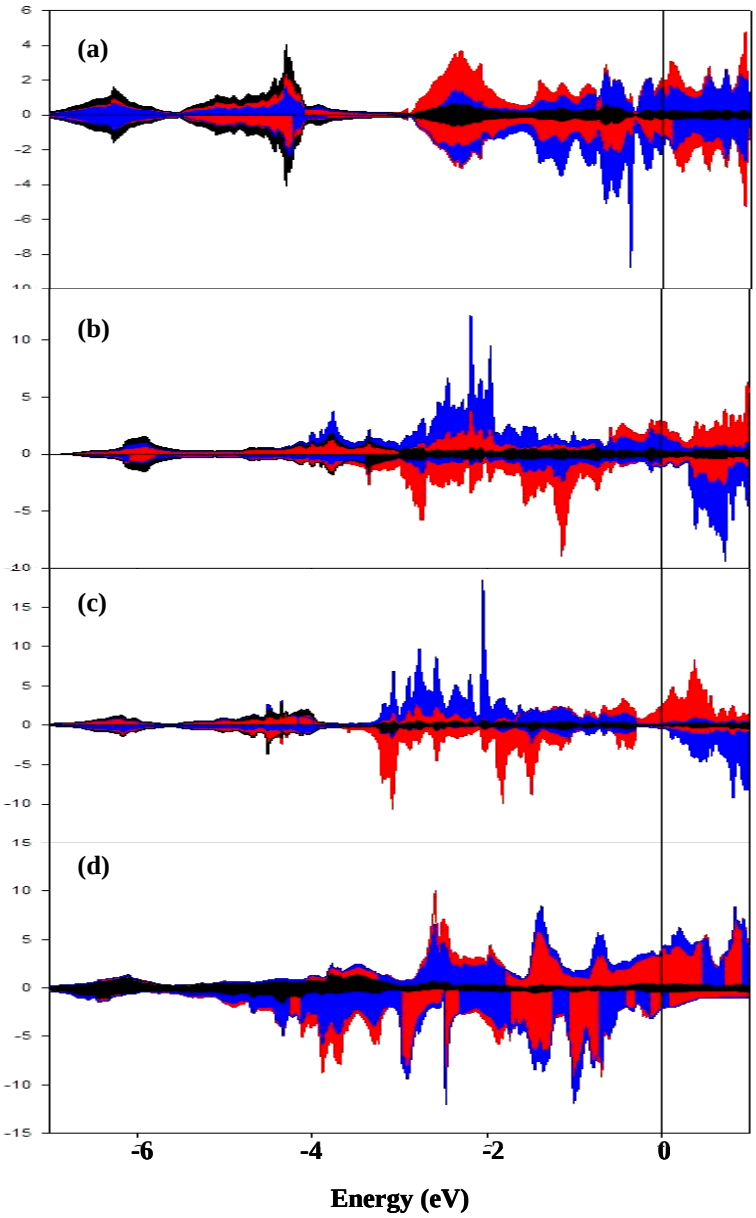

Figure 7. Spin polarized DOS of MM′As. (a) Cr_2As, (b) Mn_2Fe, (c) MnFeAs, and (d) Fe_2As. All plots are shown with one equivalent contributions from M(I) in tetrahedral site (in red), M(II) in square pyramidal site (in blue), and arsenide contributions (in black). Normalized Fermi energy is shown in solid line.

DOS curves than seen in Cr_2As, as shown in Figure 7.

Throughout the MM′As series, higher local moments were obtained at the square pyramidal site than at the tetrahedral site. The values of the calculated local moments for the M(II) sites were all very close to the measured magnetic moments. However, our calculations indicated higher local magnetic moments at the M(I) sites in contrast to the measured local moments that were often quenched in their tetrahedral environments in the MM′As structure. The nature of these atypical quenched moments was not examined carefully and our results suggested that higher local moments should be considered.

Figure 8 illustrates crystal field splitting schemes for M(I) and M(II) sites in local tetrahedral and square pyramidal fields, respectively. Combining the crystal fields and a local magnetic fields gives rise to possible d-orbital splitting patterns as shown. When the Mn(II) atoms are coordinated by arsenides in the square pyramidal field, two possible splitting scenarios could be considered. These different schemes result in a different number of unpaired electrons for a Mn^{2+} d^5 configuration as one (left) and three (right). The estimated (spin-only) local magnetic moments for these series are 1.73 μ_B (left) and 3.87 μ_B (right). The experimentally determined local magnetic moment of Mn(II) is 3.6 μ_B and the calculated moment by LMTO was 3.5 μ_B, both of which suggest that the more probable scheme is the latter one (right). As for Fe(I), the experimental local moment in MnFeAs was obtained to be 0.2 μ_B, which is not usually observed for Fe in intermetallic compounds. For Fe to have the quenched local magnetic moment in the tetrahedral field, significant orbital overlaps are necessary to minimize the number of unpaired electrons as shown in Figure. The local moment obtained by our electronic structure calculations was 1.9 μ_B, which matches the estimated moment of

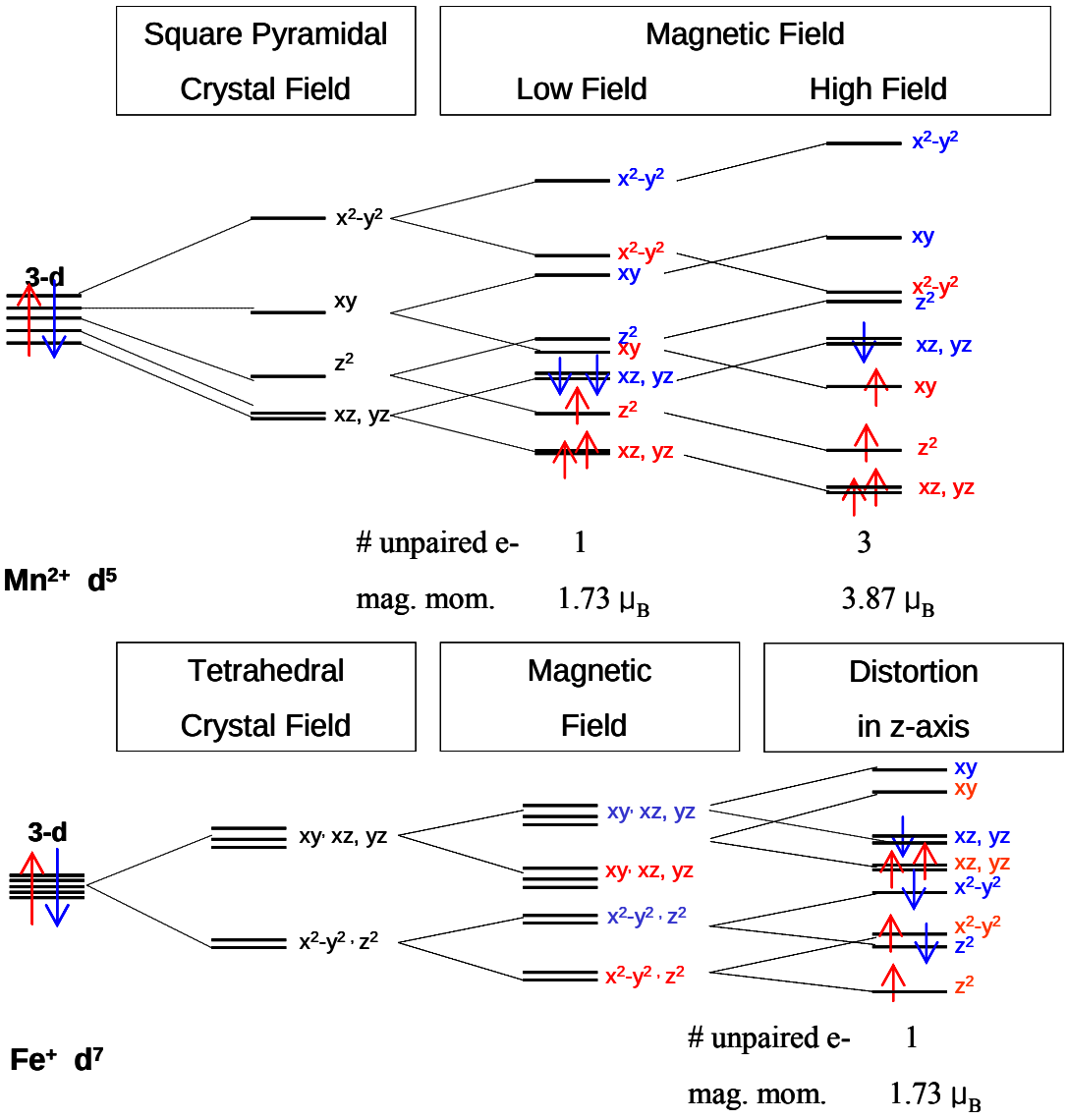

Figure 8. Crystal field splitting scheme at local symmetries around Mn and Fe.

1.73 μ_B from the splitting scheme for low spin Fe^+ d^7. In order to achieve this local moment, a tetragonal distortion of the local tetrahedral field is necessary. One of the problems associated with the estimation of local magnetic moments enters with the in-plane spin-spin interactions between M(I) sites. In spite of the assumption considering only ferromagnetically ordered spin states within the M(I) layer, when in-plane interactions are antiferromagnetically oriented, the resulting overall moment for that plane is quenched.

COHP curves for selected interatomic interactions in MnFeAs are shown in Figure 9. The first noticeable feature in these COHP curves is the Fermi level locating near the peaks of the Fe(I)–Fe(I) and Fe(I)–Mn(II) minority spin states showing greater bonding character, whereas the majority spin states have the nonbonding character. The shorter interactions are found between metal and arsenides throughout the structure. The majority spin states of the Fe(I)–As bond at 2.45 Å is optimized while the Mn(II)–As bonding states start to fill antibonding orbitals 3 eV below the Fermi level.

Conclusions

We have investigated the electronic structures and transition metal local magnetic moments in tetragonal MM′As using first principles calculations. The calculated local magnetic moments agree well with the experimental value for the square pyramidal M(II) site, but disagree for the M(I) tetrahedral site in MnFeAs. The calculated DOS and COHP analysis revealed greater contribution to electronic stability arises from the M(I) *d* states and their bonding interactions with arsenides optimized.

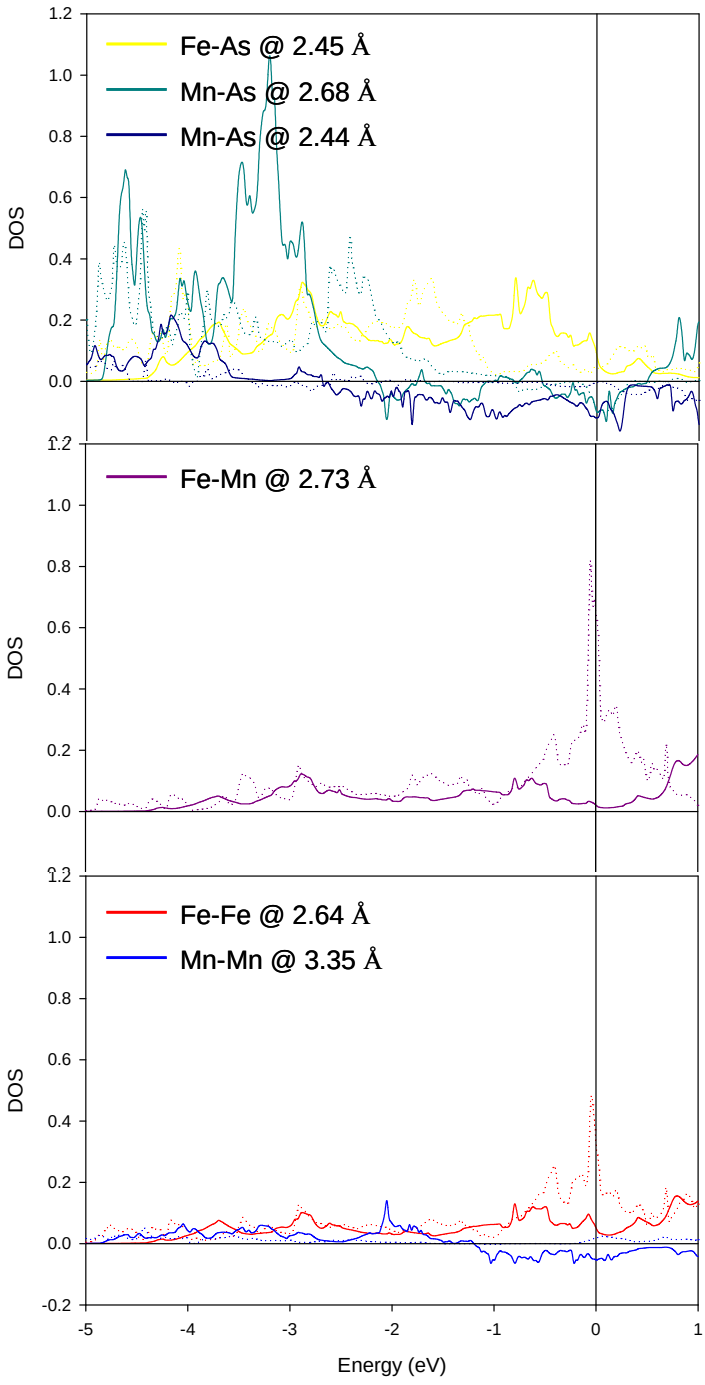

Figure 9. Calculated COHP curves of selected bondings in MnFeAs. Majority spin states are shown in solid lines, minority spin states are shown in dotted lines.

References

[1] Watanabe, H.; Nakagawa, Y.; Sato, K.; *J. Phy. Soc. Jpn*. **1965,** 20**,** 2244.

[2] Yuzuri, M.; *J. Phy. Soc. Jpn.* **1960**, 15, 2007.

[3] Yuzuri, M.; Yamada, M.; *J. Phy. Soc. Jpn*. **1960**, 15, 1845.

[4] Pauling, L.; Sherman, J.; *Z. Krist*. **1932**, 81, 1.

[5] Yamaguchi, Y.; Watanabe, H.; Yamauchi, H.; Tomiyoshi, S.; *J. Phy. Soc. Jpn*. **1972**, 32, 958.

[6] Goodenough: Magnetism and Chemical Bonds, *Intersci. Publ., N. Y.,* **1963**, 295.

[7] Yuzuri, M.; Yamada, M.; *J. Phy. Soc. Jpn*. **1960**, 15, 1845.

[8] Austin, A. E.; Adelson, E.; Cloud, W. H.; *J. Appl. Phys*., **1962**, 3(33), 1356.

[9] Katsuraki, H. J. *Phys. Soc. Japn.* **1964**, 19, 1988.

[10] Achiwa, N.: private communication

[11] Katsuraki, H.; Suzuki, K. *J. Appl. Phys*. **1965**, 36(3), 1094.

[12] Achiwa, N.; Yano, S.; Yuzuri, M.; Takaki, H. *J. Phys. Soc. Japn*. **1967**, 22, 156.

[13] Katsuraki, H.; Achiwa, N. *J. Phys. Soc. Japn*. **1966**, 21(11), 2238.

[14] Elander, M.; Hagg, G.; Westgren, A. *Arkiv. Kemi, Mineral. Geol*. **1936**, 12B(1).

[15] Yoshii, S.; Katsuraki, H. *J. Phys. Soc. Japan.* **1966**, 21, 205.

[16] Heyding, R. D.; Calvert, L. D. *Canad. J. Chem*. **1957**, 35, 449.

[17] Nowotny, H.; Halla, F.; *Z. Phys. Chem*. **1937**, 36, 322.

[18] Sugiyama, K.; Kanomata, T.; Ido, H.; Date, M. *J. Phys. Soc. Japan.* **1988**, 57, 1558.

[19] Baron, V.; Neronin, M.; Rundlöf, H.; Tellgren, R. *J. Magn. Magn. Mater.* **1997**, 169, 271.

[20] The Stuttgart Tight-Binding LMTO-ASA program Version 4.7; Max-Planck-Institut für Festkörperforschung, Stuttgart, Germany **1998**.

[21] Von Barth, U.; Hedin, L. *J. Phys. C* **1972**, 5, 1629.

[22] Koelling, D. D.; Harmon, B.N. *J. Phys. C* **1977**, 10, 3107.

[23] Jepsen, O.; Anderson, O. K. *Z. Phys. B* **1995**, 97, 35.

[24] Dronskowski, R.; Blöchl, P. *J. Phys. Chem*. **1993**, 97, 8617.

[25] Blöchl, P. E.; Jepsen, O.; Andersen, O.K. *Phys Rev.* **1994**, B49, 16223.

[26] Bragg, W. L.; Williams, E. J. *Proc. R. Soc. London, Ser. A* **1935**, 151, 540.

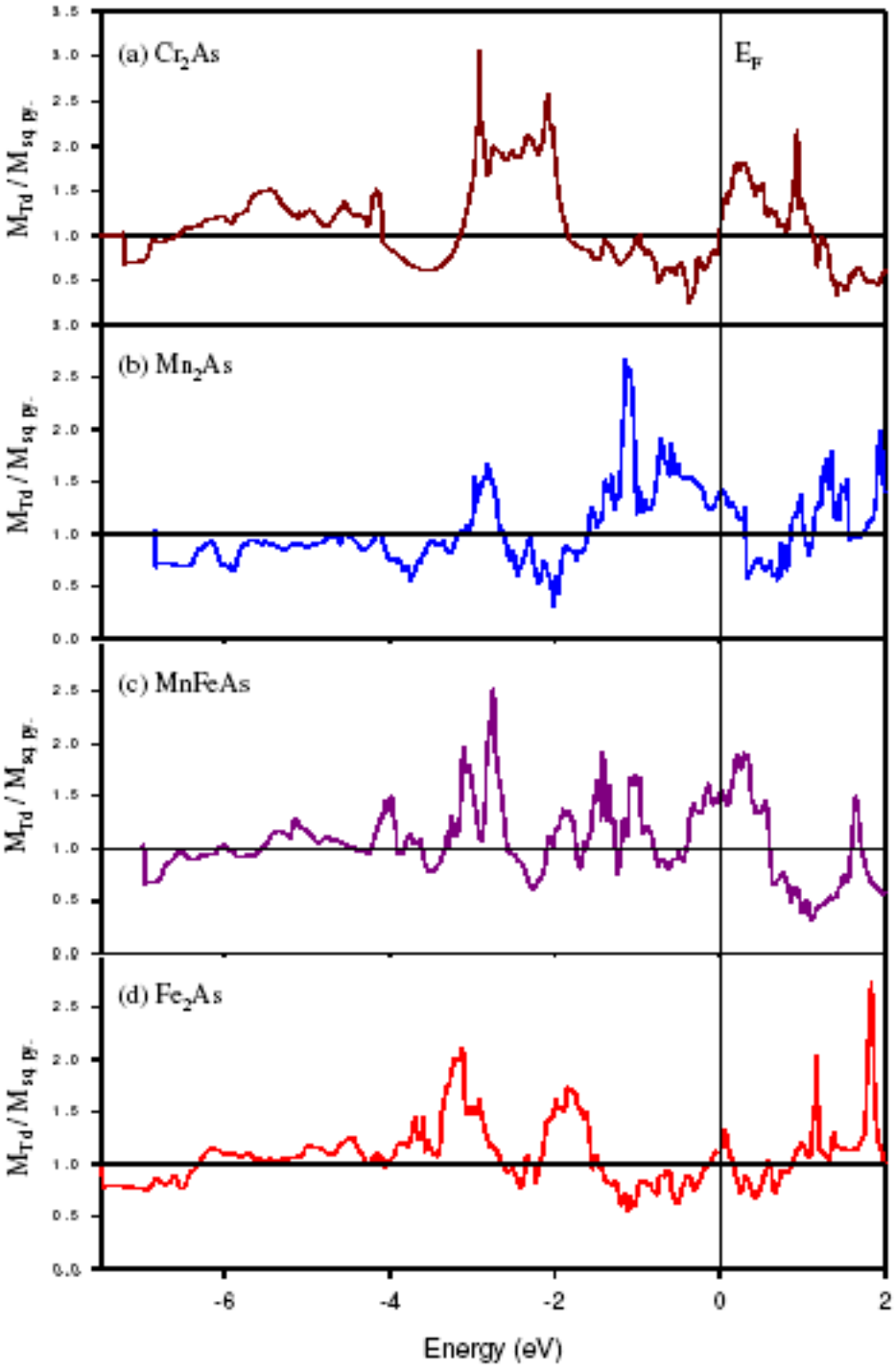

Supplement figure 1. Relative DOS curves of metal sites. Metal site's DOS ratio, $\frac{M_{Td}}{M_{sq.py}}$, is plotted against energy: (a) Cr_2As, (b) Mn_2As, (c) MnFeAs, and Fe_2AS. Horizontal line indicates the Fermi energy.

CHAPTER 7

General Conclusions

This research project has focused on exploring the complex chemistry of structure-bonding-property relationships in *γ*-brass phases as well as their crystallographic and electronic structural correlations with Heusler and Zintl phases. The studies of the location of the Fermi level in DOS and COHP curves, offer better understanding for the effects of *vec* changes on chemical composition, crystal structure, and magnetic property in these compounds.

Changing chemical composition by allowing shared site occupancies and/or by creating vacancies. Our study on flux-grown large single crystals of the $RENi_{1-x}Ge_3$ series provides the understanding the relationships between chemical composition and crystal structure. Increasing *vec* along the Lanthanide series, vacancies at the Ni site of $RENiGe_3$ increase up to the Er compound followed by lattice distortions. With this chemical pressure with the lanthanide contraction, COHP analysis has suggested that Ni deficiencies occur to minimize this antibonding population to achieve electronically driven structural stability.

Distorting the lattice structure to specifically eliminate the antibonding interactions. The study on $Cr_xFe_{1-x}Ga$ series illustrates how trigonal distortion occurs from the cubic γ-brass structure, and how the magnetically active 3*d* elements behave in magnetically frustrated environments. The band structure calculations indicate the Fermi energy is located near the pseudogap which favors the structural distortion to accommodate the changes in *vec*.

Shifting the majority spin states to lower energy and minority spin states to higher energy to create itinerant magnetic order. The study on MM′As offers the understanding of the spin orientations of 3*d* metal in tetrahedral and square pyramidal environments for various valence electron counts. Band calculations indicate the majority and minority states split especially in the vicinity of the Fermi level to maintain structural stability especially at the tetrahedral site.

The $Ti_{0.80(2)}Ni_{1.83(2)}Ga_{1.12}$ compound synthesized during the course of this investigation provide an introduction to the intermetallic phase that bridges the Heusler phase and the γ-brass structure with an interesting array of subjects for further study with some synthetic problems which should be addressed. Band structure calculations indicate that the short interatomic contacts are optimized, and the chemical composition, atomic distribution, as well as structure are strongly influenced by a pseudogap in the DOS curve. This represents a link between Hume-Rothery electron phases and polar intermetallics.

APPENDIX 3.1

Single Crystal Structure of Cr_3Ga

Introduction

During crystal structure studies of $Cr_{1-x}Fe_xGa$ series, a binary compound Cr_3Ga was found. The stoichiometric mixture of CrGa was heated in sealed, evacuated silica tubes at 1323 K for 80 hours. After cooling at the rate of 1 K/min. to 1123 K, the sample was annealed at 1123 K for 1 week. The reaction was terminated by turning off the furnace. The Cr_3Si-type Cr_3Ga crystallizes in cubic structure, which was first reported by Girgis by powder X-ray diffraction experiment.[1] In this section, we report the refinement results by single crystal X-ray diffraction experiment.

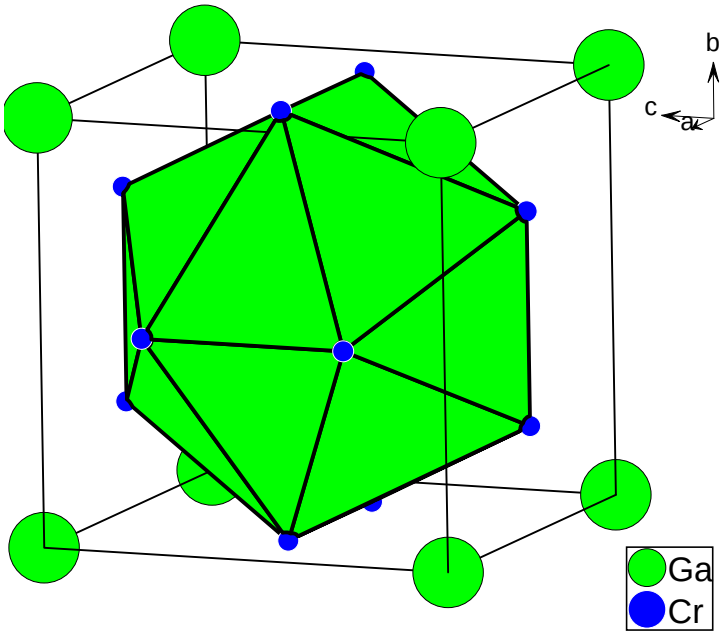

Discussion

Details of X-ray single crystal diffraction experiment structural data and

crystallographic data recording/refinement parameters for Cr_3Ga are listed in the Table 1. The refined site occupancies and fractional coordinates with isotropic / anisotropic thermal displacement parameters are listed in Table 2 & 3.

Table 1. Crystal diffraction data and structure refinement for Cr_3Ga.

Empirical formula	Cr_3Ga
Formula weight	121.72
Temperature	293(2) K
Wavelength	0.71073 Å
Crystal system	Cubic
Space group	$Pm\bar{3}n$ (no. 223)
Unit cell dimensions	a = 4.6573(5) Å
Volume	101.019(19) $Å^3$
Z	2
Absorption coefficient	18.175 mm^{-1}
F(000)	110
Crystal size	20 x 20 x 20 mm^3
Theta range for data collection	6.19 to 28.06°.
Index ranges	$-6 \le h \le 5$, $-5 \le k \le 5$, $-3 \le l \le 6$
Reflections collected	496
Independent reflections	32 [R(int) = 0.0625]
Completeness to theta	96.9 %
Refinement method	Full-matrix least-squares on F^2
Data / restraints / parameters	32 / 0 / 5
Goodness-of-fit on F^2	1.618
Final R indices [I > 2sigma(I)]	R_1 = 0.0276, wR_2 = 0.0710
R indices (all data)	R_1 = 0.0276, wR_2 = 0.0710
Extinction coefficient	0.07(3)
Largest diff. peak and hole	0.939 and -1.076 e.$Å^{-3}$

Table 2. Atomic coordinates and equivalent isotropic displacement parameters ($Å^2 \times 10^3$) for Cr_3Ga. U_{eq} is defined as one third of the trace of the orthogonalized U_{ij} tensor.

	Wyck.	Occupancy	x	y	z	U_{eq}
Ga	2*a*	1	0	0	0	3(1)
Cr	6*c*	1	1/4	0	1/2	5(1)

Table 3. Anisotropic displacement parameters ($Å^2 \times 10^3$) for Cr_3Ga. The anisotropic displacement factor exponent takes the form: $-2\pi^2[h^2 a^{*2} U_{11} + ... + 2 h k a^* b^* U_{12}]$

	U_{11}	U_{22}	U_{33}	U_{23}	U_{13}	U_{12}
Ga	3(1)	3(1)	3(1)	0	0	0
Cr	5(2)	5(1)	5(1)	0	0	0

Reference

[1] Girgis, K. Acta Crystallographica. 1958, 11, 604.

APPENDIX 4.1

Crystal Structures of $V_{0.6}(Co_{1-x}Ga_x)_{2.67}$ series and $Nb_{2.3(1)}RhGa_{1.4(1)}$

ABSTRACT

A new series of compounds, $V_{1-y}\square_y(Co_{1-x}Ga_x)_4$ ($0.5 \leq x \leq 0.375$; $0.09 \leq y \leq 0.04$) series and $Nb_{2.3(1)}RhGa_{1.4(1)}$ have been prepared and their crystal structures were characterized by powder and single crystal X-ray diffraction experiments. The new phases crystallize in a cubic $Sc_{11}Ir_4$-type (*G*-phase) structure with space group $Fm\bar{3}m$ (No. 225), $Z = 4$.

Introduction

During our investigations in search of isostructural and/or distorted γ-brass phases in intermetallic gallides, we have synthesized five compounds in V-Co-Ga system and one Nb-Rh-Ga compound adopting the 26-atom γ-brass cluster as a building block in a face-centered cubic lattice.

Synthesis. Vanadium (purity 99.7%, Ames Lab.), cobalt (99.995%, Ames Lab.), and gallium (99.9999%, *Alfa Aesar*) were taken as starting materials for synthesis. A mixture of different loading compositions (Table 1.) was placed in an evacuated ($< 10^{-4}$ torr) and sealed-off silica tube. The alloys were melted at 1373 K for 24 hours, and the product was slowly cooled down (1 K/min) to 1123 K followed by 48 hours of annealing. The product appears to be stable against decomposition in both air and moisture over a period of several months at room temperature.

Figure 1. Unit cell structure and γ-brass cluster representation of $V_{0.6}(Co_{1-x}Ga_x)_{2.67}$ series. (a) unit cell structure is shown with Ga in green, V in blue, and Co in red. (b) γ-brass cluster representation is shown. (c) Co(3) site is highlighted in black. (d) Co(2) site is highlighted in grey.

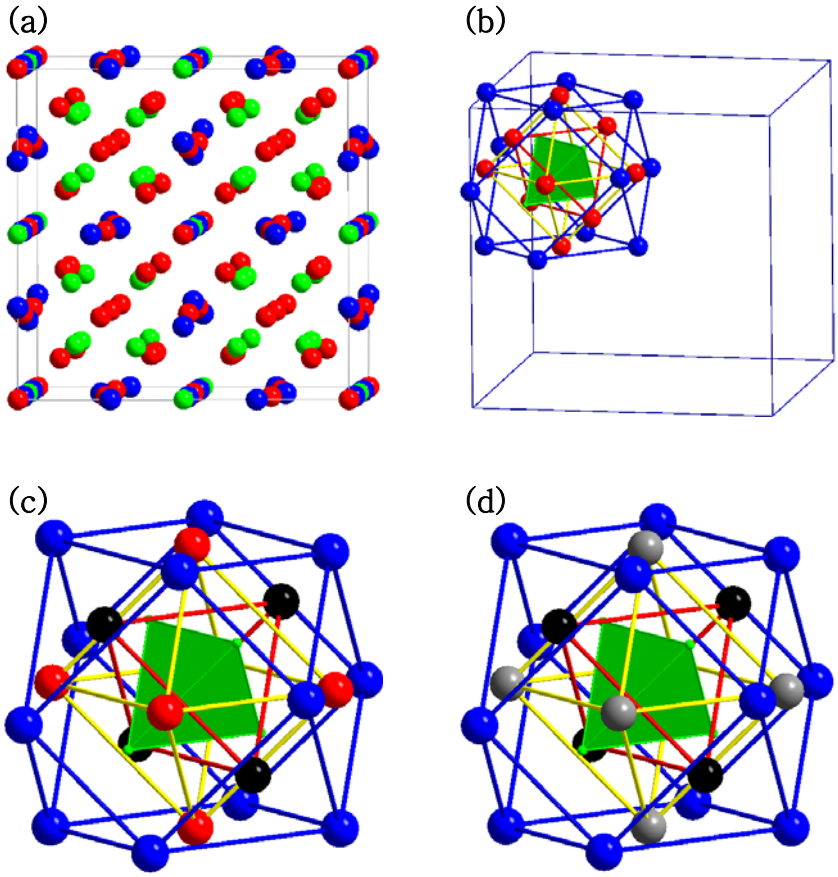

Discussion.

$V_{1-y}\square_y(Co_{1-x}Ga_x)_4$ crystallizes in the $Sc_{11}Ir_4$-structure type, Pearson symbol *cP*120. This structure is face-centered cubic, space group $Fm\bar{3}m$ (No. 225), with six atomic positions in the asymmetric unit. A summary of crystallographic data, atomic positions, site occupancy factors, and temperature displacements factors are listed in Tables 1-3.

---------- Table 1 - 3 ----------

Figure 1 shows the unit cell structure of $V_{1-y}\square_y(Co_{1-x}Ga_x)_4$. The structure is characterized by the presence of a 26-atom γ-brass cluster as its fundamental building block. This cluster contains four polyhedral units: an inner tetrahedron, an outer tetrahedron, an octahedron encapsulating two tetrahedra, and an outermost cuboctahedron (Figure 1). Throughout these systems, the inner tetrahedron is made only with Ga atoms and the cuboctahedron with only V atoms. However, one sample showed a mixed occupancy in the Co site, which forms the octahedron with Co:Ga=90:10. Also, another site that forms the outer tetrahedron was found to have Co/Ga mixing from 10 to 30% Ga content, with one sample showing full occupancy with only Co. In a previous study (Gourdon & Miller), experimental and theoretical results indicated that the outer tetrahedron and the octahedron attracts atoms with lower valence electron density, and the inner tetrahedron and the cuboctahedron attracts atoms with greater valence electron density.[1] In $V_{1-y}\square_y(Co_{1-x}Ga_x)_4$ series, Ga atoms ($\chi_{Pauling}$=1.81) contributing 13 electrons (ten 3*d* + three 4*p*) occupy the inner tetrahedron site. The outer tetrahedron site and the octahedron site are preferably occupied by Co atoms with minor Ga mixing. However, in the $V_{1-y}\square_y(Co_{1-x}Ga_x)_4$ series, the most electropositive V atoms ($\chi_{Pauling}$=1.63) with five 3*d* valence electrons fully occupy the cuboctahedron site, which showed opposite preference in having greater valence electron density in the previous study. In γ-brass structures, the 26-atom clusters are isolated, whereas these clusters are connected by sharing the cuboctahedron faces in the $V_{1-y}\square_y(Co_{1-x}Ga_x)_4$ structure.

Table 1. Powder and Single Crystal X-ray diffraction Structure Refinement Results of $V_{1-y}\square_y(Co_{1-x}Ga_x)_4$ series and $Nb_{2.3(1)}RhGa_{1.4(1)}$.

Loading Composition	$VCoGa_2$	$VCo_{1.25}Ga_{1.75}$	$VCo_{1.5}Ga_{1.5}$	$VCo_{1.75}Ga_{1.25}$	VCo_2Ga	$NbRhGa_2$
PXRD						
a, Å	11.7392(1)	11.7415(1)	11.7408(7)	11.7155(1)	11.7352(1)	
Volume, Å^3	1617.8(0)	1618.7(0)	1618.4(2)	1608.0(0)	1616.1(0)	
Single crystal XRD						
Refined composition	$V_{0.96(2)}Co_{2.5(0)}Ga_{1.5(0)}$	$V_{0.96(1)}Co_{2.0(1)}Ga_{2.0(1)}$	$V_{0.91(2)}Co_{2.1(1)}Ga_{1.9(1)}$	$V_{0.92(4)}Co_{2.3(2)}Ga_{1.7(2)}$	$V_{0.94(4)}Co_{2.2(2)}Ga_{1.8(2)}$	$Nb_{2.3(1)}RhGa_{1.4(1)}$
Formula weight	249.31	249.31	238.52	249.31	238.52	2698.59
Temperature	293(2) K	293(2) K	293(2) K	293(2) K	293(2) K	293(2) K
Wavelength	0.71073 Å	0.71073 Å	0.71073 Å	0.71073 Å	0.71073 Å	0.71073 Å
Crystal system	Cubic	Cubic	Cubic	Cubic	Cubic	Cubic
Space group	$Fm\overline{3}m$	$Fm\overline{3}m$	$Fm\overline{3}m$	$Fm\overline{3}m$	$Fm\overline{3}m$	$Fm\overline{3}m$
Unit cell dimensions	a = 11.7282(14) Å	a = 11.7194(14) Å	a = 11.7202(14) Å	a = 11.7195(14) Å	a = 11.7256(14) Å	a = 12.1952(14) Å
Volume	1613.2(3) Å^3	1609.6(3) Å^3	1609.9(3) Å^3	1609.6(3) Å^3	1612.1(3) Å^3	1813.7(4) Å^3
Z	12	12	12	12	12	12
Absorption coefficient	14.438 mm^{-1}	14.471 mm^{-1}	12.537 mm^{-1}	14.470 mm^{-1}	12.520 mm^{-1}	29.079 mm^{-1}
F(000)	1344	1344	1296	1344	1296	4752
Crystal size	25 x 25 x 25 mm^3	25 x 25 x 25 mm^3	25 x 25 x 25 mm^3	25 x 25 x 25 mm^3	25 x 25 x 25 mm^3	25 x 25 x 25 mm^3
Theta range for data collection	3.01 to 35.09°.	3.01 to 34.67°.	3.48 to 34.39°.	3.01 to 34.67°.	3.48 to 34.37°.	3.34 to 28.72°.
Index ranges	$0 \le h \le 12$, $0 \le k \le 13$, $1 \le l \le 18$	$0 \le h \le 12$, $0 \le k \le 13$, $1 \le l \le 18$	$0 \le h \le 12$, $0 \le k \le 13$, $2 \le l \le 18$	$-18 \le h \le 18$, $-18 \le k \le 18$, $0 \le l \le 18$	$0 \le h \le 12$, $0 \le k \le 13$, $2 \le l \le 18$	$0 \le h \le 10$, $0 \le k \le 11$, $2 \le l \le 16$
Reflections collected	331	330	326	3410	328	230
Independent reflections	219 [R(int) = 0.0430]	218 [R(int) = 0.0228]	215 [R(int) = 0.0434]	218 [R(int) = 0.0812]	216 [R(int) = 0.1036]	156 [R(int) = 0.0779]
Completeness to theta	96.50%	100.00%	99.10%	100.0 %	99.50%	99.10%
Refinement method	Full-matrix least-squares on F^2					
Data / restraints / parameters	219 / 0 / 17	218 / 0 / 19	215 / 0 / 18	218 / 0 / 18	216 / 0 / 18	156 / 0 / 19
Goodness-of-fit on F^2	0.512	0.523	0.597	1.434	0.628	0.665
Final R indices [$I > 2$sigma(I)]	R_1 = 0.0269, wR_2 = 0.0262	R_1 = 0.0230, wR_2 = 0.0136	R_1 = 0.0257, wR_2 = 0.0230	R_1 = 0.0545, wR_2 = 0.0549	R_1 = 0.0358, wR_2 = 0.0302	R_1 = 0.0433, wR_2 = 0.0360
R indices (all data)	R_1 = 0.1211, wR_2 = 0.0414	R_1 = 0.0720, wR_2 = 0.0182	R_1 = 0.1435, wR_2 = 0.0453	R_1 = 0.0701, wR_2 = 0.0571	R_1 = 0.2173, wR_2 = 0.0699	R_1 = 0.1548, wR_2 = 0.0573
Extinction coefficient	0.00070(3)	0.000326(6)	0.00063(3)	0.00028(4)	0.000109(14)	0.000014(7)
Largest diff. peak / hole	0.967 / -1.361 e.Å^{-3}	1.301 / -0.907 e Å^{-3}	1.602 / -1.083 e. Å^{-3}	2.104 / -1.696 e. Å^{-3}	1.573 / -2.088 e. Å^{-3}	1.860 / -1.403 e.Å^{-3}

Table 2. Atomic coordinates and equivalent isotropic displacement parameters ($Å^2 \times 10^3$) for $V_{1-y}\square_y(Co_{1-x}Ga_x)_4$ series and $Nb_{2.3(1)}RhGa_{1.4(1)}$. U_{eq} is defined as one third of the trace of the orthogonalized U_{ij} tensor.

	Wyck.	Occup.	x	y	z	U_{eq}
Ga1	*32f*	1	0.1524(1)	0.3476(1)	0.1524(1)	11(1)
Ga2	*4b*	1	0	1/2	0	15(1)
Co1	*4a*	1	0	0	0	14(2)
Co2	*24d*	1	1/4	1/4	0	8(1)
Co3	*32f*	1	0.1203(1)	0.1203(1)	0.1203(1)	6(1)
V1	*24e*	0.96(2)	0	-0.2788(3)	0	8(1)
Ga1	*32f*	1	0.1515(1)	0.3485(1)	0.1515(1)	11(1)
Ga2	*4b*	1	0	1/2	0	14(1)
Co1	*4a*	1	0	0	0	10(1)
Ga3	*24d*	1	1/4	1/4	0	8(1)
Co3	*32f*	1	0.1208(1)	0.1208(1)	0.1208(1)	8(1)
V1	*24e*	0.96(1)	0	-0.2779(2)	0	9(1)
Ga1	*32f*	1	0.1513(1)	0.3487(1)	0.1513(1)	10(1)
Ga2	*4b*	1	0	1/2	0	13(2)
Co1	*4a*	1	0	0	0	8(2)
Co2	*24d*	1	1/4	1/4	0	6(1)
M3 Co3	*32f*	0.71(9)	0.1209(2)	0.1209(2)	0.1209(2)	6(1)
Ga3		0.29(9)	0.1209(2)	0.1209(2)	0.1209(2)	6(1)
V1	*24e*	0.91(2)	0	-0.2780(4)	0	3(1)
Ga1	*32f*	1	0.1516(1)	0.3484(1)	0.1516(1)	11(1)
Ga2	*4b*	1	0	1/2	0	14(1)
Co1	*4a*	1	0	0	0	10(1)
Co2	*24d*	1	1/4	1/4	0	7(1)
M3 Co3	*32f*	0.75(5)	0.1208(1)	0.1208(1)	0.1208(1)	7(1)
Ga3		0.25(5)	0.1208(1)	0.1208(1)	0.1208(1)	7(1)
V1	*24e*	0.94(1)	0	-0.2781(2)	0	7(1)

Ga1	*32f*	1	0.1524(2)	0.3476(2)	0.1524(2)	8(1)
Ga2	*4b*	1	0	1/2	0	20(4)
Co1	*4a*	1	0	0	0	11(4)
Co2	*24d*	1	1/4	1/4	0	3(1)
M3 Co3	*32f*	0.81(16)	0.1205(3)	0.1205(3)	0.1205(3)	4(1)
Ga3	*32f*	0.19(16)	0.1205(3)	0.1205(3)	0.1205(3)	4(1)
V1	*24e*	0.94(4)	0	-0.2783(7)	0	1(2)
Rh1	*24d*	1	1/4	1/4	0	12(1)
Nb1	*4b*	0.87(3)	0	0	1/2	26(5)
Nb2	*24e*	0.91(4)	0	0	-0.2132(5)	12(2)
Nb3	*32f*	1	0.1210(4)	0.1210(4)	0.3790(4)	23(2)
Ga1	*4a*	1	0	0	0	73(12)
Ga2	*32f*	0.94(4)	0.3471(3)	0.3471(3)	0.1529(3)	17(2)

Table 3. Anisotropic displacement parameters ($Å^2 \times 10^3$) for $V_{1-y}\square_y(Co_{1-x}Ga_x)_4$ series and $Nb_{2.3(1)}RhGa_{1.4(1)}$. The anisotropic displacement factor exponent takes the form: $-2\pi^2[\, h^2\, a^{*2} U_{11} + \ldots + 2\, h\, k\, a^*\, b^*\, U_{12}\,]$

	U_{11}	U_{22}	U_{33}	U_{23}	U_{13}	U_{12}
Ga1	11(1)	11(1)	11(1)	-1(1)	1(1)	-1(1)
Ga2	15(1)	15(1)	15(1)	0	0	0
Co1	14(2)	14(2)	14(2)	0	0	0
Co2	9(1)	9(1)	7(1)	0	0	3(1)
Co3	6(1)	6(1)	6(1)	0(1)	0(1)	0(1)
V1	7(1)	8(2)	7(1)	0	0	0
Ga1	11(1)	11(1)	11(1)	-3(1)	3(1)	-3(1)
Ga2	14(1)	14(1)	14(1)	0	0	0
Co1	10(1)	10(1)	10(1)	0	0	0
Co2	9(1)	9(1)	7(1)	0	0	2(1)
Co3	8(1)	8(1)	8(1)	0(1)	0(1)	0(1)
V1	8(1)	10(1)	8(1)	0	0	0

Ga1	10(1)	10(1)	10(1)	-1(1)	1(1)	-1(1)
Ga2	13(2)	13(2)	13(2)	0	0	0
Co1	8(2)	8(2)	8(2)	0	0	0
Co2	6(1)	6(1)	5(2)	0	0	3(1)
M3	6(1)	6(1)	6(1)	0(1)	0(1)	0(1)
V1	3(2)	3(2)	3(2)	0	0	0
Ga1	11(1)	11(1)	11(1)	-2(1)	2(1)	-2(1)
Ga2	14(1)	14(1)	14(1)	0	0	0
Co1	10(1)	10(1)	10(1)	0	0	0
Co2	8(1)	8(1)	5(1)	0	0	2(1)
M3	7(1)	7(1)	7(1)	0(1)	0(1)	0(1)
V1	7(1)	9(1)	7(1)	0	0	0
Ga1	8(1)	8(1)	8(1)	2(1)	-2(1)	2(1)
Ga2	20(4)	20(4)	20(4)	0	0	0
Co1	11(4)	11(4)	11(4)	0	0	0
Co2	4(2)	4(2)	2(3)	0	0	4(2)
M3	4(1)	4(1)	4(1)	1(1)	1(1)	1(1)
V1	1(3)	0(4)	1(3)	0	0	0
Rh1	14(2)	14(2)	9(2)	0	0	-4(2)
Nb1	26(5)	26(5)	26(5)	0	0	0
Nb2	10(2)	10(2)	17(3)	0	0	0
Nb3	23(2)	23(2)	23(2)	-8(2)	-8(2)	8(2)
Ga1	73(12)	73(12)	73(12)	0	0	0
Ga2	17(2)	17(2)	17(2)	-1(2)	-1(2)	1(2)

References

[1] Gourdon, O.; Gout, D.; Williams, D. J.; Proffen, T.; Hobbs, S.; Miller, G. J. *Inorg. Chem*. **2007**, 46, 251.

APPENDIX 4.2

Crystal Structure of $Ti_{0.48(1)}NiGa_2$

Introduction

During our attempts to grow large single crystals of Ti-Ni-Ga compounds using Ga-flux, a new compound $Ti_{0.48(1)}NiGa_2$ was found. Loading Ti : Ni : Ga = 0.54 : 1 : 4.6 in an alumina crucible encapsulated in a sealed and evacuated silica tube yielded large (ca. 3 – 5 mm) single crystals. The starting mixture was heated at 1323 K for 2 hours. After cooling at the rate of 1 K/min. to 1123 K, the sample was annealed at 1123 K for 2 days. After temperature was lowered to 523 K over 5 hours, remaining Ga-flux was removed by centrifuging, followed by etching in 0.1 M HCl (aq). The $Ti_{0.48(1)}NiGa_2$ crystallizes in a new monoclinic structure, Pearson code o*F*56 and *Wyckoff* sequence *omhdba*. In this section, we report the refinement results by single crystal X-ray diffraction experiment.

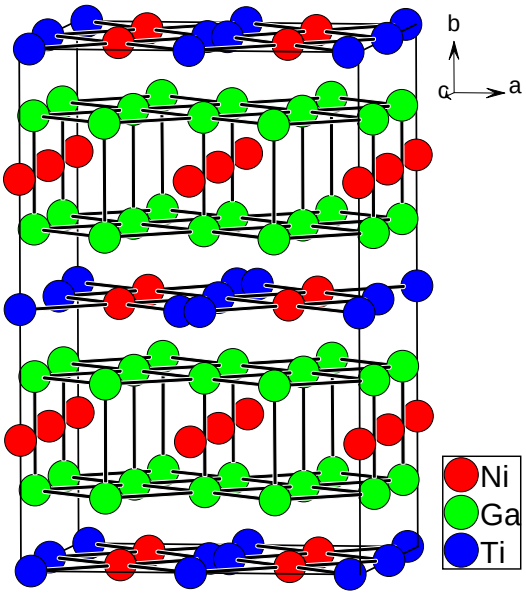

Discussion

Details of X-ray single crystal diffraction experiment structural data and crystallographic data recording/refinement parameters for $Ti_{0.48(1)}NiGa_2$ are listed in the Table 1. The refined site occupancies and fractional coordinates with isotropic / anisotropic thermal displacement parameters are listed in Table 2 & 3.

Table 1. Crystal diffraction data and structure refinement for $Ti_{0.48(1)}NiGa_2$.

Empirical formula	$Ti_{0.48(1)}NiGa_2$
Formula weight	176.33
Temperature	293(2) K
Wavelength	0.71073 Å
Crystal system	Orthorhombic
Space group	*Fmmm* (no. 69)
Unit cell dimensions	a = 8.1564(16) Å
	b = 12.414(3) Å
	c = 8.1283(16) Å
Volume	823.0(3) $Å^3$
Z	8
Absorption coefficient	12.665 mm^{-1}
F(000)	648
Crystal size	35 x 35 x 35 mm^3
Theta range for data collection	3.28 to 28.62°.
Index ranges	$0 \le h \le 10$, $0 \le k \le 16$, $0 \le l \le 10$
Reflections collected	315
Independent reflections	315 [R(int) = 0.0000]
Completeness to theta	100.00%
Refinement method	Full-matrix least-squares on F^2
Data / restraints / parameters	315 / 0 / 30
Goodness-of-fit on F^2	0.468
Final R indices [I > 2sigma(I)]	R_1 = 0.0330, wR_2 = 0.0878
R indices (all data)	R_1 = 0.0682, wR_2 = 0.1070
Extinction coefficient	0.00145(17)
Largest diff. peak and hole	1.067 and -1.832 e.$Å_{-3}$

Table 2. Atomic coordinates and equivalent isotropic displacement parameters ($Å^2 \times 10^3$) for $Ti_{0.48(1)}NiGa_2$. U_{eq} is defined as one third of the trace of the orthogonalized U_{ij} tensor.

	Wyck.	Occupancy	x	y	z	U_{eq}
Ga1	16m	1	1/2	0.3586(1)	0.2500(4)	23(1)
Ga2	16o	1	0.2503(4)	0.3592(1)	0	22(1)
Ni1	8d	1	1/4	1/2	1/4	10(1)
Ni2	8h	1	1/2	0.2503(4)	0	10(1)
Ti1	4b	1	0	1/2	0	6(1)
Ti2	8g	0.465(15)	0.4701(17)	1/2	0	30(5)

Table 3. Anisotropic displacement parameters ($Å^2 \times 10^3$) for $Ti_{0.48(1)}NiGa_2$. The anisotropic displacement factor exponent takes the form: $-2\pi^2[h^2 a^{*2} U_{11} + ... + 2 h k a^* b^* U_{12}]$

	U_{11}	U_{22}	U_{33}	U_{23}	U_{13}	U_{12}
Ga1	40(1)	24(1)	6(1)	1(1)	0	0
Ga2	7(1)	43(1)	17(1)	0	0	0(1)
Ni1	8(1)	15(1)	7(1)	0	1(2)	0
Ni2	7(1)	16(1)	8(1)	0	0	0
Ti1	12(3)	4(2)	3(3)	0	0	0
Ti2	21(10)	42(7)	29(6)	0	0	0

APPENDIX 4.3

Single Crystal Structure of $NbGa_3$

Introduction

During our attempts to grow large single crystals of Nb-Rh-Ga compounds using Ga-flux, a binary compound $NbGa_3$ was found. Loading Nb : Rh : Ga = 1 : 1 : 10 in an alumina crucible encapsulated in a sealed and evacuated silica tube yielded large (ca. 2 mm) truncated cubic single crystals. The starting mixture was heated at 1323 K for 2 hours. After cooling at the rate of 1 K/min. to 1123 K, the sample was annealed at 1123 K for 2 days. After temperature was lowered to 523 K over 5 hours, remaining Ga-flux was removed by centrifuging, followed by etching in 0.1 M HCl (aq). The $TiAl_3$-type $NbGa_3$ crystallizes in tetragonal structure, which was first reported by Meissner by powder X-ray diffraction experiment.[1] In this section, we report the refinement results by single crystal X-ray diffraction experiment.

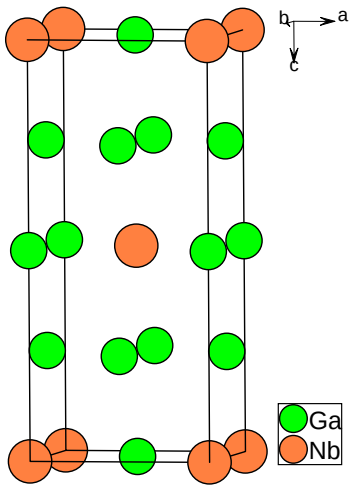

Discussion

Details of X-ray single crystal diffraction experiment structural data and crystallographic data recording/refinement parameters for $NbGa_3$ are listed in the Table 1. The refined site occupancies and fractional coordinates with isotropic / anisotropic thermal displacement parameters are listed in Table 2 & 3.

Table 1. Crystal diffraction data and structure refinement for $NbGa_3$.

Empirical formula	$NbGa_3$
Formula weight	614.14
Temperature	293(2) K
Wavelength	0.71073 Å
Crystal system	tetragonal
Space group	*I4/mmm*
Unit cell dimensions	a = 3.7936(5) Å
Volume	b = 3.7936(5) Å
Z	c = 8.7449(17) Å
Absorption coefficient	125.85(3) $Å^3$
F(000)	1
Crystal size	36.805 mm^{-1}
Theta range for data collection	272
Index ranges	35 x 35 x 35 mm^3
Reflections collected	4.66 to 34.84°.
Independent reflections	$-3 \le h \le 4$, $0 \le k \le 6$, $0 \le l \le 13$
Completeness to theta	151
Refinement method	106 [R(int) = 0.0129]
Data / restraints / parameters	99.1 %
Goodness-of-fit on F^2	Full-matrix least-squares on F^2
Final R indices [I > 2sigma(I)]	106 / 0 / 8
R indices (all data)	0.860
Extinction coefficient	R_1 = 0.0206, wR_2 = 0.0429
Largest diff. peak and hole	R_1 = 0.0240, wR_2 = 0.0439

Table 2. Atomic coordinates and equivalent isotropic displacement parameters ($Å^2 \times 10^3$) for $NbGa_3$. U_{eq} is defined as one third of the trace of the orthogonalized U_{ij} tensor.

	Wyck.	Occupancy	x	y	z	U_{eq}
Ga1	2*b*	1	0	0	1/2	13(1)
Ga2	4*d*	1	0	1/2	1/4	12(1)
Nb	2*a*	1	0	0	0	9(1)

Table 3. Anisotropic displacement parameters ($Å^2 \times 10^3$) for $NbGa_3$. The anisotropic displacement factor exponent takes the form: $-2\pi^2[h^2 a^{*2} U_{11} + ... + 2 h k a^* b^* U_{12}]$

	U_{11}	U_{22}	U_{33}	U_{23}	U_{13}	U_{12}
Ga1	11(1)	11(1)	17(1)	0	0	0
Ga2	13(1)	13(1)	11(1)	0	0	0
Nb	9(1)	9(1)	7(1)	0	0	0

Reference

[1] Meissner, H. G.; Schubert, K. *Zeitschrift fuer Metallkunde*. **1965**, 56, 475.

APPENDIX 5.1

Anisotropic Physical Properties of RNi_xGe_3 Series

(R = Y, Ce-Nd, Sm, Gd-Lu)

(manuscript in preparation for submission to Physical Review B)

E. D. Mun, [#%] *S. L. Bud'ko,* [#] *P. C. Canfield*[#%]
Hyunjin Ko, [#&] *Gordon J. Miller*[#&]

[#]Ames Laboratory US DOE and [%]Department of Physics and Astronomy, Iowa State University, Ames, IA 50011-3111, USA

[&]Department of Chemistry, Iowa State University, Ames, IA 50011-3111, USA

(our crystallography and chemical composition studies will be part of this paper)

ABSTRACT

The magnetic, transport, and thermal properties of the $RNiGe_3$ compounds are discussed in terms of a combined elementary magnon (*spin waves*) excitation, magnetic superzone formation, and crystalline electric field (CEF). We have studied flux-grown single crystals by measuring magnetic susceptibility, magnetization, electrical resistivity, magnetoresistance, and specific heat. A clear anisotropy and an antiferromagnetic ordering of the lanthanide series (Ce-Nd, Sm, Gd-Tm) have been observed above 1.8 K from the magnetic susceptibility and all of these members showed a metamagnetic transition at 2 K for fields below 70 kOe except Sm. The resistivity of these series follows metallic behavior in the high-temperature region and below ordering temperatures shows unusual behavior as a function of temperature. For heavy rare-earth compounds (R = Gd, Tb, Dy, Ho) just below their ordering

temperatures the resistivities and magnetoresistances exhibited a significant anisotropy and unusual anomalies between different current directions. These anomalies are interpreted in terms of the formation of magnetic superzones. At low temperature, the magnetic contribution to the specific heat is well described by linearized antiferromagnetic spin wave analysis and shows a broad peak above ordering temperature due to the contribution of excited state energy levels. In an antiferromagnet, an anisotropy can have a huge effect on thermodynamic properties because of interplay with exchange energy. The low-temperature specific heat and magnetic susceptibility data show strong influences of magnetic interaction. The entropy calculated from the specific heat measurements and the reduction of magnetic susceptibility show that there is considerable effect of CEF's in these compounds. We have analyzed the experimental results by taking into account CEF and detailed analyses are given.

APPENDIX 5.2

Single Crystal Structure of $ErNi_{1.53(1)}Ge_2$

Introduction

During our studies on flux-grown single crystals of $RENi_{1-x}Ge_3$ series, a byproduct crystal was obtained from $ErNiGe_3$. X-ray diffraction analyses yielded a monoclinic $ErNi_{1.53(1)}Ge_2$. The $ErNi_{1.53(1)}Ge_2$ crystallizes in a new monoclinic structure, Pearson code m*C*76 and *Wyckoff* sequence j^5i^9. In this section, we report the refinement results by single crystal X-ray diffraction experiment.

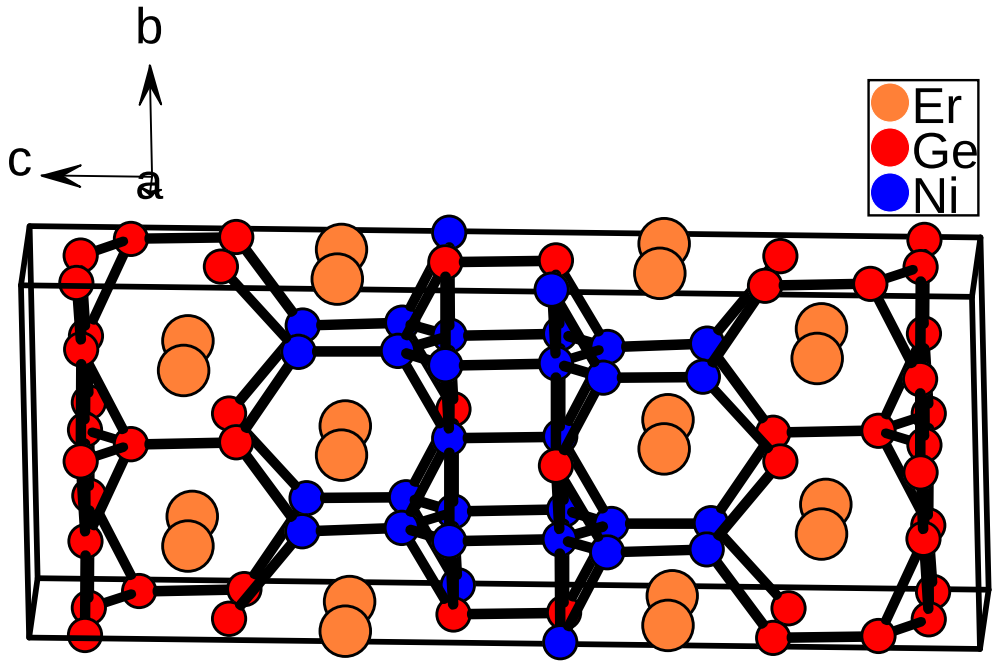

Discussion

Details of X-ray single crystal diffraction experiment structural data and

crystallographic data recording/refinement parameters for $ErNi_{1.53(1)}Ge_2$ are listed in the Table 1. The refined site occupancies and fractional coordinates with isotropic / anisotropic thermal displacement parameters are listed in Table 2 & 3.

Table 1. Crystal diffraction data and structure refinement for $ErNi_{1.53(1)}Ge_2$.

Empirical formula	$ErNi_{1.53(1)}Ge_2$
Formula weight	402.06
Temperature	293(2) K
Diffractometer; Wavelength	*STOE-IPDS2* ; 0.71073 Å
Crystal system	Monoclinic
Space group	*C2/m*
Unit cell dimensions	a = 8.0044(16) Å
	b = 7.9260(16) Å β = 100.67(3)°.
	c = 21.562(4) Å
Volume	1344.3(5) $Å^3$
Z	16
Absorption coefficient	28.213 mm^{-1}
F(000)	1536
Crystal size	40 x 20 x 20 mm^3
Theta range for data collection	2.88 to 34.99°.
Index ranges	$-12 \le h \le 12$, $-12 \le k \le 12$, $0 \le l \le 34$
Reflections collected	5797
Independent reflections	3094 [R(int) = 0.1113]
Completeness to theta	99.0 %
Refinement method	Full-matrix least-squares on F^2
Data / restraints / parameters	3094 / 0 / 102
Goodness-of-fit on F^2	1.093
Final R indices [I > 2sigma(I)]	R_1 = 0.0696, wR_2 = 0.2316
R indices (all data)	R_1 = 0.1137, wR_2 = 0.2591
Extinction coefficient	0.00111(11)
Largest diff. peak and hole	4.287 and -4.423 e.$Å^{-3}$

Table 2. Atomic coordinates and equivalent isotropic displacement parameters ($Å^2 \times 10^3$) for $ErNi_{1.53(1)}Ge_2$. U_{eq} is defined as one third of the trace of the orthogonalized U_{ij} tensor.

	Wyck.	Occup.	*x*	*y*	*z*	U_{eq}
Er(1)	4*i*	1	0.1642(2)	0	0.3310(1)	19(1)
Er(2)	8*j*	1	0.0841(1)	-.2500(1)	0.1683(1)	18(1)
Er(3)	4*i*	1	0.1671(2)	1/2	0.3311(1)	19(1)
Ge(4)	8*j*	1	-0.2200(3)	-.2724(2)	0.0589(1)	17(1)
Ge(5)	4*i*	1	0.0505(3)	0	0.0581(1)	16(1)
Ge(6)	4*i*	1	0.0088(3)	1/2	0.0582(1)	17(1)
Ge(7)	4*i*	1	-0.1406(4)	0	0.2187(1)	16(1)
Ge(8)	4*i*	1	0.3534(4)	0	0.2069(2)	20(1)
Ge(9)	4*i*	1	-0.1957(4)	0	0.1085(1)	20(1)
Ge(10)	4*i*	1	0.4722(4)	0	0.4419(2)	28(1)
Ni(11)	8*j*	1	-0.1075(3)	0.2551(3)	0.2859(2)	17(1)
Ni(12)	8*j*	1	0.2220(4)	0.2501(3)	0.4419(1)	20(1)
Ni(13)	4*i*	1	-0.0284(4)	0	0.4417(2)	20(1)
Ni(14)	8*j*	0.57(2)	0.4453(5)	0.2486(5)	0.3902(2)	18(1)

Table 3. Anisotropic displacement parameters ($Å^2 \times 10^3$) for $ErNi_{1.53(1)}Ge_2$. The anisotropic displacement factor exponent takes the form: $-2\pi^2[\, h^2\, a^{*2} U_{11} + \ldots + 2\, h\, k\, a^*\, b^*\, U_{12}\,]$

	U_{11}	U_{22}	U_{33}	U_{23}	U_{13}	U_{12}
Er(1)	14(1)	18(1)	25(1)	0	6(1)	0
Er(2)	17(1)	17(1)	20(1)	0(1)	7(1)	0(1)
Er(3)	14(1)	18(1)	25(1)	0	6(1)	0
Ge(4)	18(1)	12(1)	21(1)	-3(1)	4(1)	0(1)
Ge(5)	10(1)	18(1)	21(1)	0	9(1)	0
Ge(6)	10(1)	19(1)	21(1)	0	2(1)	0
Ge(7)	17(1)	18(1)	15(1)	0	6(1)	0
Ge(8)	17(1)	17(1)	28(1)	0	6(1)	0
Ge(9)	17(1)	21(1)	21(1)	0	6(1)	0
Ge(10)	18(1)	39(2)	28(2)	0	9(1)	0
Ni(11)	13(1)	11(1)	28(1)	-3(1)	8(1)	0(1)
Ni(12)	28(1)	14(1)	19(1)	0(1)	6(1)	0(1)
Ni(13)	9(1)	32(2)	20(1)	0	5(1)	0
Ni(14)	15(2)	17(2)	24(2)	0(1)	7(1)	-1(1)

APPENDIX 6.1

Single Crystal Structure of CeA_2Ge_2 (A = Au, Ag)

Introduction

Single crystal structure refinements of CeA_2Ge_2 (A = Au, Ag) are reported in this section. . The CeA_2Ge_2 crystallizes in the $CeAl_2Ga_2$-type[1] tetragonal structure, Pearson code t*I*10 and *Wyckoff* sequence *eda*. In this section, we report the refinement results by single crystal X-ray diffraction experiment.

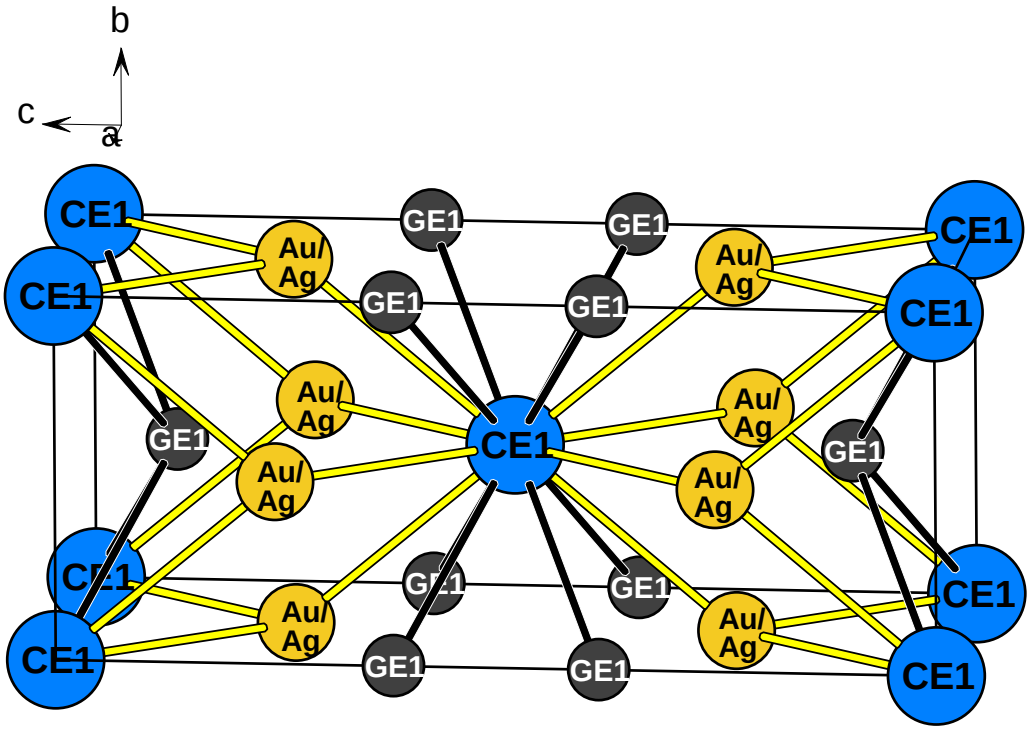

Discussion

Details of X-ray single crystal diffraction experiment structural data and crystallographic data recording/refinement parameters for $CeAu_2Ge_2$ and $CeAg_2Ge_2$

are listed in the Table 1. The refined site occupancies and fractional coordinates with isotropic / anisotropic thermal displacement parameters are listed in Table 2 & 3.

Table 1. Crystal diffraction data and structure refinement for CeA_2Ge_2 (A = Au, Ag).

Empirical formula	$CeAu_2Ge_{1.9(1)}$	$CeAg_2Ge_2$
Formula weight	679.23	501.04
Temperature	293(2) K	293(2) K
Wavelength	0.71073 Å	0.71073 Å
Crystal system	tetragonal	tetragonal
Space group	*I4/mmm* (no. 139)	*I4/mmm* (no. 139)
Unit cell dimensions	a = 4.3941(6) Å	a = 4.2958(6) Å
	c = 10.455(2) Å	c = 10.969(2) Å
Volume	201.87(6) $Å^3$	202.43(6) $Å^3$
Z	1	1
Absorption coefficient	48.971 mm^{-1}	17.478 mm^{-1}
F(000)	280	216
Crystal size	30 x 30 x 30 mm^3	30 x 30 x 30 mm^3
Theta range for data collection	3.90 to 34.74°.	3.71 to 34.29°.
Index ranges	$-6 \le h \le 6$, $-6 \le k \le 6$, $0 \le l \le 16$	$-6 \le h \le 6$, $-6 \le k \le 6$, $0 \le l \le 17$
Reflections collected	831	839
Independent reflections	153 [R(int) = 0.1648]	154 [R(int) = 0.0809]
Completeness to theta	98.7 %	100.00%
Refinement method	Full-matrix least-squares on F^2	
Data / restraints / parameters	153 / 0 / 10	154 / 0 / 9
Goodness-of-fit on F^2	1.171	1.247
Final R indices [I > 2sigma(I)]	R_1 = 0.0743, wR_2 = 0.1641	R_1 = 0.0296, wR_2 = 0.0476
R indices (all data)	R_1 = 0.0784, wR_2 = 0.1683	R_1 = 0.0332, wR_2 = 0.0484
Extinction coefficient	0.021(6)	0.033(2)
Largest diff. peak / hole	11.110 / -11.363 e.$Å^{-3}$	2.160 / -2.963 e.$Å^{-3}$

Table 2. Atomic coordinates and equivalent isotropic displacement parameters ($Å^2 \times 10^3$) for CeA_2Ge_2 (A = Au, Ag). U_{eq} is defined as one third of the trace of the orthogonalized U_{ij} tensor.

	Wyck.	Occupancy	x	y	z	U_{eq}
Ce	2*a*	1	0	0	0	15(1)
Au	4*d*	1	0	1/2	1/4	18(1)
Ge	4*e*	0.95(4)	0	0	0.3834(3)	16(1)
Ce	2*a*	1	0	0	0	15(1)
Ag	4*d*	1	0	1/2	1/4	18(1)
Ge	4*e*	1	0	0	0.3891(1)	16(1)

Table 3. Anisotropic displacement parameters ($Å^2 \times 10^3$) for CeA_2Ge_2 (A = Au, Ag). The anisotropic displacement factor exponent takes the form: $-2\pi^2[\, h^2\, a^{*2} U_{11} + \ldots + 2\, h\, k\, a^*\, b^*\, U_{12}\,]$

	U_{11}	U_{22}	U_{33}	U_{23}	U_{13}	U_{12}
Ce	14(1)	14(1)	25(1)	0	0	0
Au	20(1)	20(1)	33(1)	0	0	0
Ge	23(2)	23(2)	22(2)	0	0	0
Ce	15(1)	15(1)	14(1)	0	0	0
Ag	18(1)	18(1)	17(1)	0	0	0
Ge	18(1)	18(1)	13(1)	0	0	0

Reference

[1] Gignoux, D.; Schmitt, D.; Zerguine, M.; Bauer, E.; Pillmayr, N.; Henry, J. Y.; Nguyen, V. N.; Rossat-Mignod, J. *J. Magn. Mag. Mater*. **1988**, 74, 1.

APPENDIX 6.2

Single Crystal Structure of $RhZr_2$

Introduction

Single crystal structure refinements of $RhZr_2$ are reported in this section. The $RhZr_2$ crystallizes type in tetragonal Al_2Cu-type structure, which was first reported by Havinga by powder X-ray diffraction experiment.[1] In this section, we report the refinement results by single crystal X-ray diffraction experiment.

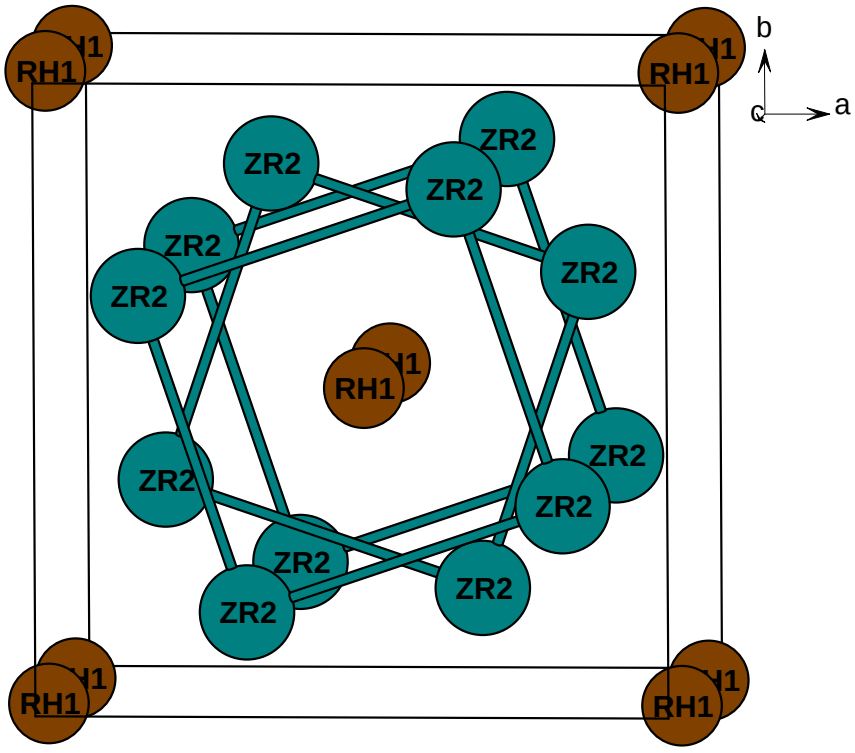

Discussion

Details of X-ray single crystal diffraction experiment structural data and crystallographic data recording/refinement parameters for $RhZr_2$ are listed in the Table 1. The refined site occupancies and fractional coordinates with isotropic / anisotropic thermal displacement parameters are listed in Table 2 & 3.

Table 1. Crystal diffraction data and structure refinement for $RhZr_2$.

Empirical formula	$RhZr_2$
Formula weight	142.68
Temperature	293(2) K
Wavelength	0.71073 Å
Crystal system	tetragonal
Space group	*I* 4/m c m (no. 140)
Unit cell dimensions	a = 6.4815(9) Å
	c = 5.5770(11) Å
Volume	234.29(7) $Å^3$
Z	4
Absorption coefficient	7.623 mm^{-1}
F(000)	250
Crystal size	35 x 40 x 35 mm^3
Theta range for data collection	4.45 to 29.20°.
Index ranges	$-5 \le h \le 6$, $0 \le k \le 8$, $0 \le l \le 7$
Reflections collected	164
Independent reflections	100 [R(int) = 0.0102]
Completeness to theta	100.0 %
Refinement method	Full-matrix least-squares on F^2
Data / restraints / parameters	100 / 0 / 8
Goodness-of-fit on F^2	0.911
Final R indices [I>2sigma(I)]	R_1 = 0.0114, wR_2 = 0.0198
R indices (all data)	R_1 = 0.0266, wR_2 = 0.0209
Extinction coefficient	0.0109(6)
Largest diff. peak and hole	0.838 and -0.500 e.$Å^{-3}$

Table 2. Atomic coordinates and equivalent isotropic displacement parameters ($Å^2 \times 10^3$) for $RhZr_2$. U_{eq} is defined as one third of the trace of the orthogonalized U_{ij} tensor.

	Wyck.	Occupancy	x	y	z	U_{eq}
Rh	4*a*	1	0	0	1/4	15(1)
Zr	8*h*	1	0.1653(1)	0.6653(1)	0	15(1)

Table 3. Anisotropic displacement parameters ($Å^2 \times 10^3$) for $RhZr_2$. The anisotropic displacement factor exponent takes the form: $-2\pi^2[h^2 a^{*2} U_{11} + ... + 2 h k a^* b^* U_{12}]$

	U_{11}	U_{22}	U_{33}	U_{23}	U_{13}	U_{12}
Rh	16(1)	16(1)	12(1)	0	0	0
Zr	15(1)	15(1)	14(1)	0	0	1(1)

Reference

[1] Havinga, E. E.; Damsma, H.; Hokkeling, P. *J. Less-Common Metals*. **1972**, 27, 169.

APPENDIX 6.3

Single Crystal X-Ray Diffraction Studies on Ternary $REFe_2Zn_{20}$ Compounds (RE = Gd, Tb)

Hyunjin Ko,[#] Shuag Jia,[%] Sergey L. Bud'ko,[&] Olivier Gourdon,[$] P. C. Canfield,[&] and Gordon J. Miller[#]*

[#] Department of Chemistry, Iowa State University and Ames Laboratory, Ames, Iowa 50011-3111,

[$] Los Alamos National Laboratory, Los Alamos, New Mexico 87545,

[%] Department of Physics and Astronomy, Iowa State University, Ames, Iowa 50011-3111

[&] Department of Physics and Astronomy, Iowa State University and Ames Laboratory, Ames, Iowa 50011-3111

ABSTRACT

Large single crystals of $GdFe_2Zn_{20}$ and $TbFe_2Zn_{20}$ have been grown in different flux concentrations and their crystal structures were analyzed by single crystal X-ray diffraction methods. The face-centered cubic lattices are found to be a = 14.1168(16) Å and 14.1232(16) Å for the $GdFe_2Zn_{20}$ system grown in a zinc-rich flux and an iron-rich flux, respectively. For the $TbFe_2Zn_{20}$ samples grown in a zinc-rich, Fe-defficient, and an Fe-rich flux compounds lattice constants are a = 13.9600(16) Å, 14.1062(16) Å, and 14.1019(16) Å. Chemical compositions were simultaneously examined by energy dispersive spectroscopy and compared with the results from the crystallographic studies. Also, the bonding interactions in $GdFe_2Zn_{20}$ and $GdCo_2Zn_{20}$ structures were studied by first principles calculations using the TB-LMTO method within density functional theory.

Introduction

The crystal structure of RET_2Zn_{20} (RE = rare-earth elements, T = transition metals) compounds, which has been reported by Jeitschko *et al*, adopts the face-centered cubic $CeCr_2Al_{20}$-type structure.[1] The structure type could be formed with many combinations of elements using rare-earth or early transition metals substituting RE elements and using aluminum instead of zinc.[2-4]

The initial motivation for this study was driven in search of materials with unusual magnetism by colleagues in the Ames Laboratory. For $GdFe_2Zn_{20}$ and $TbFe_2Zn_{20}$, the project was started with the particular interest to elucidate the mechanism of remarkably high ferromagnetic transition temperatures.[5] During multiple synthetic trials to grow crystals best suited for physical property measurements, we found anomalous behavior in the transition temperatures depending on the flux concentrations in which the crystals were grown. Thus, identifying accurate chemical compositions was critical to correctly establish any correlations between chemical composition and the physical properties. In this paper, we report single crystal X-ray refinement results of $GdFe_2Zn_{20}$ crystals grown in two different flux concentrations and $TbFe_2Zn_{20}$ crystals grown in three different concentrations. Also, the structural was examined with respect to orbital interactions within of $GdFe_2Zn_{20}$ and $GdCo_2Zn_{20}$ by electronic structure calculations.

Experimental

Synthesis Single crystals of $GdFe_2Zn_{20}$ and $TbFe_2Zn_{20}$ were prepared by the flux-growth method using Zn as a flux by mixing the pure elements and heating to elevated temperatures. $GdFe_2Zn_{20}$ crystals were grown in two separate flux concentrations: one in a “Zn-rich” flux loaded according to the mole ratio Gd : Fe : Zn

of 2 : 4 : 94 (crystal A) and another in a "Fe-rich" flux loaded according to Gd : Fe : Zn = 2 : 5 : 93 (crystal B). Three samples were grown for $TbFe_2Zn_{20}$ single crystals with a "standard" flux Tb : Fe : Zn = 2 : 4 : 94 (crystal C), a "Zn-rich" flux 1 : 2 : 97 (crystal D), and an "Fe-rich" flux 2 : 5 : 93 (crystal E). Detailed synthetic procedures are reported in a separate paper.[5]

Single Crystal Structure Refinements. Several single crystals of approximately $0.1 \times 0.1 \times 0.1$ mm dimensions were extracted from both $GdFe_2Zn_{20}$ and $TbFe_2Zn_{20}$ samples for X-ray structural determinations. Room-temperature X-ray diffraction data were collected on a *STOE-IPDS2* (Image Plate Diffraction System) single crystal diffractometer with Mo *K*α radiation (λ= 0.71073 Å; 50 kV and 40 mA) using a PG(002)-monochromator. A numerical absorption correction was applied to the data using program *X-shape* (*STOE*), which corrects symmetry equivalent reflections while optimizing a convex polyhedron for the crystal shape. The resulting polyhedron from the correction resembled the real crystal form as observed under the microscope. According to the large linear absorption of Gd, the consideration of the difference in the path lengths of symmetry equivalent reflections resulted in an improvement of R_{int} for all the crystals. The intensity data sets were used to solve and refine the crystal structures with the *SHELXTL* program suite. Structures were solved by direct methods and refined by full-matrix least squares against F^2 using all data.[6] Detailed data recording and refinement process conditions are shown in Table 1. The unit cell structure and local coordination environments around each element, as well as the electron density map for Tb systems are shown in Figures 1 and 2.

---------- Figures 1 and 2 ----------

---------- Tables 1 and 2 ----------

The distances between the imaging plate and the crystals were set at 100 mm for Gd-systems and 60mm for Tb-systems. Two additional single crystals from all the products were isolated to perform corresponding diffraction experiments and yielded very good agreement and confirmed the presented results. The total numbers of reflections of the data set recorded were A=7887, B=7904, and C=5290, D=5625, E=5685. The lattice was determined to have face-centered-cubic symmetry with unit cell parameters: a = 14.1168(16) Å and 14.1232(16) Å respectively (Z = 8) for A and B Gd-systems; and for Tb-systems: a = 13.9600(16) Å, 14.1062(16) Å, and 14.1019(16) Å respectively for C, D, and E.

---------- Tables 3 and 4 ----------

The positional parameters and mean square displacements are listed in Tables 3 and 4. The 20 parameters including the anisotropic thermal parameters and the site occupancies were simultaneously refined for all Zn and Fe atoms while the RE occupancy parameter was held constant. The refined parameters are listed in Tables 5 and 6.

---------- Tables 5 and 6 ----------

Powder Neutron Diffraction Time-of-flight (TOF) neutron diffraction data were collected at 11 K, 30 K and 295 K for crystal C on the Neutron Powder Diffractometer (NPDF) at the Manuel Lujan Neutron Scattering Center of Los Alamos National Laboratory. This instrument is a high-resolution powder diffractometer located at flight path 1, 32m from the spallation neutron target. The data were collected using the 148°, 119°, 90° and 46° banks, which cover a d-spacing range from 0.12 to 7.2 Å.

The structures at 295 K were qualitatively analyzed using the GSAS with a Rietveld profile analysis program.[7-9] The profile fitting and refinements were

performed using simultaneously the four banks (148°, 119°, 90° and 46°) for unit cell parameters, atomic positions, and equivalent isotropic displacement parameters as well as the background coefficients, scale factors, isotropic strain terms in the profile function, and sample absorption. However, the refinements processes to obtain accurate chemical composition were failed to get converged possibly due to the presence of the impurity Zn phase diffraction lines overlapping with the main phase lines.

Chemical Analysis One of the main purposes of this investigations was to carefully examine the effects of the flux concentrations on the corresponding compositions of the flux-grown single crystals. Therefore, it was imperative for us to have independent studies of the chemical compositions other than by means of X-ray diffraction analysis. All single crystal samples were cut in the middle and the cross sections were surveyed by the Energy Dispersive Spectroscopy (EDS) using a *JEOL 840A* scanning electron microscope, equipped with an *IXRF Systems Iridium X-ray analyzer* with *Kevex* Quantum thin-window Si(Li) detector for quantitative chemical analysis with standardless method and a 20 kV accelerating voltage and a 30 mA beam current. The results showed no significant oxygen content. For the Gd-systems A and B, the EDS analysis surveyed on ca. 10 points indicated that system crystallizes with close to fully occupied stoichiometric compositions. However, the Tb-systems showed slightly deviated Fe : Zn contents for each crystal, as shown in Figure 3.

---------- Figure 3 ----------

Electronic Structure Calculation To understand the electronic properties of these systems, electronic structures were calculated for $GdFe_2Zn_{20}$ and $GdCo_2Zn_{20}$ self-consistently by using the tight-binding linear muffin-tin-orbital (TB-LMTO)

method[10-13] within the atomic sphere approximation (ASA) using the *LMTO Version 47* program with a local spin density approximation (LSDA)[14] to treat exchange and correlation. All relativistic effects except spin-orbit coupling were taken into account using a scalar relativistic approximation.[15] The radii of the overlapping, space filling Wigner-Seitz (WS) atomic spheres were obtained by requiring the overlapping potential to be the best possible approximation to the full potential according to an automatic procedure.[16] The WS radii for the atomic sites determined by this procedure are in the ranges 2.146 Å for Gd, 1.506 Å for Fe, 1.550 Å for Co, and 1.655 - 1.670 Å for Zn. For $GdFe_2Zn_{20}$ calculations, the unit cell parameter is 0.41 % longer than for $GdCo_2Zn_{20}$, thus two additional sites were filled with empty spheres with WS radii of 0.815 - 0.865 Å. The basis set included 4*s*, 4*p* and 3*d* orbitals for transition metals, and for the rare-earth Gd atom, the 4*f* electrons were treated as core electrons, therefore only including 6*s* and 5*d* in the basis set. The reciprocal space integrations to determine the self-consistent charge density, densities of states (DOS) and crystal orbital Hamilton populations (COHP)[17] were performed by the tetrahedron method[18] using 301 irreducible *k*-points on the corresponding Brillouin zones.

Results and Discussions

Gd-Fe-Zn: Diffraction symmetry and systematic absences confirms the $Fm\bar{3}m$ spacegroup as reported by Jeitschko et.al. However, our studies indicated the possible mixing of Fe and Zn atoms in the 16*c* and 96*g* sites consistent with the corresponding concentrations of the flux that the crystals were grown in. For specimen (A), our data yielded a better refinement with shared site occupancies on the 16*c* metal sites and for specimen (B) further mixing on the 96*g* site. Strictly from the single crystal structure refinement results yielding the lowest refinement factors, the empirical formula for

(A) and (B) crystals, respectively, were determined to be $GdFe_{2.12(2)}Zn_{19.74(4)}$ and $GdFe_{5.125(2)}Zn_{18.375(1)}$.

Tb-Fe-Zn: The initial refinement results with lowest possible refinement factors showed similar mixing of the Fe and Zn atoms in the $TbFe_2Zn_{20}$ systems, but to a greater degree. When the crystals were grown in a Zn-rich flux, such as in crystal (D), only about 10% of the 16*c* site is shared with Fe atoms leading to a slightly richer Fe content in the unit cell than the 1 : 2 : 20 stoichiometric compound ($TbFe_{2.280(6)}Zn_{19.624(2)}$). Moreover, in the Fe-rich flux-grown crystal (E), further mixing occurs by replacing about 15% of the 16*c* site as well as a small sharing of about 3% into the 96*g* by Fe atoms, which gives rise to the higher Fe content of $TbFe_{2.640(3)}Zn_{19.378(3)}$. At this point, it is noticeable that only the 16*c* sites and 96*g* sites are tolerant for Fe atoms to partially occupy. However, again, our independent composition studies allowed us to accept the structure with no shared occupancies but with deficiencies in Zn sites to account for the decreased relative electron density. The final refinement results are summarized in Tables 2, 4, and 6.

---------- Figure 3 and 4 ----------

In Figure 4, the neutron powder diffraction pattern of $TbFe_2Zn_{20}$ with profile indexing lines are shown. We found the existence of a trace amount of elemental Zn in the powder pattern as noted in the shaded areas.

Fe atoms in the 16*d* sites occupy the center of one icosahedron coordinated by 12 Zn/Fe atoms in 96*g* and 48*f* sites, and the Zn atoms in 16*c* sites occupy the neighboring center of icosahedra also coordinated by Zn/Fe atoms. Alternating Fe-centered and Zn-centered icosahedra makes the fundamental tetrahedral building block of the lattice structure, sharing vertices with each other and giving rise to the network of icosahedra. The rare-earth metals in the structure are surrounded by 16

transition metals making a Frank-Kasper polyhedron.

Throughout the refinement processes on all crystals (A) – (E), similar problems occurred on refining the thermal displacement parameters of the 16*c* Zn1 sites and 16*d* Fe sites as shown in Tables 3 and 4. The observed thermal displacement parameters on Zn1 site were much larger than the other Zn sites. The Zn2 and Zn3 sites are both coordinating tightly around the Fe atoms at ca. 2.5 - 2.7 Å; on the other hand, the Zn1 atoms are only bound to the rare-earth metals at 3.056 Å, which results in the enlarged thermal displacement parameters. Also, the dense icosahedral coordination around Fe atoms gives rise to a shrinkage in their thermal displacement parameters.

Ideally, transition metal 3*d* orbitals are degenerate as 5 equivalent *hg* orbitals in a regular icosahedra field. Considering that the system is rich in Zn atoms and the Fe and rare-earth metals are only dilutively populated in the structure without any direct Fe-Fe interactions, the Fe atom would have two unpaired electrons resulting in a local magnetic moment close to its atomic local moment. Any significant increase or decrease in the local magnetic moment would suggest the possible existence of Fe-Fe interactions between Fe atoms at the center of the icosahedron and any Fe atoms composing the icosahedron, as well as a resulting decrease of the point symmetry. Assuming no mixed occupancies of Zn sites, the rare-earth metals are positioned in the center of the Frank-Kasper polyhedron coordinated by 16 Zn atoms.

In Figure 5, DOS and –COHP curves are drawn for $GdFe_2Zn_{20}$ (left) and $GdCo_2Zn_{20}$ (right). Zn 3*d* states are filled and well below the Fermi level for both systems. But going from Fe to Co does change the DOS curves: for instance, the Co 3*d* states in $GdCo_2Zn_{20}$ are split and widen showing two degenerate state profiles. In $GdFe_2Zn_{20}$, on the other hand, the Fe 3*d* states are narrowly concentrated around –2.5

eV. The Fermi energy of $GdFe_2Zn_{20}$ is closer to the Fe 3*d* states. From the COHP analysis, two sets of significant interactions were found between Fe-Zn, Co-Zn, and Zn-Zn contacts. In the Fe-system, Zn-Zn interactions are nearly optimized only filling bonding states, whereas Fe-Zn interactions are not optimized by filling part of their antibonding states. The same is observed for the Zn-Zn bonding optimization in the Co-system, but the Co-Zn interaction is nearly optimized. This possibility of shifting the bond orders without destabilizing too much in terms of total energy could explain the ease in the structure formation for the variety of compounds in this type of crystal structure.

Acknowledgements

This manuscript has been authored by Iowa State University of Science and Technology under Contract No. W-7405-ENG-82 with the U.S. Department of Energy. The United States Government retains and the publisher, by accepting the article for publication, acknowledges that the United States Government retains a non-exclusive, paid-up, irrevocable, world-wide license to publish or reproduce the published form of this manuscript, or allow others to do so, for United States Government purposes.

References

[1] Nasch, T.; Jeitschko, W.; Rodewald, U. *Z. Naturforsch*. **1997**, 52b, 1023.

[2] Gross, N.; Nasch, T.; Jeitschko, W. J. *Solid State Chem*. **2001**, 161, 288.

[3] Li, P.; Dai, S.; Li, C. *Mater. Sci. Eng*. **2000**, A 280, 128.

[4] Jackson, A.; Mahajan, Y.; Kirchoff, S. *Scr. Metall*, **1986**, 20, 1247.

[5] Jia, S.; Bud'ko, S.; Samolyuk, G.; Canfield, P. *Nat. Phys*. **2007**, 3, 334.

[6] SHELXTL; Brucker AXS, Inc.; Madison, WI, **1996**.

[7] Rietveld, H. M. *J. Appl. Crystallogr*. **1969**, 2, 65

[8] Hunter, B. A.; Howard, C. J. Rietica; Australian Nuclear Science and Technology Organization: Menai, Australia (2000).

[9] Quantum Design; Quantum Design, Inc.; San Diego, CA, **2000**.

[10] Andersen, O. K. *Phys. Rev.* **1975**, B12, 3060.

[11] Andersen, O. K.; Jepsen, O. *Phys. Rev. Lett.* **1984**, 53, 2571.

[12] Andersen, O. K.; Jepsen, O.; Glötzel, D. In *Highlights of Condensed-Matter Theory*; Bassani, F.; Fumi, F.; Tosi, M. P.; Lambrecht, W. R. L.; Eds.; North-Holland: New York, **1985**.

[13] Andersen, O. K. *Phys. Rev.* **1986**, B34, 2439.

[14] Von Barth, U.; Hedin, L. *J. Phys. C* **1972**, 5, 1629.

[15] Koelling, D. D.; Harmon, B.N. *J. Phys. C* **1977**, 10, 3107.

[16] Jepsen, O.; Anderson, O. K. *Z. Phys. B* **1995**, 97, 35.

[17] Dronskowski, R.; Blöchl, P. *J. Phys. Chem*. **1993**, 97, 8617.

[18] Blöchl, P. E.; Jepsen, O.; Andersen, O.K. *Phys Rev.* **1994**, B49, 16223.

[19] Hofmann, W.; Jaeniche, W. *Naturwissenschaften* **1935**, 23, 851.

[20] Desando, R.; Lange, R. *J. Chem. Phys*. **1949**, 17, 1293.

[21] Perricone, A.; Noël, H. *J. Alloys Compd.* **2004***,* 383, 251.

[22] Tremolet de Lacheisserie, E. du. *Magnetostriction: Theory and Applications of Magnetoelasticity.* Boca Raton, FL: CRC Press, **1993**.

[23] Hoffmann R. *Solids and Surfaces: A chemist's View of Bonding in Extended Structures*, VCH, 3 **1988**.

[24] Hoffmann, R. *J. Chem. Phys*. **1963**, 39, 1397.

[25] Burdett, J. K. Chemical Bonding in Solids, Oxford University Press, New York, **1995**.

[26] Ammeter, J. H.; Bürgi, H. B; Thibeault, J. C.; Hoffmann, R. *J. Am. Chem. Soc.* **1978**, 100, 3686.

[27] Pauling, L.; Kamb, B. *Proc. Natl. Acad. Sci. USA*, **1986**, 83, 3569.

[28] The Stuttgart Tight-Binding LMTO-ASA program Version 4.7; Max-Planck-Institut für Festkörperforschung, Stuttgart, Germany **1998**.

Table 1. X-ray single crystal diffraction experiment structural data and crystallographic data recording/refinement conditions for $GdFe_2Zn_{20}$

Crystal	**A**	**B**
Refined composition	$GdFe_2Zn_{20}$	$GdFe_2Zn_{20}$
Space Group	$Fm\bar{3}m$	$Fm\bar{3}m$
Z	8	8
Unit cell dimensions (Å)	a = 14.1168(16)	a =14.1232(16)
F(000)	2864	5732
Angular range 2θ	2.50 to 29.22°	2.50 to 29.20°
hkl ranges	$-19 \le h \le 19$	$-19 \le h \le 16$
	$-19 \le k \le 18$	$-19 \le k \le 19$
	$-19 \le l \le 17$	$-19 \le l \le 19$
Total reflection recorded	7887	7904
R_{int}	0.0793	0.1009
Absorption coefficient (mm^{-1})	19.974	39.872
Refinement method	Full-matrix least-squares on F^2	Full-matrix least-squares on F^2
Observed reflections ($I > 2\sigma(I)$)	217	217
Completeness to max 2θ (%, °)	99.5 / 29.22	99.5 / 29.20
Restraints	0	0
No. of refined parameters	17	17
GOodness-Of-Fit on F^2	1.445	1.456
Final R indices ($I > 2\sigma(I)$)	R_1 = 0.0268	R_1 = 0.0322
	wR_2 = 0.0554	wR_2 = 0.0790
R indices (all data)	R_1 = 0.0272	R_1 = 0.0322
	wR_2 = 0.0555	wR_2 = 0.0790
Extinction coefficient	0.00132(8)	0.00062(6)
Residual electron density ($Å^{-3}$, peak / hole)	1.814 / -0.928	0.991 / -1.257

Table 2. X-ray single crystal diffraction experiment structural data and crystallographic data recording/refinement conditions for $TbFe_2Zn_{20}$ single crystals C, D, & E.

Crystal	**C**	**D**	**E**
refined composition	$TbFe_2Zn_{19.1(4)}$	$TbFe_2Zn_{19.2(4)}$	$TbFe_2Zn_{20}$
Space Group	$Fm\bar{3}m$	$Fm\bar{3}m$	$Fm\bar{3}m$
Z	8	8	8
Unit cell dimensions (Å)	a = 13.9600(16)	a =14.1062(16)	a = 14.1019(16)
F(000)	2868	2868	2868
Angular range, θ	2.53 to 20.06°	4.09 to 34.56°	4.09 to 35.07°
hkl ranges	$-16 \le h \le 19$	$-22 \le h \le 22$	$-22 \le h \le 22$
	$-19 \le k \le 18$	$-22 \le k \le 22$	$-22 \le k \le 22$
	$-19 \le l \le 18$	$0 \le l \le 22$	$0 \le l \le 22$
Total reflection recorded	5290	5625	5685
R_{int}	0.2859	0.1314	0.0991
Absorption coefficient (mm^{-1})	20.816	20.176	20.194
Refinement method	Full-matrix least-squares on F^2	Full-matrix least-squares on F^2	Full-matrix least-squares on F^2
Observed reflections ($I > 2\sigma(I)$)	211	326	332
Completeness to max 2θ (%, º)	100 / 29.06	99.7 / 34.73	98.5 / 35.07
Restraints	0	0	0
No. of refined parameters	20	20	17
GOodness-Of-Fit on F^2	1.626	1.314	1.566
Final R indices ($I > 2\sigma(I)$)	R_1 = 0.0512	R_1 = 0.0636	R_1 = 0.0514
	wR_2 = 0.1260	wR_2 = 0.1355	wR_2 = 0.1327
R indices (all data)	R_1 = 0.0538	R_1 = 0.0679	R_1 = 0.0674
	wR_2 = 0.1268	wR_2 = 0.1371	wR_2 = 0.1745
Extinction coefficient	0.00058(9)	0.00081(10)	0.00100(18)
Residual electron density ($Å^{-3}$, peak / hole)	1.168 / -1.262	3.281 / -3.972	3.373 / -4.062

Table 3. X-ray single crystal diffraction experiment refined site occupancies and fractional coordinates with isotropic thermal displacement parameters for Zn-rich flux grown crystal A and Fe-rich flux grown single crystal B $GdFe_2Zn_{20}$.

Atom	*Wyck.*	Occ.	*x*	*y*	*z*	$U_{iso.}$
crystal A						
Gd	8*a*	1	1/8	1/8	1/8	0.006(1)
Zn1	16*c*	1	0	0	0	0.021(1)
Zn3	48*f*	1	1/8	1/8	0.4893(1)	0.010(1)
Zn2	96*g*	1	0.0587(1)	0.0587(1)	0.3266(1)	0.014(1)
Fe	16*d*	1	1/2	1/2	1/2	0.006(1)
crystal B						
Gd	8*a*	1	1/8	1/8	1/8	0.005(1)
Zn1	16*c*	1	0	0	0	0.020(1)
Zn2	48*f*	1	1/8	1/8	0.4893(1)	0.009(1)
Zn3	96*g*	1	0.0587(1)	0.0587(1)	0.3266(1)	0.014(1)
Fe	16*d*	1	1/2	1/2	1/2	0.005(1)

Table 4. X-ray single crystal diffraction experiment refined site occupancies and fractional coordinates with isotropic thermal displacement parameters for $TbFe_2Zn_{20}$ single crystals C, D, and E.

atom	*Wyck.*	Occ.	*x*	*y*	*z*	$U_{iso.}$
crystal C						
Tb	8*a*	1	1/8	1/8	1/8	0.004(1)
Zn1	16*c*	0.95(3)	0	0	0	0.015(2)
Zn2	96*g*	0.96(2)	1/8	1/8	0.4891(2)	0.05(1)
Zn3	48*f*	0.94(1)	0.0589(1)	0.0589(1)	0.3262(1)	0.009(1)
Fe	16*d*	1	1/2	1/2	1/2	0.004(1)
crystal D						
Tb	8*a*	1	1/8	1/8	1/8	0.008(1)
Zn1	16*c*	0.92(3)	0	0	0	0.018(2)
Zn2	96*g*	0.97(2)	1/8	1/8	0.4891(2)	0.010(1)
Zn3	48*f*	0.97(2)	0.0589(1)	0.0589(1)	0.3262(1)	0.015(1)
Fe	16*d*	1	1/2	1/2	1/2	0.007(1)
crystal E						
Tb	8*a*	1	1/8	1/8	1/8	0.009(1)
Zn1	16*c*	1	0	0	0	0.022(1)
Zn2	96*g*	1	1/8	1/8	0.4893(1)	0.013(1)
Zn3	48*f*	1	0.0589(1)	0.0589(1)	0.3263(1)	0.017(1)
Fe	16*d*	1	1/2	1/2	1/2	0.008(1)

Table 5. X-ray single crystal diffraction experiment refinement anisotropic displacement parameters for $GdFe_2Zn_{20}$ crystals A and B.

Atom	U_{11}	U_{22}	U_{33}	U_{12}	U_{13}	U_{23}
crystal A						
Gd	0.006(1)	0.006(1)	0.006(1)	0	0	0
Zn1	0.021(1)	0.021(1)	0.021(1)	-0.005(1)	-0.005(1)	-0.005(1)
Zn2	0.010(1)	0.010(1)	0.010(1)	-0.003(1)	0	0
Zn3	0.016(1)	0.016(1)	0.011(1)	-0.005(1)	-0.001(1)	-0.001(1)
Fe4	0.006(1)	0.006(1)	0.006(1)	0.000(1)	0.000(1)	0.000(1)
crystal B						
Gd	0.005(1)	0.005(1)	0.005(1)	0	0	0
Zn1	0.020(1)	0.020(1)	0.020(1)	-0.005(1)	-0.005(1)	-0.005(1)
Zn2	0.009(1)	0.009(1)	0.009(1)	-0.003(1)	0	0
Zn3	0.015(1)	0.015(1)	0.010(1)	-0.005(1)	-0.001(1)	-0.001(1)
Fe4	0.005(1)	0.005(1)	0.005(1)	0.000(1)	0.000(1)	0.000(1)

Table 6. X-ray single crystal diffraction experiment refinement anisotropic displacement parameters for $TbFe_2Zn_{20}$ single crystals C, D, and E.

	U_{11}	U_{22}	U_{33}	U_{12}	U_{13}	U_{23}
crystal C						
Tb	0.004(1)	0.004(1)	0.004(1)	0	0	0
Zn1	0.015(2)	0.015(2)	0.015(2)	-0.005(1)	-0.005(1)	-0.005(1)
Zn2	0.006(1)	0.006(1)	0.005(1)	-0.003(1)	0	0
Zn3	0.011(1)	0.011(1)	0.006(1)	-0.005(1)	-0.001(1)	-0.001(1)
Fe	0.004(1)	0.004(1)	0.004(1)	0.000(1)	0.000(1)	0.000(1)
crystal D						
Tb	0.008(1)	0.008(1)	0.008(1)	0	0	0
Zn1	0.018(2)	0.018(2)	0.018(2)	-0.006(1)	-0.006(1)	-0.006(1)
Zn2	0.010(1)	0.010(1)	0.011(1)	-0.003(1)	0	0
Zn3	0.017(1)	0.017(1)	0.011(1)	-0.005(1)	-0.001(1)	-0.001(1)
Fe	0.007(1)	0.007(1)	0.007(1)	-0.001(1)	-0.001(1)	-0.001(1)
crystal E						
Tb	0.009(1)	0.009(1)	0.009(1)	0	0	0
Zn1	0.022(1)	0.022(1)	0.022(1)	-0.005(1)	-0.005(1)	-0.005(1)
Zn2	0.013(1)	0.013(1)	0.013(1)	-0.003(1)	0	0
Zn3	0.018(1)	0.018(1)	0.013(1)	-0.005(1)	0.000(1)	0.000(1)
Fe	0.008(1)	0.008(1)	0.008(1)	-0.001(1)	-0.001(1)	-0.001(1)

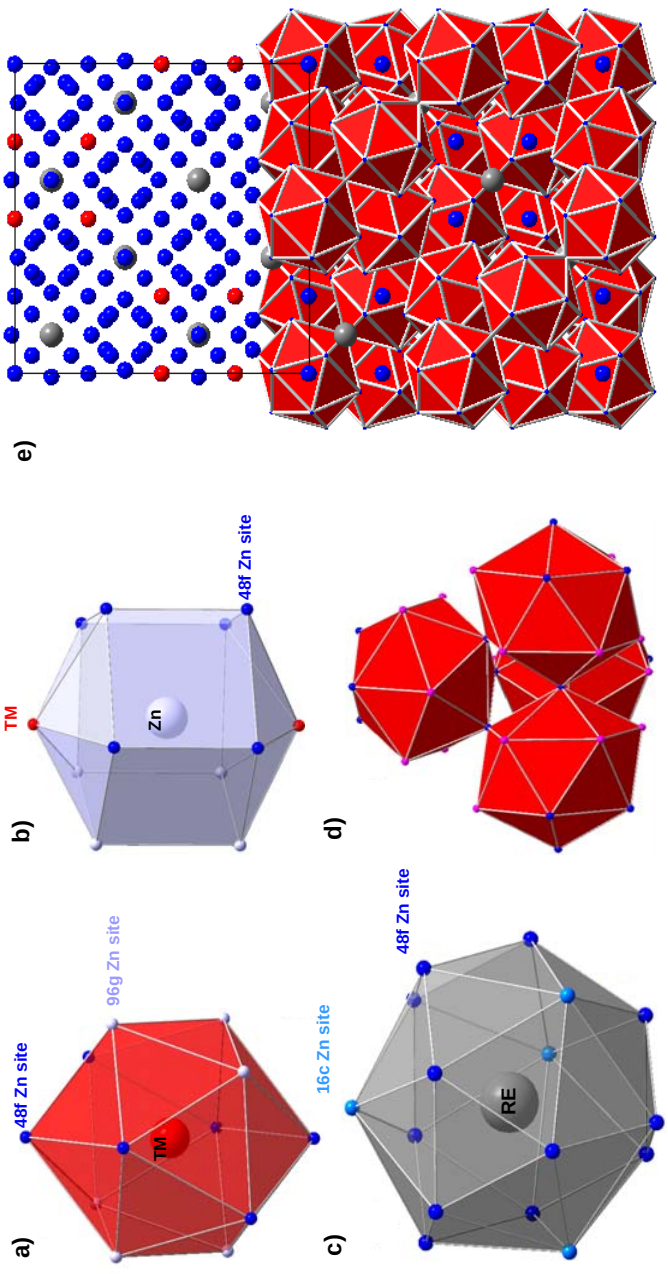

Figure 1. The $REFe_2Zn_{20}$ structure. The RE atoms are shown in grey, Fe in red, and Zn atoms are denoted in blue spheres. a) the icosahedron coordination around Fe atoms, b) Zn atoms coordinated by 10 Zn atoms and 2 Fe atoms. c) RE metals are coordinated by 16 Zn atoms making a Frank-Kasper polyhedron. d) Fe icosahedra network sharing vertices. e) unit cell projection view.

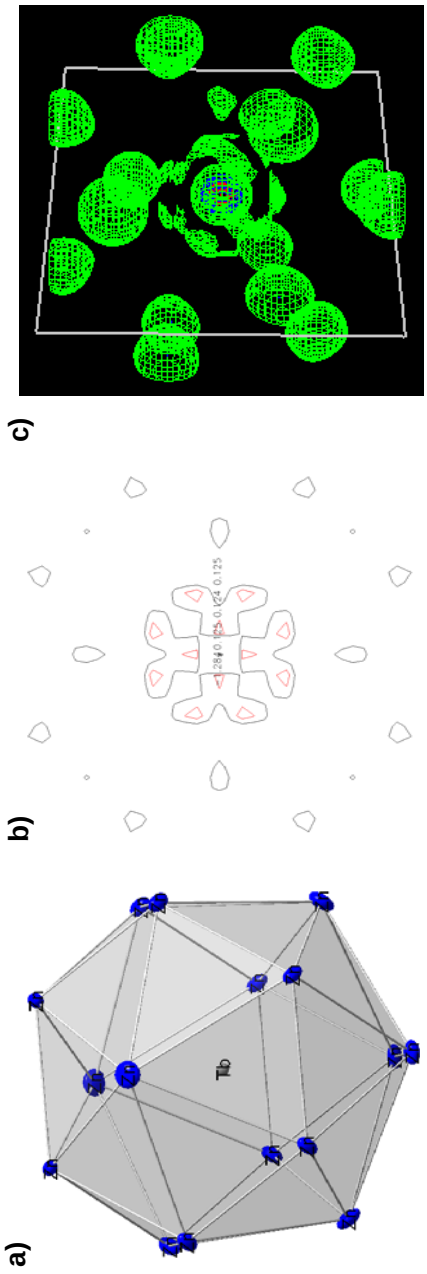

Figure 2. Thermal displacement ellipsoids and electron density maps on Tb and it's environment.

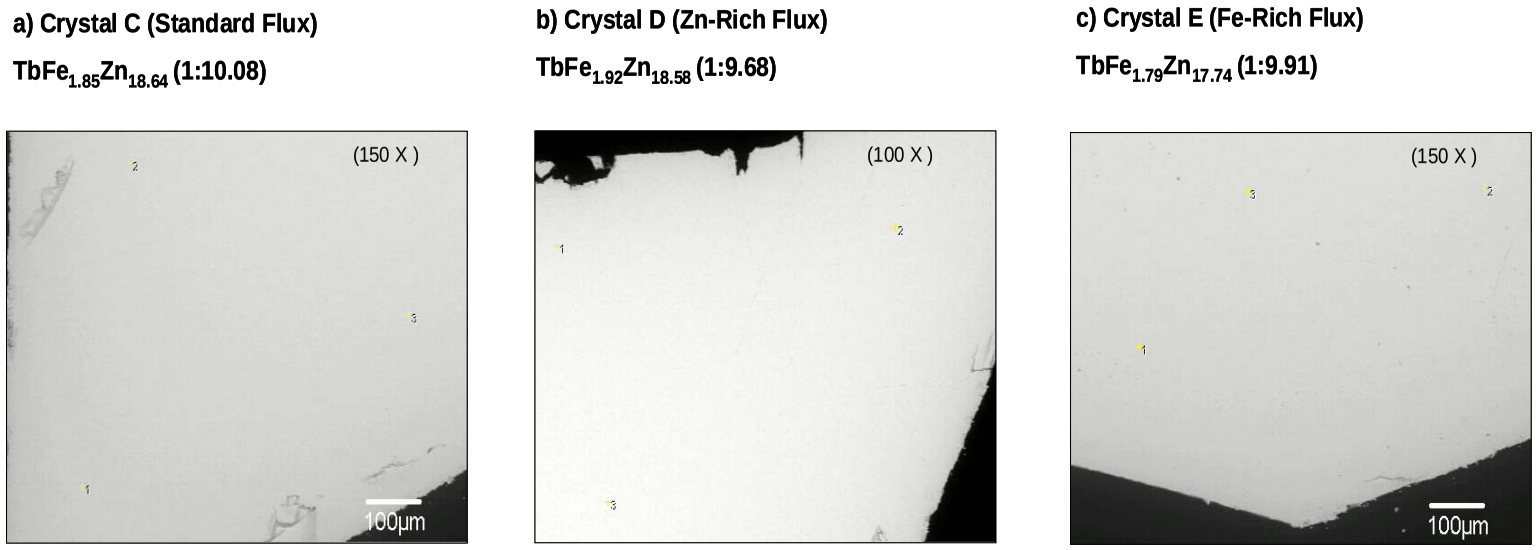

Figure 3. EDS chemical analysis on the single crystals C, D, and E.

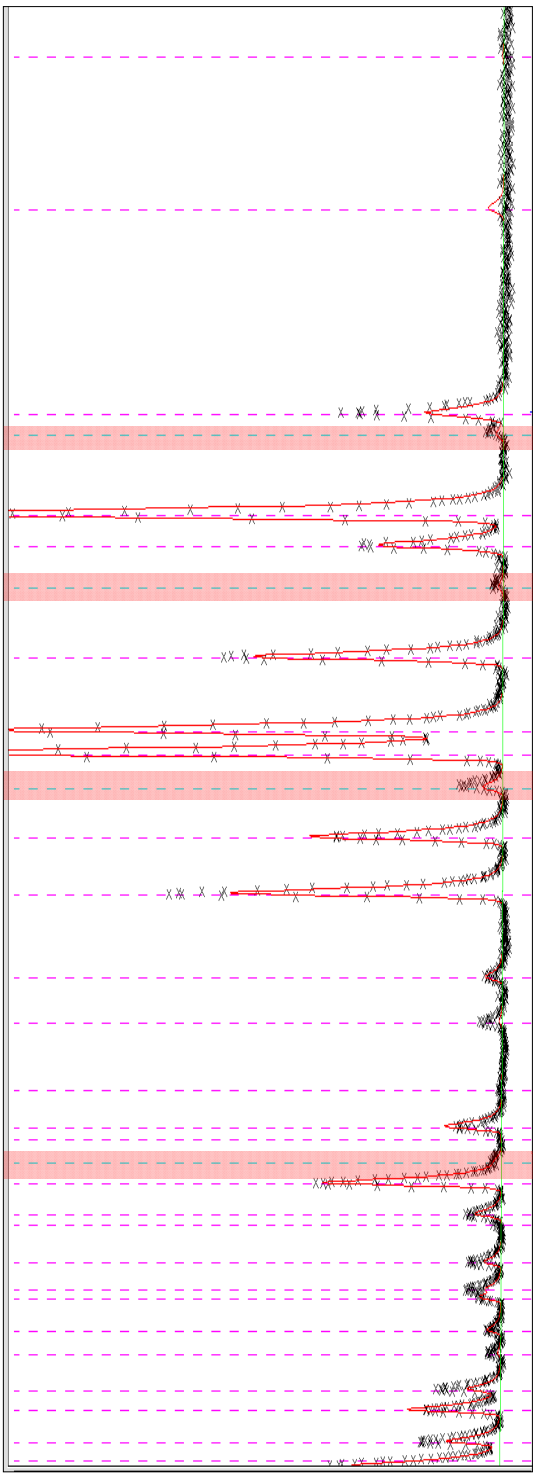

Figure 4. Neutron powder diffraction pattern of $TbFe_2Zn_{20}$. Elemental Zn phase lines are highlighted in pink shaded areas.

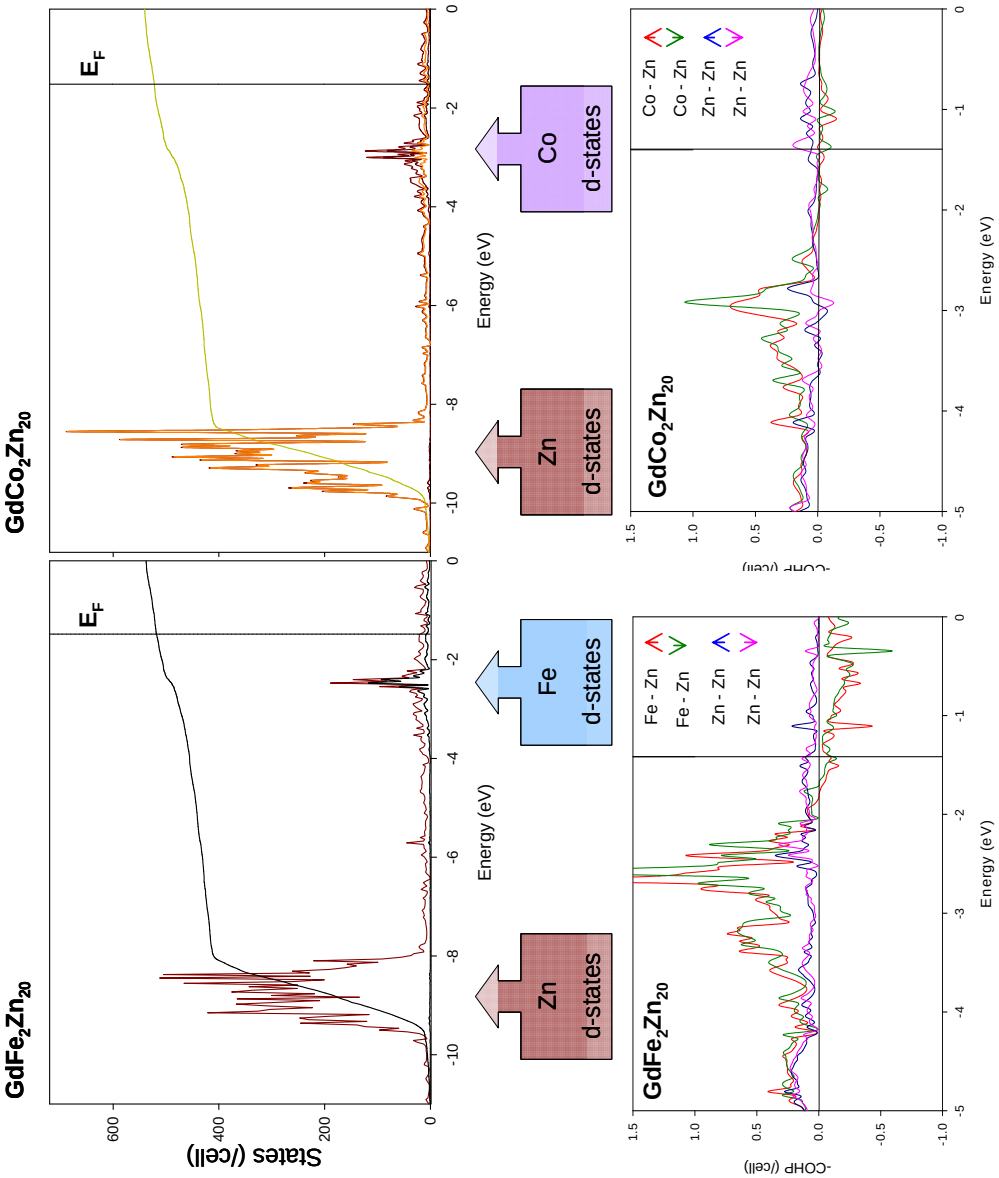

Figure 5. DOS and COHP curves of $GdFe_2Zn_{20}$ and $GdCo_2Zn_{20}$

Acknowledgements

My thesis reflects the help of a number of people. I would like to extend my gratitude to my advisor and committee chairman, Professor Gordon J. Miller, for his support and encouragement throughout my graduate studies. He's been a true mentor to me both professionally and personally. I would also like to give special thanks to my program of study committee members Professor John D. Corbett, Professor Mark Gordon, Professor L. Keith Woo, and Professor Vitalij Pecharsky for their insightful comments and suggestions. I would like to thank all previous and current members of the Miller group and my friends and family for their support which made it possible for me to survive the graduate student life.